The development of a post-growth technology for the fabrication of III-nitride based blue laser diodes

Zhirnov, Evgeny Nicolaevich

Award date:
2005

Awarding institution:
University of Bath

THE DEVELOPMENT OF A POST-GROWTH TECHNOLOGY FOR THE FABRICATION OF III-NITRIDE BASED BLUE LASER DIODES

Evgeny Nicolaevich Zhirnov

A thesis submitted for the degree of Doctor of Philosophy

University of Bath

Department of Physics

June 2005

ProQuest LLC
789 East Eisenhower Parkway
P.O. Box 1346
Ann Arbor, MI 48106-1346

Acknowledgments

This dissertation would not have been possible without the support and help from my family, colleagues, and friends. Special thanks go to my wife and my mother for their moral support and encouragement through all of my research.

I deeply appreciate the opportunity for my PhD study at Bath University that was provided by *Arima Optoelectronic Ltd.* and personally by the director of this Company and my supervisor Prof. Wang Nang Wang. Prof. Wang provided a friendly, supportive, and collaborative environment in our group. Without his personal guidance and support this dissertation would have been incomplete.

Many thanks go to Dr. Philip Shields and Mr. Alan Gott for reviewing this dissertation. Their suggestions and comments greatly improved the quality of this thesis.

I am indebted to Dr. Sergey Stepanov for growing a high quality laser structure and for his assistance through all of my study.

I would also like to thank all of my colleagues and friends from Bath for their moral support and fellowship.

Abstract

This thesis covers main aspects for the post-growth fabrication of GaN-based laser diodes. The related technological processes, developed and/or optimized within the research, are described. These include *p*-type GaN activation, inductively coupled plasma (ICP) etching, ridge waveguide fabrication, ohmic contacts formation, laser facet fabrication, and high reflectivity facet coating. All these processes combined together yielded a complete post-growth laser fabrication technology also presented in the thesis. Laser diodes were successfully fabricated using this technology and extensively characterized. The devices showed excelle nt electrical and reasonably good optical characteristics. The lowest threshold current density for lasing achieved under pulsed current operation was 48 kA/cm^2 for laser diodes with uncoated facets. Possible methods to improve laser performance are outlined in the thesis.

The developed technological processes are important and practical for other III-nitride applications. An innovative ridge waveguide fabrication process significantly simplifies the fabrication of any small-scale electronic devices. The study of thermal activation of *p*-type GaN demonstrates the catastrophic effect of a SiO_2 capping layer deposited by a plasma enhanced chemical vapor deposition (PECVD) technique on *p*-GaN layers during high temperature annealing. The study of ICP etching of AlGaN layers with Cl_2-based plasmas has significance for the plasma processing of III-nitrides.

This dissertation includes extensive theoretical and literature-review sections. The presented information provides essential background for fuller understanding of selected topics and also allows for some freedom in the processing. This makes this dissertation useful for further modification and/or optimization of the developed post-growth technology.

Contents

1 Introduction

1.1 Applications for III-nitrides

The III-nitrides, namely GaN, InN, AlN, and their alloys, cover the range of bandgaps from 0.7* to 6.2 eV. Furthermore, in a wurtzite form, these semiconductors have direct room temperature bandgaps that makes III-nitrides especially attractive for optoelectronic device applications, such as light emitting diodes (LEDs), laser diodes (LDs), and photo-detectors. Alloyed nitride semiconductors are expected to span a continuous range of photon energies from visible into ultraviolet wavelengths. Outstanding thermal and chemical stability makes III-nitrides promising for high-temperature applications. Excellent electron transport properties, including high electron mobility and high saturated drift velocity, suggest the nitrides are ideal for high-frequency electronic devices. Finally, nitrides possess very high breakdown fields, allowing to produce high-power electronic devices. Significant progress has been made in III-nitride growth and processing during the last fifteen years. As a result, a large number of commercial applications have entered the market. This section outlines the primary applications for III-nitrides with special attention paid to III-nitride based laser diodes and their use in optical data-storage devices.

The largest market for III-nitrides is light emitting diodes (LEDs) used for lighting and illumination. The worldwide market for LEDs has grown nearly 50% per year since 1995 and is projected to exceed $3.0 billion in 2005 (Strategies Unlimited, 2003). Nitride-based blue and green LEDs are widely used for signaling, back-lighting, interior and exterior automotive lighting, decorative and household lighting, large-area displays, traffic lights, etc. Their small size, low operation voltage, and long lifetime make LEDs an ideal choice for these applications. The largest market segment (over 40%) for these devices is currently in mobile appliances such as back-lighting for cell phones, cameras, LCD displays, etc. Another important application for blue-violet LEDs is solid-state white-light sources produced either with phosphor wavelength converters or in combination with red and green LEDs. At the moment this market segment is less than 5% of the total LED market. However, it is expected to grow sixfold from $85 million in 2002 to over $500 million in 2007 (Strategies Unlimited, 2003). LEDs offer compactness and lower energy consumption compared to conventional light bulbs. It is expected that solid-state light sources will become ten times more efficient than incandescent lamps and twice as efficient as fluorescent lamps.[1] LEDs also reduce maintenance costs due to their significantly longer lifetimes. Finally, these devices will significantly improve light colour performance providing higher Colour Rendering Index (CRI). For the wide use of solid-state lighting, some major technological issues need to be solved including cost reduction, improvement in light extraction efficiency and colour performance, heat management, photon mixing, etc. The solid-state lighting industry aims to replace conventional incandescent lamps by 2007 and most fluorescent lamps by 2012. Thereby this market sector can become the largest for LEDs in the near future, as the general illumination market is over $12 billion.

Another promising market for III-nitrides is blue-violet laser diodes for optical data-storage, laser printing, optical scanners, high-resolution photolithography, biomedical technology, sensing, telecommunication devices, laser projection displays, etc. This market is rapidly growing and is projected to reach over $400 million in 2007 (Strategies Unlimited, 2003). This figure assumes a nearly eightfold reduction in the laser diode price,

* Different papers give different values of the bandgap for InN, ranging from 0.7 to 1.9 eV.

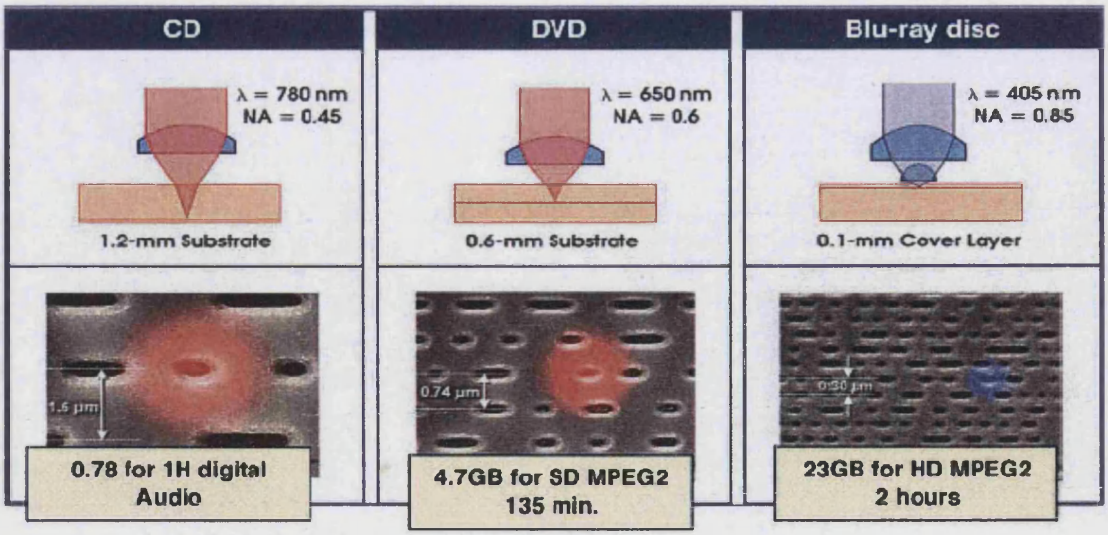

Fig. 1.1. Comparison of different optical data-storage formats.

namely $40 per device in 2007 compared to $300 at present. The major market segment for the nitride laser diodes is optical data-storage devices (CDs and DVDs). These applications are related to a reduced laser spot size caused by a shorter wavelength. It is known that the spot size of a focused laser beam is diffraction limited and is proportional to the square of the laser wavelength. As a result, replacing conventional infrared (780 nm) and red (650 nm) lasers, employed in present CD and DVD devices, respectively, with a blue laser diode allows for smaller pits, presenting 1 and 0 of digital data. Thereby more information can be saved on the same size optical disc. Current DVD technology has some additional improvements in optics and error correction that allow optical disc capacity to increase by an additional factor of four. It results in 4.7 GB of data on a present single-layer DVD disc compared with 650 MB on a present CD disc. A blue laser can increase the storage capacity further. Comparison of different optical data-storage formats is presented in Fig. 1.1.[2] It is worth noting that a 400 nm wavelength range is probably a limit for the developed optical disc technology due to the plastics and polymers used in the discs. These have strong absorption below 400 nm.

The increased storage capacity for optical discs makes it possible to move the media industry towards high-definition television (HDTV). A next-generation optical disc format, called Blu-Ray, has been recently developed by thirteen leading electronics companies to meet requirements for HDTV (official web-site http://www.blu-ray.com/). This format, employing a 405 nm laser diode, enables the recording, rewriting, and playback of up to 27 GB of data on a single-sided single-layer disc. This is sufficient to record over 2 hours of high-definition or more than 13 hours of standard-definition TV. A dual-layer disc doubles the storage capacity. The first Blu-Ray DVD recorder, announced by Sony in 2003, is now available for a price of around $3,800. However, recent progress made in the technology and strong competition for the developing market can reduce this price significantly. It is important to note that a number of alternative technologies, also employing blue laser diodes, have been developed for high-density optical storage. Toshiba and NEC developed a format called Advanced Optical Disc (AOD). This uses a 405 nm laser diode and allows slightly lower storage capacity (20 GB on a single-sided single-layer disc). However, this format is compatible with a current DVD encoding system and new devices can be produced in existing DVD plants. Another format, called Enhanced Versatil Disk (EVD), has been developed by Sanyo. It is expected to hold 54 GB of data on a single-sided single-layer disc compared to 27 GB of Blu-Ray. It is expected

that new high-density DVD devices will replace the current DVD technology within the next few years, regardless of the format finally employed.

Blue-violet laser diodes are very attractive for other applications such as laser printing, optical scanners, and high-resolution photolithography. These applications are also related to the reduced laser spot size allowing a significant increase in resolution. For example, current commercial laser printers employing a 780 nm laser diode with a typical optical system, provide a resolution of 600 dot-per-inch (dpi). Higher resolution requires more complicated and expensive optical systems. However, with the typical optics, a 400 nm laser diode can double this resolution. Another promising application for a nitride laser diode is laser projection displays. With the addition of a blue laser to existing red and green laser diodes, full-color high-resolution display devices can be produced. These devices may replace expensive halide lamp projection technology in the future. Blue-violet laser diodes can also play an important role for a number of sensing applications including fluorescence spectroscopy, detection of chemical, biological weapons, explosives, etc. They are very useful for a variety of biomedical applications such as cancer diagnostics, tissue welding, acne treatment, etc. An outstanding review on blue LD and LED applications has been recently presented by Bergh.

1.2 Progress in III-nitride laser diodes

Optically pumped stimulated emission from GaN was first observed more than 30 years ago.[3] However, low quality epitaxial layers and difficulties to obtain *p*-type material hindered the realization of current-injection laser diodes. The first significant breakthrough was the use of AlN[4, 5] or GaN[6] nucleation layers to obtain high-quality GaN films. Subsequently, *p*-type conductivity was achieved by low-energy electron beam irradiation (LEEBI) treatment,[7] by thermal annealing,[8] and by minority-carrier injection.[9] Finally, in 1992 Nakamura and Mukai[10] first succeeded in growing high-quality InGaN films. As a result, the first InGaN/GaN double-heterostructure (DH) LED and the first InGaN MQW pulsed LD were demonstrated by Nakamura *et al.* (Nichia Chemical Industries) in 1993[11] and in 1995,[12] respectively. In 1996 the same group reported the first room-temperature (RT) continuous wave (CW) operation with a lifetime of ~1 s,[13] and a year later they improved the laser lifetime to more than 10,000 h.[14] Subsequently a number of other groups around the world have demonstrated laser emission from III-nitride structures by electrical pumping, some of them have also reached CW operation.

An up-to-date review of fabricated III-nitride laser diodes, based on available published results, is presented in Table 1-1. As can be seen, leading players in this field are well-known companies producing semiconductors and electronics, such as Nichia (Japan), Toyoda Gosei (Japan), Sony (Japan), Toshiba (Japan), Fujitsu (Japan), Sharp (Japan/UK), Sanyo (Japan), Pioneer (Japan), NEC (Japan), NTT (Japan), Matsushita (Japan), Cree (USA), Xerox (USA), Agilent Technologies (USA), Osram (Germany), Samsung (Korea), and Unipress (Poland). Some companies (Nichia, Sony, Cree, and Samsung) are already at the commercial stage of laser diode production. At the same time only four universities, including Meijo University (Japan), University of California (Santa Barbara, USA), University of Bremen (Germany), and Fraunhofer-Institut für Angewandte Festkörperphysik (Germany), have reported on successful realization of III-nitride pulsed laser diodes. However, CW operation has yet to be achieved by a university. To our knowledge, we are the first university in the UK to successfully fabricate a pulsed GaN-based laser diode. A fabrication process and characteristics of our devices are presented in Chapter 9. Recently Sheffield University also demonstrated a III-nitride laser diode, but post-growth processing was made in China. On the contrary, we conducted growth and all processing steps in-house at Bath University.

Table 1-1. A review of fabricated III-nitride laser diodes.

Year (paper submission)	Organization	Lasing/ Lifetime	λ (nm)	J_{th} (kA/cm^2)	U_{th} (V)	P_{max}/facet (mW)	Diff. Quantum Effic./facet (%)	Substrate	Facets	Laser type/ geometry (μm)	HR facet coatings (%)	Reference
1995	**Nichia Chem. Ind.**	pulsed	417	4.0	34.0	215.0	13.0	c-face sapphire	etched	Stripe/ 1500×30	Front: 70 Rear: 70	12
		pulsed	416	9.6	26.0	76.0	4.2	a-face sapphire	cleaved	Stripe/ 1200×20	Front: 70 Rear: 70	15
1996	**Nichia Chem. Ind.**	pulsed	410	8.0	28.0	44.0	3.3	(111) $MgAl_2O_4$	polished	Stripe/ 1500×20	Front: 70 Rear: 70	16
		pulsed	419	13.0	28.0	33.0	12.0	(111) $MgAl_2O_4$	polished	Stripe/ 500×10	Front: 70 Rear: 70	17
		pulsed	411	3.0	24.0	3.5	30.0	a-face sapphire	cleaved	Ridge/ 600×10	Front: 70 Rear: 70	18
		pulsed	404	6.4	11.0	300.0	13.0	c-face sapphire	etched	Ridge/ 700×2	Front: 30 Rear: 30	19
		233 K cw/ >30 min	411	8.7	11.0	9.5	8.0	c-face sapphire	etched	Ridge/ 600×4	Front: 30 Rear: 30	20
		RT cw/ 1 s	408	9.0	8.0	5.0	5.0	c-face sapphire	etched	Ridge/ 700×2	Front: 30 Rear: 30	13
		RT cw/ 24-40 min	400	7.0	6.5	5.0	5.0	c-face sapphire	etched	Ridge/ 300×4	Front: 30 Rear: 30	21
		RT cw/ 27-35 h	405	3.6	5.5	-	-	c-face sapphire	etched	Ridge/ 550×4	Front: 30 Rear: 30	22 23 24
	Meijo Univ., Japan &Toyoda Gosei &Pioneer Corp.	pulsed	376	2.9	16.0	-	-	c-face sapphire	cleaved	Stripe*/ 1000×10	no	25
	Toshiba Corp.	pulsed	417	50.0	20.0	-	-	c-face sapphire	cleaved	Stripe*/ 1000×10	no	26
1997	**Nichia Chem. Ind.**	RT cw/ -	400	4.0	7.0	40.0	-	c-face sapphire	etched	Ridge/ 550×4	Front: no Rear: yes	27
		RT cw/ 100 h	400	8.8	5.5	-	-	c-face sapphire	etched	Ridge/ 550×4	Front: 50 Rear: 50	28
		RT cw/ 300 h	416	4.2	4.3	50.0	13.0	c-face sapphire	etched	Ridge/ 450×4	Front: 50 Rear: 50	29
		RT cw/ >1150 h	397 404 401	4.0	5.0	-	-	ELOG on c-sapphire	etched	Ridge/ 300×4 550×4	Front: 50 Rear: 50	30 31 32
		RT cw/ >10 000 h	401	3.0	4.9	-	-	ELOG on c-sapphire	etched	Ridge/ 450×4	Front: 50 Rear: 50	14
	Fujitsu Lab.	pulsed/ >5 h	414	16.0	140.0	20.0	-	6H-SiC	cleaved	Ridge/ 700×3.5	no	33
	Cree Research Inc.	pulsed/ >1 h	403	48.0	42.0	-	-	6H-SiC	cleaved	Ridge/ 500×...	no	34
	Univ. of California, Santa Barbara, USA	pulsed/ >6 h	420	12.6- -19.0	-	17.6- -67.0	1.1- -4.2	c-sapphire a-sapphire	etched cleaved	Stripe*/ 400-2000× ×3-20	no	35 36 37 38
	Xerox Palo Alto Research Center	pulsed	426	25.0	18.0	20.0	-	c-face sapphire	etched	Stripe*/ 500×4	no	39
	Toshiba Corp.	pulsed	414	20.0	-	-	-	c-face sapphire	cleaved	Inner stripe	-	40
		pulsed	413	10.6	18.0	20.0	5.3	c-face sapphire	cleaved	Stripe*/ 500×10	no	41
1998	**Nichia Chem. Ind.**	RT cw/ 780 h	393	7.0	6.0	-	-	GaN	etched	Ridge/ 550×3	Front: 50 Rear: 50	42
		RT cw/ 10 000 h	409	5.0	6.0	90.0	-	GaN	etched/ cleaved	Ridge/ 450×3	Front: 50 Rear: 50	43
		+50 °C cw/ 180 h	411	7.0	6.0	160.0	26.0	GaN	cleaved	Ridge/ 400×3	Front: 50 Rear: 50	44
		+50 °C cw/ 160-250 h	408	1.2- -3.0	6.0	420.0	39.0	ELOG on c-sapphire	cleaved	Ridge/ 450×3	Front: no Rear: 50	45 46 47
		+50 °C cw/ 160 h	400	6.0	5.0	30.0	-	GaN	cleaved	Ridge/ 450×2	Front: no Rear: 50	47 48
	Meijo Univ., Japan & Hewlett-Packard	pulsed	410	30.0	18.0	-	-	c-face sapphire	FIB etched	Ridge/ 500×5	no	49 50

	Fujitsu Lab.	pulsed	405--427	12.0	15.0	100.0	-	6H-SiC	cleaved	Ridge/ 700×4	Front: 90 Rear: 90	51 52
		250 K cw/ 1 s	406	12.0	12.6	-	-	6H-SiC	cleaved	Ridge/ 700×4.5	Front: 90 Rear: 90	53
		RT cw/ -	408	5.6	12.0	-	-	6H-SiC	cleaved	Ridge/ 500×3	Front: 90 Rear: 90	54
	Pioneer Corp.	pulsed	411	41.0	35.0	-	-	a-face sapphire	cleaved	Ridge/ 500×4	no	55
	Univ. of California, Santa Barbara, USA	pulsed	420	-	-	-	2.5	c-face sapphire	FIB polished	Stripe*/ 400×...	no	56
	Xerox Palo Alto Research Center	pulsed	419--432	20.0--44.0	19.0	50.0	-	c-face sapphire	etched	Stripe*/ 300-1000× ×4-20	no	57
		pulsed	403	16.0	16.0	-	-	c-face sapphire	etched + 3rd DFB	Stripe*/ 1000×20	no	58 59
		pulsed	401	5.7	9.0	50.0	15.0	c-face sapphire	etched	Ridge/ 300-1000× ×4-20	Front: yes Rear: yes	60
	Sony Corp.	pulsed/ >5 h	418	9.5	18.0	60.0	-	c-face sapphire	cleaved	Stripe*/ 1800×5	no	61
		RT cw/ -	411	11.7	11.5	-	-	c-face sapphire	cleaved	Ridge/ 1000×4	Front: 64 Rear: 88	62
	Cree Research Inc.	pulsed	407	7.1	15.7	-	0.8	*n*-6H-SiC	cleaved	Stripe*/ 500-600× ×3-5	Front: 93 Rear: 99	63
1999	**Nichia Chem. Ind.**	+50 °C cw/ 3 000 h	409	3.6--3.9	4.3--5.1	30.0--40.0	-	pendeo on c-sapphire	cleaved	Ridge/ 450×2 600×2	Front: no Rear: 50	64 65 66
		RT cw/ 200 h	450	4.6	6.1	-	-	ELOG on c-sapphire	cleaved	Ridge/ 650×2	Front: no Rear: 50	67
	Xerox Palo Alto Research Center	RT cw/ >1 h	401 402 407	8.3--8.9	6.3--6.5	3.0	2.9--5.7	a-face sapphire	etched	Ridge/ 300-1500× ×3	Front: yes Rear: yes	68 69 70 71
	Fujitsu Lab.	RT cw/ 57 h	404	4.0	8.3	-	-	4H-SiC	cleaved	Ridge/ 500×3	Front: 90 Rear: 90	72 73
	Meijo Univ., Japan & Hewlett-Packard	pulsed	405	15.0	15.0	30.0	8.1	c-face sapphire	-	Ridge/ 500×3	-	74
	Sony Corp.	RT cw/ -	400	4.1	9.0	35.0	-	c-face sapphire	cleaved	Buried-ridge/ 700×2-4	-	75 76 77
	Pioneer Corp.	pulsed	399	13.8	24.0	-	-	a-face sapphire	cleaved	Ridge/ 1000×5	no	78
	Univ. of California, Santa Barbara, USA	pulsed	420	4.8	21.8	-	-	ELOG on c-sapphire	etched	Ridge/ 400-1600× ×5-15	no	79 80
		pulsed	414	52.0	-	20.0	-	-	etched+ 3rd DFB	Stripe*/ 800×5	-	81 82
	NEC Corp.	RT cw/ -	408	10.9	10.5	-	-	FIELO *n*-GaN	cleaved	Ridge/ 440×3	Front: 93 Rear: 93	83
		RT cw/ -	412	5.4	7.5	-	-	FIELO *n*-GaN	cleaved	Ridge/ 330×2-4	Front: 95 Rear: 95	84 85
	Matsushita Electric Industrial Corp.	RT cw/ -	395	11.0	11.4	-	-	c-face sapphire	cleaved	Ridge/ 1000×4	Front: 58 Rear: 94	86
	Samsung Advanced Inst. of Technology	pulsed	415--421	20.3	16.5	-	-	c-face sapphire	etched	Stripe*/ 800×10	no	87 88
		pulsed	401	25.5	15.1	-	-	c-face sapphire	3rd DBR/ edge emitting	Ridge/ 500×3	-	89
2000	**Nichia Corp.** *(without S.Nakamura)*	+60 °C cw/ 15 000 h	405	2.8	4.5	30.0	-	ELOG on bulk GaN	cleaved	Ridge/ 650×1.8	Front: no Rear: 50	90 91
		+50 °C cw/ 5 000 h	450	2.8	4.5	-	-	ELOG on bulk GaN	cleaved	Ridge/ 650×2.5	Front: 50 Rear: 50	92 93
	Sony Corp.	RT cw/ >500 h	407	3.6	4.9	35.0	-	pendeo on c-sapphire	cleaved	Ridge/ 500-750× ×2-3.5	Front: 10 Rear: 95	77 94 95
	Xerox Palo Alto Research Center	RT cw/ 1 h	402	10.0	5.4--7.3	-	-	c-sapphire a-sapphire	etched	Ridge/ 300×2-4	Front: 95 Rear: 95	96
		RT cw/ >15 h	400	5.9--7.8	7.5	20.0	-	ELOG on c-sapphire	etched	Ridge/ 400-800×2	Front: no Rear: 90	97 98
		RT cw/ -	400	6.5	5.9--8.1	30.0--100.0	22.0	ELOG on c-sapphire replaced by copper	etched	Ridge/ 400-800× ×2-3	Front: no Rear: 90	99 100 101
	OSRAM Opto Semiconductors	pulsed	416--428	17.0	25.0	-	-	*n*-SiC	cleaved	Stripe*/ 600-1200× ×3-8	Front: 50 Rear: 98	102 103

	Agilent Technologies	RT cw/ >2 min	401	9.1	7.6	-	-	sapphire	etched	Ridge/ 1100×2	Front: no Rear: yes	104
	Toyoda Gosei Corp.	RT cw/ -	408	4.0	8.0	-	-	sapphire	etched	Stripe/ 300-700× ×2-5	Front: 80 Rear: 90	105
2001	**Nichia Corp.** *(without S.Nakamura)*	+50 °C cw/ 3 000 h	460	3.3	4.6	-	-	ELOG on bulk GaN	cleaved	Ridge/ 675×2.5	Front: 50 Rear: 50	91 106
		RT cw/ 500-2 000 h	369- -372	3.5	4.6- -4.8	-	-	ELOG on c-sapphire	etched	Ridge/ 600×2.5	Front: 50 Rear: 50	91 107 108 109
	Sony Corp.	+50 °C cw/ >1 000 h	409	2.8	4.8	50.0	-	pendeo on c-sapphire	cleaved	Ridge/ 600×2.3	Front: 10 Rear: 95	110 111
		RT cw/ -	409	4.3	-	150.0	-	pendeo on c-sapphire	cleaved	Ridge/ 600×1.7	-	112
		+60 °C cw/ 15 000 h	410	3.7	4.1	100.0	-	pendeo on c-sapphire	cleaved	Ridge/ 600×1.5	Front: 10 Rear: 95	113 114
	NEC Corp.	pulsed	-	1.6	-	40.0	-	FIELO *n*-GaN	cleaved	Ridge by selective re-growth	Front: 80 Rear: 95	115 116
	NTT Corp.	pulsed	401	26.0	21.5	-	-	*n*-6H-SiC	etched+ selective regrowth	HMF	-	117
2002	**Nichia Corp.** *(without S.Nakamura)*	RT cw/ -	480	5.4	5.8	-	-	ELOG on bulk GaN	cleaved	Ridge/ 600×2.5	Front: 50 Rear: 50	118
	Xerox Palo Alto Research Center	RT cw/ -	399	5.4	5.8	100.0	-	ELOG on c-sapphire replac. by diamond	etched	Ridge/ 800×2	Front: no Rear: 90	119
	Univ. of California, Santa Barbara, USA *(with S. Nakamura)*	pulsed	420	8.0	12.0- 15.0	-	-	ELOG on c-sapphire	etched	Ridge/ 400-1600× ×2-15	no	120
	OSRAM Opto Semiconductors	RT cw/ 143 h	407	5.3	5.9	-	-	*n*-SiC	cleaved	Ridge/ 600×2.5	Front: 70 Rear: 98	121
	Univ. of Bremen, Germany &Swiss Federal Inst. of Technology, Switzerland	pulsed	401	16.2	35.0	262.0	-	c-face sapphire	RIE etched + crystallog. wet etched	Stripe*/ 500×20	Front: no Rear: yes	122
	High Pressure Research Center Unipress, Poland	pulsed	402- -427	10.0	30.0	-	3.0	bulk *n*-GaN	cleaved	Ridge/ 500×10	Front: 50 Rear: 50	123
	OSRAM Opto Semiconductors &Univ. Stuttgart, Germany	pulsed	408	66.0	11.2	-	-	*n*-SiC	2nd DBR/ surface emitting	Ridge/ 500×2	-	124
2003	**Nichia Corp.** *(without S.Nakamura)*	+30 °C cw/ 2 000 h	365	3.6	4.8	-	-	ELOG on bulk GaN	etched	Ridge/ 600×2.3	Front: 50 Rear: 50	125 126
	Sony Corp.	RT cw/ >700 h	407	2.3	4.5	940.0	-	*n*-GaN	cleaved	Ridge/ 600×10	Front: 10 Rear: 95	127
		+60 °C cw/ >10 000 h	407	3.6	4.2	150.0	-	pendeo on c-sapphire	cleaved	Ridge/ 600×1.4	Front: 10 Rear: 95	128
	Palo Alto Research Center Incorporated	RT cw/ -	368- -378	5.0	6.7	5.0	4.0	c-face sapphire	etched	Ridge/ ...×2	Front: 50 Rear: 90	129 130
		pulsed	360	23.0	-	45.0- -80.0	1.3- -4.2	c-face sapphire	etched	Stripe*/ 400-1500× ×10-30	no	129 131
	Toshiba Corp.	pulsed	413	7.6	8.0	-	-	c-face sapphire	cleaved	Stripe/ 1000×10	no	132
	Samsung Advanced Inst. of Technology	+50 °C cw/ 1 000 h	405	3.3- -3.7	4.4- -4.8	170.0	-	pendeo on c-sapphire	cleaved	Ridge/ 500-600×2	Front: no Rear: yes	133 134
	Sharp Corp.	RT cw/ -	402	2.9	4.5- -4.7	80.0	-	*n*-GaN	cleaved	Ridge/ 500×2	Front: no Rear: yes	135 136
	Sanyo Electric Corp.	RT cw/ 2 000 h	405	-	-	90.0	-	LAMOS/ c-sapphire	-	Ridge/ 750×...	Front: 5 Rear: 95	137
	High Pressure Research Center Unipress, Poland	pulsed	405- -415	12.0	-	-	4.0	bulk *n*-GaN	cleaved	Ridge/ 500×15	Front: 50 Rear: 90	138
		pulsed	412	3.5	8.0	1.9W	-	bulk *n*-GaN	cleaved	Ridge/ 500×15	Front: 50 Rear: 50	139 140
	Sharp Laboratories of Europe Limited, UK	pulsed	400	30.0	33.0	-	-	c-face sapphire	RIE + wet etched	Ridge/ 1000×5	no	141
	NTT Corp.	pulsed	405	-	-	-	-	*n*-6H-SiC	etched+ selective regrowth	HCSELD	-	142
2004	**Sony Corp.**	+60 °C cw/ >1 400 h	400	4.2	4.2	150.0	-	*n*-GaN	cleaved	Ridge/ 600×1.4	Front: 10 Rear: 95	143

	Samsung Advanced Inst. of Technology	+60 °C cw/ 10 000 h	405	2.8	4.3	300.0	-	pendeo on c-sapphire	cleaved	Ridge/ 600×2	Front: no Rear: yes	144
	Sanyo Electric Corp.	RT cw/ -	405	-	-	200.0	-	*n*-GaN	-	Ridge/ 600×...	Front: 5 Rear: 95	145
	Meijo Univ., Japan	pulsed	351	7.3	7.7- -10.4	-	-	sapphire	cleaved	Ridge/ 500×5.5	-	146 147
	High Pressure Research Center Unipress, Poland	pulsed	408	12.0	9.0	830.0	11.5	bulk *n*-GaN	cleaved	Ridge/ 500×15	no	148
	Sharp Laboratories of Europe Limited, UK	pulsed	402	22.0	34.0	-	-	c-face sapphire	RIE + wet etched	Ridge/ 500-1500× ×5	no	149
		pulsed	400 394	11.0 7.0	29.0 10.0	-	-	c-face sapphire/ *n*-GaN	RIE + wet etched/ cleaved	Ridge/ 600-1000× ×2-5	Front: 50 Rear: 90	150 151 152
	Toyoda Gosei Corp.	RT cw/ -	405	-	4.7	150.0	-	pendeo on c-sapphire /*n*-GaN	cleaved	Ridge/ -	Front: AR Rear: HR	153
	Cree Research Inc.	RT cw/ 200-4 000 h	348- -410	3.0- 4.0	5.0- 6.2	-	15.0- -40.0	ELOG on SiC	cleaved	Ridge/ 500×2	Front: yes Rear: yes	154
	Fraunhofer-Institut für Angewandte Festkörperphysik, Germany	pulsed	400- -410	7.5	-	-	-	sapphire	etched	Ridge/ 500×2-4	no	155

** - stripe is formed by current confinement (open contact window in dielectric material on the top of a wide mesa), not by etching. It is also called a gain-guided laser diode.*

Almost all successful laser diodes demonstrated up to now have been grown using metal-organic chemical vapor deposition (MOCVD) technique. Only very recently Sharp Laboratories of Europe Limited (UK)[141, 149, 150, 151, 152] and later High Pressure Research Center Unipress (Poland) succeeded using molecular beam epitaxy (MBE). Laser structures grown by different groups are very similar and mainly based on separate-confinement-heterostructure (SCH) with a different number of quantum wells in the active region. A similar structure employed by our group is described in detail in Chapter 2. On the contrary, a variety of different substrates have been employed for laser structure growth with various levels of success. As can be seen in Table 1-1, the best results were obtained on sapphire and bulk GaN substrates using either epitaxial lateral overgrowth (ELOG) or its modification, called pendeo-epitaxy. These techniques significantly reduce the density of threading dislocations in the active region. This improves electrical characteristics and remarkably increases the lifetime of devices.[66, 128] Several groups (Fujitsu, Cree, Osram, and NTT) concentrated on SiC substrates, which allow better thermal management, easier cleaved facet formation, and a back-side *n*-contact. However epilayers grown on SiC substrates have a poorer crystalline quality compared to those grown on sapphire substrates. Recently Cree reported very promising results using the ELOG method on a SiC substrate. Free-standing GaN substrates also offer reasonable thermal conductivity, easy facet formation, and a back-side *n*-contact. However, they are very expensive and not widely available yet. Furthermore, quality of these substrates is often unacceptable for laser structure growth and processing. This dissertation considers post-growth processing and contains only brief information on laser structure growth. However, the crystalline structure and arrangement of III-nitrides on different substrates are considered in section 7.4.

As can be seen in Table 1-1, laser structures have been processed to fabricate different types of laser devices (ridge, stripe, and gain-guided). The best results were obtained using the ridge geometry with a very narrow (~2 μm) ridge waveguide. This allows a significant reduction in operation current and single transverse mode operation required for the DVD application. This laser geometry is also employed by our group and is described in Chapter 2. Furthermore, a new self-alignment method was developed by our group for ridge formation (Chapter 5), which allows a simplified laser fabrication process. As shown in Table 1-1, laser facets have been mainly formed either by etching (RIE and its high plasma density modifications) or by cleaving. However, dry-etched facets are

problematic for the DVD application because etched facets cannot be made to extend to the free edge of a device. As a result, a large portion of light is lost and the output laser beam and far field pattern required for the optical disk application are distorted. Hence, cleaving is a preferable method at present. Different methods of laser facet formation are presented in Chapter 7. As also shown in Table 1-1, most of research groups have employed high reflectivity (HR) coatings to laser facets. This allows increased reflectivity of the facets and reduction of the threshold current. The HR coatings for III-nitride laser diodes are considered in Chapter 8.

As the optical data-storage is stated to be the primary application for III-nitride laser diodes, critical requirements need to be specified. Regardless of an optical disc format, the main required laser parameters are similar. First, laser diodes should operate at DC current (CW operation) with optical power of more than 30 mW for writing or 5 mW for reading only. Secondly, single-mode operation is required to collimate a laser beam to a small spot. Multi-mode operation adversely affects the focused beam spot and degrades signal quality significantly. Thirdly, a beam aspect ratio (a ratio of a beam divergence angle perpendicular to a junction plane to a beam divergence angle parallel to the plane) less than 3.0 is required. High aspect ratios deteriorate the coupling efficiency of the laser beam to a focusing lens. Finally, the device lifetime should be longer than 10,000 h. When all these requirements are satisfied, laser diodes should be optimized to operate at a modulation frequency higher than 24 MHz and an optical noise of less than -125dB/Hz at 1 mW.

1.3 Outline of the dissertation

This dissertation is composed of 10 chapters including an Introduction and Conclusion. Chapter 1 provides a brief introduction to III-nitride laser diodes, including primary applications for blue-violet lasers and an up-to-date review on lasers fabricated around the world. Chapter 2 presents the structure and design of laser diodes fabricated by our group. The structure and geometry are standard for III-nitride laser diodes. Thereby, no special attention was paid to structure growth and optimization. The growth was conducted at Bath University by Dr. Sergei Stepanov using a commercial MOCVD system.

A very important part of my dissertation is Chapters 3 – 8, illustrating different technological processes with III-nitrides. The main aim of my research was to develop a complete post-growth technology for fabrication of a III-nitride laser diode. This technology can be separated into a few individual processes, each of them being essential and requiring separate optimization. Chapters 3 – 8 describe the main processes involved in the laser fabrication. They are arranged in the same order as corresponding processes during the fabrication. The chapters are independent of each other and can be considered as individual parts. All of them contain my experimental results on process optimization, except for Chapters 6 and 8, which contain sufficient processing information on contacts and high reflectivity facet coating, respectively. Some of the technological chapters include extensive theoretical and literature reviews, which may be skipped if the reader is mainly interested in my results. The detailed information on selected topics allows for some freedom in the processing and makes this dissertation useful for further optimization of post-growth processing.

Chapter 9 describes a complete laser fabrication process including all single optimized processes presented in Chapters 3 – 8. Laser diodes were successfully fabricated and characterized, the results are also presented in this chapter. Finally, Chapter 10 draws some conclusions and outlines directions for a future work.

1.4 References

[1] A. A. Bergh, Phys. Stat. Sol. (a) 201, 2740 (2004).

[2] G. Flinn, Photonics Spectra (January 2004), pp. 114–115.

[3] D. Dingle, K. L. Shaklee, R. F. Leheny, and R. B. Zetterstrom, Appl. Phys. Lett. 19, 5 (1971).

[4] S. Yoshida, S. Misawa, and S. Gonda, Appl. Phys. Lett. 42, 427 (1983).

[5] H. Amano, N. Sawaki, I. Akasaki, and T. Toyoda, Appl. Phys. Lett. 48, 353 (1986).

[6] S. Nakamura, Japan. J. Appl. Phys. 30, L1705 (1991).

[7] H. Amano, I. Akasaki, T. Kozawa, K. Hiramatsu, N. Sawak, K. Ikeda, and Y. Ishi, J. Lumin. 40–41, 121 (1988).

[8] S. Nakamura, T. Mukai, M. Senoh, and N. Iwasa, Jpn. J. Appl. Phys. 31, L139 (1992).

[9] S. J. Pearton, J. W. Lee, and C. Yuan, Appl. Phys. Lett. 68, 2690 (1996).

[10] S. Nakamura and T. Mukai, Jpn. J. Appl. Phys. 31, L1457 (1992).

[11] S. Nakamura, M. Senoh, and T. Mukai, Jpn. J. Appl. Phys. 32, L8 (1993).

[12] S. Nakamura, M. Senoh, S. Nagahama, N. Iwasa, T. Yamada, T. Matsushita, H. Kiyoku, and Y. Sugimoto, Jpn. J. Appl. Phys. 35, L74 (1996).

[13] S. Nakamura, M. Senoh, S. Nagahama, N. Iwasa, T. Yamada, T. Matsushita, Y. Sugimoto, and H. Kiyoku, Appl. Phys. Lett. 69, 4056 (1996).

[14] S. Nakamura, M. Senoh, S. Nagahama, N. Iwasa, T. Yamada, T. Matsushita, Y. Sugimoto, and H. Kiyoku, Jpn. J. Appl. Phys. 36, L1568 (1997).

[15] S. Nakamura, M. Senoh, S. Nagahama, N. Iwasa, T. Yamada, T. Matsushita, H. Kiyoku, and Y. Sugimoto, Jpn. J. Appl. Phys. 35, L217 (1996).

[16] S. Nakamura, M. Senoh, S. Nagahama, N. Iwasa, T. Yamada, T. Matsushita, H. Kiyoku, and Y. Sugimoto, Appl. Phys. Lett. 68, 2105 (1996).

[17] S. Nakamura, M. Senoh, S. Nagahama, N. Iwasa, T. Yamada, T. Matsushita, H. Kiyoku, and Y. Sugimoto, Appl. Phys. Lett. 68, 3269 (1996).

[18] S. Nakamura, M. Senoh, S. Nagahama, N. Iwasa, T. Yamada, T. Matsushita, Y. Sugimoto, and H. Kiyoku, Appl. Phys. Lett. 69, 1477 (1996).

[19] S. Nakamura, M. Senoh, S. Nagahama, N. Iwasa, T. Yamada, T. Matsushita, Y. Sugimoto, and H. Kiyoku, Appl. Phys. Lett. 70, 616 (1997).

[20] S. Nakamura, M. Senoh, S. Nagahama, N. Iwasa, T. Yamada, T. Matsushita, Y. Sugimoto, and H. Kiyoku, Appl. Phys. Lett. 69, 3034 (1996).

[21] S. Nakamura, M. Senoh, S. Nagahama, N. Iwasa, T. Yamada, T. Matsushita, Y. Sugimoto, and H. Kiyoku, Appl. Phys. Lett. 70, 868 (1997).

[22] S. Nakamura, M. Senoh, S. Nagahama, N. Iwasa, T. Yamada, T. Matsushita, Y. Sugimoto, and H. Kiyoku, Appl. Phys. Lett. 70, 1417 (1997).

[23] S. Nakamura, MRS Internet J. Nitride Semicond. Res. 2, 5 (1997).

[24] S. Nakamura, IEEE journal of selected topics in quantum electronics 3, 435 (1997).

[25] I. Akasaki, S. Sota, H. Sakai, T. Tanaka, M. Koike, and H. Amano, Electron. Lett. 32, 1105 (1996).

[26] K. Itaya, M. Onomura, J. Nishio, L. Sugiura, S. Saito, M. Suzuki, J. Rennie, S. Nunoue, M. Yamamoto, H. Fujimoto, Y. Kokubun, Y. Ohba, G. Hatakoshi, and M. Ishikawa, Jpn. J. Appl. Phys. 35, L1315 (1996).

[27] S. Nakamura, M. Senoh, S. Nagahama, N. Iwasa, T. Yamada, T. Matsushita, Y. Sugimoto, and H. Kiyoku, Appl. Phys. Lett. 70, 2753 (1997).

[28] S. Nakamura, IEEE journal of selected topics in quantum electronics 3, 712 (1997).

[29] S. Nakamura, M. Senoh, S. Nagahama, N. Iwasa, T. Yamada, T. Matsushita, Y. Sugimoto, and H. Kiyoku, Jpn. J. Appl. Phys. 36, L1059 (1997).

[30] S. Nakamura, M. Senoh, S. Nagahama, N. Iwasa, T. Yamada, T. Matsushita, H. Kiyoku, Y. Sugimoto, T. Kozaki, H. Umemoto, M. Sano, and K. Chocho, Appl. Phys. Lett. 72, 211 (1998).

[31] S. Nakamura, M. Senoh, S. Nagahama, N. Iwasa, T. Yamada, T. Matsushita, H. Kiyoku, Y. Sugimoto, T. Kozaki, H. Umemoto, M. Sano, and K. Chocho, Journal of Crystal Growth 189/190, 820 (1998).

[32] S. Nakamura, IEEE journal of selected topics in quantum electronics 4, 483 (1998).

[33] A. Kuramata, K. Domen, R. Soejima, K. Horino, S. Kubota, and T. Tanahashi, Jpn. J. Appl. Phys. 36, L1130 (1997).

[34] G.E. Bulman, K. Doverspike, S.T. Sheppard, T.W. Weeks, H.S. Kong, H.M. Dieringer, J.A. Edmond, J.D. Brown, J.T. Swindell, and J.F. Schetzina, Electron. Lett. 33, 1556 (1997).

[35] M. P. Mack, A. C. Abare, P. Kozodoy, M. Hanson, S. Keller, U. K. Mishra, L. A. Coldren, S. P. DenBaars, Compound Semiconductors, 1997 IEEE International Symposium on 8-11 Sept., 367 (1997).

[36] M. P. Mack, A. Abare, M. Aizcorbe, P. Kozodoy, S. Keller, U. K. Mishra, L. Coldren, and S. DenBaars, MRS Internet J. Nitride Semicond. Res. 2, 41 (1997).

[37] M.P. Mack, A.C. Abare, M. Hansen, P. Kozodoy, S. Keller, U. Mishra, L.A. Coldren, S.P. DenBaars, Journal of Crystal Growth 189/190, 837 (1998).

[38] A. C. Abare, M. P. Mack, M. Hansen, R. K. Sink, P. Kozodoy, S. Keller, J. S. Speck, J. E. Bowers, U. K. Mishra, L. A. Coldren, and S. P. DenBaars, IEEE journal of selected topics in quantum electronics 4, 505 (1998).

[39] M. Kneissl, D. P. Bour, N. M. Johnson, L. T. Romano, B. S. Krusor, R. Donaldson, J. Walker, and C. Dunnrowicz, Appl. Phys. Lett. 72, 1539 (1998).

[40] S. Nunoue, M. Yamamoto, M. Suzuki, C. Nozaki, J. Nishio, L. Sugiura, M. Onomura, K. Itaya, and M. Ishikawa, Jpn. J. Appl. Phys. 37, L1470 (1998).

[41] M. Onomura, J. Nishio, S. Saito, S. Nunoue, G. Hatakoshi, Lasers and Electro-Optics, CLEO/Pacific Rim '97, Pacific Rim Conference on 14-18 July, 286 (1997).

[42] S. Nakamura, M. Senoh, S. Nagahama, N. Iwasa, T. Yamada, T. Matsushita, H. Kiyoku, Y. Sugimoto, T. Kozaki, H. Umemoto, M. Sano, and K. Chocho, Appl. Phys. Lett. 72, 2014 (1998).

[43] S. Nakamura, M. Senoh, S. Nagahama, N. Iwasa, T. Yamada, T. Matsushita, H. Kiyoku, Y. Sugimoto, T. Kozaki, H. Umemoto, M. Sano, and K. Chocho, Jpn. J. Appl. Phys. 37, L309 (1998).

[44] S. Nakamura, M. Senoh, S. Nagahama, N. Iwasa, T. Yamada, T. Matsushita, H. Kiyoku, Y. Sugimoto, T. Kozaki, H. Umemoto, M. Sano, and K. Chocho, Appl. Phys. Lett. 73, 832 (1998).

[45] S. Nakamura, M. Senoh, S. Nagahama, N. Iwasa, T. Yamada, T. Matsushita, H. Kiyoku, Y. Sugimoto, T. Kozaki, H. Umemoto, M. Sano, and K. Chocho, Jpn. J. Appl. Phys. 37, L627 (1998).

[46] S. Nakamura, Journal of Crystal Growth 195, 242 (1998).

[47] S. Nakamura, Materials Science and Engineering B59, 370 (1999).

[48] S. Nakamura, M. Senoh, S. Nagahama, N. Iwasa, T. Yamada, T. Matsushita, H. Kiyoku, Y. Sugimoto, T. Kozaki, H. Umemoto, M. Sano, and K. Chocho, Jpn. J. Appl. Phys. 37, L1020 (1998).

[49] H. Katoh, T. Takeuchi, C. Anbe, R. Mizumoto, S. Yamaguchi, C. Wetzel, H. Amano, I. Akasaki, Y. Kaneko, and N. Yamada, Jpn. J. Appl. Phys. 37, L444 (1998).

[50] C. Ambe, T. Takeuchi, H. Katoh, K. Isomura, T. Satoh, R. Mizumoto, S. Yamaguchi, C. Wetzel, H. Amano, I. Akasaki, Y. Kaneko, N. Yamada, Materials Science and Engineering B59, 382 (1999).

[51] A. Kuramata, K. Domen, R. Soejima, K. Horino, S. Kubota, and T. Tanahashi, Journal of Crystal Growth 189/190, 826 (1998).

[52] A. Kuramata, K. Horino, K. Domen, Fujitsu Sci. Tech. J. 34, 191 (1998).

[53] R. Soejima, A. Kuramata, S. Kubota, K. Domen, K. Horino, and T. Tanahashi, Jpn. J. Appl. Phys. 37, L1205 (1998).

[54] A. Kuramata, S. Kubota, R. Soejima, K. Domen, K. Horino, and T. Tanahashi, Jpn. J. Appl. Phys. 37, L1373 (1998).

[55] Y. Kimura, M. Miyachi, H. Takahashi, T. Tanaka, M. Nishitsuka, A. Watanabe, H. Ota, and K. Chikuma, Jpn. J. Appl. Phys. 37, L1231 (1998).

[56] M. P. Mack, G. D. Via, A. C. Abare, M. Hansen, P. Kozodoy, S. Keller, J. S. Speck, U. K. Mishra, L. A. Coldren, and S. P. DenBaars, Electron. Lett. 34, 1315 (1998).

[57] D. P. Bour, M. Kneissl, L. T. Romano, M. D. McCluskey, C. G. Van deWalle, B. S. Krusor, R. M. Donaldson, J. Walker, C. J. Dunnrowicz, and N. M. Johnson, IEEE journal of selected topics in quantum electronics 4, 498 (1998).

[58] D. Hofstetter, R. L. Thornton, L. T. Romano, D. P. Bour, M. Kneissl, and R. M. Donaldson, Appl. Phys. Lett. 73, 2158 (1998).

[59] D. Hofstetter, R. L. Thornton, L. T. Romano, D. P. Bour, M. Kneissl, R. M. Donaldson, and C. Dunnrowicz, MRS Internet J. Nitride Semicond. Res. 4S1, G2.2 (1999).

[60] M. Kneissl, D. P. Bour, L. T. Romano, D. Hofstetter, M. D. McCluskey, R. Donaldson, C. Dunnrowicz, N. M. Johnson, Lasers and Electro-Optics Society Annual Meeting, LEOS '98. IEEE vol. 2, 1-4 Dec., 350 (1998).

[61] F. Nakamura, T. Kobayashi, T. Asatsuma, K. Funato, K. Yanashima, S. Hashimoto, K. Naganuma, S. Tomioka, T. Miyajima, E. Morita, H. Kawai, and M. Ikeda, Journal of Crystal Growth 189/190, 841 (1998).

[62] T. Kobayashi, F. Nakamura, K. Naganuma, T. Tojyo, H. Nakajima, T. Asatsuma, H. Kawai, and M. Ikeda, Electron. Lett. 34, 1494 (1998).

[63] G. E. Bulman, K. Doverspike, K. Haberern, H. Dieringer, H. S. Kong, J. Edmond, Y.-K. Song, M. Kuball, A. Nurmikko, Lasers and Electro-Optics Society Annual Meeting, LEOS '98. IEEE, vol. 2, 3-4 Dec, 348 (1998).

[64] S. Nakamura, M. Senoh, S. Nagahama, T. Matsushita, H. Kiyoku, Y. Sugimoto, T. Kozaki, H. Umemoto, M. Sano, and T. Mukai, Jpn. J. Appl. Phys. 38, L226 (1999).

[65] S. Nakamura, Phys. Stat. Sol. (a) 176, 15 (1999).

[66] S. Nakamura, Semicond. Sci. Technol. 14, R27 (1999).

[67] S. Nakamura, M. Senoh, S. Nagahama, N. Iwasa, T. Matsushita, and T. Mukai, Appl. Phys. Lett. 76, 22 (2000).

[68] M. Kneissl, D. P. Bour, C. G. Van de Walle, L. T. Romano, J. E. Northrup, R. M. Wood, M. Teepe, and N. M. Johnson, Appl. Phys. Lett. 75, 581 (1999).

[69] M. Kneissl, D. P. Bour, C. G. Van de Walle, L. T. Romano, J. E. Northrup, R. M. Wood, M. Teepe, T. Schmidt, and N. M. Johnson, Phys. Stat. Sol. (a) 176, 49 (1999).

[70] D. P. Bour, M. Kneissl, C. G. Van de Walle, G. A. Evans, L. T. Romano, J. Northrup, M. Teepe, R. Wood, T. Schmidt, S. Schoffberger, and N. M. Johnson, IEEE Journal of Quantum Electronics 36, 184 (2000).

[71] M. Kneissl, C. G. Van de Walle, D. P. Bour, L. T. Romano, L. L. Goddard, C. P. Master, J. E. Northrup, N. M. Johnson, Journal of Luminescence 87-89, 135 (2000).

[72] A. Kuramata, S. Kubota, R. Soejima, K. Domen, K. Horino, P. Hacke, and T. Tanahashi, Jpn. J. Appl. Phys. 38, L481 (1998).

[73] A. Kuramata, S. Kubota, R. Soejima, K. Domen, K. Horino, T. Tanahashi, Lasers and Electro-Optics Society 2000 Annual Meeting. LEOS 2000. 13th Annual Meeting. IEEE vol. 2, 13-16 Nov., 649 (2000).

[74] T. Takeuchi, T. Detchprohm, M. Yano, M. Yamaguchi, N. Hayashi, M. Iwaya, K. Isomura, K. Kimura, H. Amano, I. Akasaki, Yw. Kaneko, S. Watanabe, Y. Yamaoka, R. Shioda, T. Hidaka, Ys. Kaneko, and N. Yamada, Phys. Stat. Sol. (a) 176, 31 (1999).

[75] T. Asano, K. Yanashima, T. Asatsuma, T. Hino, T. Yamaguchi, S. Tomiya, K. Funato, T. Kobayashi, and M. Ikeda, Phys. Stat. Sol. (a) 176, 23 (1999).

[76] T. Asatsuma, H. Nakajima, S. Hashimoto, T. Yamaguchi, H. Yoshida, S. Tomiya, T. Asano, T. Hino, M. Ozawa, T. Miyajima, T. Kobayashi, and M. Ikeda, Journal of Crystal Growth 221, 640 (2000).

[77] T. Miyajima, H. Yoshida, K. Yanashima, T. Yamaguchi, T. Asatsuma, K. Funato, S. Hashimoto, H. Nakajima, M. Ozawa, T. Kobayashi, S. Tomiya, T. Asano, S. Uchida, S. Kijima, T. Tojyo, T. Hino, M. Ikeda, Materials Science and Engineering B82, 248 (2001).

[78] M. Miyachi, H. Ota, Y. Kimura, A. Watanabe, T. Tanaka, H. Takahashi, and K. Chikuma, Jpn. J. Appl. Phys. 38, L1237 (1999).

[79] M. Hansen, P. Fini, L. Zhao, A. C. Abare, L. A. Coldren, J. S. Speck, S. P. DenBaars, Appl. Phys. Lett. 76, 529 (2000).

[80] M. Hansen, P. Fini, L. Zhao, A. Abare, L. A. Coldren, J. S. Speck, and S. P. DenBaars, MRS Internet J. Nitride Semicond. Res. 5S1, W1.3 (2000).

[81] A. C. Abare, M. Hansen, J. S. Speck, S. P. DenBaars, and L. A. Coldren, Electron. Lett. 35, 1559 (1999).

[82] A. C. Abare, M. Hansen, J. S. Speck, L. A. Coldren, S. P. DenBaars, Device Research Conference Digest, 57th Annual, 198 (1999).

[83] M. Kuramoto, C. Sasaoka, Y. Hisanaga, A. Kimura, A. Yamaguchi, H. Sunakawa, N. Kuroda, M. Nido, A. Usui, and M. Mizuta, Jpn. J. Appl. Phys. 38, L184 (1999).

[84] M. Kuramoto, C. Sasaoka, Y. Hisanaga, A. Kimura, A.A. Yamaguchi, H. Sunakawa, N. Kuroda, M. Nido, A. Usui, and M. Mizuta, Phys. Stat. Sol. (a) 176, 35 (1999).

[85] M. Mizuta, Phys. Stat. Sol. (a) 180, 163 (2000).

[86] A. Tsujimura, A. Ishibashi, Y. Hasegawa, S. Kamiyama, I. Kidoguchi, N. Otsuka, R. Miyanaga, G. Sugahara, M. Suzuki, M. Kume, K. Harafuji, and Y. Ban, Phys. Stat. Sol. (a) 176, 53 (1999).

[87] T. I. Kim, Lasers and Electro-Optics, CLEO/Pacific Rim '99, The Pacific Rim Conference on vol. 2, 30 Aug.-3 Sept., 288 (1999).

[88] Y. Park, B. J. Kim, J. W. Lee, O. H. Nam, C. Sone, H. Park, E. Oh, H. Shin, S. Chae, J. Cho, I.-H. Kim, J.S. Khim, S. Cho, and T.I. Kim, MRS Internet J. Nitride Semicond. Res. 4, 1 (1999).

[89] J. Cho, S. Cho, B. J. Kim, S. Chae, C. Sone, O. H. Nam, J. W. Lee, Y. Park, and T. I. Kim, Appl. Phys. Lett. 76, 1489 (2000).

[90] S. Nagahama, N. Iwasa, M. Senoh, T. Matsushita, Y. Sugimoto, H. Kiyoku, T. Kozaki, M. Sano, H. Matsumura, H. Umemoto, K. Chocho, and T. Mukai, Jpn. J. Appl. Phys. 39, L647 (2000).

[91] S. Nagahama, T. Yanamoto, M. Sano, and T. Mukai, Phys. Stat. Sol. (a) 190, 235 (2002).

[92] S. Nagahama, T. Yanamoto, M. Sano, and T. Mukai, Jpn. J. Appl. Phys. 40, 3075 (2001).

[93] S. Nagahama, N. Iwasa, M. Senoh, T. Matsushita, Y. Sugimoto, H. Kiyoku, T. Kozaki, M. Sano, H. Matsumura, H. Umemoto, K. Chocho, T. Yanamoto, and T. Mukai, Phys. Stat. Sol. (a) 188, 1 (2001).

[94] M. Takeya, K. Yanashima, T. Asano, T. Hino, S. Ikeda, K. Shibuya, S. Kijima, T. Tojyo, S. Ansai, S. Uchida, Y. Yabuki, T. Aoki, T. Asatsuma, M. Ozawa, T. Kobayashi, E. Morita, and M. Ikeda, Journal of Crystal Growth 221, 646 (2000).

[95] T. Asano, T. Tojyo, K. Yanashima, M. Takeya, T. Hino, S. Ikeda, S. Kijima, S. Ansai, K. Shibuya, S. Goto, S. Tomiya, Y. Yabuki, T. Aoki, S. Uchida, M. Ikeda, Semiconductor Laser Conference, Conference Digest. 2000 IEEE 17th International 25-28 Sept., 109 (2000).

[96] D. P. Bour, M. Kneissl, C. G. Van de Walle, J. Northrup, L. T. Romano, M. Teepe, R. Wood, T. Schmidt, and N. M. Johnson, Phys. Stat. Sol. (a) 180, 139 (2000).

[97] M. Kneissl, D. P. Bour, L. Romano, C. G. Van de Walle, J. E. Northrup, W. S. Wong, D. W. Treat, M. Teepe, T. Schmidt, and N. M. Johnson, Appl. Phys. Lett. 77, 1931 (2000).

[98] M. Kneissl, Lasers and Electro-Optics Europe, Conference Digest. 2000 Conference on 10-15 Sept., 1 (2000).

[99] W. S. Wong, M. Kneissl, P. Mei, D. W. Treat, M. Teepe, and N. M. Johnson, Appl. Phys. Lett. 78, 1198 (2001).

[100] M. Kneissl, W. S. Wong, D. W. Treat, M. Teepe, N. Miyashita, and N. M. Johnson, IEEE journal on selected topics in quantum electronics 7, 188 (2001).

[101] M. Kneissl, W. S. Wong, D. W. Treat, M. Teepe, N. Miyashita, and N. M. Johnson, Phys. Stat. Sol. (a) 188, 23 (2001).

[102] S. Bader, B. Hahn, H.-J. Lugauer, A. Lell, A. Weimar, G. Bruderl, J. Baur, D. Eisert, M. Schieubeck, S. Heppel, A. Hangleiter, and V. Harle, Phys. Stat. Sol. (a) 180, 177 (2000).

[103] V. Harle, B. Hahn, H.-J. Lugauer, S. Bader, G. Bruderl, J. Baur, D. Eisert, U. Strauss, U. Zehnder, A. Lell, and N. Hiller, Phys. Stat. Sol. (a) 180, 5 (2000).

[104] G. Hasnain, T. Takeuchi, R. Schneider, S. Song, R. Twist, M. Blomqvist, C. Kocot, and C. Flory, Electron. Lett. 36, 1779 (2000).

[105] M. Koike, S. Yamasaki, Y. Tezen, S. Nagai, S. Iwayama, and A. Kojima, MRS Internet J. Nitride Semicond. Res. 5S1, W1.2 (2000).

[106] S. Nagahama, T. Yanamoto, M. Sano, and T. Mukai, Appl. Phys. Lett. 79, 1948 (2001).

[107] S. Nagahama, T. Yanamoto, M. Sano, and T. Mukai, Jpn. J. Appl. Phys. 40, L788 (2001).

[108] S. Nagahama, T. Yanamoto, M. Sano, and T. Mukai, Jpn. J. Appl. Phys. 40, L785 (2001).

[109] S. Nagahama, T. Yanamoto, M. Sano, and T. Mukai, Jpn. J. Appl. Phys. 41, 5 (2002).

[110] T. Tojyo, T. Asano, M. Takeya, T. Hino, S. Kijima, S. Goto, S. Uchida, and M. Ikeda, Jpn. J. Appl. Phys. 40, 3206 (2001).

[111] T. Miyajima, T. Tojyo, T. Asano, K. Yanashima, S. Kijima, T. Hino, M. Takeya, S. Uchida, S. Tomiya, K. Funato, T. Asatsuma, T. Kobayashi, and M. Ikeda, J. Phys.: Condens. Matter 13, 7099 (2001).

[112] S. Kijima, T. Tojyo, S. Goto, M. Takeya, T. Asano, T. Hino, S. Uchida, and M. Ikeda, Phys. Stat. Sol. (a) 188, 55 (2001).

[113] T. Tojyo, S. Uchida, T. Mizuno, T. Asano, M. Takeya, T. Hino, S. Kijima, S. Goto, Y. Yabuki, and M. Ikeda, Jpn. J. Appl. Phys. 41, 1829 (2002).

[114] T. Asano, M. Takeya, T. Tojyo, T. Mizuno, S. Ikeda, K. Shibuya, T. Hino, S. Uchida, and M. Ikeda, Appl. Phys. Lett. 80, 3497 (2002).

[115] M. Kuramoto, A. Kimura, C. Sasaoka, T. Arakida, M. Nido, and M. Mizuta, Jpn. J. Appl. Phys. 40, L925 (2001).

[116] M. Kuramoto, C. Sasaoka, N. Futagawa, M. Nido, and A. A. Yamaguchi, Phys. Stat. Sol. (a) 192, 329 (2002).

[117] T. Akasaka, S. Ando, T. Nishida, H. Saito, and N. Kobayashi, Appl. Phys. Lett. 79, 1414 (2001).

[118] S. Nagahama, T. Yanamoto, M. Sano, and T. Mukai, Phys. Stat. Sol. (a) 194, 423 (2002).

[119] M. Kneissl, W. S. Wong, D. W. Treat, M. Teepe, N. Miyashita, N. M. Johnson, Materials Science and Engineering B93, 68 (2002).

[120] M. Hansen, J. Piprek, P. M. Pattison, J. S. Speck, S. Nakamura, and S. P. DenBaars, Appl. Phys. Lett. 81, 4275 (2002).

[121] V. Kummler, G. Bruderl, S. Bader, S. Miller, A. Weimar, A. Lell, V. Harle, U. T. Schwarz, N. Gmeinwieser, and W. Wegscheider, Phys. Stat. Sol. (a) 194, 419 (2002).

[122] T. Bottcher, C. Zellweger, S. Figge, R. Kroger, Ch. Petter, H.-J. Buhlmann, M. Ilegems, P. L. Ryder, and D. Hommel, Phys. Stat. Sol. (a) 191, R3 (2002).

[123] P. Prystawko, R. Czernecki, M. Leszczynski, P. Perlin, P. Wisniewski, L. Dmowski, H. Teisseyre, T. Suski, I. Grzegory, M. Bockowski, G. Nowak, and S. Porowski, Phys. Stat. Sol. (a) 192, 320 (2002).

[124] V. Dumitru, H. Schweizer, H. Grabeldinger, R. Harle, S. Bader, G. Brurderl, A. Weimar, A. Lell, and V. Harle, Electron. Lett. 39, 372 (2003).

[125] S. Masui, Y. Matsuyama, T. Yanamoto, T. Kozaki, S. Nagahama, and T. Mukai, Jpn. J. Appl. Phys. 42, L 1318 (2003).

[126] T. Mukai, S. Nagahama, T. Kozaki, M. Sano, D. Morita, T. Yanamoto, M. Yamamoto, K. Akashi, and S. Masui, Phys. Stat. Sol. (a) 201, 2712 (2004).

[127] S. Goto, M. Ohta, Y. Yabuki, Y. Hoshina, K. Naganuma, K. Tamamura, T. Hashizu, and M. Ikeda, Phys. Stat. Sol. (a) 200, 122 (2003).

[128] M. Ikeda, T. Mizuno, M. Takeya, S. Goto, S. Ikeda, T. Fujimoto, Y. Ohfuji, and T. Hashizu, Phys. Stat. Sol. (c) 1, 1461 (2004).

[129] M. Kneissl, D. W. Treat, M. Teepe, N. Miyashita, and N. M. Johnson, Phys. Stat. Sol. (a) 200, 118 (2003).

[130] M. Kneissl, D. W. Treat, M. Teepe, N. Miyashita, and N. M. Johnson, Appl. Phys. Lett. 82, 2386 (2003).

[131] M. Kneissl, D. W. Treat, M. Teepe, N. Miyashita, and N. M. Johnson, Appl. Phys. Lett. 82, 4441 (2003).

[132] Y. Ohba and S. Iida, Phys. Stat. Sol. (a) 200, 126 (2003).

[133] O. H. Nam, K. H. Ha, J. S. Kwak, S. N. Lee, K. K. Choi, T. H. Chang, S. H. Chae, W. S. Lee, Y. J. Sung, H. S. Paek, J. H. Chae, T. Sakong, and Y. Park, Phys. Stat. Sol. (c) 0, 2278 (2003).

[134] J. S. Kwak, T. Jang, K. K. Choi, Y. J. Sung, Y. H. Kim, S. Chae, S. N. Lee, K. H. Ha, O. H. Nam, and Y. Park, Phys. Stat. Sol. (a) 201, 2649 (2004).

[135] S. Ito, Y. Yamasaki, S. Omi, K. Takatani, T. Kawakami, T. Ohno, M. Ishida, Y. Ueta, T. Yuasa, and M. Taneya, Phys. Stat. Sol. (a) 200, 131 (2003).

[136] S. Ito, Y. Yamasaki, S. Omi, K. Takatani, T. Kawakami, T. Ohno, M. Ishida, Y. Ueta, T. Yuasa, and M. Taneya, Jpn. J. Appl. Phys. 43, 96 (2004).

[137] T. Kunisato, T. Kano, H. Ohbo, N. Hayashi, Y. Nomura, T. Yamaguchi, M. Bata, M. Shono, M. Sawada, and A. Ibaraki, Lasers and Electro-Optics, CLEO '03. Conference on 1-6 June, 245 (2003).

[138] T. Suski, G. Franssen, P. Perlin, R. Bohdan, A. Bercha, P. Adamiec, F. Dybala, W. Trzeciakowski, P. Prystawko, M. Leszczynski, I. Grzegory, and S. Porowski, Appl. Phys. Lett. 84, 1236 (2004).

[139] P. Perlin, M. Leszczynski, P. Prystawko, C. Skierbiszewski, M. Siekacz, G. Franssen, S. Grzanka, P. Wiœniewski, I. Grzegory, and S. Porowski, Phys. Stat. Sol. (c) 1, 1505 (2004).

[140] P. Prystawko, R. Czernetzki, L. Gorczyca, G. Targowski, P. Wisniewski, P. Perlin, M. Zielinski, T. Suski, M. Leszczynski, I. Grzegory, and S. Porowski, Journal of Crystal Growth 272, 274 (2004).

[141] S. E. Hooper, M. Kauer, V. Bousquet, K. Johnson, J. M. Barnes, and J. Heffernan, Electron. Lett. 40, 33 (2004).

[142] T. Akasaka, T. Nishida, T. Makimoto, and N. Kobayashi, Appl. Phys. Lett. 84, 4104 (2004).

[143] T. Mizuno, M. Takeya, S. Ikeda, T. Fujimoto, Y. Ohfuji, K. Oikawa, M. Taniguchi, H. Ichinokura, T. Hashizu, and M. Ikeda, Semiconductor Laser Conference, Conference Digest. 2004 IEEE 19th International 21-25 Sept., 63 (2004).

[144] O. H. Nam, K. H. Ha, J. S. Kwak, S. N. Lee, K. K. Choi, T. H. Chang, S. H. Chae, W. S. Lee, Y. J. Sung, H. S. Paek, J. H. Chae, T. Sakong, J. K. Son, H. Y. Ryu, Y. H. Kim, and Y. Park, Phys. Stat. Sol. (a) 201, 2717 (2004).

[145] Y. Bessho, T. Kano, T. Yamaguchi, D. Inoue, Y. Nomura, M. Shono, Semiconductor Laser Conference, Conference Digest. 2004 IEEE 19th International 21-25 Sept., 65 (2004).

[146] K. Iida, T. Kawashima, A. Miyazaki, H. Kasugai, S. Mishima, A. Honshio, Y. Miyake, M. Iwaya, S. Kamiyama, H. Amano, and I. Akasaki, Jpn. J. Appl. Phys. 43, L499 (2004).

[147] K. Iida, T. Kawashima, A. Miyazaki, H. Kasugai, S. Mishima, A. Honshio, Y. Miyake, M. Iwaya, S. Kamiyama, H. Amano, and I. Akasaki, Journal of Crystal Growth 272, 270 (2004).

[148] C. Skierbiszewski, Z. R. Wasilewski, M. Siekacz, A. Feduniewicz, P. Perlin, P. Wisniewski, J. Borysiuk, I. Grzegory, M. Leszczynski, T. Suski, and S. Porowski, Appl. Phys. Lett. 86, 011114 (2005).

[149] J. Heffernan, M. Kauer, S. E. Hooper, V. Bousquet, and K. Johnson, Phys. Stat. Sol. (a) 201, 2688 (2004).

[150] J. Heffernan, M. Kauer, K. Johnson, C. Zellweger, V. Bousquet, S. E. Hopper, Lasers and Electro-Optics Society, LEOS 2004. The 17th Annual Meeting of the IEEE Vol. 1, Nov. 8-9, 280 (2004).

[151] S. E. Hooper, M. Kauer, V. Bousquet, K. Johnson, C. Zellweger, and J. Heffernan, Journal of Crystal Growth XX, XXX (2004).

[152] J. Heffernan, M. Kauer, K. Johnson, C. Zellweger, S. E. Hooper, and V. Bousquet, Phys. Stat. Sol. (a) 202, 868 (2005).

[153] H. Watanabe, T. Umezaki, J. Minoura, M. Ohashi, N. Arazoe, R. Nakamura, T. Hatano, T. Sonoyama, Y. Watanabe, M. Okawachi, and S. Iwayama, Phys. Stat. Sol. (a) 201, 2672 (2004).

[154] J. Edmond, A. Abare, M. Bergman, J. Bharathan, K. L. Bunker, D. Emerson, K. Haberern, J. Ibbetson, M. Leung, P. Russel, D. Slater, Journal of Crystal Growth 272, 242 (2004).

[155] F. Sommer, T. Stephan, F. Vollrath, K. Köhler, M. Kunzer, S. Müller, P. Schlotter, W. Pletschen, U. Kaufmann, and J. Wagner, Phys. Stat. Sol. (a) 201, 2628 (2004).

2 Laser diode structure and design

This chapter presents the structure and design of laser diodes employed by our group. The structure and geometry are standard for III-nitride laser diodes. Furthermore, the aim of my research was to develop a post-growth technology for laser diode fabrication. Thereby, this chapter contains only brief information on structure growth and optimization. More detailed information can be found in numerous papers on III-nitride laser diodes. It is important to note, that fabrication of nitride lasers is primarily limited by growth technology. At Bath University, the growth of the laser structure was optimized by Dr. Sergei Stepanov. The chapter also underlines critical issues of post-growth processing which should be developed and optimized for successful laser diode fabrication.

The structure was grown on a 2-inch c-face (0001) sapphire substrate using a metalorganic chemical vapor deposition (MOCVD) system operating at low pressure (AIXTRON 200/HT). No epitaxial lateral overgrowth (ELOG) or pendeo-epitaxy technique was used to reduce the density of threading dislocations in the active region. These techniques allow improved device characteristics, but require significantly more complicated growth and post-growth processing. Trimethylgallium (TMGa), trimethylaluminum (TMAl), trimethylindium (TMIn), and ammonia (NH_3) were used as the source material of Ga, Al, In, and N, respectively. Silane (SiH_4) and biscyclopentadienylmagnesium (Cp_2Mg) were used as the *n*- and *p*-type dopant source, respectively. The chemical precursors were transported using hydrogen carrier gas. Prior to the growth of the structure, a 25 nm-thick GaN buffer layer was deposited onto the substrate at a low temperature of 500 °C. Subsequently, the reactor temperature was raised to 1050 °C to transform this amorphous film into a single crystal. The purpose of the buffer layer is to initiate epitaxial growth on the sapphire substrate, which has a large 13% lattice mismatch with GaN. After that a 2 μm-thick undoped GaN layer was grown to reduce the density of threading dislocations in the structure.

The grown undoped GaN layer was used as the base for the epitaxial laser structure. First, a 1.5 μm-thick *n*-GaN contact layer was grown on the base. The contact layer was followed by the growth of a separate-confinement heterostructure (SCH) including lower *n*- and upper *p*-type cladding layers. The cladding layers consisted of *n*-type and *p*-type $Al_{0.13}Ga_{0.87}N$/GaN (2.8/2.8 nm) superlattices with 100 and 70 layer pairs respectively. The waveguide layers and active region were sandwiched between the cladding layers. The lower *n*- and upper *p*-type waveguides were 0.13 μm-thick *n*-GaN and 0.15 μm-thick *p*-GaN layers respectively. The multi-quantum-well (MQW) active region contained 10 pairs of 2.5 nm-thick $In_{0.1}Ga_{0.9}N$ well layers and 16.5 nm-thick GaN barrier layers. The last GaN barrier was replaced by a 23 nm-thick *p*-$Al_{0.29}Ga_{0.71}N$ capping barrier layer. This layer serves both to suppress electron overflow from the QWs and to prevent dissociation of the InGaN layers during following growth.[1, 2] Finally, a 60 nm-thick *p*-GaN layer was grown on the top of the SCH structure followed by a thin p+-contact layer. This layer promotes the formation of a low-resistance Ohmic *p*-contact.

The ridge waveguide laser design employed by our group is presented in Fig. 2.1. The insulating sapphire substrate prevents the realization of a vertical current injection structure. Thereby, an *n*-contact is generally deposited on the *n*-GaN contact layer, which requires plasma etching through the whole structure. This design also requires etching a narrow 300 nm-high ridge stripe, passivating the surface with a SiO_2 insulation layer, and opening a contact window on the top of the stripe. A relatively large *p*-contact is deposited on the top of this window and on the surrounding insulation layer. The ridge stripe serves for both lateral current confinement and for weak lateral optical confinement within a narrow active region. For transverse single-mode laser operation, required for a DVD

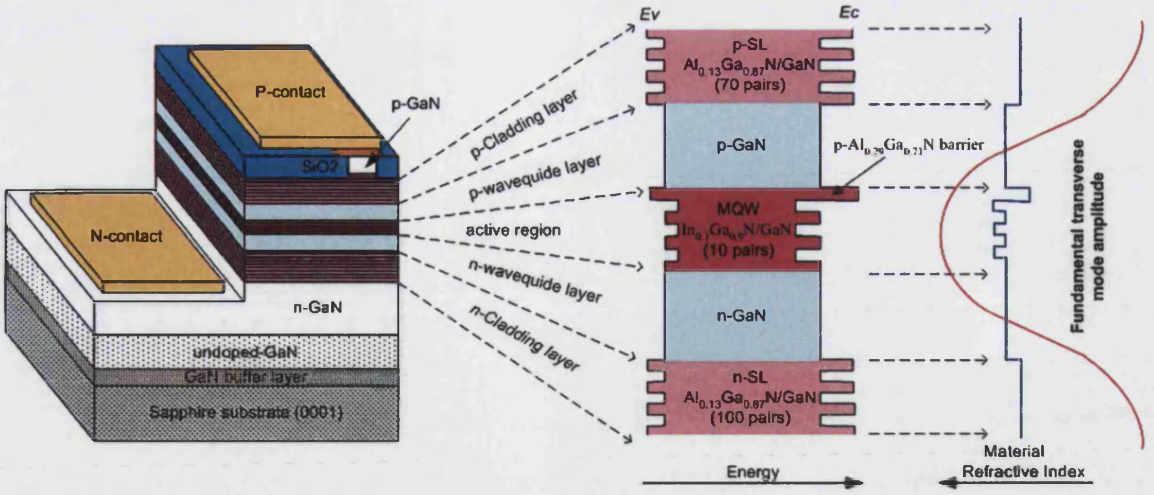

Fig. 2.1. Schematic drawings of the laser diode design, energy bandgap diagram of the SCH region under forward bias, refractive index profile, and fundamental transverse mode amplitude.

application, the width of the stripe should be 2–3 μm compared to 4–6 μm for conventional GaAs-based lasers. Laser facets can be formed by plasma etching but etched facets cannot be made to extend to the free edge of a sample. As a result, a large portion of light would be lost and the output laser beam and far field pattern, required for the optical disk application, would be distorted. Thus, cleaved facets were suggested for our laser design. The laser cavity lengths employed for III-nitride lasers by different research groups range from 300 to 1500 μm, as can be seen in Table 1.1. High reflectivity (HR) coating can be employed to increase the facet reflectivity and, hence, to reduce the threshold current.

A schematic energy bandgap diagram of the SCH region under forward bias is presented in Fig. 2.1. As can be seen, the QWs in the active region are sandwiched between the waveguide layers with wider bandgaps. As a result, injected carriers mainly recombine in the QWs and the wavelength peak of emission is defined by the In composition (bangap energy) and the width of the QWs. The top AlGaN barrier in the active region is used to prevent electron overflow from the active region.[1, 2] Recombination of carriers outside of the wells would reduce the internal quantum efficiency. This is not a problem for injected holes, which mainly recombine within the QWs due to their low mobility. For optical confinement in the vertical (transverse) direction, the waveguide-active region is sandwiched by the cladding layers with wider bandgaps and, hence, with lower refractive indices. The difference in refractive indices guides the light to propagate along the waveguide, as can be seen in Fig. 2.1 for the fundamental transverse mode. The lower cladding layer should be thick enough to minimize the fraction of light propagating in the *n*-GaN contact layer. This layer acts as a parasitic waveguide and can result in vertical multi-mode operation.[3] The upper cladding layer should also be sufficiently thick to prevent the optical mode overlapping with the *p*-contact metals, which are very absorbing. The most straightforward method is using AlGaN layers as cladding layers. However, thick layers with a relatively high (5–10%) Al content tend to crack due to thermal expansion differences and lattice mismatches between GaN and AlGaN layers. Thereby, AlGaN/GaN strained-layer superlattices (SLSs) are widely used, which prevent the tensile strained cladding layers from cracking. [4, 5, 6, 7, 8, 9] Lateral optical and current confinement is promoted by the ridge waveguide geometry. A small lateral refractive index step is produced by etching close to the waveguide region and depositing the SiO_2 insulation layer around the ridge stripe. The lateral index step strongly depends on the etch depth. The lateral optical confinement is a function of both the remaining cladding layer thickness and the ridge width. For narrower stripes the index step (etch depth) should be greater to maintain a high lateral optical confinement. However, for lateral single-mode

operation, narrow ridges and small index steps are preferable. Thus, there are tradeoffs between low threshold operation and lateral single-mode operation. Furthermore, the ridge geometry affects the vertical mode operation. For fundamental transverse mode operation a ridge width less than 2 μm is required.[10] Finally, the light is guided along a laser cavity formed by the optical confinement in both vertical and lateral directions. The facets located at the ends of the laser cavity reflect a part of the light back, providing conditions for laser generation. The active region located within this cavity generates a number of photons under current injection. Once population inversion in the QWs is achieved, reflected photons stimulate emission of further photons with the same energy and in the same direction, the light is amplified, and strong stimulated emission is observed at the cavity edges. The quality of the structure is crucial for laser diodes because the gain in the structure should be larger than all losses for laser generation. This means that each photon should generate the emission of at least one new photon before it is absorbed or scattered.

For the selected laser diode design a number of technological processes should be developed and/or optimized. First, *p*-type layers are generally insulating or semi-insulating after MOCVD growth and require to be activated. Secondly, plasma etching of the laser structure needs to be optimized for relatively deep (~2 μm), smooth, and reproducible etching. Thirdly, ridge waveguide fabrication is extremely challenging and requires an innovative technological process. Fourthly, low-resistance ohmic contacts to both *n*-GaN and *p*-GaN layers are required. Fifthly, smooth reproducible cleaving of laser facets is also a difficult technological task and requires optimization. Finally, HR facet coating should be considered for III-nitride laser diodes. All these technological processes are considered in the following chapters (Chapters 3 – 8). Chapter 9 presents a complete post-growth technology for III-nitride laser diode fabrication and the characterization of fabricated laser diodes.

---

[1] M. Ikeda and S. Uchida, Phys. Stat. Sol. (a) 194, 407 (2002).

[2] M. Hansen, J. Piprek, P. M. Pattison, J. S. Speck, S. Nakamura, and S. P. DenBaars, Appl. Phys. Lett. 81, 4275 (2002).

[3] D. P. Bour, M. Kneissl, C. G. Van de Walle, J. Northrup, L. T. Romano, M. Teepe, R. Wood, T. Schmidt, and N. M. Johnson, Phys. Stat. Sol. (a) 180, 139 (2000).

[4] S. Nakamura, Semicond. Sci. Technol. 14, R27 (1999).

[5] S. Nakamura, M. Senoh, S. Nagahama, N. Iwasa, T. Yamada, T. Matsushita, Y. Sugimoto, and H. Kiyoku, Jpn. J. Appl. Phys. 36, L1568 (1997).

[6] S. Nakamura, M. Senoh, S. Nagahama, N. Iwasa, T. Yamada, T. Matsushita, H. Kiyoku, Y. Sugimoto, T. Kozaki, H. Umemoto, M. Sano, and K. Chocho, Appl. Phys. Lett. 72, 211 (1998).

[7] S. Nakamura, M. Senoh, S. Nagahama, N. Iwasa, T. Yamada, T. Matsushita, H. Kiyoku, Y. Sugimoto, T. Kozaki, H. Umemoto, M. Sano, and K. Chocho, Journal of Crystal Growth 189/190, 820 (1998).

[8] S. Nakamura, IEEE journal of selected topics in quantum electronics 4, 483 (1998).

[9] S. Nakamura, M. Senoh, S. Nagahama, T. Matsushita, H. Kiyoku, Y. Sugimoto, T. Kozaki, H. Umemoto, M. Sano, and T. Mukai, Jpn. J. Appl. Phys. 38, L226 (1999).

[10] S. Nakamura, M. Senoh, S. Nagahama, N. Iwasa, T. Yamada, T. Matsushita, H. Kiyoku, Y. Sugimoto, T. Kozaki, H. Umemoto, M. Sano, and K. Chocho, Jpn. J. Appl. Phys. 37, L1020 (1998).

3 P-type GaN activation

3.1 Introduction

The III–V nitrides are expected to be made *p*-type by substituting group II elements such as Zn, Mg, Be and Ca for Ga sites to form single acceptors. However, all of these elements form deep acceptors. Mg was found to be the shallowest with a reported activation energy between 120 and 250 meV obtained by various characterization techniques.[1, 2, 3, 4, 5, 6, 7, 8, 9, 10, 11, 12, 13, 14, 15, 16] The wide range of measured data might be caused by the inconsistencies in activation conditions and/or the different Mg doping concentrations in GaN:Mg.[1, 17] Another reason could be the large difference in temperatures at which the electrical and optical measurements were made.[18] Nevertheless, the fairly high activation energy results in the ionization of less than 10% of the Mg atoms at room temperature. This implies that the Mg concentration should be approximately two-orders of magnitude larger than the desired hole concentration.[19]

Ion implantation is not as efficient at creating *p*-type conductivity in GaN as doping during epitaxial growth. However, when MOCVD is used as the growth method, it is also difficult to obtain *p*-type conductivity without subsequent post-growth treatment. For many years it was not possible to achieve *p*-type doping in GaN due to the high residual *n*-type background (nitrogen vacancies or Si or O impurities) and the high ionization energy level of most acceptor dopants. As-grown GaN was always *n*-type with carrier concentration $\sim 10^{16}$ cm^{-3}.[20] However, even in GaN:Mg in which the Mg concentration was easily sufficient to produce *p*-type conductivity, the material was generally semi-insulating.

It was first shown in 1988 by Amano *et al.*[21] that *p*-type conductivity can be achieved by activating Mg-doped GaN using low-energy electron beam irradiation (LEEBI). They were studying cathodoluminescence (CL) of Mg-doped GaN and observed that electron irradiation increased the efficiency of the luminescence by up to 2 orders of magnitude and caused the samples to become conducting and *p*-type. The hole concentration was estimated to be $\sim 2 \times 10^{16}$ cm^{-3} and the mobility ~ 8 $cm^2/V \cdot s$. In 1989 they demonstrated the first *p-n* junction GaN LED realized by LEEBI treatment.[22] Shortly afterwards Nakamura demonstrated that the activation of Mg can also be realized by thermal annealing at ~600 °C.[23] The resistivity, hole carrier concentration and mobility were reported to be 2 $\Omega \cdot cm$, 3×10^{17} cm^{-3} and 10 $cm^2/V \cdot s$, respectively. Pearton *et al.*[24] subsequently demonstrated that minority-carrier injection by forward biasing a diode structure also activated the Mg acceptors at 175 °C. Recently several new activation methods for Mg-doped GaN were reported such as photo-enhanced thermal activation (under UV light irradiation)[25] and microwave or RF treatment activation.[26, 27] At the present time, thermal annealing is the most common method to activate as-grown Mg-doped GaN.

It is well established that in MOCVD grown Mg-doped GaN, compensation is enabled by the presence of atomic hydrogen during growth and the formation of neutral Mg–H complexes during cooldown. The thermal activation is accomplished by the dissociation of Mg–H complexes and the thermal release of H at elevated temperatures, while the LEEBI treatment or minority-carrier injection cause the dissociated H to transfer to a metastable, nonpassivating state. The detailed mechanisms of the passivation and activation of Mg-doped GaN are illustrated in this chapter. The results of our group on *p*-GaN thermal activation in air with and without a SiO_2 capping layer are also presented and discussed.

3.2 Passivation of GaN with hydrogen

In MOCVD growth of GaN there are numerous potential sources of hydrogen, since the growth reaction proceeds as:

$$(CH_3)_3Ga + NH_3 \rightarrow GaN + CH_4 \uparrow + H_2 \uparrow$$

Pearton *et al.*[28] suggested that atomic hydrogen (H^0, H^+, or H^-) diffuses into GaN during the growth and the subsequent cooling down and can form neutral complexes with dopants. It results in the increased resistivity of semiconductors, and increased carrier mobility as ionized impurity scattering is reduced. It is especially essential in Mg-doped GaN where this interaction results in the complete passivation of acceptors. Ohba *et al.*[29] examined Mg passivation with hydrogen during MOCVD growth. The SIMS measurements revealed that the H-atom concentration incorporated in GaN films linearly increased with increasing Mg concentration and was nearly equal to Mg concentration. It was related to the formation of complex Mg-H. The confirmation of Mg passivation with hydrogen during MOCVD growth also comes from the fact that *p*-GaN may be achieved by Mg doping in molecular beam epitaxy (MBE) material without following postgrowth treatment, because of the absence of the hydrogen during the growth.[19, 28]

Nakamura *et al.*[30] were the first to report the thermal passivation of Mg-doped GaN material previously activated by LEEBI treatment during the annealing in H-containing ambients at temperatures above 600 °C. The passivation was attributed to hydrogen incorporation into GaN during the annealing. However, as it was found later, the LEEBI treatment can only transfer hydrogen in as-grown GaN:Mg to a non-passivating state (the mechanism is illustrated below) and does not remove the H from the layers.[31, 32] Post-irradiation annealing at ~200 °C in air or N_2 was found to restore the Mg passivation with hydrogen. In all probability, the results obtained by Nakamura *et al.* were also related to the thermal repassivation of Mg with remained hydrogen. Nevertheless, some interesting changes in PL spectra were observed after the passivation. The intensity of blue emission became significantly weaker and broad deep-level (DL) emission (750 nm) appeared. These changes exactly corresponded to the resistivity change after NH_3-ambient annealing. Thereby, the authors assumed that DL emission is caused by levels of Mg-H complexes, and blue emission is caused by Mg-related levels. The subsequent annealing in N_2 ambient again restored the Mg activation and partially restored the original PL spectra of LEEBI-treated films.

Brandt *et al.*[33] exposed MBE grown autodoped (*n*-type) GaN, *n*-type GaN:Si, and *p*-type GaN:Mg epilayers to remote microwave plasma operating at 2 Torr. This technique excludes effects due to charged particle bombardment of the sample or its illumination from the plasma. To increase the sensitivity, the GaN samples for SIMS were treated with a plasma containing deuterium instead of hydrogen. The carrier concentration after isochronal (1 h) hydrogenation was unchanged for *n*-type epilayers, while it was significantly reduced for *p*-type Mg-doped GaN at temperatures above 500 °C. The secondary ion mass spectrometry (SIMS) analysis revealed that the deuterium concentration found after passivation at 600 °C in GaN:Mg was about the same as the concentration of Mg. On the contrary, in *n*-type Si-doped GaN no incorporation of deuterium was detected. Very similar results were reported by Gotz *et al.*[34] for MOCVD grown *n*-type GaN:Si and *p*-type GaN:Mg (previously annealed under N_2 flow at 800 °C for 20 min to remove as-grown hydrogen) layers. It is also consistent with the results obtained by Theys *et al.*[35] after deuterium plasma treatment. SIMS measurements showed that the deuterium was deeply incorporated in Mg-doped layers after 7 hours exposure at a temperature as low as 490 °C with the same level as the Mg concentration while it did not diffuse significantly at the same conditions for Mg-free layers. The formation of

magnesium-hydrogen complexes was suggested to account for the experimental results observed.

Polyakov *et al.*[36] performed deuterium plasma treatment to investigate H thermal plasma incorporation into the GaN layers with different Fermi level positions. It was found that at 350 °C hydrogen diffused rapidly in heavily Mg-doped material (Fermi level close to Ev+0.15 eV), considerably slower in high-resistivity *p*-type GaN:Zn (Ev+0.9 eV). On the contrary for conductive and semi-insulating *n*-GaN samples no measurable hydrogen was detected after the treatment at such temperatures. However, the treatment of these samples at 550 °C for 50 h also produced very measurable deuterium profiles in both *n*-type samples.

Hydrogen passivation was also reported to take place for other possible acceptors such as Ca and C. Zolper *et al.*[37] realized *p*-GaN using the implantation of Ca^+, followed by RTA annealing at 1100 °C. Hall measurements showed that the ionization energy of Ca was ~168 meV, similar to Mg. It was found that Ca acceptors in GaN can be passivated by atomic hydrogen at low temperature (250 °C) and sequentially reactivated by thermal annealing at ~500 °C. Abernathy *et al.*[38] reported carbon doping of GaN using CCl_4 in metal organic molecular beam epitaxy, with maximum hole concentrations of $\sim 3 \times 10^{17}$ cm^{-3}. Exposure of the GaN:C samples to hydrogen plasma at 250 °C reduced the hole concentration by approximately a factor of three, with an accompanying increase in hole mobility. Annealing of the hydrogenated material restored the initial concentration at ~450 °C.[39] The passivation mechanism for these dopants was proposed to be the same as for magnesium.

Hydrogen is also unintentionally incorporated during many device process steps such as plasma etching, plasma enhanced chemical vapor deposition (PECVD), annealing in NH_3 or H_2, boiling in water or solvent, and wet chemical etching. Pearton *et al.*[40] found that boiling in water is an effective method of introducing hydrogen. It diffuses very rapidly under these conditions because the H flux is low enough to avoid the H–H pairing reactions in the material. It was reported that GaN boiled in D_2O water at 100 °C for 30 min showed incorporation of deuterium up to ~1 μm in the material. The exposure of undoped GaN to a solution of KOH/D_2O, which is used to etch selectively AlN over GaN, for 20 min at fairly low temperature (25 °C) also leads to incorporation of deuterium to a depth of ~0.5 μm. PECVD deposition of dielectrics such as SiN_x and SiO_2 for masking and surface passivation also causes extensive hydrogen passivation due to the silane discharge containing hydrogen. Pearton *et al.* reported that Electron Cyclotron Resonance Chemical Vapor Deposition (ECR-CVD) of SiN_x onto GaN at 250 °C produced ^2H incorporation depths of ~0.7 μm using SiD_4/N_2. The presence of hydrogen in plasma chemistry during the dry etching of GaN at elevated sample temperatures can also cause it to diffuse into the bulk of the sample and passivate dopants or defects. The incorporation depth of 0.5–2 μm after 40 sec at the sample temperature of 170 °C was reported.[41] Room temperature etching minimizes indiffusion of hydrogen from the plasma. Thus, hydrogen may be included into GaN at many stages of a device fabrication process, particularly when *p*-type layers are uppermost in the structure (i.e., LEDs and lasers).

3.3 Theory of hydrogen in GaN

The first attempts to describe the behavior of hydrogen in GaN were made by Neugebauer and Van de Walle.[42, 43] The authors performed density functional calculations for cubic (zinc-blende) GaN, which has a higher symmetry than the wurtzite structure. It was proposed that the results are valid for H in both zinc-blende and wurtzite GaN. However, Wright[44] later found that the H behavior in the wurtzite structure differs from that in the zinc-blende. The density-functional calculations revealed some significant differences illustrated below.[44, 45]

- It was found that the H^+ position in the lattice is significantly different. In the zinc-blende, the nitrogen antibonding (AB_N) site is more stable, whereas there are two types of nitrogen-antibonding (AB_N) and bond-centered (BC) sites in the wurtzite due to its lower symmetry. Both Myers *et al.* and Neugebauer and Van de Walle calculated the diffusion barrier for H^+ to be 0.7 eV. This ensures a high mobility even at temperatures slightly above room temperature.
- The most stable site for H^- was also calculated to be different in the wurtzite. In the zinc-blende, H^- is stable at the gallium antibonding (AB_{Ga}) or tetrahedral gallium ($T_{d,Ga}$) sites, whereas in the wurtzite it is stable at the center of the trigonal channel along the c axis. The diffusion barrier for H^- in the zinc-blende and wurtzite was estimated to be 1.9 and 1.6 eV respectively. Both of these values are significantly lower than 3.4 eV given by Neugebauer and Van de Walle. Therefore, this implies that H^- has noticeable mobility in GaN at growth and processing temperatures.
- The formation energy of H^0 was found to be insensitive to position due to its neutrality in both zinc-blende and wurtzite structures, while Neugebauer and Van de Walle predicted the Ga antibonding site (AB_{Ga}) to be the most energetically stable position in the zinc-blende. Wright gives a very low diffusion barrier of 0.6 eV for H^0 instead of 3.4 eV calculated by Neugebauer and Van de Walle. It also indicates the high mobility of H^0 in GaN.
- The formation energy of neutral H_2 was found to be very sensitive to position and the stable sites are also fairly different in the two crystal structures. In wurtzite, the stable site is at the center of the trigonal channel with the H-H bond parallel to the c axis. In zinc-blende, H_2 sits near a ($T_{d,Ga}$) site in the trigonal channel with the H-H bond parallel to a <111> direction. As a result, the H_2 formation energy in the wurtzite was estimated to be 0.56 eV lower than in the zinc-blende. The interstitial H_2 was predicted to be immobile in GaN.
- It was also found that there are several configurations in the wurtzite structure, where two bonded H^+ ions have formation energies lower than for isolated H^+ ions. The author suggested that hydrogen clustering may also play a role in *p*-type material.

Figure 3.1 presents the formation energies for the most stable sites in the zinc-blende and wurtzite as a function of Fermi level. Both plots are similar to each other and to the plot presented by Neugebauer and Van de Walle. However, the Wright's H_2 formation energies were found to be about 0.7 eV lower than that obtained by Neugebauer and Van de Walle. The author suggested that the relatively low formation energy for H_2 may have important consequences for the behavior of hydrogen in GaN.

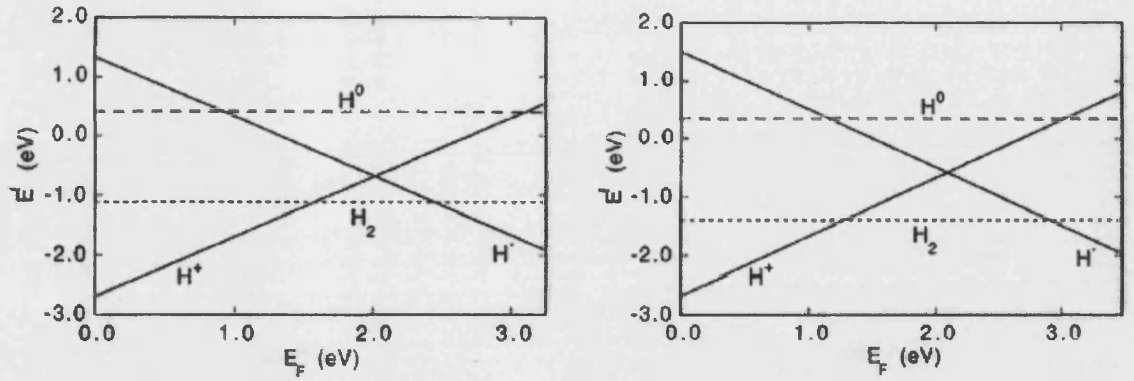

Fig. 3.1. Formation energies (per hydrogen atom) as a function of Fermi level ($0=E_v$) in (a) zinc-blende and (b) wurtzite GaN.

The most complete study of hydrogen behavior in wurtzite GaN and its related passivation of dopants was performed by the group from Sandia National Laboratories, New Mexico.[44, 45, 46, 47, 48, 49, 50, 51] The authors first used density-functional theory (DFT) employing the local-density approximation (LDA).[44, 45, 46] However, they subsequently found that this approximation resulted in some inconsistencies with experimental observations. To resolve this problem, the generalized-gradient approximation (GGA) was employed.[49, 50, 51] The latest model of hydrogen behavior in wurtzite GaN is illustrated below.

Figure 3.2 presented the GGA configurations for hydrogen in wurtzite GaN. The calculations revealed the energy minima for H^0 (Fig. 3.2(a)) and H^- (Fig. 3.2(b)) at the center of the *c*-axis channel. H^0 is 0.78 Å from a plane of Ga atoms and 1.22 Å from a plane of N atoms, while H^- is 0.65 Å from a Ga-atom plane and 1.35 Å from a N-atom plane. The energy minimum for H_2 (Fig. 3.2(c)) was also calculated to be at the center of the *c*-axis channel with the H–H bond oriented parallel to the *c* axis. One hydrogen atom is 0.47 Å from a Ga-atom plane, the other is 0.79 Å from a N-atom plane, and the H–H bond length 0.74 Å. The theory indicated that H^+ forms a strong bond with N. Four local energy minima were identified for H^+. Two are N antibonding sites with the N–H bonds oriented parallel ($AB_{\|}$, Fig. 3.2(d)) and roughly perpendicular ($AB_{\perp}$, Fig. 3.2(e)) to the *c* axis, with N–H bond lengths of 1.04 and 1.05 Å respectively. The other two are bond-centered sites with the N–H bonds oriented parallel ($BC_{\|}$, Fig. 3.2(f)) and roughly perpendicular ($BC_{\perp}$, Fig. 3.2(g)) to the *c* axis, with N–H bond lengths of 1.02 and 1.03 Å respectively.

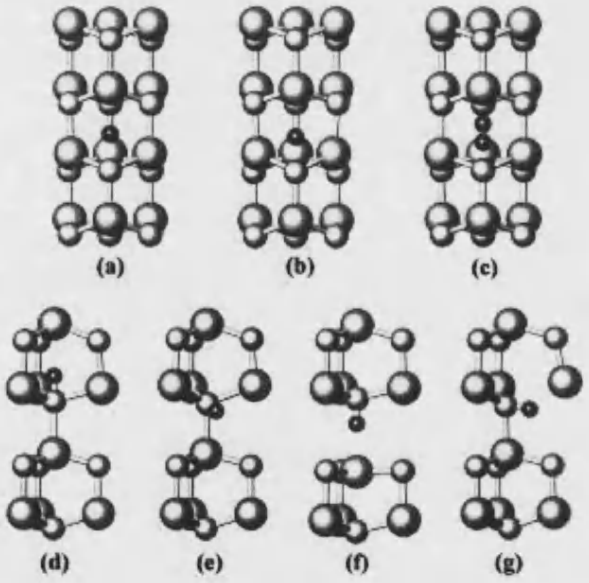

Fig. 3.2. GGA configurations for H in wurtzite GaN. The H states are (a) H^0; (b) H^-; (c) H_2; (d) $AB_{\|}$ H^+; (e) $AB_{\perp}$ H^+; (f) $BC_{\|}$ H^+; (g) $BC_{\perp}$ H^+ (large, light colored spheres denote Ga; medium, light colored spheres denote N; and small, dark colored spheres denote H).

Figure 3.3 shows the calculated GGA formation energies as a function of Fermi level for $BC_{\parallel}$ H^+, H^-, H^0, and H_2 in wurtzite GaN. The $BC_{\parallel}$ site for H^+ was found to have the lowest formation energy whereas the $AB_{\perp}$ site is 0.21 eV higher, the $BC_{\perp}$ site is 0.23 eV higher, and the $AB_{\parallel}$ site is 0.39 eV higher. As can be seen, H^+ is predicted to be the most stable H species when the Fermi level is below 1.48 eV, H^- is predicted to be the most stable when the Fermi level is above 2.70 eV, and H_2 is predicted to be the most stable when the Fermi level is between these values. The capacitance–voltage (*C-V*) measurements confirmed that hydrogen in *p*-GaN exists in the positive charge state. The relatively large formation energy of the neutral hydrogen H^0 in the GaN makes it unstable with respect to the charged states for all positions of the Fermi level. Thereby, the authors concluded that H^0 is never the principal constituent in solution.

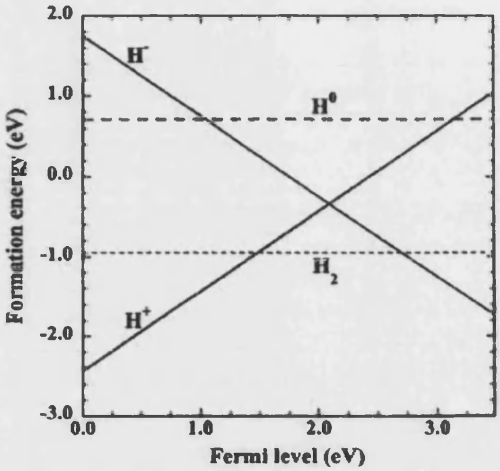

Fig. 3.3. GGA formation energies as a function of Fermi level for $BC_{\parallel}$ H^+, H^-, H^0, and H_2 in wurtzite GaN.

The diffusion activation energies in wurtzite GaN in the *c*-axis direction were calculated to be 1.0 eV for H^+, 0.5 eV for H^0, and 1.4 eV for H^-. The migration barriers for the diffusion perpendicular to the *c*-axis were estimated to be 0.9 eV for H^+ and 1.5 eV for H^-. It implies that H^+ migration perpendicular to the *c*-axis is faster than parallel migration, while for H^- it is faster parallel to the *c*-axis. The interstitial H_2 was predicted to be immobile in GaN. The calculated diffusion activation energy for H^+ was found to be in good agreement with the experimentally estimated one (~1.2 eV). With this migration barrier and very low formation energy for H^+ the diffusion and incorporation of hydrogen into *p*-type GaN is expected to take place at fairly low temperatures. On the contrary, the diffusion activation energy and formation energy for H^- in *n*-GaN are higher than those for H^+ in *p*-GaN. This could be the reason for the significant incorporation of hydrogen into *p*-GaN material at 500 °C in a hydrogen plasma, whereas there is no detectable incorporation of H into *n*-GaN at these conditions.[33, 35, 34, 36] It could also prevent the high incorporation of hydrogen into *n*-GaN during the growth, and thus explain why Si remains electrically active even when H is present in the process ambient.

The authors suggested that for H^- and H^0 the migration occurs through a series of jumps from one equilibrium state to another. The diffusion of H^+ was proposed to involve a series of jumps from one N atom to another with the reorientation of the initial N–H^+ bond toward the next N atom between jumps. The proposed path for H^+ migration in the c axis direction is presented in Fig. 3.4. It involves N–H bond reorientation from a $BC_{\parallel}$ site (Fig. 3.4(a)) to an $AB_{\parallel}$ site (Fig. 3.4(b)) at the initial N atom, followed by a jump through a saddle point (Fig. 3.4(c)) to a $BC_{\parallel}$ site (Fig. 3.4(d)) at the final N atom.

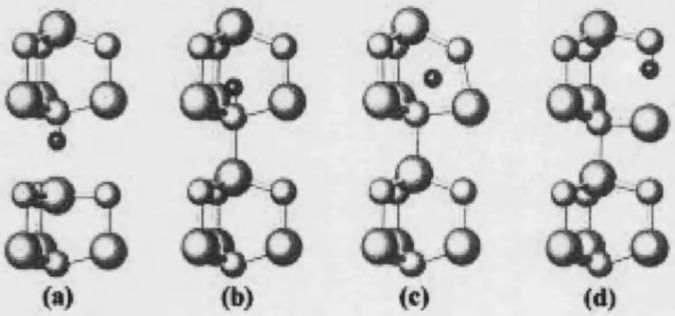

Fig. 3.4. Path for H^+ migration that produces displacement perpendicular and parallel to the *c* axis.
The configurations are (a) $BC_{\parallel}$ H^+; (b) $AB_{\parallel}$ H^+; (c) the transition state; (d) $BC_{\parallel}$ H^+ (large, light colored spheres denote Ga; medium, light colored spheres denote N; and small, dark colored spheres denote H^+).

Neugebauer and Van de Walle[42] and Myers *et al.* suggested that Mg-H complex in both cubic (zinc-blende) and wurtzite GaN structures consists of H at an antibonding site of a N neighbor of the Mg, with the N–H bond aligned parallel to the Mg–N bond. The Sandia National Laboratories' group extended their previous study using density-functional-theory (DFT) and the generalized-gradient approximation (GGA) rather than the local-density approximation (LDA) to clarify the configuration of Mg-H complex in GaN.

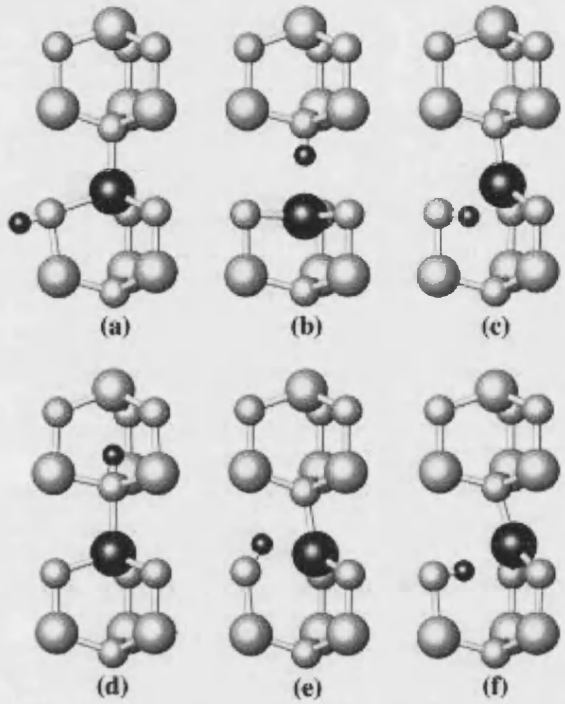

Fig. 3.5. Neutral Mg-H configurations corresponding to local-energy minima: (a) $N_{\perp}AB_{\perp,Mg}$, (b) $N^{\parallel}BC^{\parallel}$, (c) $N_{\perp}AB_{\perp,Ga}$, (d) $N^{\parallel}AB^{\parallel}$, (e) $N_{\perp}AB^{\parallel}$, (f) $N_{\perp}BC_{\perp,Mg}$ (large, light-colored spheres denote Ga; small, light-colored spheres denote N; large, dark-colored spheres denote Mg; and small, dark-colored spheres denote H).

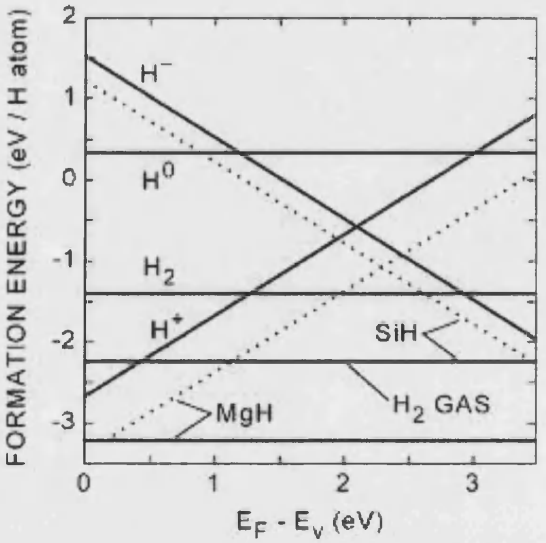

Fig. 3.6. Formation energies for Mg-H and Si-H complexes from density-functional theory.[45]

Six configurations for local-energy minima of the neutral Mg-H complex obtained from the calculations are illustrated in Fig. 3.5. It was found that $N_{\perp}AB_{\perp,Mg}$ (Fig. 3.5(a)) has the largest binding energy (0.62 eV) and therefore is the strongest Mg-H state. $N^{\parallel}BC^{\parallel}$ (Fig. 3.5(b)) was found to be less strongly bound than $N_{\perp}AB_{\perp,Mg}$ by 0.08 eV, whereas the four other configurations have binding energies at least 0.24 eV lower than $N_{\perp}AB_{\perp,Mg}$. The binding energies are given with respect to Mg^{-} and the $BC^{\parallel}$ configuration of H^{+} in GaN lattice, which was previously stated to have the lowest formation energy. Similarly, for the neutral Si–H complex, the binding energy of 0.3 eV relative to isolated H^{-} and Si^{+} was calculated.

Figure 3.6 presents the formation energies for Mg-H ($N_{\perp}AB_{\perp,Mg}$ state) and Si-H complexes as a function of Fermi level in wurtzite GaN at zero temperature.[45] When the Fermi level is close to the valence-band edge, both H^{+} and the Mg–H complex are substantially lower in energy than H_2 gas. However, the hydrogen cannot be absorbed from the gas into *p*-type material at low temperatures. The activation barrier for the adsorption of hydrogen on GaN surface from H_2 gas was calculated to be as high as 1.92 eV using DFT. This is consistent with experimental results, which revealed that high temperatures are required for the uptake of H into GaN:Mg from H_2 gas[52] whereas atomic H (i.e. created in hydrogen plasma discharge) adsorbs at a much lower temperatures (~500 °C).[33, 35, 34, 36] Thereby, GaN:Mg can be easily passivated during hydrogen plasma exposure at moderate temperatures. However at high GaN growth temperatures (>1000 °C) hydrogen can also be absorbed into GaN material from the H_2 phase so that Mg acceptors are passivated when a sample is cooled down to room temperature.

The mechanism of the formation of Mg-H complexes can be proposed as following. A high temperature causes the hydrogen to be absorbed from the H_2 gas phase or from atomic hydrogen created by plasma discharge. The H passivation of the Mg acceptor, combined with electrical compensation by H^+ not attached to Mg, causes the Fermi level to rise, shifting the state energies to the point where uptake of hydrogen is no longer favored. Competition between passivation and compensation of the Mg was suggested to be governed by the opposing influences of the lower formation energy of the Mg–H complex and the higher entropy of H^+ due to its larger number of available sites.[45] An analogous situation was suggested to be in Si-doped GaN where the Fermi level is close to the conduction-band edge. However, the authors mentioned, the H energies never reach the low level achieved in the *p*-type material.

Density-functional theory was also used to examine energy variations along the reaction paths. The authors revealed that two exothermic reactions producing interstitial H_2 from H^+ and H^- and from two H^0 atoms are effectively barrierless. The same was found for the formation of Mg-H from H^+ and Mg^- or from H^0 and Mg^0, and for the formation of Si-H from H^- and Si^+ or from H^0 and Si^0. The reaction of H^+ with Si-H to form Si^+ and H_2 was found to occur readily. The hole capture by Si-H to form Si^+ and H^0 also occurs with no barrier. On the contrary, the dissociation of the Mg-H complex through interaction with another H was estimated to be energetically barred when the second H is H^+ or H^0, and very slow when it is H^- because of the small mobility of the latter species. The dissociation of Mg-H through the capture of a thermal electron is also inhibited by a large energy barrier. The interstitial H_2 was found to dissociate much more easily to $H^+ + H^-$ rather than to $H^0 + H^0$. The electron capture by H^+ was predicted to have a barrier between 0.3 and 1.6 eV, while the hole capture by H^- is barrier-free. Electron capture by H^0 was found to occur with no barrier, whereas hole capture by this species has a barrier of 0.17 eV.

The experimental confirmation of the Mg-H complex comes from infrared (IR) vibrational spectroscopy measurements. The local vibrational mode (LVM) for the $N_{\perp}AB_{\perp,Mg}$ configuration of the Mg-H complex was calculated to be at 3137 cm^{-1} using DFT calculations with the generalized-gradient approximation (GGA). This value is very close to 3125 cm^{-1} obtained by IR vibrational spectroscopy.[47, 53, 54] Gotz *et al.* were the first to report the direct spectroscopic evidence for the existence of the Mg–H complex. The LVM at 3125 cm^{-1} was found to decrease in inverse proportion to the increase of *p*-conductivity after annealing. Glerjaud *et al.* also reported that a broad signal at 3125 cm^{-1} was observed in MOCVD grown GaN. It disappeared after the annealing at 800 °C when *p*-type GaN was obtained. Thereby it can be stated that the passivation of Mg acceptors in GaN is related to Mg-H complex and the post-growth *p*-type activation occurs through its dissociation.

3.4 A review of *p*-GaN activation techniques

3.4.1 Thermal activation

Activation in N_2 ambient

At the present time, thermal annealing is the most common method to activate MOCVD grown Mg-doped GaN. Nakamura *et al.* first reported that *p*-type GaN:Mg was successfully achieved by using this technique. The resistivity of GaN:Mg annealed in a N_2 ambient for 20 min as a function of the annealing temperature is presented in Fig. 3.7. As can be seen, almost no change was observed after the annealing between room temperature and 400 °C. However, at ~500 °C the resisitivity began to decrease suddenly. At a temperature of 900 °C, the resistivity, hole carrier concentration and mobility became 2 Ω·cm, 3 × 10^{17} cm^{-3} and 10 $cm^2/V{\cdot}s$, respectively. Above 700 °C, the resistivity was almost constant between 2 and 5 Ω·cm. The authors noticed that the results of thermal annealing under vacuum conditions (0.001 Torr) at 700 °C for 20 min without N_2 ambient were almost identical to the case of N_2-ambient annealing. It was later found that the resistivity measured after GaN etching was relativily independent of the etching depth in the range used (0 – 3.0 μm). This implies that the annealing effect is not limited by the surface area nearby.

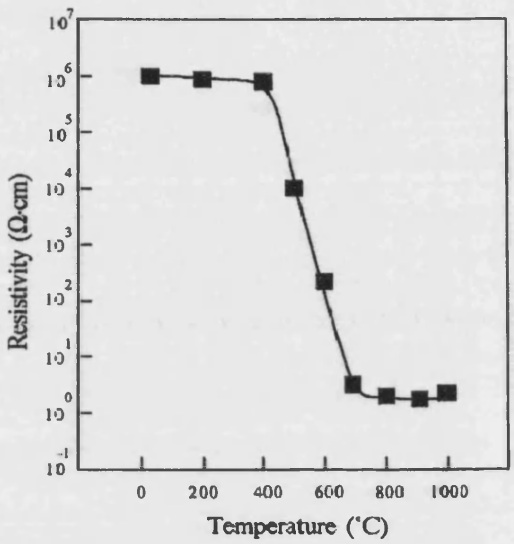

Fig. 3.7. Resistivity of Mg-doped GaN films as a function of annealing temperature.

Nakamura *et al.* also observed significant changes in the photoluminescence (PL) spectra of the annealed samples. Fig. 3.8 shows that the intensity of blue emission (~450 nm) became significantly stronger after annealing at 700 °C. The decrease in the intensity after annealing at 800 °C was attributed to the thermal dissociation of GaN. A broad deep-level (DL) emission (~750 nm) observed for the as-grown samples almost disappeared after annealing at temperatures greater than 600 °C. This corresponds to the abrupt decrease in resistivity at these temperatures. Thereby, the DL emission was ascribed to Mg-H complexes and its intensity changes were related to the *p*-type conduction mechanism.

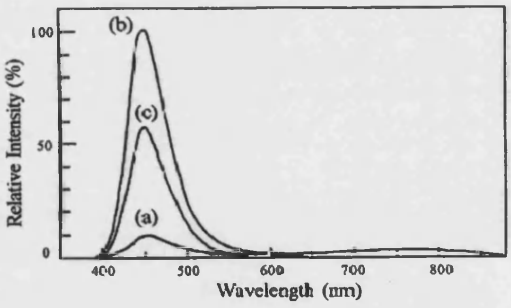

Fig. 3.8. Photoluminescence of (a) as-grown GaN:Mg films and annealed at (b) 700 °C and (c) 800 °C temperature.

Gotz *et al.* performed variable temperature Hall effect measurements to estimate the activation energy of Mg in GaN films grown by MOCVD. Figure 3.9 presents hole concentrations as a function of reciprocal temperature for the samples annealed at 600, 700, and 775 °C for 5 min in a RTA system in N_2. As can be seen, the activation of only a shallow acceptor was observed after annealing at 600 °C. The data for samples after annealing at 700 and 775 °C were ascribed to the thermal activation of a shallow acceptor for temperatures above 200 K with impurity band conduction at lower temperatures.

The authors attributed it to the generation of Mg-related acceptor states in the band gap of GaN due to the dissociation of Mg-H complexes. The calculated acceptor activation energy was 182, 176, and 170 meV for the samples annealed at 600, 700, and 775 °C respectively. The solid lines in Fig. 3.9 present calculated hole concentrations corresponding to these values. The reduction of the activation energy was attributed to increasing acceptor concentration. Nakano *et al.* also reported the dependence of Mg activation energy from annealing temperature. Capacitance-voltage (*C-V*) measurements revealed two deep acceptor levels with activation energies at 135 and 160 meV above the valence band. It was found that the shallower level only occurred when the samples were annealed at temperatures between 650 and 700 °C. It corresponded to the significant increase in effective acceptor concentration.

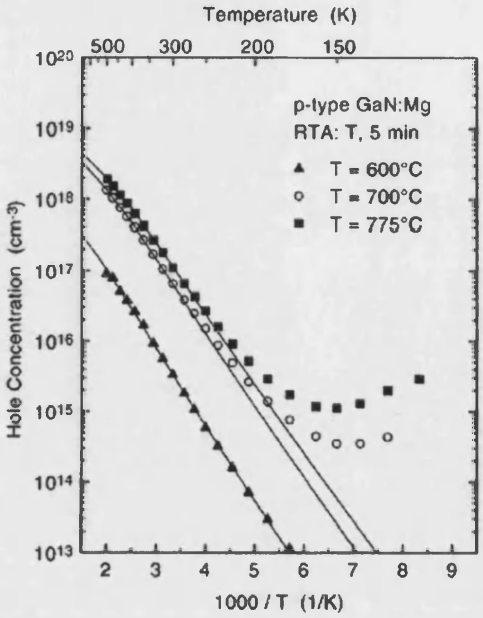

Fig. 3.9. Hole concentrations in annealed Mg-doped GaN samples as a function of reciprocal temperature.

Thereby, in order to activate Mg dopants in GaN, the annealing process should be carried out in the temperature range of 600 – 1000 °C. However, when the temperature is higher than 700 °C, thermal dissociation of GaN may occur. The out-diffusion of Mg can also take place close to the surface. SIMS measurements revealed that Mg started to diffuse out in the surface region (~200 nm from a surface) when the annealing (10 min in N_2) was performed at temperatures over 800 °C. Additionally, the high temperature annealing can affect the quality of InGaN layers in the multiple quantum well (MQW) LED and LD structures. Youn *et al.*[55] investigated the influence of activation temperature on the optical performance of InGaN/GaN MQW LED structure using PL, EL, and *I–V* measurements. Figure 3.10 presents EL and PL peak intensities as a function of Mg activation temperature. As can be seen, when the activation temperature increased, the optical performance of the LED tended to degrade. The authors concluded that *p*-GaN layer activation should be carried out at the lowest possible temperature to obtain the best optical properties of the InGaN/GaN MQWs.

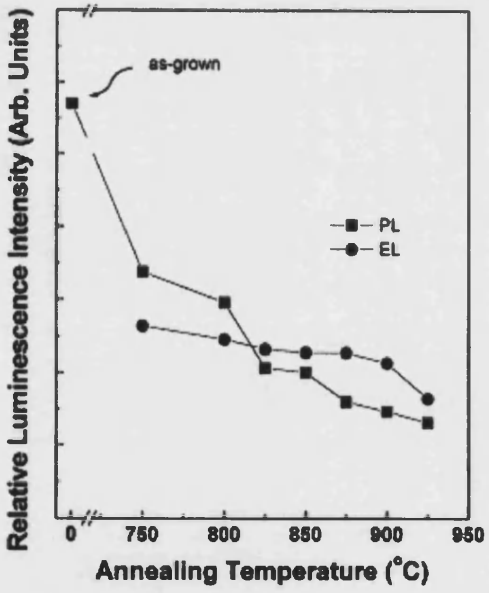

Fig. 3.10. The peak intensities of the PL and EL of InGaN/GaN MQW LED structures activated at various Mg activation temperatures.

Activation in oxidizing ambients

A promising method to reduce the thermal damage is annealing in an oxygen containing ambient. Koide *et al.*[56] studied the effects of annealing in oxygen and nitrogen mixed ambients on Au-based Ohmic contacts to *p*-type GaN. They first observed that the addition of oxygen to the nitrogen gas reduced both contact resistances and resistivity of the *p*-GaN epilayers after annealing at temperatures of 500 – 600 °C. Several further groups[57, 58, 59, 60] have reported that Mg activation in oxidizing ambients occurs at lower temperatures compared to pure N_2 or vacuum conditions. Oxygen is one of the most important residual impurities in GaN, and is generally believed to be responsible for the *n*-type conductivity of unintentionally doped material.[61] The source of the residual oxygen is generally an impurity in NH_3 used as a precursor for metal organic chemical vapor deposition (MOCVD). It was shown that intentional oxygen doping during MOCVD growth produces a donor level at Ec–78 meV, with banding occurring at high concentrations.[62] Autodoping can also occur in situations such as epitaxial lateral overgrowth (ELOG) with a SiO_2 mask, or during annealing with SiO_2 encapsulant layers. However, no oxygen diffusion into GaN films was detected after the thermal annealing in an O_2 ambient.[63] This implies that the role of oxygen during the annealing is to enhance the surface reaction for the removal of hydrogen in the film, but not to activate the acceptors in the GaN bulk.

Hull *et al.* performed annealing of MOCVD GaN:Mg layers from 5 to 90 min at a temperature of 600 – 900 °C in the following ambients: ultrahigh purity (UHP) N_2 with an O_2 gettering apparatus, UHP N_2 without an O_2 gettering apparatus, 99.5% UHP N_2/0.5% UHP O_2, and 90% UHP N_2/10% UHP O_2. Figure 3.11 shows the resistivity of GaN:Mg layers annealed for 20 min in different ambients as a function of activation temperature. It is clear that for samples activated in O_2 containing ambients the resistivity was considerably lower at any given temperature than that for samples activated in the gettered N_2. Even samples activated in UHP N_2 without gettering apparatus showed lower resistivity, suggesting the unintentional incorporation of O_2 during the processing of *p*-GaN. The Hall measurements also confirmed the increase in hole concentration and the decrease in mobility in the samples activated in O_2. Figure 3.12 presents the hydrogen concentration SIMS depth profile for the samples annealed at 700 °C. The hydrogen concentration was greater than 1×10^{19} cm^{-3} when activated in gettered N_2, while it decreased to $4–5 \times 10^{18}$ cm^{-3} when activated in 10% O_2/90% N_2. Thereby, the authors proposed that the lower resistivity of the GaN:Mg following activation in the presence of O_2 was related to the enhanced removal of hydrogen from the layers. Figure 3.13 shows

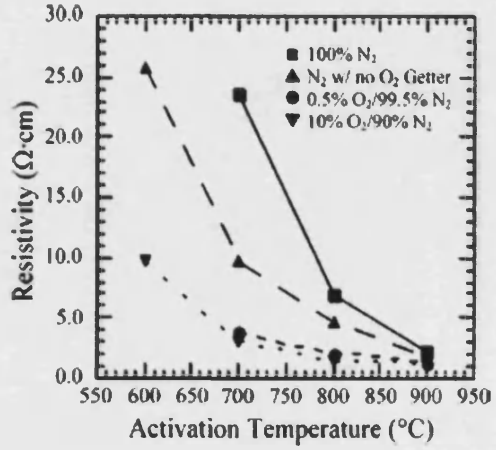

Fig. 3.11. Resistivity of GaN:Mg films annealed for 20 min in different ambients as a function of activation temperature.

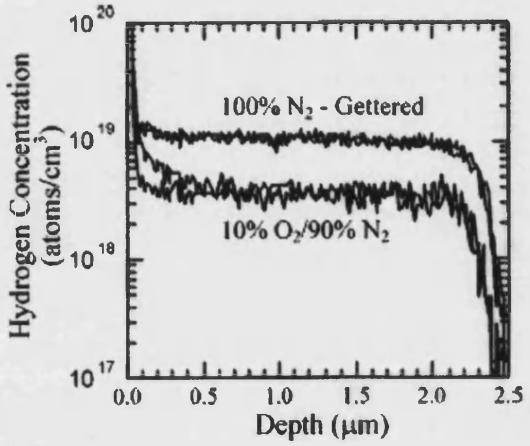

Fig. 3.12. H concentration SIMS depth profile in GaN:Mg films annealed at 700 °C in different ambients.

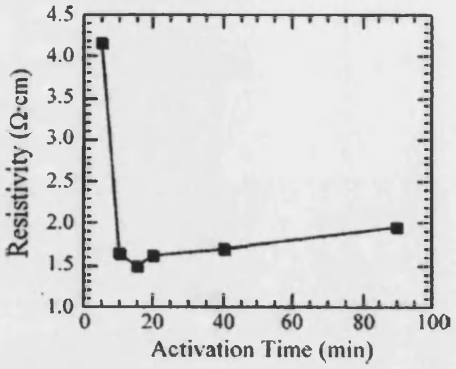

Fig. 3.13. Resistivity of GaN:Mg films annealed at 700 °C in 10% O_2/90% N_2 as a function of activation time.

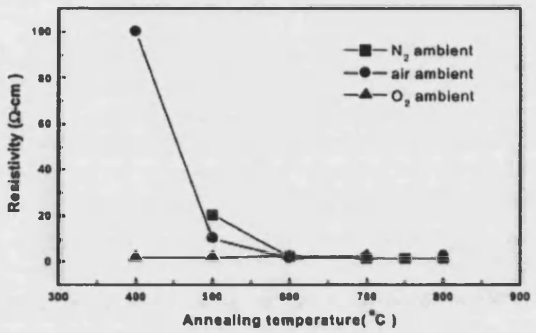

Fig. 3.14. Resistivity of GaN:Mg films annealed for 25 min in different ambients as a function of activation temperature.

the resistivity of *p*-GaN as a function of activation time at 700 °C in 10% O_2/90% N_2. As can be seen, the resistivity increased slightly after longer activation times. It was attributed to either the penetration of oxygen into the surface of *p*-GaN or defect oxidation. However, the reason could also be the thermal dissociation of GaN for long annealing times.

Kuo *et al.* compared the thermal activation of MOCVD grown GaN:Mg performed for 25 min in pure N_2, pure O_2, and air ambient. Figure 3.14 shows the resistivity of the samples annealed in different ambients as a function of annealing temperature. As can be seen, annealing in O_2 resulted in low resistive films at a temperature as low as 400 °C whereas the same resistivity was only achieved at 600 °C in air or N_2. The authors suggested that O_2 enhanced the Mg-H dissociation through the formation of H_2O. They also proposed that the small amount of oxygen in air could promote the activation at lower temperatures compared to the annealing in pure N_2 ambient.

Takeya *et al.* proposed using low-temperature long activation time annealing to reduce the thermal damage in the active layers of LED and LD structures even more. MOCVD grown GaN:Mg layers were annealed in air at 385, 415, and 485 °C and characterized using Hall measurements. Figure 3.15 shows hole concentration as a function of the square root of annealing time. As can be seen, the hole concentration increased in proportion to the square root of annealing time. Thereby, the authors assumed that Mg activation was related to hydrogen diffusion. Arrhenius analysis of the activation rate for three different temperatures yielded an activation energy of ~1.7 eV (Fig. 3.15, inset). The hole concentration reached approximately ~10^{18} cm^{-3} after 80 h at 385 °C. The authors stated that this was the first time that a hole concentration of ~10^{18} cm^{-3} was achieved by thermal activation below 400 °C.

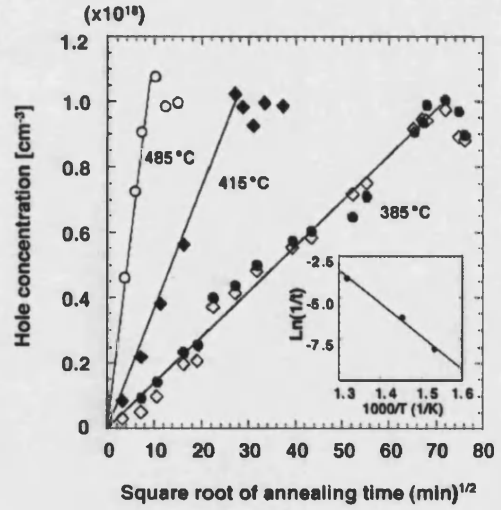

Fig. 3.15. Relationship between hole concentration and annealing time for low-temperature long-time annealing in air.

Activation with a SiO_2 capping layer

The thermal activation of GaN:Mg capped with a SiO_2 layer may have two opposite effects. On the one hand, results similar to annealing in O_2-containing ambients can be expected due to the possible interaction between oxygen diffused from the SiO_2 and hydrogen dissociated in GaN. Additionally, the SiO_2 capping layer can also be useful to prevent GaN thermal dissociation at high annealing temperatures. On the other hand, this layer can hinder desorption of hydrogen from the GaN surface. Furthermore, oxygen diffused from SiO_2 into GaN during annealing can compensate the hole concentration. Pearton *et al.* investigated the oxygen diffusion from a SiO_2 capping layer to MBE grown *p*-type GaN:Mg layers and found that the O concentration and depth of incorporation in GaN showed clear increases after annealing at temperatures higher than 700 °C. Thereby, the authors suggested that the use of SiO_2 as a mask for ELOG of GaN and as a capping layer could produce *n*-type autodoping of the material by oxygen incorporation. However, they could not measure any change in the carrier concentration after annealing using Hall measurements.

Lee *et al.*[64] performed thermal activation of MOCVD grown GaN:Mg layers coated with sputtered SiO_2 (~0.5 μm thick). The annealing was conducted at temperatures of 850, 900, and 950 °C in a N_2 ambient for 30 min. The control samples without a SiO_2 capping layer were also annealed at the same conditions. Figure 3.16 shows the hole concentrations in Mg-doped GaN layers annealed with and without a SiO_2 capping layer. The hole concentration of the GaN:Mg layers capped with SiO_2 after annealing was much higher than that of samples annealed without SiO_2 at all temperatures. More specifically, the concentration changes with the variation of annealing temperature were fairly similar. The authors speculated that the cracking of Mg-H complexes and the out-diffusion of hydrogen increased with the increase of the annealing temperature from 850 to 950 °C. The decrease of the hole concentration above 900 °C was attributed to the increase of out-diffusion of Mg at this temperature. Thereby, the authors concluded that the SiO_2 cap layer plays an important role in preventing the out-diffusion of cracked Mg during activation annealing. However, the other possible explanation can be the enhanced hydrogen removal from GaN induced by the oxygen diffused from the capping layer. The decrease in hole concentration above 900 °C for the samples with the SiO_2 capping layer could be caused by the higher diffusion of oxygen introducing shallow donor levels in GaN. For samples annealed without a capping layer this decrease was probably related to the thermal dissociation of GaN. Thereby, the SiO_2 capping layer can also be useful to prevent GaN degradation at high annealing temperatures.

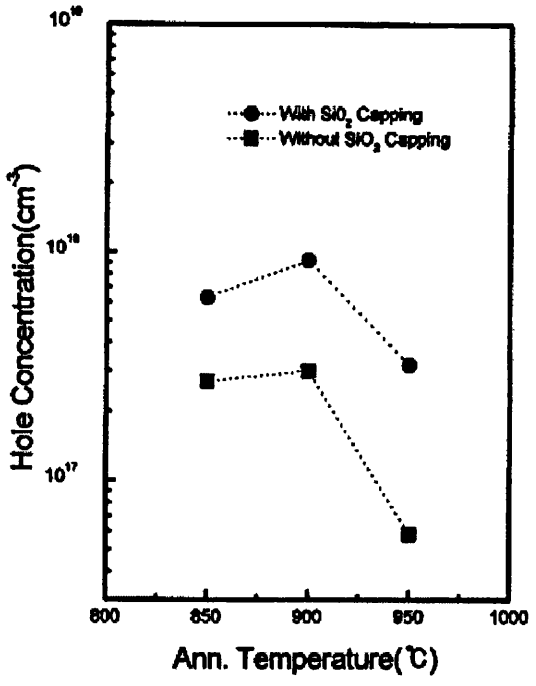

Fig. 3.16. Hole concentrations in GaN:Mg layers annealed with and without the SiO_2 capping layer as a function of annealing temperature.

Figure 3.17 shows the relative intensities of the photoluminescence (PL) spectra measured at room temperature (RT) of the GaN layers annealed with and without the SiO_2 layer. The intensity of the samples annealed with SiO_2 increased with the annealing temperature from 850 °C to 900 °C, and slightly decreased at 950 °C, similar to the data

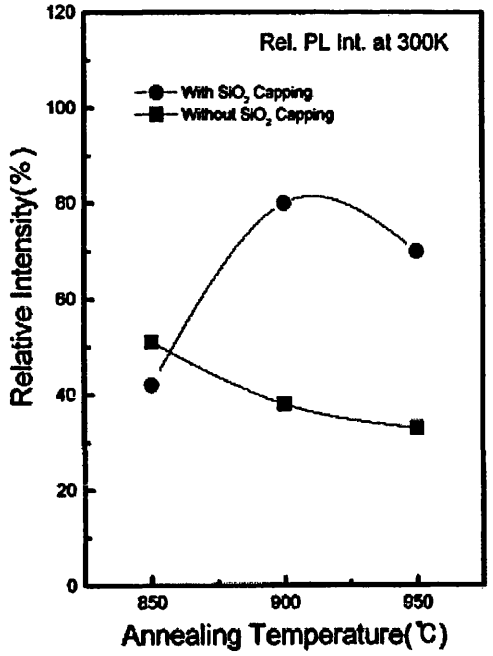

Fig. 3.17. PL intensity of GaN:Mg layers annealed with and without the SiO_2 capping layer as a function of annealing temperature.

for hole concentration. In contrast, the intensities of the layers annealed without a capping layer decreased continuously with the annealing temperature. Furthermore, for the samples annealed with SiO_2 the intensity peak was at 435 nm at all given temperatures. This was attributed to the emission of the donor-acceptor pair (DAP) transition. However, the peak of intensity for the samples annealed without SiO_2 was found to shift from 435 nm, to 423 and 415 nm for the temperatures of 850, 900 and 950 °C respectively. The authors suggested that this shift resulted from the change of Mg energy level due to the thermal effect caused by higher temperatures of 900 °C and 950 °C. Thereby, the SiO_2 capping layer can also be useful to prevent the degradation of GaN optical properties at high annealing temperatures.

Activation with Ni and Pd thin films

Waki *et al.* reported that activation also occurs at lower temperatures if the GaN surface is coated either with a Ni or with a Pd[65] film. It is known that Ni and Pd are widely used in hydrogen storage alloys to increase the hydrogen desorption rate.[66] The authors suggested that Ni and Pd films could also facilitate the removal of H from GaN during annealing, similar to the effect of O_2-containing ambients. A Ni (Pd) film with a thickness of approximately 1.5 nm was deposited on GaN:Mg layers grown by MOCVD. Subsequently the samples were annealed in N_2 ambient for 10 min at a temperature from 200 to 800 °C and cleaned in boiling aqua-regia to remove the metal. Figure 3.18 shows the hole concentration and Fig. 3. 19 shows the resistivity as a function of the annealing temperature for samples activated with a Ni and with a Pd film respectively. For samples annealed without the metal films, *p*-type conduction was obtained by annealing above 600

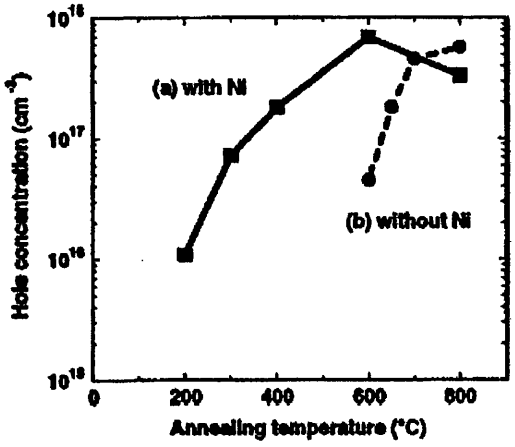

Fig. 3.18. Hole concentration in GaN:Mg films annealed (a) with Ni and (b) without Ni film in N_2 ambient for 10 min as a function of annealing temperature.

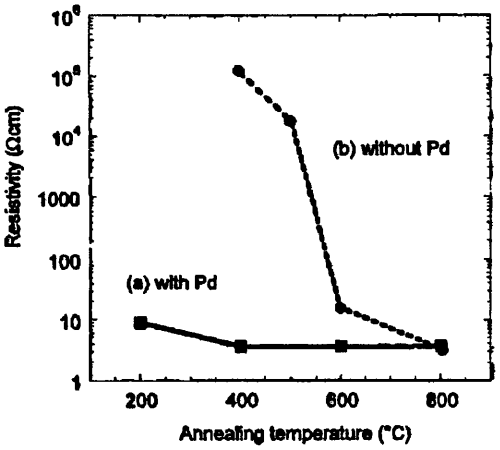

Fig. 3.19. Resistivity of GaN:Mg films annealed (a) with Pd and (b) without Pd film in N_2 ambient for 10 min as a function of annealing temperature.

°C. On the other hand, *p*-type conduction was obtained at a temperature as low as 200 °C for the sample annealed either with the Ni or with the Pd film. It was stated that this annealing temperature was the lowest ever reported for obtaining MOCVD grown *p*-GaN by thermal annealing. Figure 3.20 shows the SIMS H profiles of the samples annealed under various conditions. One can see the reduction in the H concentration after the annealing. In the case of the samples annealed with the Ni film, the H concentration reduction after annealing was more evident at the same temperatures. Thereby, the present authors concluded that the Ni and Pd films on the GaN surface dramatically enhance the removal of hydrogen, which results in the activation of Mg-doped GaN at very low temperatures. Nevertheless, these data cannot be considered as completely correct. For the Hall effect measurements the authors deposited Ni electrodes and annealed them at 550 °C in N_2 ambient for 10 min to obtain Ohmic contacts. Although they found that the annealing at 550 °C without Ni film did not activate acceptors in GaN, this contact treatment could affect the final results.

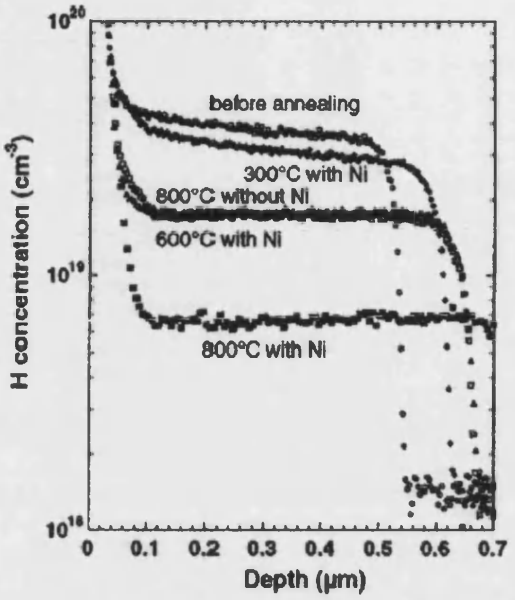

Fig. 3.20. SIMS profiles of H concentration for GaN:Mg films annealed with and without a Ni film in N_2 ambient for 10 min.

Annealing under UV irradiation

Kamiura *et al.* reported that the activation temperature can also be reduced by ultraviolet (UV) irradiation during annealing. GaN samples were annealed for an hour in a nitrogen ambient with and without the irradiation of UV light with a peak wavelength around 350 nm. Without UV irradiation, the resistivity and mobility decreased, and the hole concentration increased simultaneously at around 550 °C. These results are consistent with those previously reported. This temperature was reduced to 450 °C by the UV radiation. The effect of UV irradiation was explained by the enhancement of the dissociation of Mg-H complexes. The authors speculated that electronic excitation reduced the thermal stability of the Mg-H complexes in GaN.

Theory of thermal activation

The most complete study of thermal activation of wurtzite Mg-doped GaN has been performed by the group from Sandia National Laboratories, New Mexico.[51, 52, 67, 68] *C–V* measurements on a GaN p/n^+ diode revealed the activation energy of 1.76 eV for the dissociation of Mg-H complex, corresponding to a sum of the H^+ diffusion activation energy and the Mg–H binding energy. This value is in a good agreement with calculated 1.62 eV using GGA density-functional theory (the diffusion activation energy of H^+ for wurtzite GaN in c axis direction is 1.0 eV; the binding energy of the most stable Mg-H state ($N_{\perp}AB_{\perp,Mg}$) with respect to Mg^- and H^+ in wurtzite GaN lattice is 0.62 eV [50]). This barrier is low enough to overcome at modest annealing temperatures (around 300 °C). It is consistent with experimental results which showed that H becomes mobile in GaN:Mg at temperature above 350 °C.[36, 48] However, much higher temperatures are required to activate Mg-doped *p*-GaN. It is obvious that the released H needs to be either removed from layers or neutralized. Otherwise it continues to compensate Mg when the sample is

cooled down again. Neugebauer and Van de Walle first proposed that there may be an activation barrier for the removal of hydrogen from the layer through desorption from the surface. This barrier results in much higher temperatures required for the activation of *p*-GaN.

Myer *et al.* performed theoretical modeling to estimate the diffusion and thermal release of hydrogen from GaN:Mg under vacuum and compared it with experimental results. The annealing at 900 °C for 1 h at a vacuum of ~10^{-7} Torr was used to remove the grown-in hydrogen from GaN:Mg grown by MOCVD. SIMS measurements showed a residual H concentration of ~10^{17} atoms/cm^3. The deuterium, employed for the experiments, was subsequently introduced by heating in D_2 gas at 700 °C for 4 h under a pressure of 0.88 bar. This treatment increased the resistivity of the material from 2.6 to 1.4 × 10^4 Ω·cm, indicating a nearly complete neutralization of the Mg acceptors. Thermal release of the D was then investigated during sequences of isothermal anneals carried out at 700 – 900 °C in a vacuum of ~10^{-7} Torr. The concentration of D was determined by nuclear-reaction analysis using the ^{3}He-induced reaction D(^{3}He, *p*)^{4}He.[69]

Figure 3.21 shows the retained fraction of D in the films after the annealing in vacuum at 700, 800, and 900 °C (filled circles) as a function of annealing time. The open circle presents a datum for the release of grown-in ^{1}H during the annealing in RTA system for 7 sec at 1000 °C in flowing N_2 gas. The obtained release rates were far smaller than it was expected for diffusion-limited flow to the surface followed by prompt desorption. The authors related it to a surface permeation barrier. The rates were estimated to be proportional to the square of the remaining concentration of D. Thereby the authors suggested that D_2 recombination is the rate-determining step during the thermal release of deuterium in vacuum. Figure 3.22 shows the SIMS depth profile of D measured after annealing at 700 °C in vacuum for 64 h. As can be seen, the profile was clearly inconsistent with a representative diffusion-controlled profile from the theoretical model. It also supports that the recombination step is rate determining, rather than the movement of H from solution onto the surface. The solid curves in Fig. 3.21 present the theoretical results corrected for the barrier energy of – 2.47 eV. As can be seen, the corrected theoretical model is very consistent with experimental results at all given temperatures. Figure 3.23 shows theoretically predicted increase in room-temperature hole concentration resulting from isothermal release of D in vacuum.

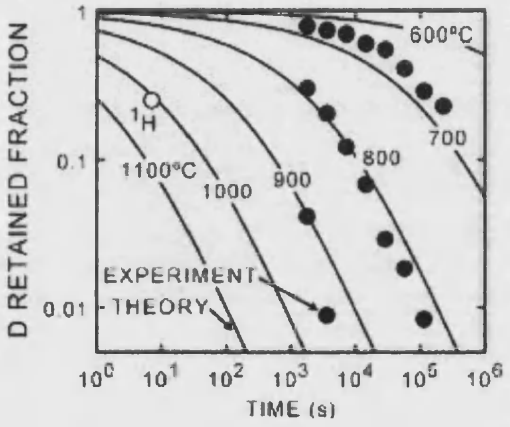

Fig. 3.21. Measured release of gas-charged D (●) or grown-in ^{1}H(○) during isothermal annealing and predictions of the fitted theoretical model.

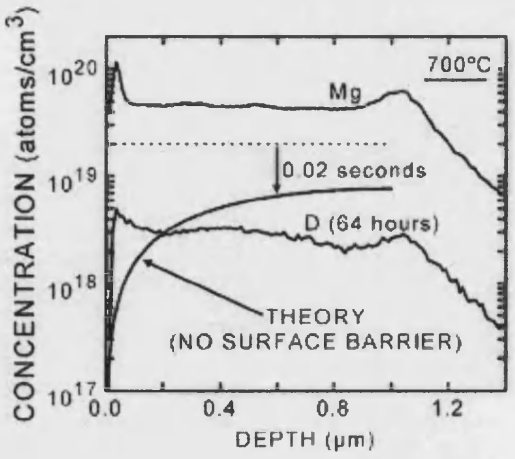

Fig. 3.22. Measured depth profiles of D and Mg in the specimen after annealing at 700 °C in vacuum for 64 h compared with a representative theoretical diffusion profile obtained assuming no surface barrier.

Wampler and Myers investigated the influence of surface impurities on the thermal release of D in vacuum. The

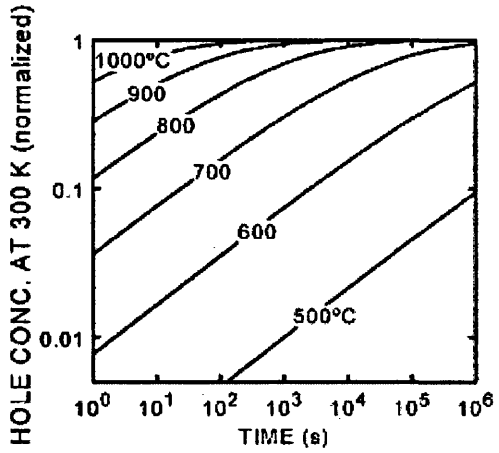

Fig. 3.23. Theoretically predicted increase in room-temperature hole concentration resulting from isothermal release of D in vacuum.

authors removed surface contamination by sputtering with nitrogen from an ion gun with 2 kV acceleration voltage. Thermal release was carried out in ultra-high vacuum of ~10^{-10} Torr. It was found that D release rates were proportional to the square of the D concentration implying that molecular recombination was a rate-determining step in the release of deuterium. These rates were not significantly faster than their previously measured under high vacuum (10^{-7} Torr) conditions from samples without in-vacuum surface cleaning. Thereby, the authors concluded that surface impurities do not significantly hinder the thermal release of hydrogen.

The following processes were proposed to be involved in the thermal release of H from GaN:Mg in vacuum:

- the dissociation of Mg-H into Mg^- and H^+
- the diffusion of H^+ to the surface
- the formation of neutral H surface state
- the molecular recombination and desorption of H_2 from the surface

The authors stated that high temperatures for H release result from both the high stability of Mg-H relative to H on the surface (the formation energy of Mg-H was calculated to be 1.1 eV/atom below that of H in the surface state) and the high barrier for the recombinative desorption of H from the surface. The first cause results in very low surface coverage of H during thermal release. This low surface coverage and the high desorption barrier cause the flux of H from the surface to be small compared to it from the bulk to the surface. Thus, it was concluded that the release of H is limited by a surface permeation barrier and is not limited by the diffusion of H to the surface.

It was illustrated above that activation occurs at lower temperatures if GaN surface is coated with Ni (Pd) films,[63, 65] or if annealing is conducted in oxidizing ambients.[57, 58, 59, 60] The authors suggested that Ni (Pd) films or O_2-containing ambient could facilitate the removal of H from the GaN surface either through enhancing recombinative desorption rate or by the removal of H from the surface through the formation of volatile products. Myers *et al.* continued their study to investigate the influence of ambient on hydrogen release from *p*-type GaN:Mg. MOCVD grown GaN:Mg layers were annealed at 900 °C for 1 h in vacuum to remove the grown-in hydrogen. The deuterium, employed for the experiments, was subsequently introduced by heating in D_2 gas at 700 °C for 4 h under a pressure of 0.87 bar. Thermal release of deuterium was carried out in vacuum of ~10^{-7} Torr, and O_2 or in ultra-high-purity N_2 ambients. The D concentration was quantitatively determined using the ^{3}He-induced nuclear reaction D(^{3}He,*p*)^{4}He.

Figure 3.24 shows the retained D fraction as a function of annealing time at 800 and 700 °C in a vacuum of ~10^{-7} Torr, ultrahigh vacuum (UHV ~10^{-10} Torr), and in O_2 gas at a low pressure of ~0.08 Torr. As can be seen, the release rates were virtually the same for all the ambients. Figure 3.25 shows the reciprocal of retained D fraction as a function of annealing time in a vacuum at 800 °C. The presented format produces a straight-line plot when the release rate is proportional to the square of the D concentration. As can be seen, in the range of $0<[\text{D fraction}]^{-1}<10$, it was almost linear. These data were attributed to second-order recombinative D-D desorption being rate-limiting in the release. In this case the release rate is proportional to the square of D surface coverage. The dashed curve in

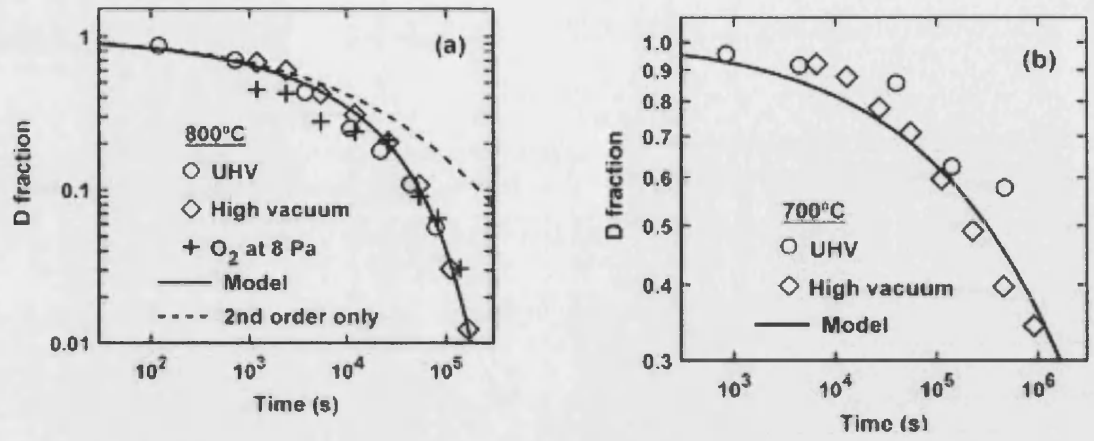

Fig. 3.24. Retained D fraction as a function of annealing time in vacuum or low O_2 pressure.

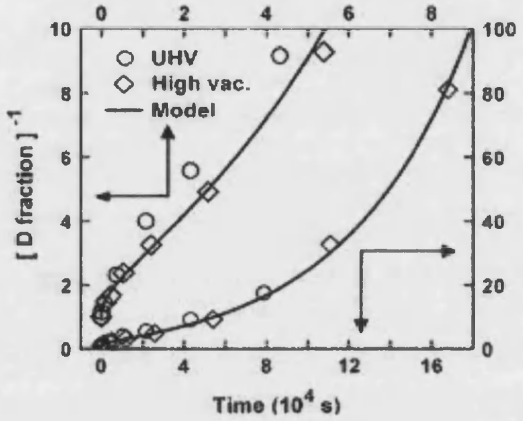

Fig. 3.25. The reciprocal of retained D fraction as a function of anneal time in vacuum at 800 °C.

Fig. 3.24(a) shows the calculated effect of the second-order process acting alone. However, the full plot (Fig. 3.25) was far from linearity in the range $10<[\text{D fraction}]^{-1}<100$, corresponding to the last 10% of the D release. The authors suggested that such release might involve the desorption of N–D species as the release proceeded and surface coverage of D became smaller. In this case, the D release rate was proposed to be proportional to the surface coverage of D, corresponding to the first-order surface process. The solid curves in Fig. 3.24 and 3.25 were plotted from the fitted model with both first- and second-order processes.

Figure 3.26 shows the retained D fraction as a function of annealing time at 800 °C in N_2 gas at a pressure of 87 kPa (0.87 bar). The vacuum results were included for comparison. The data were plotted in a semilog format to produce a straight line when the release rate is proportional to the surface coverage of D (the first-order surface process). As can be seen, as the fraction of D became small, the data approached a straight-line variation for both ambients. The impact of the N_2 was small initially but increased later compared to vacuum annealing. The fitted theoretical coefficient of the first-order surface process was estimated to be 5.7 times larger in the presence of N_2. The authors suggested that the N_2 gas accelerated the thermal release of D from the surface by promoting the formation of volatile N–D species, resulting in a first-order surface process.

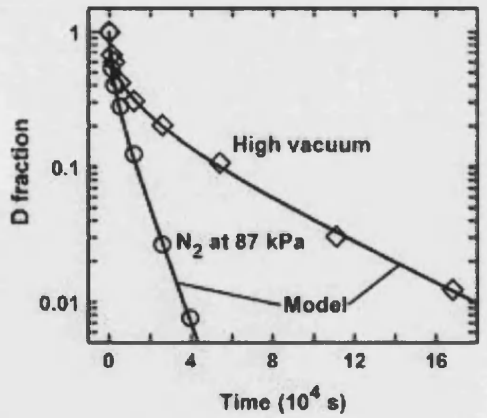

Fig. 3.26. Retained D fraction as a function of annealing time at 800 °C in vacuum and in N_2.

Figure 3.27 shows the retained D fraction as a function of annealing time at 700 °C in a vacuum and in O_2 gas at pressures of 80 and 800 Pa (0.0008 and 0.008 bar). The oxygen penetration into *p*-GaN was found to be negligible at the study conditions and was

proposed not to introduce significant number of donors in the structure. The release rates in O_2 ambients were found to be proportional to D surface coverage, suggesting that the first-order surface process was the dominant. The abrupt slowing of D release in O_2 ambients at the retained fraction of about 0.3 was ascribed to oxidation of the GaN surface. It is important to note that the similar abrupt slowing was observed during the annealing in O_2 at 800 °C and it also occurred at about 0.3 retained fraction of D. The solid curve in Fig. 3.27 presents the theoretical model matching well the experimental data until the process was interrupted by oxidation. The authors suggested that the O_2 gas accelerated the D release from the surface through the formation and desorption of volatile O–D species such as D_2O. This enhancement was much stronger compared to N_2 impact, regardless of the smaller pressures of O_2. It was explained by the easier dissociation of O_2.

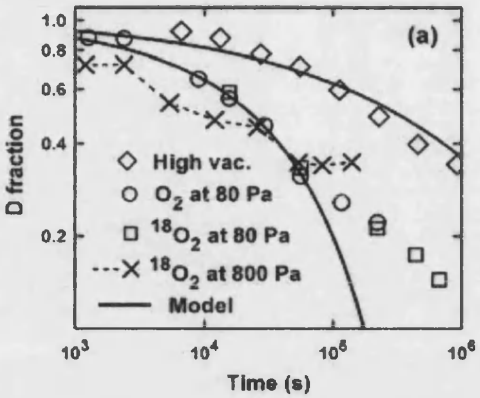

Fig. 3.27. Retained D fraction as a function of annealing time at 700 °C in vacuum and in O_2.

Myers *et al.*[67] also exposed as-grown GaN:Mg samples, containing the grown-in ^1H, to electron–cyclotron-resonance (ECR) N_2 plasmas (2×10^{-4} Torr pressure, 250 W microwave power, ion mean energy ~20 eV) at 600 and 700 °C for 1h. Fourier-transform infrared spectroscopy showed that the absorption peak associated with Mg-H complex (3125 cm^{-1}) was unchangeable after the 600 °C exposure and was slightly reduced after the 700 °C exposure. The authors concluded that plasma exposure did not greatly enhance the release of H from *p*-type materials compared to the thermal release in vacuum at the same conditions. Recently Myers and Seager also reported that the release of protium (^1H) or deuterium (D) was increased by several orders of magnitude in an ambient containing H_2 gas of the other isotope. It was suggested that the release was accelerated by modifying the surface conditions in H-reactive ambients. The authors concluded that it supports a picture of the release in which recombinative desorption from the surface is rate limiting.

3.4.2 LEEBI (Low-Energy Electron Beam Irradiation) activation

The first *p*-type conductivity in MOCVD grown Mg-doped GaN was unintentionally obtained by Amano *et al.* using low-energy electron beam irradiation (LEEBI). They were studying cathodoluminescence (CL) of Mg-doped GaN and observed that electron irradiation increased the efficiency of the luminescence by up to 2 orders of magnitude and caused the samples to become conducting and *p*-type. The obtained hole concentration was estimated to be ~2×10^{16} cm^{-3} and the mobility ~8 $cm^2/V \cdot s$. In 1989 they realized the first *p-n* junction GaN LED using LEEBI treatment. Although the thermal annealing at the present time is the most common method to activate *p*-type GaN grown by MOCVD, the LEEBI activation may have some potential advantages for certain applications. In the case of LEEBI treatment, the region showing *p*-type conductivity is restricted to the irradiation area. Thereby, LEEBI treatment is expected to be effective in realization of a current confinement structure, which can be directly patterned in any desired form. Very small structures such as quantum-size devices, microscopic light emitters, and blue lasers can be fabricated. However, as it is shown below, the reversal of the activation at fairly low temperatures (below 200 °C) may be problematic for the application of LEEBI in GaN devices.

Nakamura *et al.* measured resistivity of GaN films after LEEBI treatment as a function of etching depth and found that the activation depth in GaN films is restricted by the penetration depth of incident electons. The penetration depth as a function of accelerating voltage for the incident electrons is presented in Fig. 3.28. The impact of irradiation time was estimated by Inamori *et al.*[70] MOCVD grown GaN:Mg samples were exposed by LEEBI with accelerating voltage of 15 kV (electron beam diameter was about 1 μm). Figure 3.29 shows resistivity of the samples as a function of irradiation time. The obtained hole concentration was reported to be as high as 2×10^{18} cm^{-3} at room temperature. It is important to note that the irradiation time probably depends on the parameters of LEEBI treatment such as accelerating voltage, electron beam spot size, and emission current of the electrons. The temperature rise of the samples due to LEEBI treatment was estimated to be about 70 K, which is too low to cause *p*-type conversion by the thermal effect.

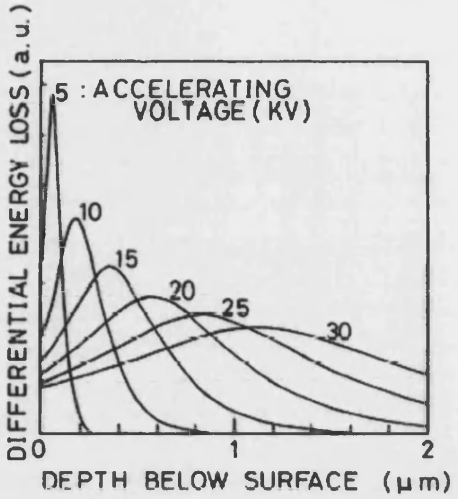

Fig. 3.28. Estimated change of the energy loss of incident electrons in GaN as a function of accelerating voltage.

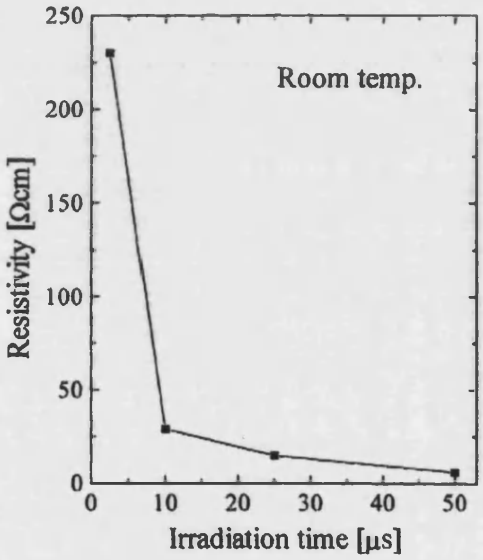

Fig. 3.29. Resistivity of LEEBI-treated GaN:Mg films as a function of irradiation time.

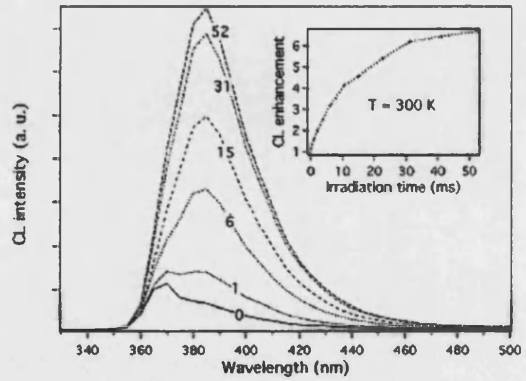

Fig. 3.30. Room-temperature CL spectra as a function of irradiation time.

The confirmation of athermal nature of LEEBI activation comes from a study of Li and Coleman.[71] They used cathodoluminescence (CL) spectroscopy to estimate the effect of LEEBI of MOCVD grown GaN:Mg (0.7 μm thick) as a function of irradiation time at both room and liquid helium temperature. The acceleration voltage was 15 kV, which corresponds to a penetration depth of 0.7 μm. The measurement emission current of electrons was one order of magnitude lower than that for the irradiation. Figure 3.30 shows the CL spectra taken at room temperature as a function of irradiation time. As can be seen, the luminescence intensity significantly increased after the annealing and was saturated at about 50 msec. A peak at 370 nm for the as-grown sample was attributed to band-edge emission, whereas a peak at 385 nm appearing after the treatment was related to Mg-related levels. To examine whether LEEBI annealing is thermal or electronic process, LEEBI treatment was performed at liquid helium temperature. The shape and total enhancement in CL spectrum were found to be very similar to the spectrum taken after the LEEBI

treatment at room temperature. Thereby, the authors concluded that LEEBI annealing is an athermal process and occurs through the generation of free electrons and holes. The generated carriers in their turn stimulate the breaking of Mg-H complexes and change the charge state of hydrogen.

The group from Sandia National Laboratories expanded their study of hydrogen behavior in GaN to investigate the LEEBI-related *p*-type activation.[31, 32] MOCVD grown GaN:Mg layers were exposed to LEEBI. One group of samples was used in the as-grown state, while the other group was annealed at 900 °C in vacuum followed by 4 h, 700 °C annealing in either D_2 or H_2. The irradiations were carried out with electron energy of 25 keV sufficient to activate 1.5-μm-thick *p*-type layer. The beam current was fixed at 2 μA. Postirradiation annealing was carried out in N_2 gas for 1 h to estimate the thermally activated restoration. The effect of LEEBI treatment on the stability of Mg-H complexes in GaN was studied by infrared optical spectroscopy. It was shown before that the absorption peak corresponding to Mg–H complex is located at 3125 cm^{-1}.[47, 53, 54] This value is in a good agreement with theoretically predicted (3137 cm^{-1}). The absorption peak corresponding Mg-D complex was experimentally found to be different and located at 2321 cm^{-1}. DFT theory was used to examine intermediate and final states during the irradiation-induced dissociation.

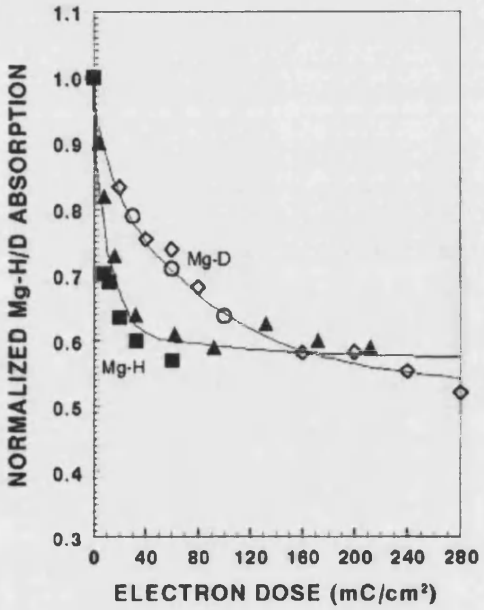

Fig. 3.31. Evolution of the Mg–H(D) LVM peak heights as a function of total LEEBI dose (filled squares, as-grown GaN; filled triangles, H_2-reloaded GaN; and open diamonds and circles, D_2 reloaded GaN).

Figure 3.31 shows the evolution of the Mg–H(D) LVM peak heights as a function of total LEEBI dose. As can be seen, the changes of the as-grown and H-reloaded samples were similar, while for D-loaded sample the initial rate of loss of Mg–D pairs was significantly slower. The curves were saturated at peak heights ~1/2 their initial values. It was found that additional exposures of 40 mC/cm^2 with a more deeply penetrating beam of 30 keV electrons still left one half of the hydrogen–acceptor pairs intact. Figure 3.32 shows the effect of postirradiation annealing in N_2 for 1 h on Mg–H(D) absorption peak heights. As can be seen, the restoration occurred predominantly in the temperature range of 150 – 200 °C. These results imply that the room-temperature LEEBI treatments did not remove the H from the specimen. The authors previously found before that isolated H in *p*-type GaN material can mainly exist as H^+. However, they stated that it did not exist in this state after the LEEBI exposure due to its positive charge would compensate the Mg acceptors and prevent electrical activation. The authors also previously found that the presence of H^+ in Mg-doped GaN more likely leads to the reformation of the Mg–H center at room

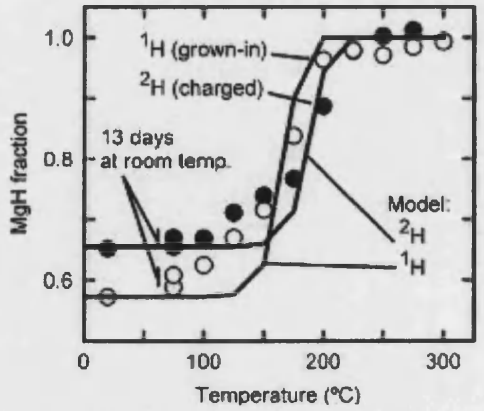

Fig. 3.32. Recovery of Mg-H(D) absorption strength during isochronal annealing after LEEBI. (the solid lines represent the fitted model).

temperature.[45, 50] Thereby, the conversion of hydrogen to a metastable neutral state was suggested to take place under LEEBI exposure.

The mechanism for LEEBI activation was proposed as following. The stable Mg–H complex (Fig. 3.33(a)) is dissociated by the impinging energetic electrons. The resultant detached H^+ migrates into the vicinity of another Mg–H complex (Fig. 3.33(b)) and captures an electron (Fig. 3.33(c)). The final electron capture enables the formation of Mg-H_2 complex (Fig. 3.33(d)), where H_2 molecule is located in the immediate vicinity of the Mg acceptor. This complex is a shallow acceptor like isolated Mg. The binding energy was calculated to be 1.51 eV relative to isolated H^+, H^-, and Mg^-. It is sufficient for the state to persist at room temperature. However, it was calculated that Mg–H_2 complex is the subject to electron-beam dissociation as well as the Mg–H center. It finally results in the balance between the opposing reactions under LEEBI exposure and the number of neutral Mg–H centers remaining.

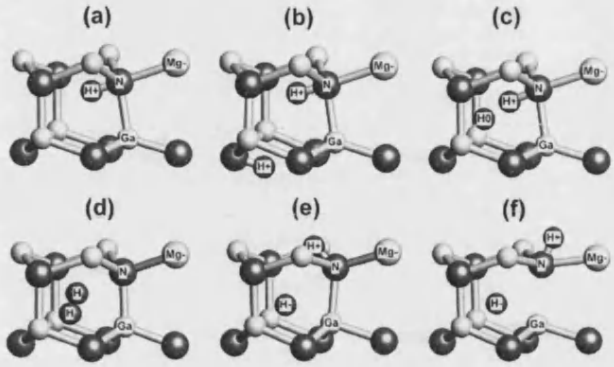

Fig. 3.33. Atomic configurations relating to LEEBI from density-functional theory.

The reverse process of the Mg-H_2 complex conversion to the more stable Mg–H center during postirradiation annealing in the absence of electron injection was proposed as following. The H_2 molecule adjacent to the Mg is thermally dissociated with the formation of H^+ and H^- (Fig. 3.33(e)). The dissociated H^+ moves through a saddle point (Fig. 3.33(e)) to a local energy minimum (Fig. 3.33(f)). Subsequently the remaining H^- captures holes forming H^0 and then the more stable H^+. Finally, one of H^+ atoms forms Mg–H with the nearby acceptor, while the other diffuses away to react with another, unattached Mg. The activation energy for the dissociation of the Mg–H_2 complex was predicted to be 1.8 eV compared to H^+ diffusion barrier of 1.2 eV. Thereby the authors concluded that the thermal repassivation rate is mainly controlled by the dissociation of the metastable state.

3.4.3 Minority-carrier-enhanced activation

Pearton *et al.* cited that in Si and GaAs material the injection of minority carriers either by forward biasing of a diode structure or by illumination with above band-gap light produces dissociation of neutral acceptor-hydrogen or donor-hydrogen complexes at temperatures at which they are normally thermally stable. The reactions for an acceptor-hydrogen complex was described as following:

$$(AH)^0 \Leftrightarrow A^- + H^+$$
$$H^+ + e^- \Leftrightarrow H^0$$

The neutral hydrogen was suggested to form diatomic or large clusters with other neutral or charged hydrogen species. It results in the activation of dopants passivated with hydrogen before the injection. The similar activation mechanism can be expected in III-nitride materials.

In 1996 Pearton *et al.* first reported that minority-carrier injection by forward biasing of a diode structure can also activate the Mg acceptors in GaN. The authors performed the annealing under NH_3 for 30 min at 500 °C for MOCVD grown *p-n* structure to introduce additional amount of hydrogen. Mesa *p-n* junction diodes were formed by

etching. Ti/Al and Ni/Au were deposited as *n*- and *p*-contact respectively. The authors conducted capacitance-voltage (*C-V*) measurements at 10 kHz at room temperature to obtain the carrier profiles in the *p*-type layer. Annealing was carried at 175 °C under open-circuit configuration and under forward current of 9 mA to inject electrons into the *p*-type. Figure 3.34 shows a series of acceptor concentration profiles of *p-n* junction sample, after annealing at 175 °C under forward bias conditions. After 1 h, the majority of these acceptors were reactivated. The Mg activation depended on depth into the *p*-type layer, which was related to the diffusion distance of the injected electrons prior to recombination. If the annealing was carried in the open-circuit configuration, no change in the carrier profile was observed after up to 20 h at 175 °C. It was concluded therefore, that the injection of electrons has a dramatic influence on the stability of the Mg-H complexes through the conversion of H^+ into the neutral state and then into the final hydrogen complexes.

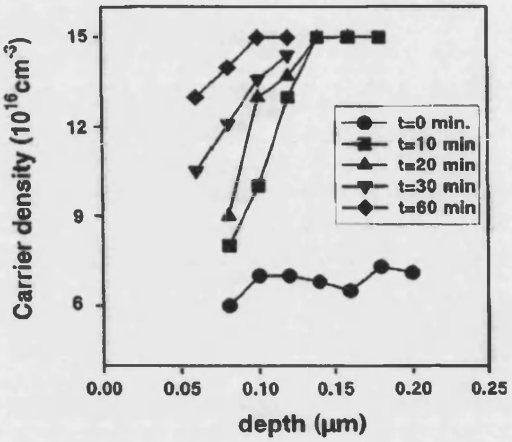

Fig. 3.34. Carrier concentration profiles in hydrogenerated GaN:Mg after annealing for various times at 175 °C under forward bias.

Miyachi *et al.*[72] performed secondary ion mass spectrometry (SIMS) measurements to examine the hydrogen concentration profile in the samples. Minority-carrier injection into Mg-doped layers during thermal annealing was conducted by applying forward bias on *p-n* junction diodes. All annealing treatments were performed under N_2 ambient for 30 min. The first annealing was conducted under forward bias, the second annealing was in the open-circuit configuration, and the other was the annealing without any coating (*p*- and *n*-contacts). The differential resistance at a forward voltage of 10 V was taken to evaluate the activation of the Mg acceptors. Figure 3.35 shows the

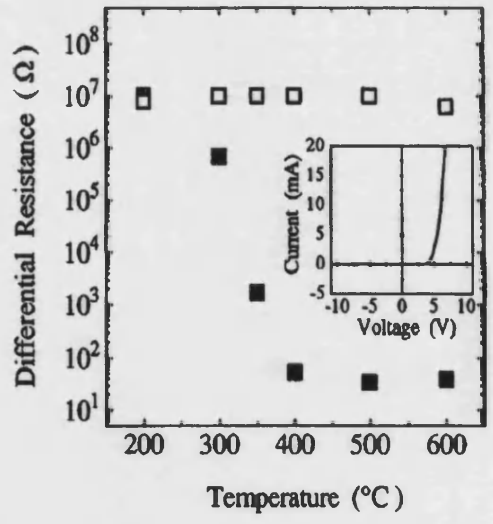

Fig. 3.35. Differential resistance at 10 V of the diodes as a function of annealing temperature under forward bias of 10 V (solid squares) and in open-circuit configuration (open squares).

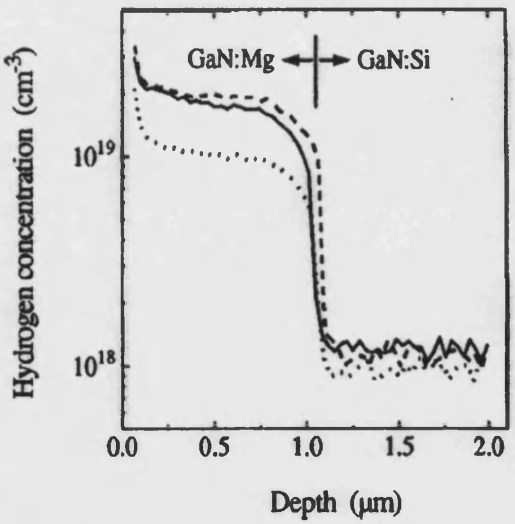

Fig. 3.36. SIMS profiles of hydrogen in GaN:Mg/GaN:Si diodes: as-grown (solid line); annealed under 10 V forward bias at 400 °C (dashed line); annealed in open-circuit configuration at 800 °C (dotted line).

differential resistance of the diodes annealed under 10 V forward bias (solid squares) and in the open-circuit configuration (open squares) as a function of the annealing temperature.

The samples annealed in open-circuit configuration were still semi-insulating after annealing at 600 °C, whereas Nakamura reported the activation of *p*-GaN at temperatures higher than 500 °C. It was attributed to a fact that these samples had metal pads on the surface. Therefore, hydrogen could not desorb out of the layers. However, for annealing under bias, the differential resistance began to decrease at ~300 °C, and saturated at five orders of magnitude smaller above 400 °C. SIMS analysis results are shown in Fig. 3.36. As can be seen, after annealing under bias at 400 °C, the hydrogen concentration was almost the same as the as-grown sample where the Mg acceptor was completely passivated by hydrogen. It indicates that hydrogen existed in a certain state in the sample annealed under bias where hydrogen did not passivate the Mg acceptor. On the contrary, the hydrogen concentration was significantly decreased after the conventional thermal annealing at 800 °C with no metal pads. It implies different activation mechanism of these techniques. The authors concluded that injected current changes the state of dissociated thermally H^+ into a certain one where hydrogen does not passivate the Mg acceptor.

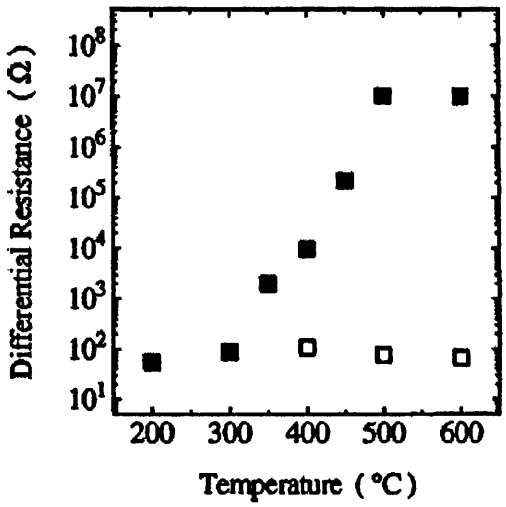

Fig. 3.37. Differential resistance of the diodes annealed under bias at 400 °C (solid squares) or annealed in open-circuit configuration at 800 °C (open squares) as a function of the temperature of additional annealing without bias.

The remaining H introduces interesting characteristics of the samples. Figure 3.37 presents the results of an additional thermal annealing in the open-circuit configuration of the samples activated by annealing under bias, and the samples activated by conventional annealing. For the samples activated by annealing under bias, in spite of the N_2 ambient, the differential resistance dramatically increases at a temperature above 350 °C, whereas it was unaffected for the samples activated by conventional annealing. This phenomenon was explained as the reionization of the remaining hydrogen and the repassivation of Mg acceptors. It was noticed that these repassivated Mg acceptors can be reactivated again by further annealing under bias.

The fact that dissociated H^+ does not compensate Mg^- acceptors implies that some additional process or processes alters the charge of the hydrogen. Pearton *et al.* proposed that the final result of the forward-bias treatment is the formation of neutral H_2 in the lattice. The group from Sandia National Laboratories also suggested that interstitial H_2 results from Mg activation under forward bias. Both H^0 and H^- were previously found to have much larger formation energies than H_2 in *p*-type material. The model for the activation of H-passivated Mg acceptors by minority-carrier injection in forward-biased *p-n* junctions was proposed as following:

$MgH \rightarrow Mg^- + H^+$ (thermal dissociation)
$H^+ + e^{-*} \rightarrow H^0$ (hot-electron capture)
$H^0 + e^{-*} \rightarrow H^-$ (hot-electron capture)
$H^+ + H^- \rightarrow H_2$

A forward voltage applied to *p-n* junction causes electrons to be injected into the *p*-type region. The injected electrons are readily captured by H^+ that has been thermally dissociated from Mg-H, producing H^0. The resulting neutral atoms react to form interstitial

H_2 before hole capture can restore the ionized state. Additionally, some of the H^0 captures a second electron to form H^-, which may combine with H^+ to form more H_2. It results in the progressive activation of the Mg acceptors. The model describing the repassivation process under open-circuit annealing was proposed as following:

$H_2 \rightarrow H^+ + H^-$ (thermal dissociation)
$H^- + h^+ \rightarrow H^0$ (hole capture)
$Mg^- + H^+ \rightarrow MgH$
$Mg^0 + H^0 \rightarrow MgH$

Density functional theory (DFT) was used to calculate the conversion rates of H_2 to Mg-H during open-circuit annealing for *p*-GaN previously activated by minority-carrier injection (Fig. 3.38). These results are consistent with experimental results obtained by Miyachi *et al.* As can be seen the interstitial H_2 persists for thousands of hours at temperatures as high as 200 °C, suggesting a thermal stability sufficient for some device applications.

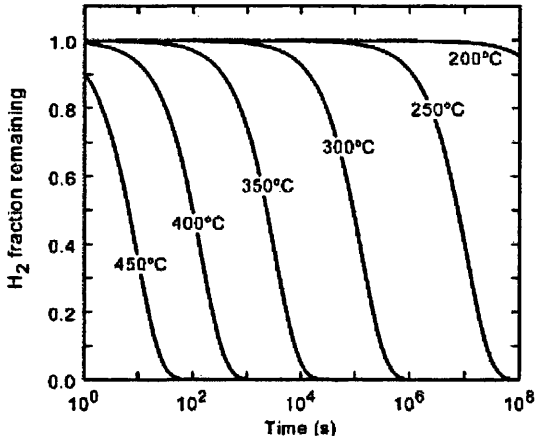

Fig. 3.38. Predicted conversion of H_2 to Mg-H during open-circuit annealing for *p*-GaN previously activated by minority-carrier injection.

The unintentional minority-carrier activation caused by residual after processing hydrogen can affect the performance of some GaN-based devices. In a heterojunction bipolar transistor the lower level of injected minority carriers can reactivate passivated Mg in the base layer, leading to an apparent time-dependent decrease in gain as the device is operated. For current confined structures realized by LEEBI treatment, it can enlarge the current spreading through the activation of adjacent passivated regions. It may also change the material resistivity in Hall measurements due to minority carrier reactivation of passivated acceptors.

Pearton *et al.* suggested that in a laser structure the high level of carrier injection would rapidly dissociate any remaining Mg-H complexes and thus would be forgiving of incomplete removal of hydrogen during the post-growth annealing treatment. Miyachi *et al.*[73] performed the annealing at low temperatures under minority-carrier injection instead of conventional thermal annealing to activate *p*-type of GaN-based MQW-SCH laser structure. The produced laser stripes were subjected to forward current injection at temperatures above 350 °C in N_2 ambient. Besides samples treated by conventional thermal annealing at 950 °C for 5 min were fabricated for comparison. Both types of laser stripes showed similar current-voltage (*I-V*) characteristics indicating almost the same hole concentration. The pulse laser operation was achieved at a current density of 13.8 kA/cm^2 and 16.9 kA/cm^2 for forward-bias annealed and conventionally annealed lasers respectively. The forward-bias annealed samples were subsequently passivated by the annealing at 350 °C in open-curcuit configuration and then reactivated under forward-bias annealing again. The threshold current density was left almost the same after four cycles. However, it seems to be arguable that electrons could penetrate to bulk *p*-type due to they are expected to recombinate in MQW region of the laser structure. The activation effect can be related to Ni/Au contact deposited on the top of *p*-layer before the forward-bias annealing. It was reported that *p*-type was thermally activated at temperatures as low as 200 °C when Ni was deposited on top. Also there was no information if the deposited

Ni/Au contact was subsequently annealed after the deposition (the usual annealing is ~500 °C).

3.4.4 Novel activation methods

Recently two new activation methods (microwave treatment and RF treatment) have been reported to be successful for Mg-doped GaN. These techniques were found to be effective even at room temperature. However, the mechanism or these activations is not established yet.

Chang *et al.* exposed MOCVD grown GaN:Mg layers to a 2.45 GHz, 560 W microwave treatment with different process time. Thermal activation was also performed at 730 °C for 20 min for comparison. Photoluminescence spectra of the samples activated with a 5 min microwave treatment and with a 20 min thermal treatment at 730 °C are shown in Fig. 3.39. As can be seen, the changes after both activation techniques are very similar. Figure 3.40 shows the resistivity of samples treated with different amount of microwave time. As can be seen, the resistivity was almost independent of the time, demonstrating a very fast activation process. The sample activated with the thermal annealing at 730 °C for 20 min showed the resistivity of 3.2 Ω·cm and the hole concentration of 6.58×10^{17} cm^{-3}. The authors proposed that the dissociation of Mg-H complexes was caused by the absorption of microwave energy. It was also shown that the hole concentration remained almost the same after removing a 1 μm-thick layer by chemical wet etching. It implies that the activation depth is probably not limited by near surface area.

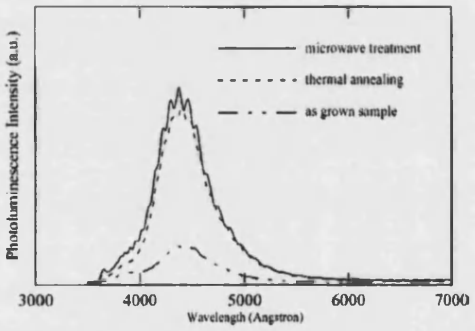

Fig. 3.39. PL spectra of GaN:Mg films: (a) as-grown; (b) with microwave treatment; (c) with thermal annealing.

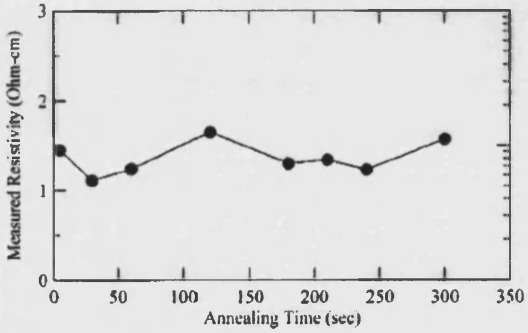

Fig. 3.40. Resistivity of GaN:Mg films with different microwave treatment time.

Takeya and Ikeda exposed MOCVD grown GaN:Mg layers, placed between RF electrodes, to strong RF electric field (13.56 MHz). Background air pressure was maintained below 10^{-5} Torr in order to prevent the generation of plasma. Figure 3.41 presents the hole concentration as a function of the product of RF time and the magnitude of the RF electric field for a room temperature treatment (solid circles) and a 300 °C treatment (open circles). As can be seen, the hole concentration increased with increasing the RF product and saturated at the product of ~1500 for 300 °C treatment. Figure 3.42 shows the time dependency of the hole concentration at the constant RF electric field of ~21 kV/cm at 300 °C. The hole concentration reached ~10^{18} cm^{-3} after ~70 s of the RF treatment. The authors proposed two possible mechanisms for the activation process. The first mechanism is due to the accelerated electron attack by the RF electric field to Mg-H bonds and/or energy absorption of polarized Mg-H complex. The other mechanism is due to the acceleration of out-diffusion of ionized hydrogen by the RF electric field.

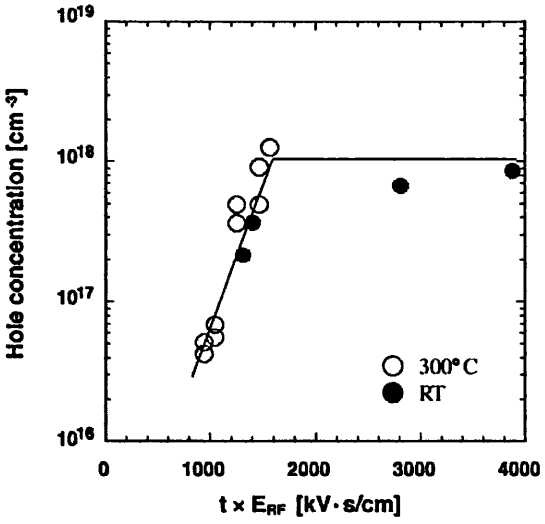

Fig. 3.41. Relationship between hole concentration and the product of RF input time, t and magnitude of electric field, E_{RF} for RF input activated samples.

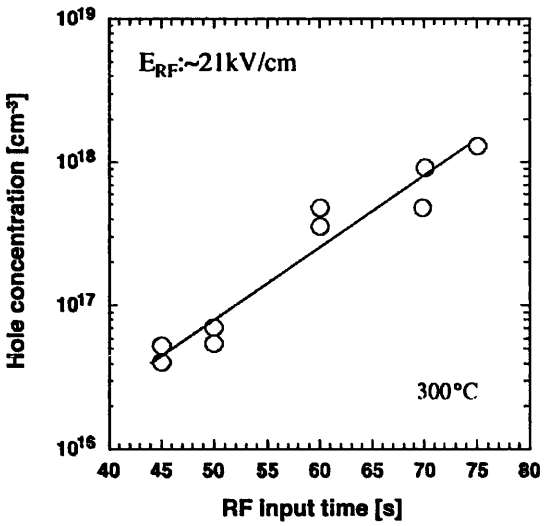

Fig. 3.42. Relationship between hole concentration and RF input time for RF activated samples at 300 °C. Magnitude of RF electric field was 21 kV/cm.

3.5 Optimization of *p*-GaN thermal activation in air with and without a SiO_2 capping layer

3.5.1 Introduction

As it is shown above, annealing in oxygen containing ambients is a very promising activation method to decrease activation temperatures and, as a result, to reduce thermal damage of InGaN layers in multiple quantum well (MQW) structures.[56, 57, 58, 59, 60] Annealing in pure O_2 was reported to result in low resistive films at temperature as low as 400 °C whereas the same resistivity was only achieved at 600 °C in N_2. Small amount of oxygen in air can also promote the activation at lower temperatures compared to annealing in pure N_2 ambient.[27, 57, 59] The mechanism of thermal activation in oxidizing ambients is considered above in this chapter. The similar results could be expected during the annealing of GaN films capped with SiO_2 layers due to possible interaction between oxygen diffused from SiO_2 and hydrogen dissociated in GaN. The SiO_2 capping layer can also be useful to prevent GaN thermal dissociation at high annealing temperatures. However, on the other hand, this layer can hinder desorption of hydrogen from GaN surface and even reduce effective hole concentration due to *n*-type autodoping of the material by oxygen incorporation. The reported data do not give the low-down on activation mechanism of Mg acceptors in GaN capped with SiO_2 layer. This section presents the results of thermal annealing in air for Mg-doped GaN layers covered with SiO_2 as well as without SiO_2. Both temperature and annealing time were varied to obtain the most detailed picture of thermal activation mechanism. This study has also been recently submitted for publication in "Applied Physics Letters" journal.

3.5.2 Experimental

The Mg-doped GaN epitaxial layer used in this study was grown on 2-in c-face (0001) sapphire substrate using metalorganic chemical vapor deposition (MOCVD) system AIXTRON operating at low pressure. Trimethylgallium (TMGa) and ammonia (NH_3) were used as the source material of Ga and N, respectively. Biscyclopentadienylmagnesium (Cp_2Mg) was used as the *p*-type dopant source. TMGa and Cp_2Mg were transported using hydrogen carrier gas. Prior to the growth of epitaxial layers, a 25 nm-thick GaN buffer layer was deposited onto the substrate at a low temperature of 500 °C. Subsequently, the reactor temperature was raised to 1050 °C to grown a 2 μm-thick undoped GaN layer, followed by a 0.7 μm-thick highly isolating (compensated) Zn-doped GaN and a 1 μm-thick Mg-doped GaN. A 5 nm-thick InGaN layer with gradual composition of In from 0 to 20% was grown on the top as a contact layer. After the growth, the wafer was cooled down in the MOCVD reactor to temperature of 500 °C in HN_3+N_2 flow during about 2 min, and from 500 °C to room temperature in pure N_2 flow during approximately 10 min. As a result, as-grown Mg-doped layer was partly activated. Resistivity of as-grown *p*-GaN measured at room temperature (RT) was around 9 Ω·cm.

After the growth, the wafer was divided into 7 × 7 mm^2 size samples using a diamond scriber. Ni/Au (20 nm/600 nm) metal dots of approximately 1 mm in diameter were evaporated in the four corners to obtain electrical contacts in Van der Pauw geometry. The first set of samples was used for annealing experiments without a SiO_2 capping layer, whereas samples from the second set were capped with 440 nm-thick SiO_2 layers using plasma enhanced chemical vapor deposition (PECVD) process. Deposition pressure and temperature were fixed at 900 mTorr and 300 °C respectively. A gas mixture of nitrogen and SiH_4 (2%) was used as the source material of silicon; nitrous oxide (N_2O)

was used as the source of oxygen. RF power density applied for the deposition was fixed at 500 W/m^2. Access to the contact dots for electrical measurements was produced using conventional photolithography technique and reactive ion etching (RIE) of SiO_2 in CHF_3 plasma. RT resistivity of *p*-GaN after PECVD deposition was around 16 Ω·cm. The third set of samples was used to verify the role of PECVD deposited SiO_2 during annealing. The samples were activated in air at 600 °C for 2 min, capped with 440 nm-thick SiO_2, and patterned using above-mentioned procedure. RT resistivity of previously activated *p*-GaN after PECVD deposition was around 1.2 Ω·cm.

The samples were annealed under air in a rapid thermal annealing (RTA) system equipped with halogen-tungsten lamps. During the annealing, the samples were located between two 6-in Si wafers and temperature was measured with a calibrated thermocouple located near a sample. Annealing temperature ranged from 200 to 900 °C for the uncoated samples and from 300 to 1100 °C for the samples with a SiO_2 capping layer. The annealing and measurements were conducted in consecutive order to obtain resistivity changes for the same sample during the annealing from 0 to around 3000 sec at the fixed temperature. Annealing time at high temperatures was restricted by the thermal damage of contact dots. Resistivity of *p*-GaN was measured using the four-point probe Van der Pauw technique.

3.5.3 Results and discussion

Resistivity of uncoated *p*-GaN samples activated in air at different temperatures as a function of annealing time is shown in Fig. 3.43. Each sample was annealed at the fixed temperature a number of times with different time intervals and measured after each annealing step. As can be seen, the resistivity rapidly increased from 9 to 13 Ω·cm during annealing at 200 and 300 °C and remained unchangeable up to 1 hr annealing. Initial degradation is also obvious for annealing at 400 and 450 °C, although subsequently the resistivity was gradually decreasing after about 30 sec annealing. This degradation is not noticeable for annealing at temperatures higher than 500 °C, probably because of rapid activation at these conditions. The reason for the initial resistivity raise is not clear yet and requires further investigations. It could be caused by low-temperature oxidation of surface conductive defects, such as Ga-vacancies acting as acceptors in GaN, while a cooldown step in a MOCVD reactor was conducted in N_2 ambient and prevented oxygen reaction with the surface. To check if this degradation is restored, a sample activated at 500 °C for 30 min (ρ = 1.14 Ω·cm) was subsequently annealed at 300 °C for 2 min. It showed no resistivity change confirming the oxidation hypothesis and implying a minor impact of this degradation on resistivity of activated *p*-GaN.

Resistivity of *p*-GaN samples with a SiO_2 capping layer activated in air at different temperatures as a function of annealing time is shown in Fig. 3.44. Resistivity of as-grown samples increased from 9 to 16 Ω·cm as a result of the PECVD deposition, which took place at temperature of 300 °C. The samples, thereby, were shortly exposed to air at this temperature during loading to a process chamber and before pumping down to process pressure. Post-deposition annealing at 300 °C did not have an effect on the resistivity, as shown in Fig. 3.44. It is consistent with the results of annealing of the uncoated samples at this temperature. Slightly higher resistivity (16 Ω·cm vs. 13 Ω·cm) could be caused by hydrogen incorporation into *p*-GaN material during the deposition, which occurred in silane discharge containing hydrogen.[33, 34, 36, 40] More importantly, the resistivity was gradually increasing during annealing at 400 °C and reached a value of 53 Ω·cm after 1 hr annealing. Annealing at 500 and 600 °C rapidly enhanced the resistivity to undetectable level (more than 500 Ω·cm for current measurements). Following activation was only detected after about 6 min at 600 °C. Initial resistivity raise was also observed at 700 °C with following activation during the annealing. Annealing at temperatures more than 800

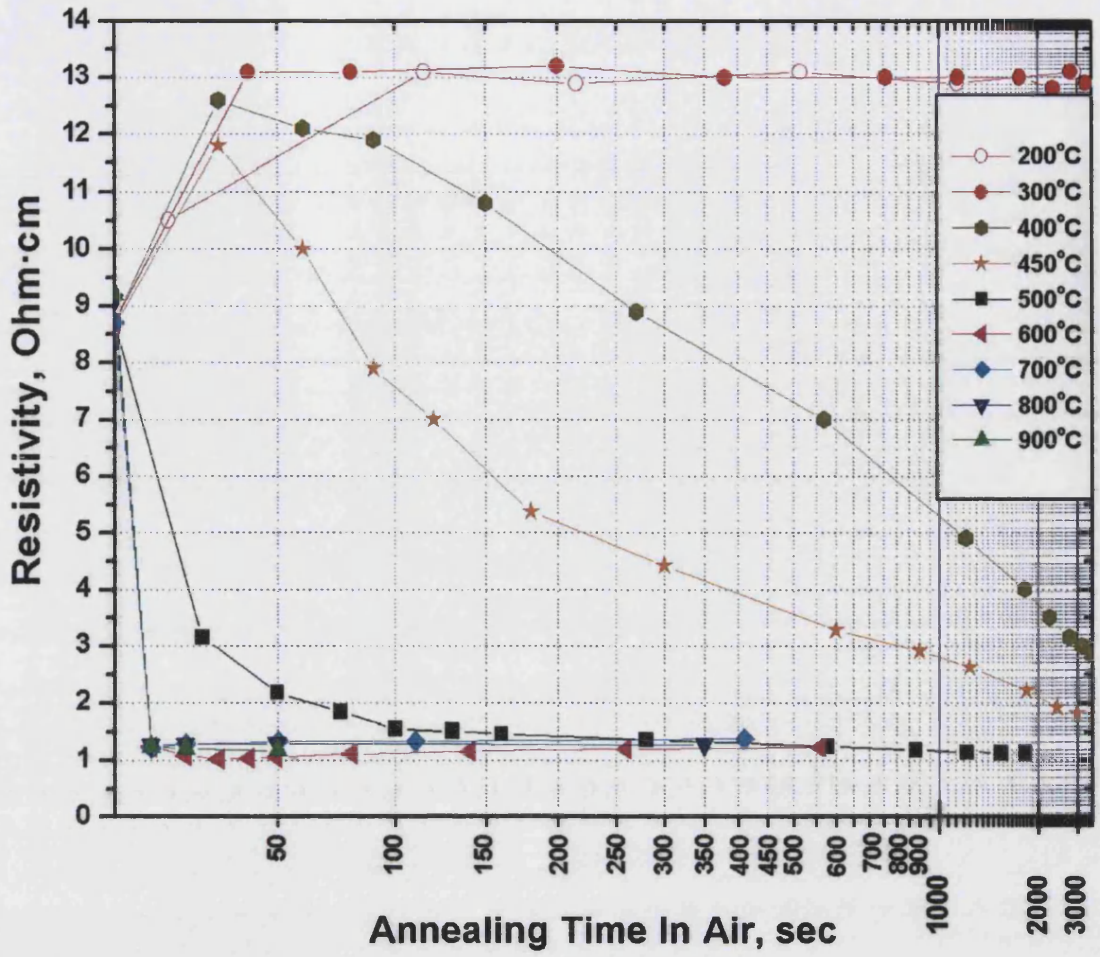

Fig. 3.43. Resistivity of uncoated GaN:Mg samples activated in air at different temperatures as a function of annealing time.

°C resulted in the decrease of the resistivity without noticeable initial degradation. The reason could be fairly fast activation at these conditions. However, this activation is extremely slow compared to activation of *p*-GaN without a SiO_2 capping layer in any ambient (vacuum, nitrogen, air, oxygen) at these temperatures. It is not consistent with the results reported by Lee *et al.* for GaN:Mg layers activated at temperature from 850 to 950 °C. The stated that resistivity of layers capped with SiO_2 was lower than that of layers without SiO_2 after activation at the same annealing time and temperatures.

Our systematic study gives the detailed picture of thermal activation in air for GaN:Mg layers both uncoated and coated with PECVD deposited SiO_2. We believe that a PECVD SiO_2 capping layer hinders desorption of hydrogen from GaN and also causes addition passivation of Mg acceptors during annealing. It results in extremely slow activation and in resistivity increase at annealing temperatures from 400 to 700 °C as the passivation initially overcomes slow activation. In all probability, this passivation comes from residual hydrogen incorporated in a SiO_2 film during PECVD deposition. The hydrogen diffuses into *p*-GaN material at temperatures higher than 400 °C and that results in passivation of Mg acceptors when the material is cooled down to room temperature. Activation probably occurs through diffusion of hydrogen from *p*-GaN into the SiO_2 film and hydrogen desorption from SiO_2 surface. Thus two opposite processes, passivation with hydrogen from SiO_2 and activation through hydrogen removal from both *p*-GaN and SiO_2, are believed to take place under thermal annealing with PECVD deposited SiO_2. The passivation is not restored after high temperature activation that was confirmed by

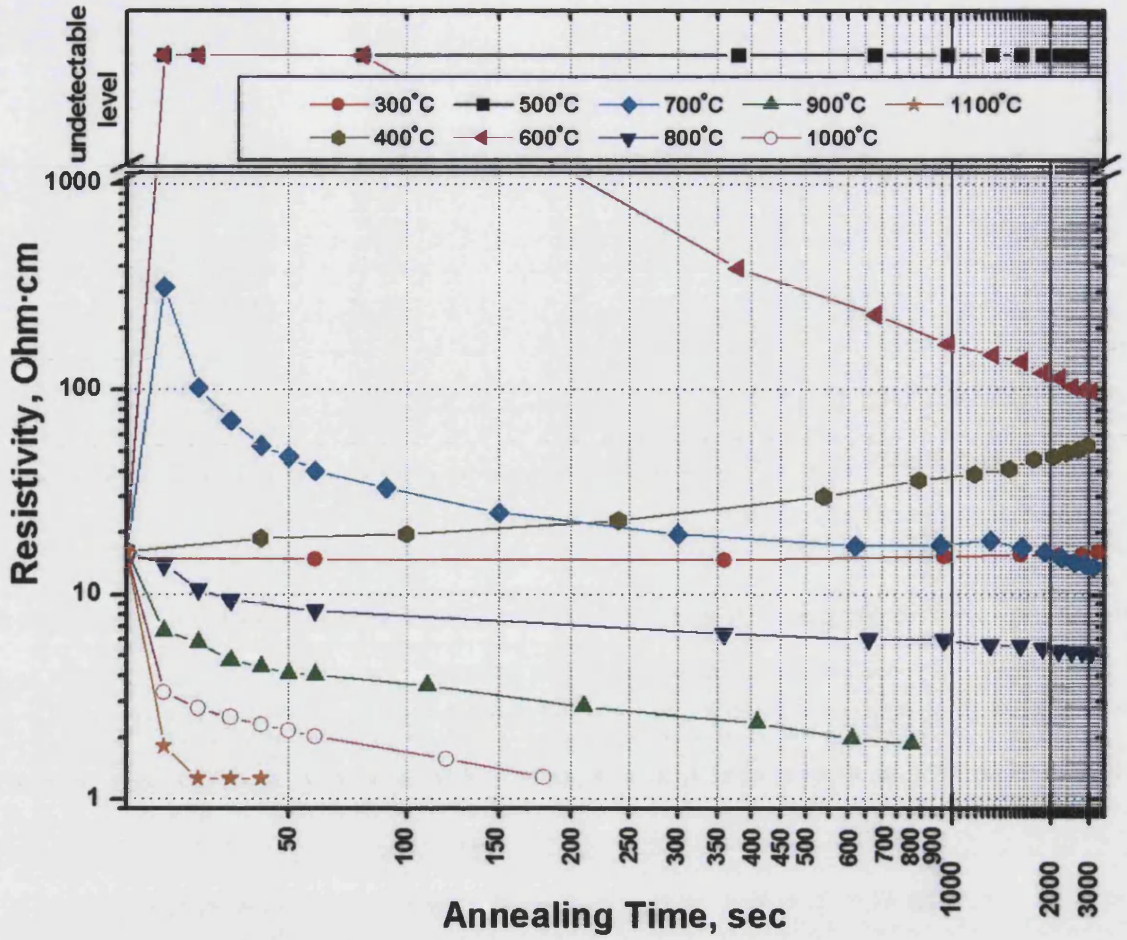

Fig. 3.44. Resistivity of GaN:Mg samples with a SiO_2 capping layer activated in air at different temperatures as a function of annealing time.

annealing of a sample previously activated at 800 °C for 50 min (ρ = 5.14 Ω·cm). No resistivity change was detected after annealing at 600 °C for 30 sec implying that hydrogen was removed from both *p*-GaN and the SiO_2 capping layer.

This mechanism is supported by experiments with *p*-GaN samples previously activated in air at 600 °C for 2 min (ρ = 1.1–1.3 Ω·cm). The samples were subsequently capped with PECVD SiO_2 and annealed in air. The results of the annealing are presented in Fig. 3.45. As can be seen, resistivity of *p*-GaN was unaffected during annealing at 500 °C, whereas it was gradually increasing during annealing at 600 °C and reached a value of 6.53 Ω·cm after 1 hr annealing. Annealing at higher temperatures also caused initial resistivity raise following by slow decrease with the lapse of time. Thus, the passivation effect of PECVD deposited PECVD SiO_2 is obvious, even though this passivation occurred at temperatures higher than 600 °C compared to 400 °C for as-grown material. It is obvious that previous activation in air left surface of the samples heavily oxidized, while as-grown samples were only shortly exposed to air at 300 °C before PECVD deposition (a loading step). It is very likely that a thin oxide layer act as a barrier for hydrogen diffusion from SiO_2 into GaN. This barrier should be higher for the heavily oxidized samples, which could finally result in higher temperatures required for hydrogen exchange between SiO_2 and activated *p*-GaN. The passivation is not restored after reactivation as it was confirmed by annealing of a sample previously annealed at 900 °C for 8 min (ρ = 1.35 Ω·cm). No resistivity change was detected after subsequent annealing at 700 °C for 5 min implying that hydrogen was removed from both *p*-GaN and the SiO_2 capping layer.

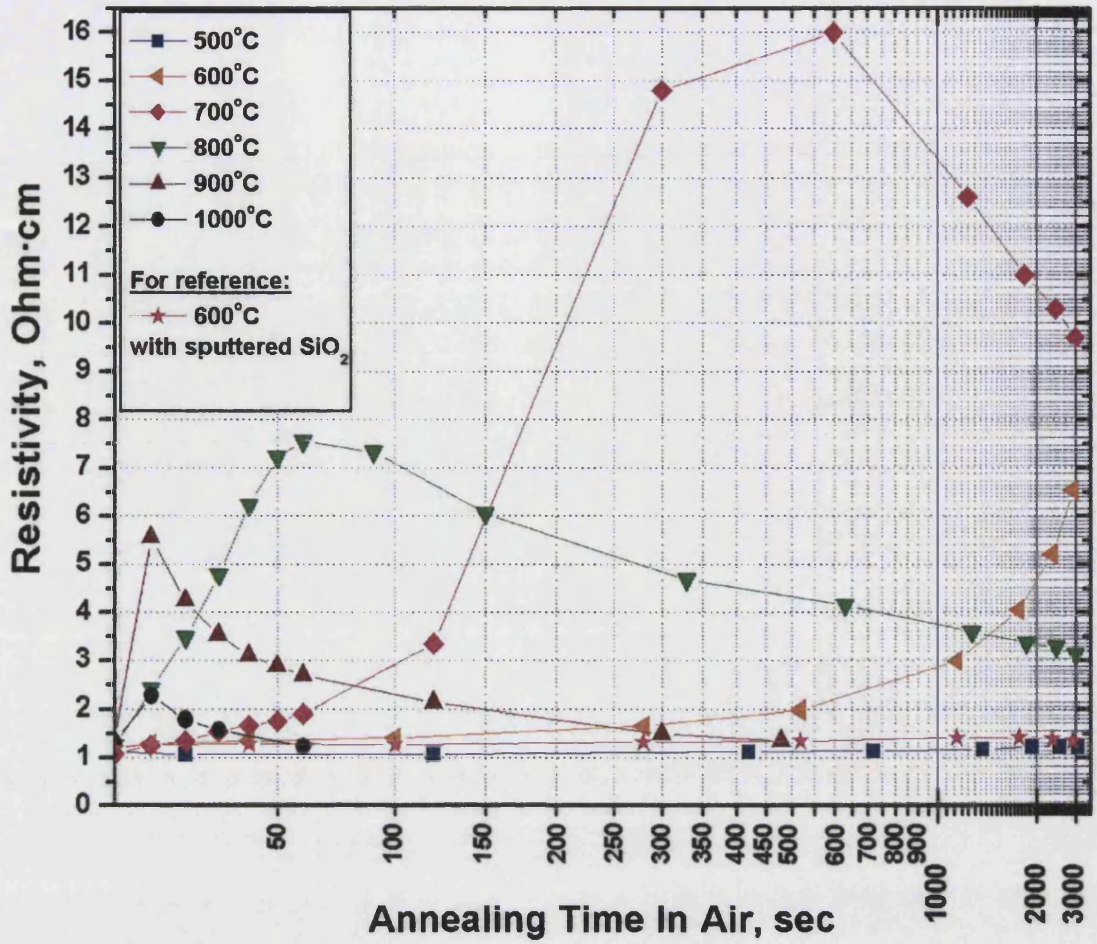

Fig. 3.45. Resistivity of activated GaN:Mg samples capped with SiO_2 layer and activated in air at different temperatures as a function of annealing time.

On the other hand, the observed resistivity raise could be caused by oxygen diffusion from SiO_2 into *p*-GaN material during annealing at elevated temperatures. The intentional oxygen doping could produce a donor level compensating Mg acceptors. However, it contradicts annealing experiments with a *p*-GaN sample activated at 600 °C for 2 min (ρ = 1.13 Ω·cm) and subsequently capped with a hydrogen-free SiO_2 layer deposited by ion beam sputtering. The results of annealing at 600 °C are presented in Fig. 3.45 as a reference. As can be seen, resistivity of *p*-GaN was unchanged during the annealing implying no significant oxygen incorporation from SiO_2. Thus, the most probable reason for the passivation observed during annealing with a PECVD SiO_2 capping layer is hydrogen unintentionally incorporated in SiO_2 during PECVD deposition. Another indirect confirmation of it comes from additional experiments with *p*-GaN samples partly passivated during annealing with a PECVD SiO_2 layer. These samples were readily activated back, after the capping layer was removed, during annealing in air at 600 °C for 2 min. It also confirms hydrogen role for passivation observed during annealing with a PECVD SiO_2 capping layer.

3.5.4 Conclusion

Thermal activation in air for MOCVD grown GaN:Mg layers both uncoated and coated with PECVD deposited SiO_2 has been systematically studied. It was found that a PECVD SiO_2 capping layer hinders desorption of hydrogen from GaN and also causes

addition passivation of Mg acceptors during annealing. It finally results in extremely slow activation and in resistivity increase at annealing temperatures from 400 to 700 °C. The PECVD SiO_2 capping layer has also catastrophic effect on previously activated *p*-GaN layers during annealing at temperatures higher than 600 °C. It was shown that this layer induces significant passivation of Mg acceptors. We believe that this passivation comes from residual hydrogen incorporated in the SiO_2 film during PECVD deposition. The hydrogen diffuses into *p*-GaN material at elevated temperatures and that results in passivation of Mg acceptors when the material is cooled down to room temperature. Activation occurs through diffusion of hydrogen from *p*-GaN into the SiO_2 film and hydrogen desorption from SiO_2 surface. Thus two opposite processes, passivation with hydrogen from SiO_2 and activation through hydrogen removal from both *p*-GaN and SiO_2, are believed to take place under thermal annealing of *p*-GaN capped with the PECVD SiO_2 layer. It restricts the use of this capping layer for activation of Mg acceptors in GaN. This phenomenon should also be taken in account during processing involving high temperature annealing of *p*-type GaN layers covered with PECVD deposited SiO_2.

3.6 References

[1] W. Gotz, N. M. Johnson, J. Walker, D. P. Bour, and R. A. Street, Appl. Phys. Lett. 68, 667 (1996).

[2] J. W. Huang, T. F. Kuech, H. Lu, and I. Bhat, Appl. Phys. Lett. 68, 2392 (1996).

[3] W. Gotz, N. M. Johnson, and D. P. Bour, Appl. Phys. Lett. 68, 3470 (1996).

[4] J. Z. Li, J. Y. Lin, H. X. Jiang, A. Salvador, A. Botchkarev, and H. Morkc, Appl. Phys. Lett. 69, 1474 (1996).

[5] A. Krtschil, H. Witte, M. Lisker, J. Christen, U. Birkle, S. Einfeldt, and D. Hommel, J. Appl. Phys. 84, 2040 (1998).

[6] D. J. Kim, D. Y. Ryu, N. A. Bojarczuk, J. Karasinski, S. Guha, S. H. Lee, and J. H. Lee, J. Appl. Phys. 88, 2564 (2000).

[7] D. Seghier and H. P. Gislason, J. Appl. Phys. 88, 6483 (2000).

[8] R. Y. Korotkov, J. M. Gregie, and B. W. Wessels, Appl. Phys. Lett. 78, 222 (2001).

[9] E. Litwin-Staszewska, T. Suski, R. Piotrzkowski, I. Grzegory, M. Bockowski, J. L. Robert, L. Kon'czewicz, D. Wasik, E. Kamin'ska, D. Cote, and B. Clerjaud, J. Appl. Phys. 89, 7960 (2001).

[10] N. D. Nguyen, M. Germain, M. Schmeits, B. Schineller, and M. Heuken, J. Appl. Phys. 90, 985 (2001).

[11] Y. Nakano and T. Kachi, Appl. Phys. Lett. 79, 1631 (2001).

[12] I. Akasaki, H. Amano, M. Kito, and K. Hiramatsu, J. Lumin. 48&49, 666 (1991).

[13] T. D. Moustakas and R. J. Molnar, Mater. Res. Soc. Symp. Proc. 281, 253 (1993).

[14] W. Gotz, N. M. Johnson, C. Chen, H. Liu, C. Kuo, and W. Imler, Appl. Phys. Lett. 68, 3144 (1996).

[15] T. Tanaka, A. Watanabe, A. Amano, H. Kobayashi, I. Akasaki, S. Yamazaki, and M. Koike, Appl. Phys. Lett. 65, 2024 (1994).

[16] M. A. L. Johnson, Z. Yu, C. Boney, W. C. Hughes, J. W. Cook, Jr., J. F. Schetzina, H. Zhao, B. J. Skromme, and J. A. Edmond, Mater. Res. Soc. Symp. Proc. 449, 215 (1997).

[17] Y. Nakano, T. Jimbo, J. Appl. Phys. 92, 5590 (2002).

[18] S. C. Jain, M. Willander, J. Narayan, R. Van Overstraeten, J. Appl. Phys. 87, 965 (2000).

[19] S. J. Pearton, F. Ren, A. P. Zhang and K. P. Lee, Materials Science and Engineering: R: Reports, Volume 30, Issues 3-6, 1 December 2000, Pages 55-212.

[20] S. C. Jain, M. Willander, J. Narayan, R. Van Overstraeten, J. Appl. Phys. 87, 965 (2000).

[21] H. Amano, I. Akasaki, T. Kozawa, K. Hiramatsu, N. Sawak, K. Ikeda, and Y. Ishi, J. Lumin. 40–41, 121 (1988).

[22] H. Amano, M. Kito, K. Hiramatsu, and I. Akasaki, Jpn. J. Appl. Phys. 28, L2112 (1989).

[23] S. Nakamura, T. Mukai, M. Senoh, and N. Iwasa, Jpn. J. Appl. Phys. 31, L139 (1992).

[24] S. J. Pearton, J. W. Lee, and C. Yuan, Appl. Phys. Lett. 68, 2690 (1996).

[25] Y. Kamiura, Y. Yamashita, and S. Nakamura, Jpn. J. Appl. Phys. 37, L970 (1998).

[26] S.-J. Chang, Y.-K. Su, T.-L. Tsai, C.-Y. Chang, C.-L. Chiang, C.-S. Chang, T.-P. Chen, and K.-H. Huang, Appl. Phys. Lett. 78, 312 (2001).

[27] M. Takeya and M. Ikeda, Jpn.J.Appl.Phys. 40, 6260 (2001).

[28] S. J. Pearton, J. C. Zolper, R. J. Shul, and F. Ren, J. Appl. Phys. 86, 1 (1999).

[29] Y. Ohba and A. Hatano, Jpn. J. Appl. Phys. 33, L1367 (1994).

[30] S. Nakamura, N. Iwasa, M. Senoh, and T. Mukai, Jpn. J. Appl. Phys. 31,1258 (1992).

[31] C. H. Seager, S. M. Myers, B. Vaandrager, and J. S. Nelson, Appl. Phys. Lett. 80, 2693 (2002).

[32] S. M. Myers, C. H. Seager, A. F. Wright, and B. L. Vaandrager, J. Appl. Phys. 92, 6630 (2002).

[33] M. S. Brandt, N. M. Johnson, R. J. Molnar, R. Singh, and T. D. Moustakas, Appl. Phys. Lett. 64, 2264 (1994).

[34] W. Gotz, N. M. Johnson, J. Walker, D. P. Bour, H. Amano, and I. Akasaki, Appl. Phys. Lett. 67, 2666 (1995).

[35] B Theys, Z Teukam, F Jomard, P de Mierry, A Y Polyakov and M Barbe, Semicond. Sci. Technol. 16, L53 (2001).

[36] A. Y. Polyakov, N. B. Smirnov, S. J. Pearton, F. Ren, B. Theys, F. Jomard, Z. Teukam, V. A. Dmitriev, A. E. Nikolaev, A. S. Usikov, and I. P. Nikitina, Appl. Phys. Lett. 79, 1834 (2001).

[37] J. C. Zolper, D. J. Rieger, A. G. Baca, S. J. Pearton, J. W. Lee, and R. A. Stall, Appl. Phys. Lett. 69, 538 (1996).

[38] C. R. Abernathy, J. D. MacKenzie, S. J. Pearton, and W. S. Hobson, Appl. Phys. Lett. 66, 1969 (1995).

[39] S. J. Pearton, C. R. Abernathy, and F. Ren, Electron. Lett. 30, 527 (1994).

[40] S. J. Pearton, R. J. Shul, R. G. Wilson, F. Ren, J. M. Zavada, C. R. Abernathy, C. Vartuli, J. Lee, J. MacKenzie, and J. R. Mileham, J. Electron. Mater. 25, 845 (1996).

[41] A. Y. Polyakov, in Hydrogen in Compound Semiconductors, edited by S. J. Pearton (Trans Tech. Publications, Switzerland, 1994), pp. 295–320.

[42] J. Neugebauer and C. G. Van de Walle, Phys. Rev. Lett. 75, 4452 (1995).

[43] J. Neugebauer and C. G. Van de Walle, Appl. Phys. Lett. 68, 1829 (1996).

[44] A. F. Wright, Phys. Rev. B 60, 5101 (1999).

[45] S. M. Myers, A. F. Wright, G. A. Petersen, C. H. Seager, W. R. Wampler, M. H. Crawford, and J. Han, J. Appl. Phys. 88, 4676 (2000).

[46] S. M. Myers and A. F. Wright, J. Appl. Phys. 90, 5612 (2001).

[47] C. Seager, S. Myers, B. Vaandrager, and J. Nelson, Appl. Phys. Lett. 80, 2693 (2002).

[48] C. H. Seager,S. M. Myers, A. F. Wright, D. D. Koleske, and A. A. Allerman, J. Appl. Phys. 92, 7246 (2002).

[49] A. F. Wright, C. H. Seager, S. M. Myers, D. D. Koleske, and A. A. Allerman, J. Appl. Phys. 94, 2311 (2003).

[50] A. F. Wright and S. M. Myers, J. Appl. Phys. 94, 4918 (2003).

[51] W. R. Wampler and S. M. Myers, J. Appl. Phys. 94, 5682 (2003).

[52] S. M. Myers, A. F. Wright, G. A. Petersen, W. R. Wampler, C. H. Seager, M. H. Crawford, and J. Han, J. Appl. Phys. 89, 3195 (2001).

[53] W. Gotz, N. M. Johnson, D. P. Bour, M. D. McCluskey and E. E. Haller, Appl. Phys. Lett. 69, 3725 (1996).

[54] B. Clerjaud, D. Côte, A. Lebkiri, C. Naud, J. M. Baranowski, K. Pakula, D. Wasik, and T. Suski, Phys. Rev. B 61, 8238 (2000).

[55] C. J. Youn, T. S. Jeong, M. S. Han, J. W. Yang, K. Y. Lim, H. W. Yu, J. Crystal Growth 250, 331 (2003).

[56] Y. Koide, T. Maeda, T. Kawakami, S. Fujita, T. Uemura, N. Shibata, and M. Murakami, J. Electron. Mater. 28, 341 (1999).

[57] B. A. Hull, S. E. Mohney, H. S. Venugopalan, and J. C. Ramer, Appl. Phys. Lett. 76, 2271 (2000).

[58] S. H. Chung, M. Lachab, T. Wang, Y. Lacroix, D. Basak, Q. Fareed, Y. Kawakami, K. Nishino, and S. Sakai, Jpn. J. Appl. Phys. 39, 4749 (2000).

[59] C. H. Kuo, S. J. Chang, Y. K. Su, L. W. Wu, J. K. Sheu, C. H. Chen, and G. C. Chi, Jpn. J. Appl. Phys. 41, L112 (2002).

[60] T.-C. Wen, S.-C. Lee, W. Lee, T.-Y. Chen, S.-H. Chan and J.-S. Tsang, Jpn. J. Appl. Phys. 40, L495 (2001).

[61] S. J. Pearton, H. Cho, J. R. LaRoche, F. Ren, R. G. Wilson, J. W. Lee, Appl. Phys. Lett. 75, 2939 (1999).

[62] B.C. Chung and M. Gershenzon, J. Appl. Phys. 72, 651 (1992).

[63] I. Waki, H. Fujioka, M. Oshima, H. Miki, and A. Fukizawa, Appl. Phys. Lett. 78, 2899 (2001).

[64] C.-R. Lee, J.-Y. Leem and B.-G. Ahn, Journal of Crystal Growth 216, 62 (2000).

[65] I. Waki, H. Fujioka, M. Oshima, H. Miki, and M. Okuyama, Phys.Stat.Sol.(b) 228, 391 (2001).

[66] H. Itoh, O. Yoshinari, and K. Tanaka, J. Alloys Compd. 231, 483 (1995).

[67] S. M. Myers, B. L. Vaandrager, W. R. Wampler, and C. H. Seager, J. Appl. Phys. 95, 76 (2004).

[68] S. M. Myers and C. H. Seager, J. Appl. Phys. 95, 520 (2004).

[69] S. Myers, G. Caskey, D. Rawl, Jr., and R. Sisson, Jr., Metall. Trans. A 14, 2261 (1983).

[70] M. Inamori, H. Sakai, T. Tanaka, H. Amano, I. Akasaki, Jpn. J. Appl. Phys. 34, 1190 (1995).

[71] X. Li and J. J. Coleman, Appl. Phys. Lett. 69, 1605 (1996).

[72] M. Miyachi, T. Tanaka, Y. Kimura, and H. Ota, Appl. Phys. Lett. 72, 1101 (1998).

[73] M. Miyachi, H. Ota, Y. Kimura, A. Watanabe, T. Tanaka, H. Takahashi, and K. Chikuma, Jpn. J. Appl. Phys. 38, L1237 (1999).

4 ICP etching of GaN

4.1 Introduction

The group of III-nitrides is typically resistant to etching in common compound semiconductor wet chemical etchants due to the inert chemical nature and high bond energies. GaN has a bond energy of 8.92 eV/atom, InN 7.72 eV/atom, and AlN 11.52 eV/atom.[1] Therefore, almost all device patterning is accomplished by using plasma etching technology. Four main dry techniques are employed to etch nitride materials: RIE (reactive ion etching), ECR-RIE (electron cyclotron resonance etching), CAIBE (chemically assisted ion beam etching), and ICP (inductively coupled plasma etching). High-density plasma etch systems show enhanced etch results for the group III-nitrides as compared to RIE due to the two–four times higher plasma density and the effective decoupling of ion energy and ion density. In recent years the majority of high-density plasma etching of III-nitrides was performed using the inductively coupled plasma etching systems due to their superior uniformity, control, and relatively low cost.

The major development of plasma etching of III-nitrides is directed toward photonic devices where high etch rate, anisotropic profile with smooth sidewalls, and nonselective etching are required. Highly anisotropic and smooth sidewall etching is especially important in the fabrication of optoelectronic devices such as laser facets, turning mirrors, and gratings. In these devices the etch depth is typically 2–4 μm and requires high etching rates to minimize processing time. They also require low etch selectivity between different layers so that the etching rate is not significantly affected by any particular layer. At the same time, they require high etch selectivity between a mask and a structure. Low selectivity may result in degradation of anisotropy and sidewall smoothness of the etched facet due to the thick mask.[2] In addition, the etched surfaces and sidewalls must be free of virtually all contamination and defects, in order to obtain ohmic contacts with low contact resistivity.

This chapter provides an up-to-date review of ICP etching of III-nitrides in Cl-based plasmas along with a theory associated with this etching technique. The results of our group on ICP etching of Al-containing layers and a laser diode (LD) structure with Cl_2/Ar plasma are also presented and discussed. The initial aim of the experiments was to optimized etching conditions for laser diode fabrication. Etching of Al-containing layers and super-lattice (SL) GaN/AlGaN structures, even with very low Al content, had always resulted in extremely slow etching rates and very rough etched surface and sidewalls. It seriously hindered progress in laser diode development due to the difficulty of forming any proper contacts to the etched surface and due to an excessively thick mask required for sufficient etching depth. During the experiments it was revealed that the coverplate cathode material has a great influence on the etching of Al-containing layers. The impact of different coverplates is considered and explained in section 4.5 of this chapter. This study has also been recently published ["Influence of cathode material and $SiCl_4$ gas on inductively coupled plasma etching of AlGaN layers with Cl_2/Ar plasma" E. Zhirnov, S. Stepanov, W. N. Wang, Y. G. Shreter, D. V. Takhin, and N. I. Bochkareva, *J. Vac. Sci. Technol. A* 22, 2336 (2004).]. The results suggest that a Si wafer, located on the top of a quartz coverplate, greatly improves etching of Al-containing layers in a Cl_2/Ar plasma and can be recommended for laser diode fabrication. Section 4.6 of this chapter presents the influence of different process parameters for this configuration, such as pressure, RF and ICP power, on the etching of GaN, $Al_{0.1}Ga_{0.9}N$, LD structure, and selectivity of the LD structure to SiO_2. The obtained data provide a wide range of parameters where smooth anisotropic etch profile, smooth etch surface, and high selectivity over a SiO_2 etching mask

are easily achieved. This study has also been recently accepted for publication ["ICP etching of III-nitride based laser structure with Cl_2/Ar plasma assisted by Si coverplate material" E. Zhirnov, S. Stepanov, W. N. Wang, A. Gott, Y. G. Shreter, D. V. Takhin, and N. I. Bochkareva, *J. Vac. Sci. Technol. A* 23, XXX (2005).]. In addition, section 4.4 of this chapter presents a study of selective etching of SiO_2 over a photoresist mask using RIE CHF_3 plasma. The aim of these experiments was to develop a process for fabrication of a smooth anisotropic mask profile required for etching of a GaN-based laser structure.

4.2 ICP-RIE theory

Etching is the most crucial step in a lithography process. Isotropic etching involves neutral species and generally proceeds to etch laterally and vertically in regions defined by mask. Thus, the dimensions of desired features can be significantly changed. Furthermore, this etching cannot be applied for some processes, such as laser facets formation, where anisotropic profile of sidewalls is required. On the other hand, anisotropic directional etching involves charged species and can achieve almost perfect reproduction of the mask with nearly anisotropic sidewalls. There are two main types of the etching used in lithography processing. Wet etching is a typical isotropic process employing a purely chemical mechanism. This etching tends to be highly selective for the correct choice of etchants and produces low damage of the etch surface. In contrast, plasma etching can produce an almost anisotropic profile. The disadvantages of the plasma etching are low selectivity, increased mask erosion, radiation damage, and poor control over process parameters such as ion flux, which affect etch process reproducibility.[3]

A plasma may be described as a conductive 'gas' with equal densities of positively and negatively charged particles. It can be created by generating a strong electric field between oppositely charged plates induced by coupling, through an impedance matching network, RF power to a gas at very low pressure. There is always a possibility of ionization of some gas atoms and molecules between the plates caused by cosmic rays, γ-rays and the like. The electrons arising from this ionization can be accelerated to high enough energies within an electric field to strip electrons from neutral atoms and molecules by collusions. At high frequencies, the electrons oscillate rapidly causing frequent collisions and converting most of the energy received into kinetic energy.[4] As a result, both neutral reactive radicals and ions are generated in the excited gas. However plasma radical etching generally produces isotropic features. Placing the electrodes inside the discharge in a parallel configuration provides ion directionality and etch anisotropy. Generally, wafers are located on a lower electrode (Fig. 4.1). In this configuration, the wafers are exposed to low energy (100–400 eV) ions and free radical bombardment. Additionally, photons, electrons, and X-rays also strike the wafers. In a plasma etcher, low pressures are necessary to prevent ion and radical collisional deactivation. For instance, the lifetime of F* radicals at low pressure is as long as 1 sec and the mean free path is a few centimeters which is sufficient to diffuse to the wafers. Although the lifetime for CF_3^+ ions is only ~10 μsec, these ions are accelerated to strike the wafers by electric fields.

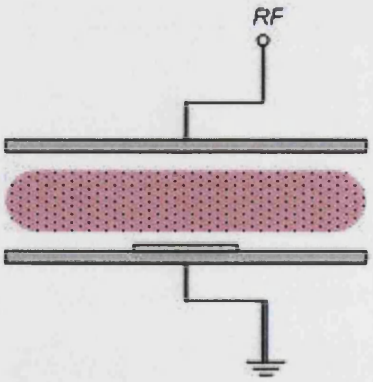

Fig. 4.1. Planar reactor with a wafer on the lower electrode.

If ions are not chemically reactive, such as argon, only physical sputtering or ion beam damage occurs (ion milling or sputter etching). This sputtering occurs through the formation of volatile or sublimed products without change in the chemical structure of the film. If the ions are chemically reactive, such as chlorine-based or fluorine-based, the sputtering takes place via the formation of new chemical compounds under the influence of gaseous ion bombardment (reactive ion etching (RIE), reactive sputter etching, reactive ion beam etching). Chemically reactive ions, physical ions, and neutral reactive radicals contribute to the etching in this case. Thus, etch rates in RIE are orders of magnitude greater than sputter etch rates. It may also lead to the increased selectivity to mask material (photoresist, Si_3N_4, SiO_2, etc.) if these materials are inert to plasma chemistry.

4.2.1 RIE system

A simplified RIE reactor is presented in Fig. 4.2. The average speed of electrons in a generated plasma is enormous compared to that of ions due to both the high temperature and low mass of the electrons. This results in the slight positive charge of the plasma due to the loss of electrons to the chamber sidewalls and cathode. The potential of the plasma (V_p) with respect to the chamber (grounded electrode) depends on the chamber construction and the etching conditions and is typically equal to +(10–30) V. The induced electric field attracts the electrons back to the plasma. The lack of electrons in the space between the plasma and the chamber and cathode leads to the decrease of excitation, followed by relaxation and photon emission, and results in "a dark region". This region is referred to as an ion sheath. The thickness of the ion sheath is a function of the ion density in the plasma and of the voltage applied between the cathode and a grounded electrode. However, large variations in the applied voltage do not change the ion sheath significantly.

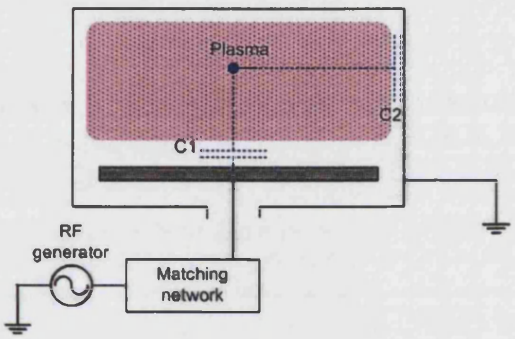

Fig. 4.2. The simplified RIE reactor.

In the equivalent circuit model the ion sheath may be replaced by a capacitor.[5] Thus, two main capacitors are presented in the circuit (C_1 – sheath between the plasma and the cathode, and C_2 – sheath between the plasma and the grounded electrode). As can be seen in Fig. 4.2, the area of the cathode is much less than that of the grounded electrode. This results in C_1 being much less than C_2:

$$C = \frac{\varepsilon \cdot S}{d} \qquad [4.1]$$

$\varepsilon \sim \varepsilon_0$ – dielectric constant of the sheath (ε_0 - for vacuum)
S – the area of the sheath ($S_1 < S_2$)
d – sheath thickness

Thus, the applied RF voltage is capacitively divided between the two sheaths (V_1 – voltage on the plasma-cathode sheath, and V_2 – voltage on the plasma-grounded electrode sheath):

$$\frac{V_1}{V_2} = \frac{C_2}{C_1} = \frac{S_2}{S_1} \cdot \frac{d_1}{d_2} \qquad [4.2]$$

The space-charge-limited current density determined by Child-Langmuir's law without collisions is expressed by Eq. 4.3 below. The ion current density is also described by Eq. 4.4 based on the Bohm criterion.[6] Accordingly, assuming that these values are equal at a sheath boundary, the d value may be obtained using Eq. 4.5 below.[5]

$$J^{+} = \frac{4}{9}\varepsilon_0 \left(\frac{2e}{M}\right)^{\frac{1}{2}} \frac{V^{\frac{3}{2}}}{d^2} \qquad [4.3]$$

$$J^{+} = 0.61eN\left(\frac{kT_e}{M}\right)^{\frac{1}{2}} \qquad [4.4]$$

$$d = \left(\frac{\varepsilon_0}{N}\right)^{\frac{1}{2}} \frac{V^{\frac{3}{4}}}{(ekT_e)^{\frac{1}{4}}} \qquad [4.5]$$

e – electric charge of an electron
M – ion mass
N – electron density
k – Boltzmann's constant
T_e – electron temperature of plasma

Combining Eq. 4.2 and Eq. 4.5 gives Eq. 4.6:

$$\frac{V_1}{V_2} = \left(\frac{S_2}{S_1}\right)^4 \qquad [4.6]$$

Thus, almost all the RF voltage drops in the cathode sheath. The cathode is capacitively separated from the RF generator through a matching network. The purpose of this network is to increase the power dissipation in a discharge by adjusting the actual impedance to the output impedance of a RF generator (usually 50 Ω), and, hence, to protect the generator. When the RF voltage is applied between the cathode and grounded electrode, and discharge is initiated, the cathode (and wafers on the top of it accordingly) collects a net negative charge during the first RF cycles due to the much higher speed of electrons. The collected negative charge repels the plasma electrons from the surface, i.e., the electron current during each following RF cycle is lower than the previous one. On the other hand, this charge attracts ions and there is an increased ion current. After 2–3 μs[7] of discharge the electron current to the cathode becomes equal to the ion current during one RF cycle. The established negative potential of the cathode (dc-bias V_{DC}) is shown in Fig. 4.3. As can be seen, the RF potential of the cathode (V_{RF}) is only positive in section (1–2), which corresponds to the electron current to the surface. In section (2–3) it is negative and corresponds to the ion current. The dc-bias voltage is usually either measured directly or inferred from the RF voltage amplitude. The potential of the plasma (V_P) is also schematically shown in Fig. 4.3. As can be seen, it correlates with the cathode RF voltage. It is higher at the positive potential of the cathode due to the loss of the electrons from the plasma. Accordingly, it is lower at the negative potential due to the preferential loss of ions.

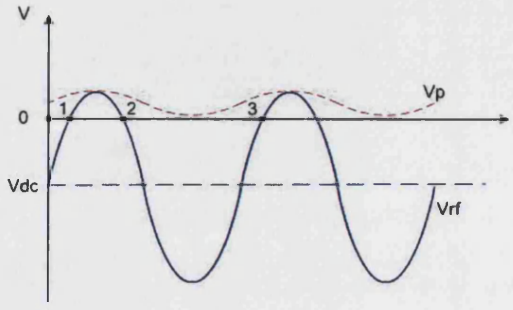

Fig. 4.3. Cathode voltage waveform with respect to the grounded electrode (chamber).

The frequency of the RF signal has a very important meaning for the ion energy distribution. If the ion transit time through the plasma sheath is large compared to the time of one RF cycle (high RF frequency), the majority of the ions entering this sheath arrive at the sample surface with energy corresponding to the plasma potential minus the dc-bias.

$$E_{ion} = e(V_P - V_{DC}) \qquad [4.7]$$

If the ion transit time is short with respect to one RF cycle (low RF frequency), each ion arrives at the surface with its own energy corresponding to the sheath potential at the moment when the ion enters the sheath. It results in the wide distribution of the ion energy. The frequency corresponding to the uniform distribution of the ions depends on etching conditions and chamber geometry. However, the results obtained by Sobolewski *et al.*[8] may be taken as a basis. They found that the ion energy distribution at around 1 MHz was wide, while at 10 MHz the ions bombarded the surface with energies close to $e(V_p - V_{DC})$.

In a plasma reactor, the etching rate is controlled by three factors: neutral atom (molecule) and free radical concentration, ion concentration, and energy of ions. The ion and radical concentration control the reaction rate, while the ion energy provides the necessary activation and controls the degree of anisotropy. The neutrals (the radicals and the neutral atoms (molecules)) strike the surface at random angles at pressures of >1 mTorr. If an anisotropic profile is required, positive ions must be created at low pressure (<10 mTorr) to strike the surface at normal incidence [Fig. 4.4(a)]. Higher pressures (>10 mTorr) result in a shortened mean free path of the ions and lead to an isotropic profile due to collisions of the ions and the neutrals in the sheath region [Fig. 4.4(b)].

The applied RF power is dissipated in RIE system by several mechanisms:[9] by stochastic electron heating, where the electrons are accelerated by reflection from the sheath; by ion acceleration across the sheath; and by the acceleration of secondary electrons emitted from the cathode surface. The latter is small if the energy of ions is less than 200 eV. The dominant mechanism in capacitive RIE discharges is the stochastic heating. The plasma density for RIE systems is in the range of 10^{14}–10^{15} m^{-3}. It results in the ion flux to the cathode in the range of 0.1–1 $A{\cdot}m^{-2}$.

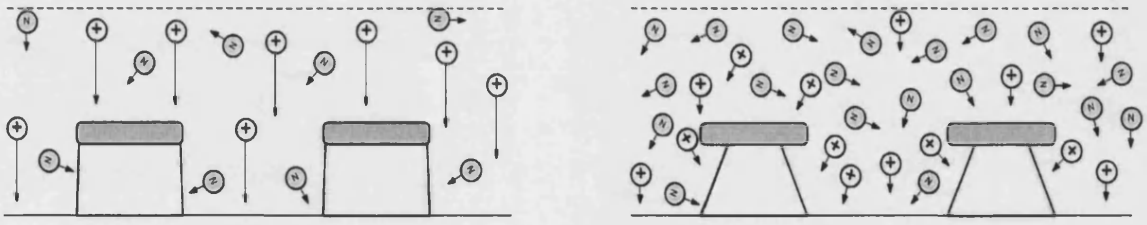

a) b)

Fig. 4.4. (a) Positive charged ions strike surface at normal incidence at <10 mTorr pressures. (b) Neutrals and ions start to collide at >10 mTorr pressures.

4.2.2 ICP-RIE system

The ICP-RIE etching system, generally called an ICP system, has been introduced for plasma processing fairly recently (1991-1995). The main advantages of this technique compared to conventional RIE systems are the independent control of the ion energy and plasma density (concentration of ions, electrons, and reactive radicals) and a much higher plasma density (10^{16}–10^{17} m^{-3} compared to 10^{14}–10^{15} m^{-3} for RIE). It results in higher etching rates, improved profile control, improved uniformity, greatly increased selectivity,

and low radiation damage of the etch surface. The ICP system combines both the capacitive (RIE) and inductive components (ICP plasma source) of the RF energy coupling mechanism. The inductive coupling via a strong magnetic field causes a high degree of ionization within the plasma. However, if the degree of ionization (ICP power) is not high enough, this mechanism is limited and the majority of the energy is transferred via a capacitive mechanism.[10] It is only when the plasma becomes highly inductively coupled that the density of the plasma is mainly defined by the ICP source power and relatively independent of the RIE power.

ICP systems can be classified according to the coupling of an ICP plasma source to a process chamber: with a remote ICP source, with a plasma transport ICP source, and with a close-coupled ICP source. The remote ICP source [Fig. 4.5(b)] is characterized by it having sufficient time and space to thermalize the species by mutual collisions after the initial excitation. The etching process is mainly promoted by long-lived radicals and energetic metastables from the remote source. Both the ion density near the cathode sheath and the ion energy are determined by the RIE power. The plasma transport ICP source also has a physical separation between a high density plasma and a workplace. However, it is designed to bring charged particles (ions and electrons) to the workplace. The close-coupled ICP source [Fig. 4.5(a)] maximizes the fraction of the charged particles which can arrive to the wafer. Thus, the ion density near the cathode sheath is mainly defined by the ICP power, while the RIE power controls the ion energy. The ICP source chambers tend to be squat cylinders, to make the curved wall a small part of the total surface. However, this construction results in poor uniformity of the ion flux. For instance, the zone with ±5% etching uniformity for a 180 mm ICP source is only equal to 100 mm. It may be improved by spacing the source further away, but this results in a loss of ion species. The close-coupled ICP is probably the most promising system due to the independent control of the ion density and ion energy. The plasma source increases the ion flux to the surface to around 10 $A \cdot m^{-2}$ compared to 0.1–1 $A \cdot m^{-2}$ in the RIE system. Thus, the majority of the RIE power is dissipated by positive ion bombardment (Eq. 4.8) and an increase of the ICP power (ion density) leads to a fall in dc-bias at fixed RIE power.

RIE power = (Ion flux to substrate) × (Ion energy) [4.8]

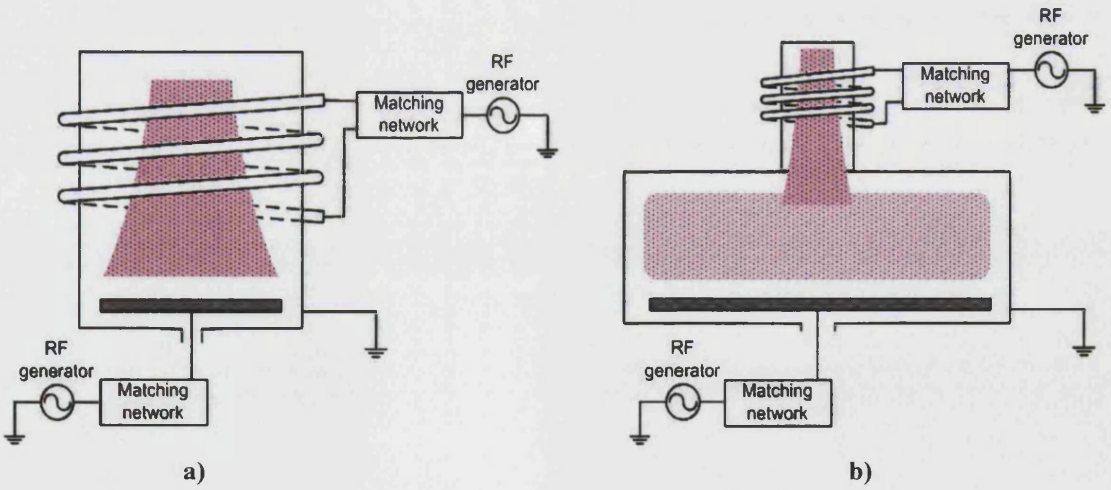

Fig. 4.5. ICP-RIE systems with (a) close-coupled ICP source and with (b) remote ICP source.

In a conventional RIE system the plasma density is limited by the capacitive method of RF energy coupling. The efficiency of this coupling becomes especially low at reduced pressures. Thus, the plasma density and etching rates also become lower. In contrast, the inductive coupling method utilized in the ICP plasma source becomes more

effective at lower pressures due to much higher ionization efficiency. A higher pressure in an ICP source leads to a lower plasma density due to increased ion and radical collisional deactivation. Thus, low pressure (1–10 mTorr) may be used in the ICP systems. This also results in longer mean free path of ions and more anisotropic etching.

4.3 A review of ICP etching of III-nitrides in Cl-based plasmas

Cl-based plasmas are commonly used for dry etching of III-nitride semiconductors due to low etch damage, high etch rate and superior uniformity. For Ga- and Al-containing films, chlorine-based plasmas typically yield fast rates with anisotropic, smooth etch profiles due to the high volatility of possible etch products. The boiling points for III-nitride etch products in different plasma chemistries are presented in Table 4-1. As can be seen, the chlorine-based plasmas form $GaCl_3$, $AlCl_3$, and NCl_3, which are volatile at 201, 183, and 71 °C, respectively. For In-containing layers, etching rates obtained at room temperature tend to be slow with a rough surface due to the low volatility of $InCl_3$ etch products (600 °C) and the preferential loss of group-V species.[11] However, under high plasma flux conditions, the $InCl_3$ etch products are sputtered away before they can passivate the surface resulting in improved etch rates and surface morphology.[12] Also, at elevated substrate temperatures (>130 °C), the volatility of the $InCl_3$ etch products increases thus improving etching results.[13, 14, 15, 16]

Table 4-1. Boiling points for possible etch products of III-nitrides etched in halogen- or CH_4/H_2-based plasmas.

Etch products	Boiling Points (°C)
$AlCl_3$	183
AlF_3	na
AlI_3	360
$AlBr_3$	263
$(CH_3)_3Al$	126
$GaCl_3$	201
GaF_3	1000
GaI_3	sublimates 345
$GaBr_3$	279
$(CH_3)_3Ga$	56
$InCl_3$	600
InF_3	>1200
InI_3	na
$InBr_3$	sublimates
$(CH_3)_3In$	134
NCl_3	<71
NF_3	-129
NBr_3	na
NI_3	explodes
NH_3	-33
N_2	-196
$(CH_3)_3N$	-33

4.3.1 Cl_2/Ar plasma

Cl_2/Ar mixing ratio, gas flow

Cl_2/Ar plasma is the most commonly used plasma chemistry. Typically Ar is added to a gas flow to facilitate plasma ignition[17] and to enhance the physical components of etching.[18] Shul *et al.*[19] reported GaN, AlN, and InN etching rates as a function of %Ar in ICP-generated Cl_2/Ar plasma. As can be seen in Fig. 4.6, GaN and AlN etching rates decreased with increasing Ar concentration, which was attributed to less available reactive Cl. A similar tendency for GaN etching rates was also reported by Kim *et al.*[20] and Shul *et al.*[21] On the contrary, the InN etching rate increased with increasing the Ar concentration implying that physical sputtering was a major contributor to the etching mechanism. It is probably a

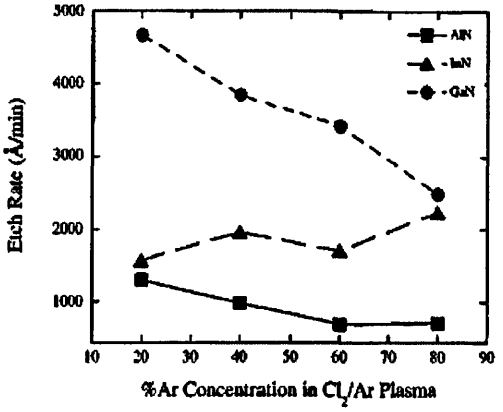

Fig. 4.6. GaN, InN, and AlN etch rates as a function of %Ar in Cl_2/Ar ICP plasma (25 sccm total gas flow, 25 °C temperature, 2 mTorr pressure, 500 W ICP power, -250 V dc-bias).

consequence of the low volatility of $InCl_3$ etch products formed at room temperature as mentioned above. At the same time Smith *et al.*[22] and Khan *et al.* observed that a gas mixture composition with 40–100% of Cl_2 in a Cl_2/Ar plasma and a total gas flow rate within 10–60 sccm had no significant impact on the etching rates of GaN, AlGaN, and AlN at a fixed dc-bias of -150 V, ICP power of 500 W, and 5 mTorr process pressure. The conflicting results of these groups could be caused by different methods of dc-bias measurements or by different constructions of the process chamber.

The ion current density and relative Cl radical intensity as a function of Ar concentration in ICP-generated Cl_2/Ar plasma were monitored by Kim *et al.* using Langmuir probe measurements and optical emission spectroscopy (OES), respectively. As can be seen in Fig. 4.7, the addition of Ar to Cl_2 plasma monotonically increased the ion density. The reason is probably the lower ionization energy of Ar in comparison with that of Cl_2.[23] On the other hand, the relative Cl radical intensity gradually decreased as %Ar increased from 20 to 100%. These results, in conjunction with the III-nitride etching rates, confirm that a chemical component of etching plays a significant role for GaN and Al(Ga)N layers, while for InN layers a physical component is more essential.

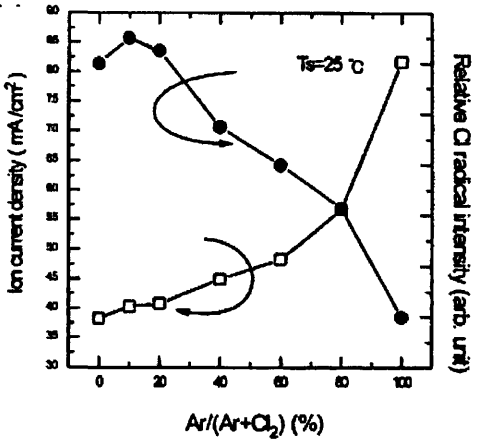

Fig. 4.7. Ion current density and relative Cl radical intensity in Cl_2/Ar ICP plasma as a function of %Ar (10 mTorr pressure, 400 W ICP power, 25 °C temperature, -120 V dc-bias).

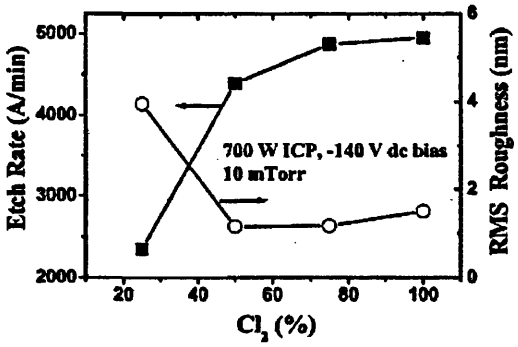

Fig. 4.8. Effect of %Cl_2 in Cl_2/Ar ICP plasma on etch rate and surface roughness of InGaN/GaN MQW LED (700 W ICP power, -140 V dc-bias, 10 mTorr pressure, 40 sccm total gas flow).

Hahn *et al.*[24] investigated the influence of %Cl_2 in a Cl_2/Ar plasma on surface roughness during ICP etching of InGaN/GaN multiple-quantum-well (MQW) LED structures. The etching rate and RMS surface roughness as a function of Cl_2 concentration are presented in Fig. 4.8. As can be seen, the etching rate increased with increasing Cl_2 concentration because of the increased number of chlorine radicals, which is consistent with the above-mentioned data. The etched surface of GaN showed the worst roughening under low chlorine percentage conditions (<25% Cl_2), but was relatively insensitive to plasma chemistry up to 75%, and slightly increased at >75%. Cho *et al.*[25] reported similar results and attributed them to the preferential sputtering of N atoms in Ar-rich discharges. The improved morphology in Cl_2-rich plasma was suggested to be due to the formation of volatile group III-chlorides that led to less disparate rate removal of Ga and N from the surface.

Process pressure

Khan *et al.* investigated GaN and $Al_{0.1}Ga_{0.9}N$ etching rates as a function of chamber pressure in Cl_2/Ar ICP-generated plasma. The optimal process pressure, corresponding to the highest etching rates, was found to be dependent on both ICP power and cathode dc-bias voltage. Keeping the ICP power at 500 W, as the dc-bias voltage was decreased from -150 to -300 V, the optimal pressure increased from 3 to 5 mTorr, as

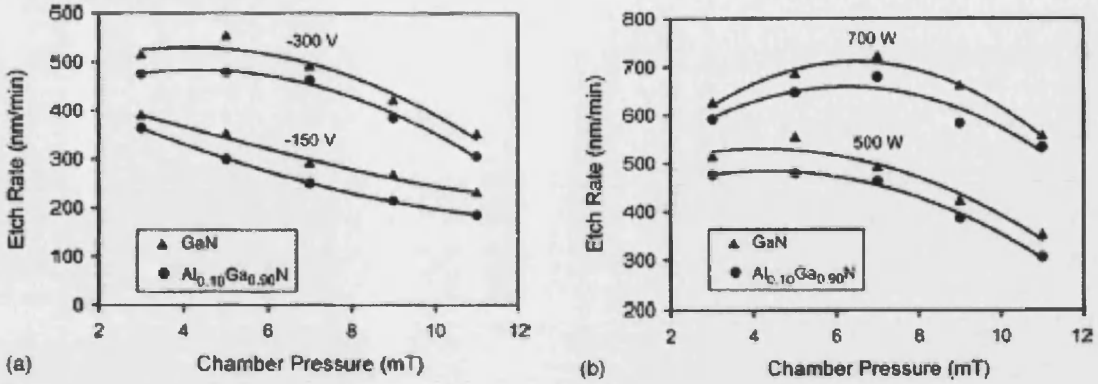

Fig. 4.9. (a) Etch rates as a function of chamber pressure for dc-bias voltage of -150 and -300 V (500 W ICP power, 25/5 sccm Cl_2/Ar gas flow rate). (b) Etch rates as a function of chamber pressure for ICP power of 500 and 700 W (-300 V dc-bias voltage, 25/5 sccm Cl_2/Ar gas flow rate).

shown in Fig. 4.9(a). Similarly, keeping the dc-bias voltage value at -300 V, as ICP power was increased from 500 to 700 W, the optimal etching pressure increased from 5 to 7 mTorr, as shown in Fig. 4.9(b). The drop in the etching rates at high pressures was probably caused by the increased collision frequency of ions, resulting in a decrease of plasma density. The drop in the etching rates at low pressures for the higher ICP power and the higher dc-bias voltage could be due to a reactant limited regime at these etching conditions.

The impact of process pressure on the density of an ICP-generated plasma can be understood from the study of Sheu *et al.*[26] The authors fixed the RF power at 100 W instead of the dc-bias and observed an enhancement in the voltage with increasing pressure, as shown in Fig. 4.10. At the fixed RF power this behavior suggests a decrease in the plasma density, probably due to increased collisional recombination at higher pressures. The etching rate of GaN increased with increasing pressure from 2 to 7 mTorr, due to both higher ion bombardment energies (higher dc-bias) and a reactant limited regime at low pressures. The etching rate reached a maximum at 7 mTorr and subsequently decreased at pressures higher than 10 mTorr, which was attributed to lowering plasma density and increasing polymer deposition. It could also be caused by a reduced mean free path of ions in the sheath region and the removal of active chlorine species from the surface at higher dc-bias voltage before they could react.[1, 27]

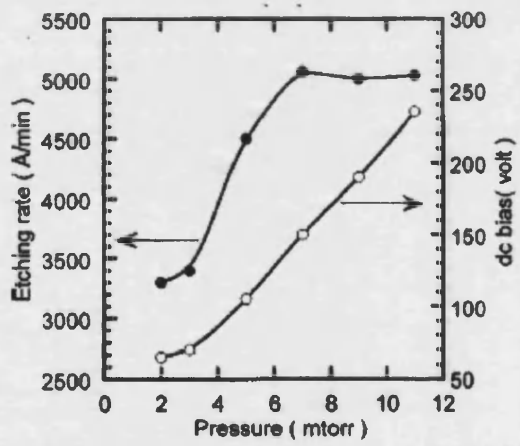

Fig. 4.10. Etch rate of GaN and dc-bias in Cl_2/Ar plasma as a function of pressure (600 W ICP power, 100 W RF power; 12/8 sccm Cl_2/Ar).

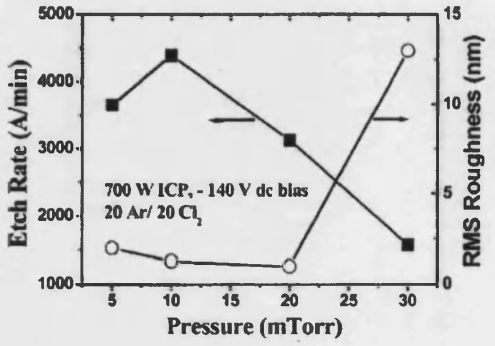

Fig. 4.11. Effect of process pressure on etch rate and surface roughness of InGaN/GaN MQW LED (700 W ICP power, -140 V dc-bias voltage, 20/20 sccm Cl_2/Ar gas flow rate).

Hahn *et al.* investigated the effect of process pressure on etching rate and RMS roughness during ICP etching of InGaN/GaN MQW LED structures in Cl_2/Ar plasma. Significant roughening of the surface was observed at pressures higher than 20 mTorr, as shown in Fig.

4.11. The reason could be polymer deposition and the poor desorption of etch products at high pressures. The etching rate behavior is consistent with the above-mentioned dependences.

DC-bias/RF power

Figure 4.12(a) presents GaN and $Al_xGa_{1-x}N$ etching rates as a function of dc-bias voltage, defined by RF power in ICP systems. As can be seen, the etching rates of all layers increased monotonically with increasing dc-bias due to enhanced ion bombardment. A similar dependence was reported for In-containing layers and was attributed to efficient sputter desorption of low volatile $InCl_3$ etching products prior to passivation of the etched surface.[28] However, the rise in etching rates was found to decline gradually and to saturate at some point. These findings are consistent with the results reported by other research groups.[21, 29] Smith et al. reported that a plateau occurred for all materials at a dc-bias value higher than 250 V. This behavior was ascribed to the ion-enhanced removal of active chlorine species from the semiconductor surface before they could react. The particular value of saturating ion energy probably depends on the ion flux to the surface. As can be seen in Fig. 4.12(b), the etching rates decreased as the value of x increased from GaN to AlN. This behavior was attributed to an increase in bond energy of $Al_xGa_{1-x}N$ with increasing x value (8.92 eV/atom for GaN and 11.52 eV/ atom for AlN). The threshold ion energies, below which etching rates are negligible, were also found to increase with Al content. Similar results were reported by Smith *et al.* The authors estimated the threshold dc-bias voltages to be less than -20 V for GaN, less than -40 V for $Al_{0.28}Ga_{0.72}N$, and between -50 and -150 V for AlN.

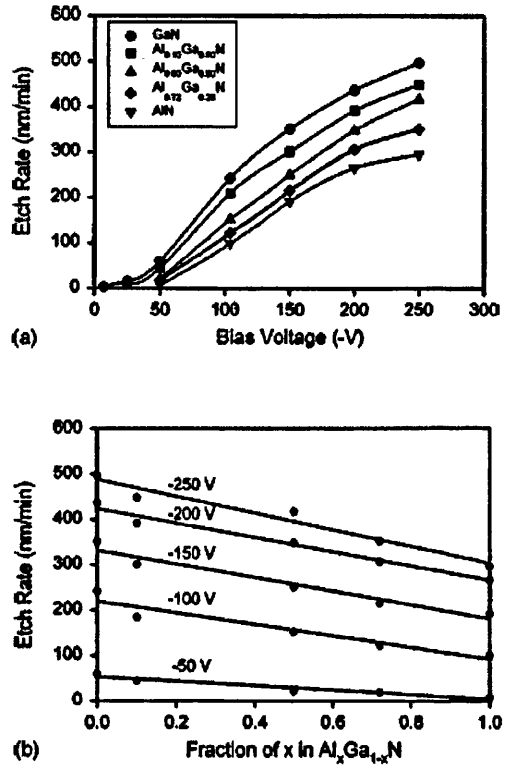

Fig. 4.12. (a) Etch rates as a function of dc-bias voltage. (b) Etch rate as a function of x in $Al_xGa_{1-x}N$ (500 W ICP power, 5 mTorr pressure, 25/5 sccm Cl_2/Ar gas flow rate).[2]

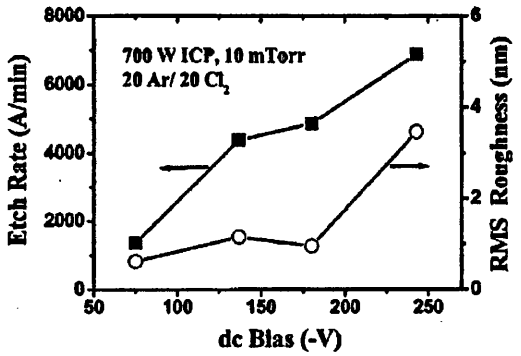

Fig. 4.13. Effect of dc-bias on etch rate and surface roughness of InGaN/GaN MQW LED (700 W ICP, 10 mTorr pressure, 20/20 sccm Cl_2/Ar).

Hahn *et al.* investigated the effect of dc-bias on etching rate and RMS roughness during ICP etching of InGaN/GaN MQW LED structures. The etching rate and the surface roughness increased with increasing ion energy as shown in Fig. 4.13. SEM analysis showed that etch depth profile became more anisotropic as the dc-bias increased due to the perpendicular nature of incident ion energies. Similar results were observed for GaN by Cho *et al.*[30] and Cho *et al.* and were attributed to the preferential sputtering of nitrogen above a threshold ion energy.

ICP power

Figure 4.14 presents GaN, $Al_{0.28}Ga_{0.72}N$, and AlN etching rates as a function of ICP power. As can be seen, the etching rates increased rapidly from 100 to 500 W due to increasing ion flux and chlorine radical density. Above 500 W the rate of increase was slightly attenuated, although no maximum was reached. This was probably caused by ion-assisted desorption of the reactive species from the surface prior to etch reactions. A similar dependence was reported for In-containing layers and was attributed to the efficient sputtering of low volatile $InCl_3$ etch products, which normally retard further etching. As can also be seen in Fig. 4.14, the etching rates of Al-containing layers were lower than that of GaN. Khan *et al.* investigated $Al_xGa_{1-x}N$ etching rates as a function of x for ICP powers of 300, 500, and 800 W (Fig. 4.15). As in the case of dc-bias, the etching rates were found to be reduced as the value of x increased from GaN to AlN. This was also attributed to the increase in bond energy of $Al_xGa_{1-x}N$ layers with higher Al content.

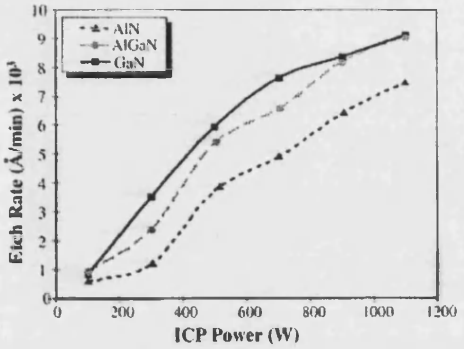

Fig. 4.14. Etch rates of GaN, $Al_{0.28}Ga_{0.72}N$, and AlN as a function of ICP power (-150 V dc-bias, 5 mTorr pressure, 20/5 sccm Cl_2/Ar gas flow rate).

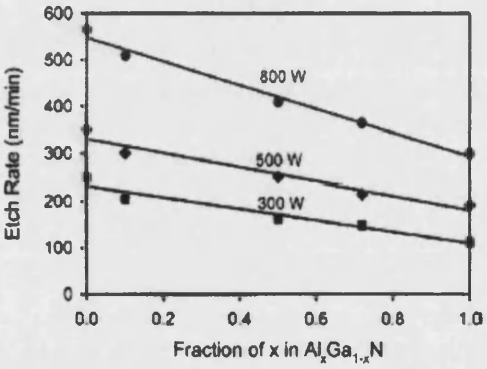

Fig. 4.15. Etch rate as a function of fraction of x in $Al_xGa_{1-x}N$ (-150 V dc-bias, 5 mTorr pressure, 25/5 sccm Cl_2/Ar gas flow rate).

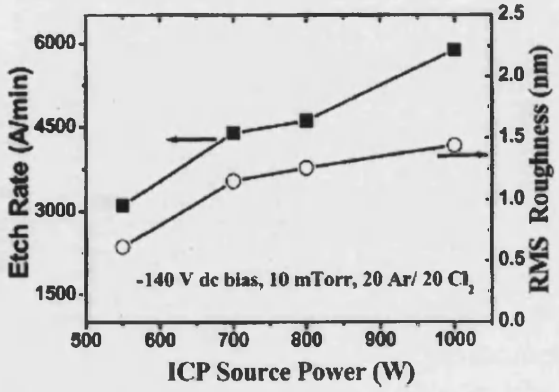

Fig. 4.16. Effect of ICP power on etch rate and surface roughness of InGaN/GaN MQW LED (-140 V dc-bias, 10 mTorr pressure, 20/20 sccm Cl_2/Ar gas flow rate).

The III-nitride etching rate behavior as a function of ICP power is fairly different at fixed RF power instead of dc-bias. Several research groups have observed an initial increase in the etching rates with increasing ICP power, followed by a plateau and a subsequent decrease at source power higher than 500–600 W.[21, 26, 28, 29, 30] It is well known that an increase in ion current density, defined by the ICP power in close-coupled systems, results in a decrease in dc-bias voltage at fixed RF power. As a result, the dc-bias is gradually reduced with increasing ICP power. The observed behavior suggests that the etching was reaction limited for low ICP power, i.e., the etching rates increased with increasing ion density, irrespective of the decrease of ion energy. However, for ICP power above 500–600 W, the etching behavior appeared to no longer be reaction limited and the etching rates decreased due to reduced ion bombardment. Furthermore, high ion flux could induce desorption of reactive species from the surface prior to etch reactions.

Hahn *et al.* investigated the effect of ICP power on etching rate and RMS roughness during ICP etching of InGaN/GaN MQW LED structures. The etching rates and the surface roughness increased with increasing ICP power, as shown in Fig. 4.16.

BCl_3 addition

Figure 4.17 shows GaN, AlN, InN etching rates, and dc-bias voltage as a function of Cl_2 concentration in $BCl_3/Cl_2/Ar$ ICP-generated plasma. As can be seen, the dc-bias initially increased as Cl_2 was added to the BCl_3/Ar plasma and then decreased at higher Cl_2 concentrations. At fixed RF and ICP power, this behavior suggests a higher ion density generated in Cl_2-based plasmas compared to BCl_3-based plasmas. Optical emission spectroscopy (OES) analysis revealed that Cl^+ and Cl^0 emission intensities were maximal at 80% Cl_2. Higher intensities compared to pure Cl_2/Ar plasma were probably caused by a catalytic role of BCl_3 on Cl_2 dissociation under plasma discharge. Malyshev *et al.*[31] found that small amount of BCl_3, added to Cl_2 ICP plasma, increased the percent dissociation of Cl_2 due to a passivation of process chamber walls by absorbed BCl_x and, hence, a lowering of $2Cl \rightarrow Cl_2$ recombination rate on the walls. Similar to plasma density, the GaN etching rate increased with increasing Cl_2 concentration up to 80% due to increasing a number of ions and reactive Cl radicals, regardless the decreasing ion energy. Alternatively, the InN and AlN etching rates were found to be less dependent on the Cl_2 concentration and were fairly comparable in Cl_2- and BCl_3-rich plasmas. The InN etching rate initially increased with the Cl_2 concentration and then decreased above 20% Cl_2, similar to dc-bias voltage. The AlN etching rate increased up to 40% Cl_2 concentration and then remained relatively constant. Slower AlN and InN etching rates at Cl_2 concentration higher than 50%, compared to GaN, were attributed to stronger bond energy for AlN and the low volatility of $InCl_3$ etch products, respectively. In BCl_3-rich plasmas the etching rates were relatively equal. A similar impact of BCl_3 addition to Cl_2/Ar ICP plasma for GaN etching was reported in the review of Pearton *et al.* The fastest GaN etching rate was observed at 80% Cl_2 where the ion current density and Cl radical density were the greatest as measured by OES and a Langmuir probe. It was also mentioned that InN and AlN etching rates showed much less dependence on plasma chemistry and were fairly comparable in Cl_2- and BCl_3-based plasmas. Remashan *et al.*[32] also observed a similar trend for GaN in BCl_3/Cl_2 ICP-generated plasma.

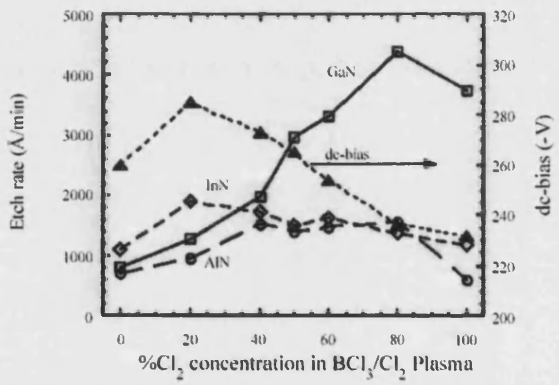

Fig. 4.17. GaN, InN, and AlN etch rates as a function of $\%Cl_2$ in $BCl_3/Cl_2/Ar$ ICP plasma (2 mTorr pressure, 40 sccm (BCl_3+Cl_2), 5 sccm Ar, 500 W ICP power, 125 W RF power, 25°C cathode temperature).

The addition of BCl_3 to Cl_2 plasma is also useful for the etching of Al-containing layers due to ability of BCl_3 to scavenge oxygen in a process chamber and prevent it from interfering with AlGaN etching with the formation of aluminum oxides.[33] Furthermore, BCl_3 can improve the sputter desorption of etch products due to its heavy ions. Wu *et al.* investigated the influence of BCl_3 added to Cl_2 ICP plasma on the etching of $Al_{0.28}Ga_{0.72}N/GaN$ heterostructure films. The etch conditions were: 15 sccm H_2/60 sccm Cl_2, 15 sccm Ar/60 sccm Cl_2, and 36 sccm BCl_3/6 sccm Cl_2, all at a chamber pressure of 20 mTorr. The RF power was adjusted in the range from 80 to 120 W to maintain a constant dc-bias of -350 V. Auger electron spectroscopy (AES) analysis was employed to investigate surface stoichiometry modifications and to give a depth profile of the etched AlGaN/GaN heterostructure. The results are presented in Fig. 4.18. As can be seen, the atomic fraction of oxygen at the surface of the sample etched in BCl_3/Cl_2 plasmas was 13%, which is significantly lower than 32% and 24% for the samples etched in H_2/Cl_2 and Ar/Cl_2 plasmas, respectively. Furthermore, atomic force microscope (AFM) analysis

revealed that, for BCl_3/Cl_2 etched samples, ultra-smooth etched surface was achieved (RMS roughness of 0.851 nm). On the contrary, H_2/Cl_2 and Ar/Cl_2 plasmas produced significant surface roughening (26.904 nm and 22.705 nm, respectively). The predominant factor affecting the etching was suggested to be the selfmasking effect of in-situ-produced aluminum oxides on the surface of the top AlGaN layer. The decrease in both RMS roughness and oxygen fraction at the surface using BCl_3/Cl_2 plasma probably implies that oxygen preferably reacted with BCl_3 to form $B_3Cl_3O_3$ trimers, a chemically inert gas which can be easily pumped out from the system.[34] Thus, the authors concluded that BCl_3/Cl_2 plasmas eliminate the formation of aluminum oxides by scavenging oxygen with BCl_3 and, hence, remove Al more effectively and significantly improve the etched surface morphology.

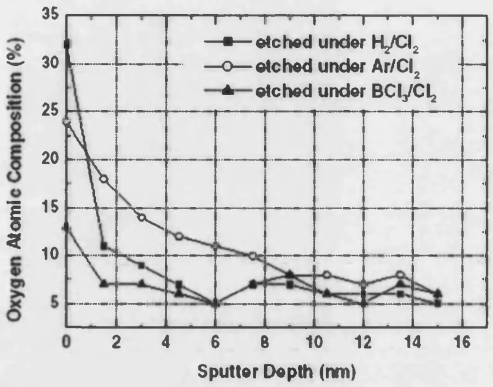

Fig. 4.18. Depth profiles of oxygen atomic fraction by AES analysis in AlGaN/GaN heterostructures after 30-nm etching using H_2/Cl_2, Ar/Cl_2 and BCl_3/Cl_2 plasmas.

The pressure dependence of GaN etching rate in $BCl_3/Cl_2/Ar$ ICP-generated plasma is similar to that in Cl_2/Ar plasmas.[1, 32] SEM analysis showed that the GaN etching profile was anisotropic and smooth at pressures up to 10 mTorr, and was undercut and poorly defined at higher pressures due to a low mean free path, collisional scattering of the ions and the increased lateral etching of GaN. The behavior of III-nitride etching rates in $BCl_3/Cl_2/Ar$ ICP plasmas as a function of either RF power (dc-bias) or ICP power is also very similar to that in Cl_2/Ar plasmas.[1, 11, 35]

H_2 addition

The inclusion of H_2 to Cl_2-based plasmas is expected to increase etching rates and also to improve surface morphology due to the removal of nitrogen through the formation of more volatile NH_3 products (boiling point of -33 °C) instead of NCl_3 (71 °C).[1, 16, 36] However, for GaAs and GaP semiconductors the addition of H_2 to chlorine-based plasmas typically results in reduced etching rates since H_2 acts as a scavenger of reactive Cl, forming HCl. Quadrupole mass spectrometry (QMS) measurements employed for ECR-generated $Cl_2/H_2/Ar$ discharge showed that the Cl concentration (indicated by m/e=35 peak intensity) decreased as more than 10% H_2 was added and the HCl concentration subsequently increased.[37] Lee *et al.*[38] also reported that OES emission of Cl radicals and Cl_2^+ ions was considerably decreased when H_2 was added to ICP-generated Cl_2 plasma and the GaN etching rate was slightly reduced. The authors also suggested that H_2 scavenged reactive species such as Cl, Cl^+, and Cl_2^+. Additionally, atomic hydrogen produced in a plasma discharge can diffuse into GaN and deactivate both donor and acceptor shallow levels causing a lowering of the free carrier concentrations.[39, 40]

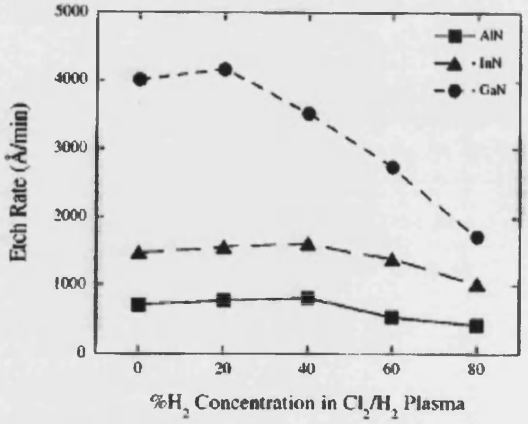

Fig 4.19. GaN, InN, and AlN etch rates as a function of $\%H_2$ in $Cl_2/H_2/Ar$ ICP plasma (25 sccm total gas flow, 5 sccm Ar, 25 °C cathode temperature, 2 mTorr pressure, 500 W ICP power, -250 V dc-bias).

Shul *et al.* investigated the influence of H_2 added to Cl_2/Ar ICP-generated plasma on the etching rates of GaN, AlN, and InN. As can be seen in Fig. 4.19, the etching rates slightly increased as H_2 was initially added and then decreased at higher concentrations. This decrease was especially evident for GaN. Shul *et al.*[41] also reported that the etching rate of GaN was maximal at the maximal concentration of Cl_2 within the range of 10–60% H_2. Similar results for GaN were presented in the review of Pearton *et al.* (maximal etching rate at 10% H_2 and a decrease at higher concentrations). Reduced rates at higher H_2 concentrations were attributed to the consumption of reactive Cl species by hydrogen. In all probability, the InN and AlN etching rates were less dependent on the H_2 concentration due to their lower dependence on reactive Cl concentration in the plasma. The behavior of the GaN etching rate as a function of pressure, RF power, or ICP power in $Cl_2/Ar/H_2$ ICP-generated plasma was found to be similar to that in Cl_2/Ar plasmas. The authors observed significant roughening of the etched surface (RMS roughness of 67 nm) at 750 W ICP power and attributed it to the preferential sputtering of N under high plasma density.

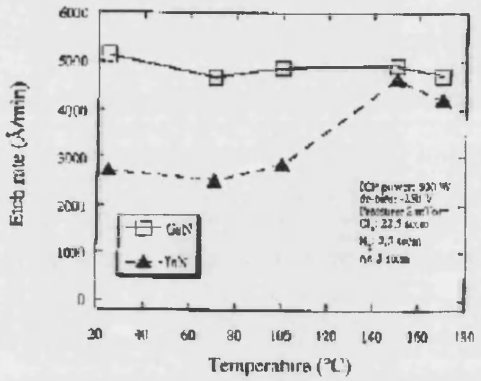

Fig. 4.20. GaN and InN etch rates as a function of temperature for $Cl_2/H_2/Ar$ plasmas (22.5 sccm Cl_2, 2.5 sccm H_2, 5 sccm Ar, 500 W ICP source power, -250 V dc-bias, 2 mTorr pressure).

The substrate temperature can affect the desorption rates of etch products, gas-surface reaction kinetics, and the surface mobility of reactants. The temperature dependence of GaN and InN etching rates in ICP-generated $Cl_2/H_2/Ar$ plasma was presented in the review of Pearton *et al.*. As can be seen in Fig. 4.20, the GaN etching rate was much faster than that of InN due to the higher volatility of $GaCl_3$ etch products (201 °C) compared to $InCl_3$ (600 °C) and showed little dependence on temperature. In contrast, the InN etching rate increased at 150 °C due to the enhanced volatility of $InCl_3$ at higher temperatures.

N_2 addition

Figure 4.21 shows the influence of N_2 added to Cl_2/Ar ICP-generated plasma on the etching rates of GaN, AlN, and InN. As can be seen, the GaN etching rate decreased with increasing N_2 concentration, which was attributed to less reactive Cl being available. The InN and AlN etching rates were less dependent on reactive Cl concentration and remained relatively constant. Similar results for GaN were presented in the review of Pearton *et al.* Sheu *et al.* investigated and compared ICP etching of GaN with Cl_2/Ar and Cl_2/N_2 plasmas at the same conditions. They found that Ar or N_2 added to Cl_2 plasma produced different chlorine ion densities, inducing a significant difference in the dc-bias voltage. The authors suggested that the addition of Ar or N_2 gases to a Cl_2-based plasma result in the different degree of dissociation for Cl_2, with lower plasma density generated in Cl_2/N_2. As a result, a very different behavior of GaN etching rate as a function of gas mixing ratio, pressure, RF and ICP power was observed in Cl_2/Ar and Cl_2/N_2.

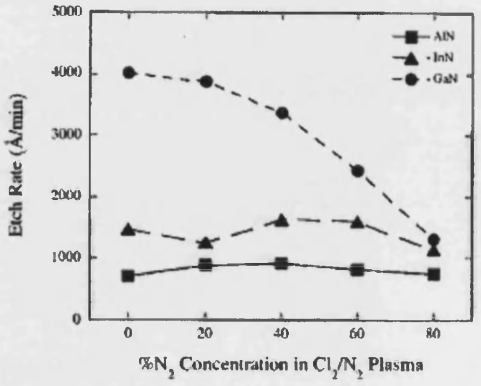

Fig. 4.21. GaN, InN, and AlN etch rates as a function of $\%N_2$ in $Cl_2/N_2/Ar$ ICP plasma (25 sccm total gas flow, 5 sccm Ar, 25 °C electrode temperature, 2 mTorr pressure, 500 W ICP power, -250 V dc-bias).

O_2 addition

Lee *et al.*[42] reported GaN, $In_{0.12}Ga_{0.88}N$, $Al_{0.1}Ga_{0.9}N$, and $Al_{0.05}Ga_{0.95}N$ etching rates as a function of O_2 added to ICP-generated Cl_2/Ar plasma. It was found that O_2 addition played a significant role in the enhancement of (In)GaN/AlGaN etch selectivity. X-Ray Photoelectron Spectroscopy (XPS) analysis showed that oxide layers were formed on the surface as a result of oxygen inclusion to the plasma chemistry. As can be seen in Fig. 4.22, the etching rates for all materials monotonically decreased with increasing O_2 flow rate due to the bond strengths of the oxides being larger than those of the nitrides. The enhanced selectivity of (In)GaN over AlGaN was attributed to a fact that the bond strength difference between Al–O (21.2 eV/atom) and Ga–O (14.7 eV/atom) is much larger than the difference between Al–N (11.5 eV/atom) and Ga–N (8.9 eV/atom). Lee *et al.* also investigated the selectivity of GaN and $In_{0.12}Ga_{0.88}N$ over $Al_xGa_{1-x}N$ as a function of RF power. As the RF power (or dc-bias) increased, the etching rates also increased due to enhanced physical sputtering. As a result, the selectivity of (In)GaN over $Al_xGa_{1-x}N$ subsequently decreased due to an increase in bond breaking efficiency for Al–O.

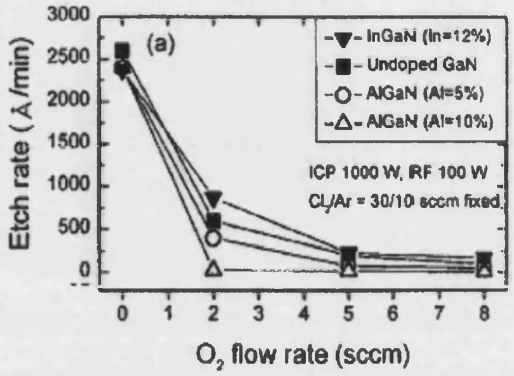

Fig. 4.22. Etch rate of GaN, $In_{0.12}Ga_{0.88}N$, $Al_{0.05}Ga_{0.95}N$, and $Al_{0.1}Ga_{0.9}N$ as a function of O_2 flow rate in $Cl_2/Ar/O_2$ ICP plasma (30/10 sccm Cl_2/Ar, 10 mTorr pressure, 1000 W ICP power, 20 °C temperature, 100 W RF power).

CH_4 addition

CH_4 is expected to increase III-nitride etching rates due to the formation of more volatile products with Ga, In, and Al compared to Cl_2-based plasmas (the boiling point of $(CH_3)_3Ga$ is 55.7 °C, $(CH_3)_3In$ is 134 °C, and $(CH_3)_3Al$ is 126 °C). But other factors such as polymer deposition on the plasma-exposed surface may reduce the final etching rate.[43] In addition, atomic hydrogen produced in the plasma discharge can diffuse into GaN and deactivate dopants. Basak *et al.*[44] investigated the influence of CH_4 added to a Cl_2/Ar plasma in a conventional RIE system. The GaN etching rate slightly increased at 4% CH_4 and subsequently decreased with increasing CH_4 concentration, $Al_{0.15}Ga_{0.85}N$ etching rate was maximal at 10% CH_4 and then also decreased. This was attributed to a competition between Cl_2 and CH_4. In all probability, similar results can be expected using the ICP technique.

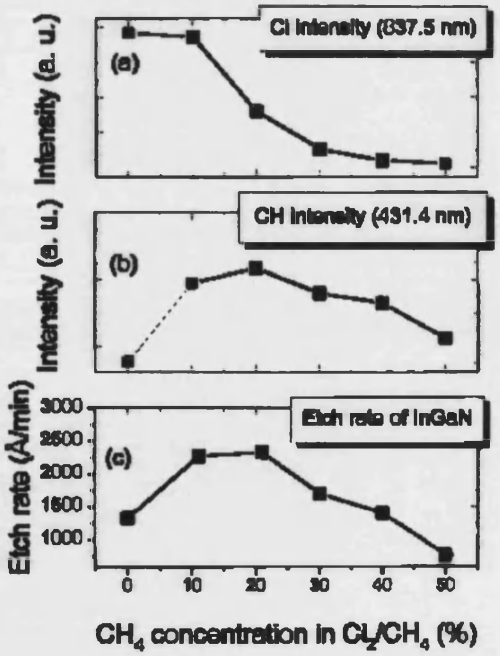

Fig. 4.23. Emission intensity of (a)Cl and (b)CH, (c) etch rate of $In_{0.12}Ga_{0.88}N$ as a function of $\%CH_4$ (30/8/16 sccm $Cl_2/H_2/Ar$, 1000 W ICP power, 100 W RF power, 10 mTorr pressure).

Lee *et al.* added CH_4 to a Cl_2/H_2/Ar ICP-generated plasma in order to improve etching of In-containing compounds. Cl radicals react with In to form nonvolatile $InCl_3$ products (600 °C), which often results in a rough etched surface for structures

containing InGaN layers. In contrast, CH-based species react with In forming volatile $(CH_3)_3In$ products (134 °C). Figure 4.23 shows the plasma emission intensity of atomic Cl (a), CH (b), and etching rate of $In_{0.12}Ga_{0.88}N$ (c) as a function of CH_4 concentration. As can be seen, the Cl emission intensity gradually decreased with increasing CH_4 concentration, which was attributed to reduced Cl_2 concentration along with the reaction of chlorine with atomic hydrogen derived from CH_4. On the other hand, the CH emission intensity increased for up to 20% of CH_4 and then slightly decreased, which was attributed to polymer formation at higher concentrations. The etching rate was closely related to the CH intensity and was considerably enhanced at 20% CH_4. Thereby, the authors suggested that etching of In-based compounds can be significantly improved by the addition of CH_4 to Cl-based plasmas. A $Cl_2/CH_4/H_2/Ar$ ICP-generated plasma was successfully employed for the etching of a GaN/InGaN MQW structure by Lee *at. al.*[45] The authors reported that the morphology of the etched surface was severely degraded by residues when the structure was etched in the absence of CH_4. This was attributed to the micromasking effect of InGaN layers whereas a smooth etched surface was obtained using CH_4 in the plasma chemistry.

SF_6 addition

Fluorine may play an important role in the dry etching of III-nitrides due to it reacting with nitrogen and producing a very volatile product NF_3 with a boiling point of -129 °C, while that of NCl_3 is 71 °C.[1, 16, 46] Shul *et al.* investigated the influence of SF_6 added to a Cl_2/Ar ICP-generated plasma on the etching rates of GaN, AlN, and InN. As can be seen in Fig. 4.24, the GaN and InN etching rates decreased as SF_6 was added. The authors mentioned that the reactive Cl concentration in ECR-generated $Cl_2/SF_6/Ar$ plasmas was decreased compared to Cl_2/Ar plasmas and formation of SCl was observed. It was suggested that a similar trend takes place in ICP systems as well. Thereby the slower etching rates were attributed to the consumption of reactive Cl radicals with S. In contrast, the AlN etching rate increased with the addition of SF_6 and reached a maximum at 20% SF_6. These results are surprising since F is expected to react with Al forming AlF_3, which has low volatility and should result in slow etching rates. The authors attributed this phenomenon to a high ion flux in the ICP system. They suggested that sputter desorption of AlF_3 occurred prior to passivation of the surface.

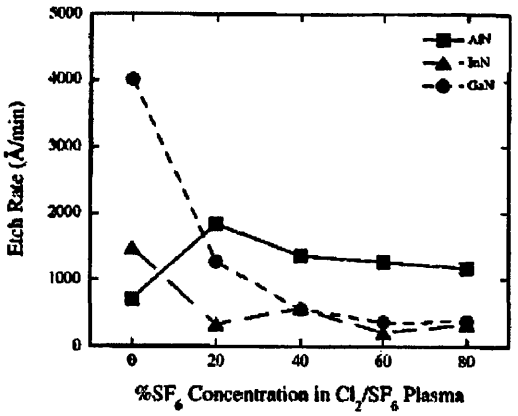

Fig. 4.24. GaN, InN, and AlN etch rates as a function of $\%SF_6$ in $Cl_2/SF_6/Ar$ ICP plasma (25 sccm total gas flow, 5 sccm Ar, 25 °C electrode temperature, 2 mTorr pressure, 500 W ICP power, -250 V dc-bias).

4.3.2 BCl_3 plasma

When boron trichloride (BCl_3) is substituted for Cl_2 in a dry etching process, GaN etching rates typically decrease due to the generation of less reactive Cl, while anisotropy increases due to increased sputter desorption efficiency. Shul *et al.* observed this trend in BCl_3/Ar and $BCl_3/H_2/Ar$ ICP-generated plasmas where the GaN etching rates were nearly six times slower compared to Cl_2-based plasmas. In contrast, InN and AlN etching rates were fairly comparable in both Cl_2 and BCl_3 plasmas implying that a chemical component of etching was less significant for these compounds. Furthermore, BCl_3 was found to be a strong reducer of native surface oxides on AlGaN and of residual oxidizing agents in a process chamber, preventing any "etch delay" effects during the etching of these layers.[47]

As a result, the etching rates of all structure layers are nearly equal in BCl_3 plasmas. This makes BCl_3-based plasmas very promising for laser facet processing where low etch selectivity between different layers is required.

Ar addition

Figure 4.25 shows the III-nitride etching rates and dc-bias as a function of $\%BCl_3$ in a ICP-generated BCl_3/Ar plasma.[48] As can be seen, the dc-bias voltage increased with increasing BCl_3 concentration, indicating a decrease in ion current density at these conditions. Thereby, Ar probably has a lower ionization energy than BCl_3. The InN etching rate significantly decreased at high boron trichloride concentration and was attributed to the build-up of a nonvolatile $InCl_3$ layer under Ar-deficient conditions. A similar behavior was observed for the other materials at more than 15% BCl_3. However, etching in pure Ar plasmas also produced extremely slow etching rates due to the absence of a chemical etching component. The behavior of III-nitride etching rates in BCl_3/Ar ICP plasmas as a function of pressure, RF power (dc-bias), and ICP power was found to be very similar to that in Cl_2/Ar plasmas.[48, 49]

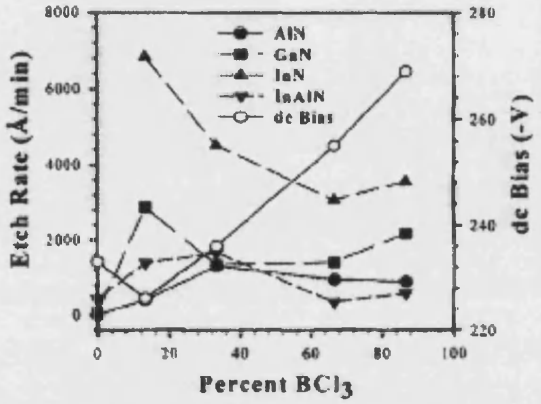

Fig. 4.25. III-nitride etch rates and dc-bias as a function of $\%BCl_3$ in BCl_3/Ar ICP plasma (5 mTorr pressure, 750 W ICP power, 250 W RF power).

N_2 addition

Shul *et al.* investigated the influence of N_2 added to a BCl_3/Ar ICP-generated plasma on etching rates of GaN, AlN, and InN. As can be seen in Fig. 4.26, the etching rates increased as N_2 was added up to 40% and then decreased at higher concentrations. It was suggested that N_2 enhanced the dissociation of BCl_3 resulting in higher concentrations of reactive Cl radicals and Cl^+ ions and, hence, in higher etching rates. A similar trend was reported by Ren *et al.*[50, 51] during ECR etching of In-containing materials. They observed peak etching rates at 25% N_2 in BCl_3/N_2 plasmas. Optical emission spectroscopy also showed the maximum emission intensity for atomic and molecular Cl at 25% N_2. Correspondingly, the BCl intensity decreased and a BN emission line appeared. A similar dependence for the GaN etching rate was recently reported by Oh *et al.*[52] The authors also observed an increase in the Cl radical emission with the addition of 40% N_2. However, they attributed this increase to the reduction of the recombination probability between B and Cl rather than BN formation.

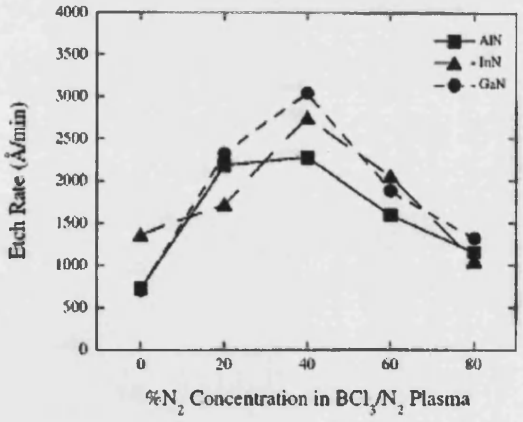

Fig. 4.26. GaN, InN, and AlN etch rates as a function of $\%N_2$ in BCl_3/N_2/Ar ICP plasma (25 sccm total gas flow, 5 sccm Ar, 25 °C electrode temperature, 2 mTorr pressure, 500 W ICP power, -250 V dc-bias).

SF_6 addition

Shul *et al.* investigated the influence of SF_6 added to a BCl_3/Ar ICP-generated plasma on the etching rates of GaN, AlN, and InN. As can be seen in Fig. 4.27, the etching rates increased by up to 20% SF_6 and then decreased sharply at higher concentrations. Quadrupole mass spectroscopy showed that the reactive Cl concentration (*m*/*e*=35) initially increased as SF_6 was added to the plasma and then decreased at SF_6 concentrations higher than 20%. Thus the authors suggested that SF_6 enhanced the dissociation of BCl_3 resulting in higher concentrations of reactive Cl and, hence, faster etching rates. However, at more than 20% SF_6, S probably consumed Cl radicals, as indicated by the formation of SCl, which resulted in a decrease of the etching rates. Oh *et al.* also reported maximal etching rate for GaN at 20% SF_6 accompanied by an increase in Cl radical intensity.

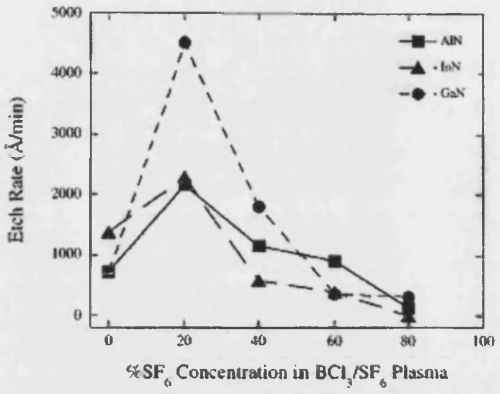

Fig. 4.27. GaN, InN, and AlN etch as a function of $\%SF_6$ in BCl_3/SF_6/Ar ICP plasma (25 sccm total gas flow, 5 sccm Ar, 25 °C electrode temperature, 2 mTorr pressure, 500 W ICP power, -250 V dc-bias).

CH_4 addition

Lee *et al.*[53] investigated the influence of CH_4 added to a BCl_3/H_2/Ar ICP-generated plasma on GaN etching rate and etched sidewall verticality. As can be seen in Fig. 4.28, the etching rate continuously decreased. On the contrary, the mesa sidewall angle increased with the addition of up to 10% CH_4. This was attributed to the erosion of the Ni mask edges with no CH_4 due to strong physical sputtering and deposition of polymerized C–H species with CH_4, which protected the mask. The authors also noticed that the etched surface became grey colored after the etching with CH_4 and recovered its original color after an O_2 plasma ashing process. This was attributed to polymerized C–H species forming on the surface under a plasma discharge, and their removal by O_2 plasma treatment.

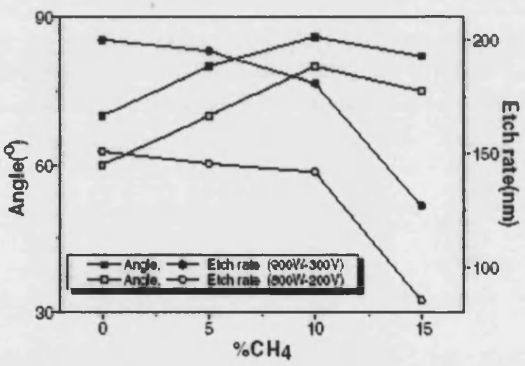

Fig. 4.28. Effects of CH_4 addition on GaN etch rate and sidewall verticality in $BCl_3/H_2/CH_4$/Ar ICP plasma (900 W ICP power, -300 V dc-bias, 4 mTorr, 60% BCl_3; and 800 W ICP power, -200 V dc-bias, 4 mTorr, 60% BCl_3).

4.3.3 $SiCl_4$ plasma

$SiCl_4$-based plasmas are widely used for etching GaAs-based materials. However, for III-nitrides there have been only a few reports and none of them, in our knowledge, about ICP etching. Zhang *et al.*[54] reported electron cyclotron resonance (ECR) etching of GaN using a $SiCl_4$/Ar plasma. Adesida *et al.*[55] were the first to report reactive ion etching (RIE) of GaN in $SiCl_4$-based plasmas. Similar to BCl_3 plasmas, $SiCl_4$ is expected to reduce residual oxidizing agents in the process chamber and to increase the sputter desorption efficiency due to heavy ions (the most reactive is $SiCl_3^+$(m=133)[56]). However, Lin *et al.*[57] reported that the etching rate of GaN in a $SiCl_4$ RIE plasma was slower than that in BCl_3 under the same conditions (RF power, pressure, gas flow). Furthermore, under the same RF power, the induced cathode dc-bias voltage was observed to be lower in $SiCl_4$

discharge than that in BCl_3. This implies that $SiCl_4$ generated a higher plasma density compared to BCl_3. Thus $SiCl_4$ may be a similar or even more efficient etchant than BCl_3 under the same dc-bias voltage.

SF_6 addition

As considered above, fluorine may play an important role in the dry etching of III-nitrides due to it reacting with nitrogen and producing a very volatile product NF_3 (boiling point of -129°C).[1, 16, 46] Besides, 20% SF_6 addition to BCl_3 plasmas was reported to significantly increase GaN etching rate because of SF_6 enhanced the dissociation of BCl_3 resulting in higher concentrations of reactive Cl. Adesida *et al.*[55] compared RIE etching of GaN in a $SiCl_4$(10 sccm) plasma with a $SiCl_4/SF_4$(10/10 sccm) plasma at the same conditions. It was observed that the etching rates were essentially identical. However, these results were obtained at a fairly high concentration of SF_4(50%) where consumption of reactive Cl by S might take place. In contrast, Karouta *et al.*[46, 58] significantly increased the GaN etching rate by adding 3 sccm SF_6 to a $SiCl_4$/Ar(10/10 sccm) RIE plasma (Fig. 4.29). This was attributed to fluorine reacting with nitrogen and producing volatile NF_3 products. A decrease in the etching rate at higher SF_6 flow (>3 sccm) was ascribed to more electrons subjected to collisions, which did not result in active species. However, this explanation seems to be arguable. Another reason could be the same as in the case of a BCl_3 plasma, where SF_6 enhanced the dissociation of BCl_3, resulting in higher concentrations of reactive Cl. The decrease in the etching rate may also be attributed to the consumption of the reactive Cl radicals by S at higher SF_6 concentration. In all probability, similar results may be expected for ICP processing.

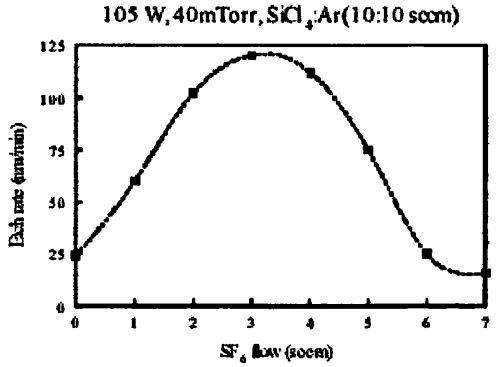

Fig. 4.29. Effect of SF_6 flow on etch rate of GaN in $SiCl_4/SF_6/Ar$ RIE plasma (105 W RF power, 40 mTorr pressure, 10/10 sccm $SiCl_4$/Ar).

4.3.4 ICP-induced damage and its recovery

Plasma-induced damage caused by dry etching may seriously degrade the electrical and optical properties of III-nitride devices. The forms of the damage may be categorized including:[1, 35, 36, 59, 60, 61, 62]

- Deposition of polymers due to the use of plasma chemistries containing CH_x radicals or due to the reaction of a photoresist mask with plasma.
- Implantation of hydrogen into the etched material and the resulting passivation of shallow dopants up to a depth of several thousand angstroms due to either the use of hydrogen in the plasma chemistry, residual water vapor in a process chamber, or erosion of a photoresist mask.
- Creation of non-stoichiometric surfaces up to a depth of 100 Å due to either preferential sputter desorption of lighter elements in films or large differences in the volatility of the etch products.
- Creation of near-surface lattice defects or dislocations, which can diffuse into material up to a depth of 1000 Å. These defects often act as deep level states and produce compensation, trapping, and recombination in the material.

Cao *et al.*[61, 63] exposed *n*-GaN to either pure N_2 or H_2 ICP discharges. They found that N_2 ions led to more serious degradation of the surface than H_2 ions of similar energy.

It was suggested that a physical etching component [ion mass ($^{28}N_2^+$, $^2H_2^+$)] is more important in influencing the electrical properties of the surface than a chemical effect, since hydrogen would preferably remove nitrogen from GaN as NH_3. Rearton *et al.* and Cao *et al.*[64] also reported that heavy Ar ions created more damage in *p*-GaN compared to light H_2 ions under the same etching conditions. Furthermore, Ping *et al.*[65] reported that plasmas with a strong chemical component ($SiCl_4$) produced less degradation than purely physical etching (Ar). The plasma damage in GaN was found to accumulate in a near-surface region even after a very short exposure time (~4 sec). Cao *et al.*[61, 63, 64] estimated the damage depth to be approximately 400–600 Å by using wet etching to remove different amounts of plasma-exposed GaN.

Damage in *n*-GaN

Improved characteristics for Ohmic contacts to plasma exposed *n*-type GaN have been reported by several groups.[66, 67, 68, 69, 70, 71] This behavior is well established to be due to the preferential removal of nitrogen under energetic ion bombardment, which leaves an excess of metallic gallium on the etched-surface. The nitrogen vacancies, acting as shallow donors,[72, 73] are sufficient to generate about a 100 Å thick layer with a doping concentration as high as 10^{19}–10^{20} cm^{-3}.[74] As a result, the tunneling probability for electrons through a metal/*n*-GaN interface is greatly enhanced and the contact resistivity is significantly reduced. A mechanism of Ohmic contact formation to plasma treated *n*-type GaN is considered in detail in Chapter 6.

Unfortunately, the effective sheet resistance of *n*-GaN underneath the highly conductive near-surface area has been found to increase after plasma exposure. It was attributed to deep compensating levels created by ion bombardment.[60, 75, 76, 77, 78] The depth and thickness of the damaged region was estimated by Cao *et al.* They used photoelectrochemical wet etching to remove different amounts of plasma-exposed *n*-GaN, followed by depositing Pt/Au contacts. The highest series resistance corresponded to an etching depth from 260 to 600 Å of GaN. Chua *et al.*[79] ascribed the highly resistive region to deep levels associated with Ga-vacancies forming a complex with oxygen species, namely V_{Ga}-O_N and V_{Ga}-$(O_N)_2$ acting as deep double and single acceptors,[80] respectively. It was suggested that these complexes partly compensate the electron concentration in *n*-GaN and, hence, result in the increased series resistance. However, this suggestion seems to be arguable and requires further investigations.

Both the increased near-surface electron concentration and the highly resistive region underneath, however, seriously degrade the performance of *n*-GaN Schottky diodes.[1, 45, 61, 63, 65, 81] Generally speaking, Schottky contacts become Ohmic due to the significantly increased tunneling current through the metal/*n*-GaN interface. Annealing is the most common method to remove plasma-induced damage and to recover current-voltage (*I-V*) characteristics.[1, 45, 61, 63, 65, 81, 82] Cao *et al.*[61, 63] investigated the effect of annealing in N_2 ambient on the reverse breakdown voltage (V_B) of Schottky contacts deposited on *n*-GaN exposed with a N_2 ICP plasma. As can be seen in Fig. 4.30, increasing the annealing temperature up to 750 °C led to substantial improvement in V_B. The small

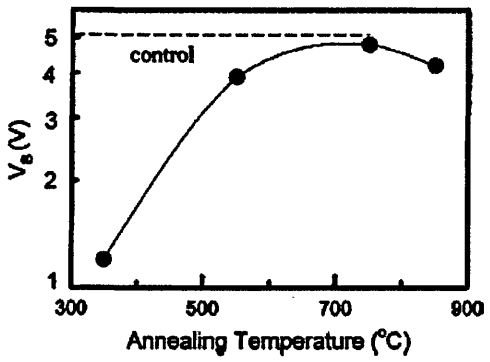

Fig. 4.30. Reverse breakdown voltage (V_B) as a function of annealing temperature in N_2 after N_2 ICP plasma exposure (500 W ICP power, -220 V dc-bias, 5 mTorr pressure).[61, 63]

degradation observed at temperatures higher than 850 °C is consistent with the temperature at which nitrogen begins leaving the surface. A stable encapsulating layer, such as AlN, can be used to prevent high-temperature loss of nitrogen.[83] The recovery of *n*-GaN Schottky diodes after annealing at 700–800 °C has been reported by several groups.[1, 45, 65, 81, 82] However, the annealing only partially restores the surface. Full recovery can only be achieved with additional wet chemical etching to remove the damaged material. Thus, a combination of annealing and a wet etch clean-up step may be practical for *n*-GaN Schottky diode processing. It is also important to notice that acceptable improvement cannot be realized if annealing is conducted after contact deposition.[63, 81] The surface damage was suggested to enhance interfacial reactions between the contacts and GaN hindering surface recovery.

Damage in *p*-GaN

Plasma exposure has a great effect on the surface characteristics of *p*-type GaN. The net concentration of acceptors can be significantly reduced in the near-surface region due to the large number of N-vacancies produced under energetic ion bombardment. At a high ion flux or a high ion energy, even surface conversion to *n*-type conductivity may take place. Pearton *et al.* and Cao *et al.* reported damage depth in *p*-GaN to be in the range of 400–500 Å. This makes it extremely difficult to fabricate Ohmic contacts with low resistivity to the etched *p*-GaN surface.[64, 84, 85, 86, 87] Chang *et al.* employed annealing in a N_2 ambient to restore surface conditions after dry etching and to improve final Ohmic contacts. The authors found that heat treatment at 700 °C improved the contacts although they did not become Ohmic completely. XPS analysis showed that annealing at 500 °C reduced the surface nitrogen content even more because nitrogen bonds were destroyed and the surface structure became very loose under plasma treatment. After annealing at 700 °C, however, the surface nitrogen and oxygen contents nearly recovered to their native amounts. And after annealing at 900 °C the GaN surface started to decompose and gallium oxide tended to form due to residual oxygen in the annealing ambient. These results are slightly different from those presented by Cao *et al.* and Pearton *et al.* for Schottky contacts to plasma exposed *p*-GaN. These authors reported that post-etch annealing in nitrogen ambient restored the initial breakdown voltage at 900 °C. This discrepancy can be caused by different quality of material and different measurement techniques employed (Ohmic vs. Schottky contacts). Nonetheless, annealing did not entirely restore the surface and complete recovery was only achieved after the removal of the damaged material.[1, 64]

Damage in a *(p-n)* junction

Damage to a *p-n* junction may occur through the degradation of sidewalls under strong plasma conditions.[1, 35] At a high ion flux or a high ion energy, the more energetic ions scattering from the surface strike the sidewalls with significant momentum. The damage probably takes a form of point defects, such as nitrogen vacancies, increasing the *n*-type conductivity of the sidewalls. Additionally, redeposition of etch products on the sidewalls may also degrade the electrical properties of the *p-n* junction.

Shul *et al.* investigated the influence of dc-bias voltage on the reverse junction current of GaN-based LEDs during mesa etching in a $BCl_3/Cl_2/Ar$ ICP-generated plasma. The authors observed that the reverse leakage current increased rapidly above -250 V dc-bias, accompanied by serious degradation of the mesa sidewalls due to erosion of the photoresist mask edges. Thus, the increase in the current was attributed to sidewall damage. Hahn *et al.* investigated the influence of dc-bias voltage on forward turn-on (V_F) and reverse breakdown (V_B) voltage of InGaN/GaN MQW LEDs during mesa etching in a Cl_2/Ar ICP-generated plasma. As the dc-bias increased from -180 to -245 V, V_F and V_B

were increased and decreased, respectively. The authors also observed sidewall contamination, which became worse at higher dc-bias voltage. It was ascribed to redeposition of etch products on the sidewalls. Thus, the deterioration in the forward and reverse voltage was also attributed to damage accumulated on the sidewalls due to energetic ion bombardment.

Shul *et al.* also studied the effect of ICP power on the reverse junction current. There was a minimal effect on the leakage current at the ICP power less than 500 W, whilst there was severe degradation at higher ICP power. This was consistent with degradation in the sidewall profile due to erosion of the photoresist mask edges. Thus, sidewall degradation was ascribed to be the main reason for the increase in the leakage current. Another reason could be an enhanced interaction of reactive neutrals with the sidewalls under high plasma density. Hahn *et al.* investigated the effect of ICP power on the forward and reverse voltage. V_F decreased slightly up to 800 W ICP power, showing a minimal effect on the turn-on voltage, but increased at 1000 W due to plasma-induced surface damage. In contrast, the breakdown voltage showed severe degradation at ICP powers lower and higher than 700 W. The authors observed heavy deposition of the etch products at lower power (<550 W). The degradation at higher ICP power was attributed to increased ion scattering and an enhanced interaction of reactive neutrals with the sidewalls.

Shul *et al.* also reported that the reverse leakage current was relatively insensitive to Cl_2 percentage in a $Cl_2/BCl_3/Ar$ ICP discharge. This fact emphasizes that a physical component of plasma etching is mainly responsible for sidewall damage. Hahn *et al.* found that the forward voltage V_F showed a similar trend to surface roughness, but the reverse voltage V_B demonstrated the worst degradation at 75% Cl_2 in Cl_2/Ar ICP plasma, accompanied by the worst sidewall contamination at this mixture. The authors concluded that the forward turn-on voltage is more sensitive to the surface roughness, while the reverse breakdown voltage is affected by damage accumulated on the mesa sidewalls.

Shul *et al.* found that after etching at low-pressure (1 mTorr) the reverse leakage current was very high. As the pressure was increased to 2 mTorr, the leakage current considerably decreased and remained relatively constant at higher pressures. The authors attributed this behavior to the high mean free path of the ions and more energetic collisions of the ions with the sidewalls at lower pressures. However, this explanation seems to be fairly arguable. A probable reason could be a reactant limited regime at pressures less than 2 mTorr. Hahn *et al.* reported that the reverse breakdown voltage V_B was relatively insensitive to process pressure, while the forward turn-on voltage V_F was relatively independent up to 20 mTorr and showed a sudden increase at higher pressures, accompanied by roughening of the surface at these conditions. The results indicate a strong relationship between the forward voltage and the roughness of the etched *n*-GaN surface.

Annealing was employed by Shul *et al.* to determine if the defects caused by plasma-induced damage of the *p-n* junction could be removed and the low reverse leakage current recovered. Nonetheless, the reverse current remained essentially constant up to annealing temperature of 500 °C and increased by more than an order of magnitude at 600 °C. In all probability, it was caused by the preferential loss of nitrogen and an increase of *n*-type conductivity of the sidewalls after the annealing. These results are similar to those obtained by Chang *et al.* for ICP treated *p*-type GaN. The surface nitrogen content was found to be further reduced after RTA-treatment at 500 °C due to the nitrogen bonds being destroyed and the surface structure becoming very loose under plasma treatment. Only after annealing at 700 °C did the nitrogen content nearly recover to its native amount and sufficient recovery of *p*-type was achieved. Thus, recovery of a *p-n* junction at higher temperature may be expected as well.

Damage in PL spectra

Plasma etching may generate extra energy states in a semiconductor band gap, acting as nonradiative recombination centers in a near surface region.[1, 32, 88] As a result, band-edge PL intensity from a plasma-exposed surface region is typically less than that from an unetched region. The nonradiative centers are usually caused by the creation of non-stoichiometric surfaces due to the preferential depletion of one of elements or by the creation of near-surface lattice defects, which can diffuse deeply into the etched material. During GaN plasma etching, nitrogen depletion commonly occurs, which results in a large number of nitrogen vacancies generated at the surface. The resulting Ga-rich surface is believed to be the main reason for the decrease in band-edge PL emission generally observed for plasma-exposed GaN. Furthermore, an increase in the ion bombarding energy may also initiate the formation of deep acceptor states near the surface. The gallium vacancy, V_{Ga}, is the most favorable native deep acceptor in GaN and this vacancy can readily form a complex with a neighbour O_N due to its low formation energy. Thereby, the presence of oxygen in the plasma or oxygen donors/impurities in the GaN promotes the formation of (V_{Ga}–O_N) complexes during processing. At the same time, (V_{Ga}–O_N) was found to play a significant role in yellow luminescence (YL) generation.[89, 90, 91, 92] Tripathy *et al.* observed a significant enhancement in YL from the etched surface and attributed it to an increased amount of (V_{Ga}–O_N) complexes after etching and related shallow-donor–deep-acceptor transitions. Similar YL behavior was observed by Lee *et al.* In contrast, Han *et al.*, Choir *et al.*[93], and Basak *et al.*[94] have reported that YL intensity was decreased after plasma etching and was attributed to plasma-induced surface defects acting as nonradiative recombination centers for the yellow emission. The contradictory results could be caused by different material quality or different plasma etching conditions.

Lee *et al.* investigated the influence of RF power on the band-edge PL intensity of *n*-GaN during etching in a $Cl_2/CH_4/H_2/Ar$ ICP-generated plasma and observed that the intensity decreased with increasing RF power. Shul *et al.* also observed a similar trend in ICP and ECR Ar plasmas. As a function of ICP power or plasma density, the PL intensity showed virtually no change at low ICP source power and then decreased as the plasma density increased. Remashan *et al.* observed that the band-edge PL intensity was lower at a higher concentration of BCl_3 in a BCl_3/Cl_2 ICP plasma. This was attributed to the heavier mass of ions in the BCl_3 plasma compared to that in the Cl_2 plasma and, hence, more damage accumulated in the surface. The authors also reported that the PL signal was the highest after etching at 5 mTorr pressure and the lowest at 20 mTorr. This was attributed to the higher dc-bias voltage generated at higher pressures due to a decrease in plasma density at fixed RF and ICP power. Thereby, stronger plasma conditions (ion mass and energy, ion flux) yield heavier PL degradation of GaN due to an enhanced disorder in the surface.

Tripathy *et al.* studied the influence of annealing on PL performance of GaN previously etched in a BCl_3/Cl_2 ICP-generated plasma. It was found that the band-edge PL intensity was significantly improved after annealing at 900 °C in N_2 ambient, while YL intensity was reduced. The authors also observed that the heat treatment resulted in an improved Ga:N ratio indicating the replacements of (Ga–O) bonds by (Ga–N) at the surface. Thus, it was deduced that oxygen atoms were the main cause of the YL. Lee *et al.* employed N_2 plasma treatment in a PECVD chamber for *n*-GaN samples, previously etched in a $Cl_2/CH_4/H_2/Ar$ ICP-generated plasma, in order to remove etch-induced damage. As a result, band-edge PL characteristics were significantly improved, which was attributed to recovery of surface stoichiometry. Auger electron spectroscopy (AES) confirmed that the N_2 plasma restored the surface nitrogen content of the etched GaN to its as-grown value. Thereby, either annealing in nitrogen or N_2 plasma treatment can be employed to improve the optical properties of etched GaN surfaces, although complete recovery can only be achieved using a wet etching step to remove the damaged material.

4.4 Optimization of SiO_2 etch mask fabrication for laser diode processing

4.4.1 Introduction

For plasma processing in the fabrication of GaN-based laser diodes, SiO_2 is commonly used as an etch mask due to its inertness to Cl-based plasmas and stability under heavy ion bombardment. Photoresist is not suitable due to excessive erosion under dry etching, which requires thick mask layers resulting in poor quality inclined sidewalls of a laser diode. Metal films are also a bad choice due to redeposition of ion-sputtered metal particles on the etched surface and the difficulty in making a metal mask with smooth edges required for laser facet processing. However, SiO_2 etch mask fabrication also needs to be optimized for smooth and anisotropic etching of III-nitrides. Wet etching, typically used for SiO_2, is not appropriate for laser processing due to the undercut sidewall profile found in etched features and losses in the critical dimensions caused by the isotropic character of the etching. Thereby, plasma processing is mainly employed for SiO_2 etch mask fabrication with photoresist commonly used as a mask. The etching is usually conducted in fluorocarbon-containing plasmas, which readily etch SiO_2 and do not significantly react with the photoresist. However, under strong plasma conditions, the photoresist also erodes at fairly rapid rates. The erosion of the photoresist can be detrimental to the image size control, anisotropic etch profile, smoothness of sidewalls, and achievable etching depth in SiO_2. Typically, a resist loss of more than 20% during processing can lead to significant overcut of the pattern sidewalls.[95] Thereby, the selectivity of SiO_2 over photoresist is one of the determinative parameters of plasma etching. This section presents our results on the selective etching of SiO_2 over Shipley 1813 photoresist in a CHF_3 RIE-generated plasma. The influence of the RIE parameters, such as process pressure, RF power, dc-bias, and etching time on SiO_2 etching rate and selectivity of the SiO_2 over the photoresist is presented and discussed. The optimized RIE process resulted in smooth vertical sidewalls and in reproducible etching rates independent of processing time.

4.4.2 Literature background on SiO_2 plasma etching

A number of papers have been published on plasma etching of SiO_2 in fluorocarbon-based plasmas.[96, 97, 98, 99, 100, 101, 102, 103, 104, 105] Schaepkens *et al.* recently published a review of SiO_2 etching in ICP fluorocarbon plasmas. It was shown that the SiO_2 etching is strongly affected by the deposition and etching of a fluorocarbon film produced by the plasma discharge. Both the fluorocarbon deposition and etching were found to be dependent on feed gas chemistry. Briefly, the deposition of fluorocarbon takes place under low ion bombarding energy (less than about -35eV, -65eV, -75eV, -125eV for C_2F_6, CHF_3, C_3F_6, and C_3F_6/H_2, respectively). At the conditions where the fluorocarbon etching takes place, substrate materials, such as SiO_2, Si_3N_4, or Si, can also be etched. Once the fluorocarbon film is thin enough that some of the ions bombardment energy and fluorine radical atoms are consumed by etching of the substrate material instead of the fluorocarbon film, the fluorocarbon etching rate is reduced. At this point steady-state conditions are reached, when the fluorocarbon etching and fluorocarbon deposition rates are in a balance.[98] The thickness of a steady-state fluorocarbon layer formed on SiO_2 at low polymerizing conditions is relatively independent of the process parameters and is less than 1.5 nm.

Schaepkens *et al.*[99] also found that the fluorocarbon deposition rate strongly decreased with increasing aspect ratio (ratio of feature depth to width) in the range of 0.8–

2.0 in an CHF_3 ICP-generated plasma, where photoresist was used as a mask. This was attributed to the reduction in arrival of neutral deposition precursor due to shadowing. In contrast, the etching rate of SiO_2 was relatively constant. However, when silicon was used as an etch mask, the SiO_2 etching rate was found to decrease rapidly for an aspect ratio larger than 2.0. This was attributed to differential charging, which occurred as a result of the difference in angular distribution for ions and electrons. The ion angular distribution is highly anisotropic, whereas the electron angular distribution is nearly isotropic. Thus, the electrons mainly arrive at the surface near the top of features and do not reach the bottom, whereas the ions reach the bottom. As a result, the ion flux to the bottom of the features is reduced and the etching rate of SiO_2 decreases.

Chu *et al.* investigated the influence of substrate temperature on the etching rate of SiO_2 in a $C_4F_8/CO/O_2/Ar$ ICP-generated plasma. The etching rate of blanket SiO_2 increased slightly from -20 to +50 °C. This was attributed to a decrease in the steady-state fluorocarbon film thickness due to the sticking probability of polymer precursors becoming lower with temperature. On the other hand, the etching rate in 200–500 nm holes decreased with increasing temperature. Furthermore, the retardation in the etching rate at high temperature was more severe for smaller diameters. This was attributed to the transport of neutral polymer precursors into the holes and their polymerization on the bottom. The decreased sticking probability on the sidewalls of the holes leads to an increase in a number of polymer precursors, which can reach the bottom of the holes. Additionally, the etching rate of a photoresist mask was found to increase significantly with temperature. The hydrocarbon decomposed from the resist can also be transferred into the contact holes and can polymerize on the bottom. The increased thickness of the polymerized layer in the holes results in a drop in the SiO_2 etching rate.

Chu *et al.* proposed several methods to lower the photoresist etching rate and, hence, to increase the selectivity of SiO_2 over resist. These methods were designed to maximize the thickness of the steady-state fluorocarbon polymer in order to control the etching rate of the photoresist. It was found that gas chemistry of fluorocarbon plasmas has a significant impact on the selectivity. The authors reported that hydrofluorocarbon (such as CHF_3 or CH_2F_2) or fluorocarbon gases with high C/F ratio (such as C_2F_4 or C_3F_6) form thicker polymeric films on wafers protecting the surface from ion bombardment. However, it may also lead to a decrease in the etching rate of SiO_2 for high-aspect ratio features.

Li *et al.* added Ar to a C_4F_6 and a C_4F_8 ICP-generated plasma in order to increase the SiO_2 etching rate. The etching rate of SiO_2, Si, and photoresist increased up to 60% Ar and then decreased as the Ar percentage was further increased. This was attributed to a decrease in the thickness of a steady-state fluorocarbon layer when Ar was added to the plasma chemistry. When more than 60% Ar was added to the fluorocarbon gas, the SiO_2 etching rate was apparently limited by a reduced fluorocarbon gas flow. It was also shown that the etching rates were higher for C_4F_8 chemistry compared to C_4F_6 at the same etching conditions due to a higher F/C ratio. However, adding Ar to C_4F_6 enabled SiO_2 etching with a higher selectivity over photoresist or Si in comparison to C_4F_8/Ar.

Rueger *et al.* investigated the SiO_2 etching rate in a CHF_3 ICP-generated plasma as a function of process pressure and ICP power. The etching rate showed an increasing trend as a function of the inductive power, even though the oxide etch yield (atoms/ion) was inversely proportional to the power. Additionally, the etch yield was found to be strongly dependent on the pressure at ICP powers below 600 W where the plasma takes on the characteristics of a conventional capacitively-coupled RIE system. In this regime the efficiency of ions significantly decreased with increasing pressure. In contrast, in the inductively-coupled regime (>600 W), the efficiency was directly proportional to the pressure.

Gaboriau *et al.* studied the SiO_2 etching rate in CF_4, C_2F_6, and CHF_3 ICP-generated plasmas as a function of process pressure and ICP power. The etching rate linearly increased with increasing ICP power and with decreasing pressure. This was attributed to variations in the ion flux to the surface, as it was confirmed by Langmuir probe measurements. The authors also added CH_4 and H_2 to C_2F_6 chemistry in order to improve the selectivity of SiO_2 over Si. However, the oxide etching rate slowly decreased, which was attributed to an increase in the (C+H)/F ratio on the surface due to atomic hydrogen scavenging atomic fluorine in the plasma discharge forming HF. The authors also reported that the SiO_2 etching rate was the highest for C_2F_6 and the lowest for a CHF_3 plasma at similar etching conditions.

4.4.3 Experimental

A 1.4 μm-thick SiO_2 layer was deposited on GaN samples by ion beam sputtering, and coated with carbon-based Shipley 1813S photoresist of thickness 1.4 μm. After photolithography via conventional flood exposure, the SiO_2 was patterned using RIE etching with a CHF_3 plasma in a Oxford PlasmaLab 80 ICP reactor. All samples were mounted on a graphite coverplate, which covered an anodized aluminium cathode. Energetic ion bombardment was provided by superimposing a RF bias (13.56 MHz) on the cathode. After etching the photoresist was stripped away using Shipley Remover 1165 in a hot bath at 60 °C. Etching rates were calculated from the depth of etched features measured with a stylus profilometer before and after the photoresist mask was removed. Surface morphology, anisotropy, and sidewall undercutting were evaluated using a scanning electron microscope (SEM) at an angle of 30° with the surface.

4.4.4 Results and discussion

The construction of our ICP system did not allow using an ICP plasma source for the experiments due to the absence of proper thermal contact between the water-cooled cathode and the samples separated with a graphite coverplate. It was previously found that using the ICP source results in a high surface temperature that induces the photoresist to melt and erode very fast. Figure 4.31 shows a SEM image of a resist mask after 2 min etching at 300 W ICP power, 30 W RF power corresponding to dc-bias of -(70–80) V, 10 mTorr pressure, 35 sccm/10 sccm CHF_3/Ar gas flow, and 10 °C cathode temperature. In all probability, the reason for the serious mask degradation was an exothermic reaction between SiO_2 and fluorine and also heating induced by the energetic ions. As a result, considerable heating of the substrate occurred at a high reaction rate and the photoresist melted.

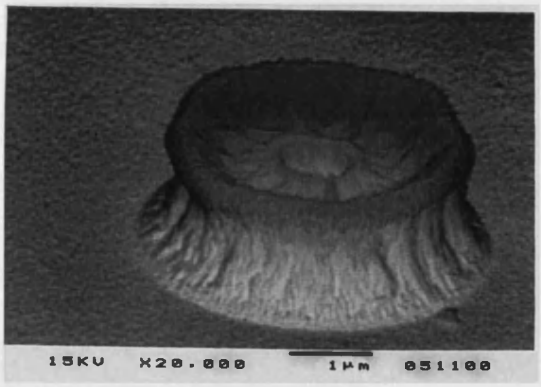

Fig. 4.31. SEM image of a photoresist mask after etching using an ICP source.

Influence of pressure

The influence of the process pressure on the etching rates of SiO_2 and photoresist is presented in Fig. 4.32. The process parameters used were as follows: 25 sccm CHF_3 flow, 100 W RF power, and 20 °C cathode temperature. As can be seen, the dc-bias was almost

constant during the experiments. Correspondingly, the ion flux to the surface and the ion energy were independent of the pressure in this range (2–20 mTorr). However, the etching rates were significantly higher at pressures lower than 5 mTorr. These results are consistent with those reported by Rueger *et al.* They found that in the capacitively-coupled regime (low ICP power) the efficiency of ions significantly decreased with increasing pressure from 6 to 20 mTorr. As a result, the etch yield (atoms/ion) dropped and the SiO_2 etching rate decreased. The initial slight drop from 4 to 2 mTorr was probably caused by a reactive

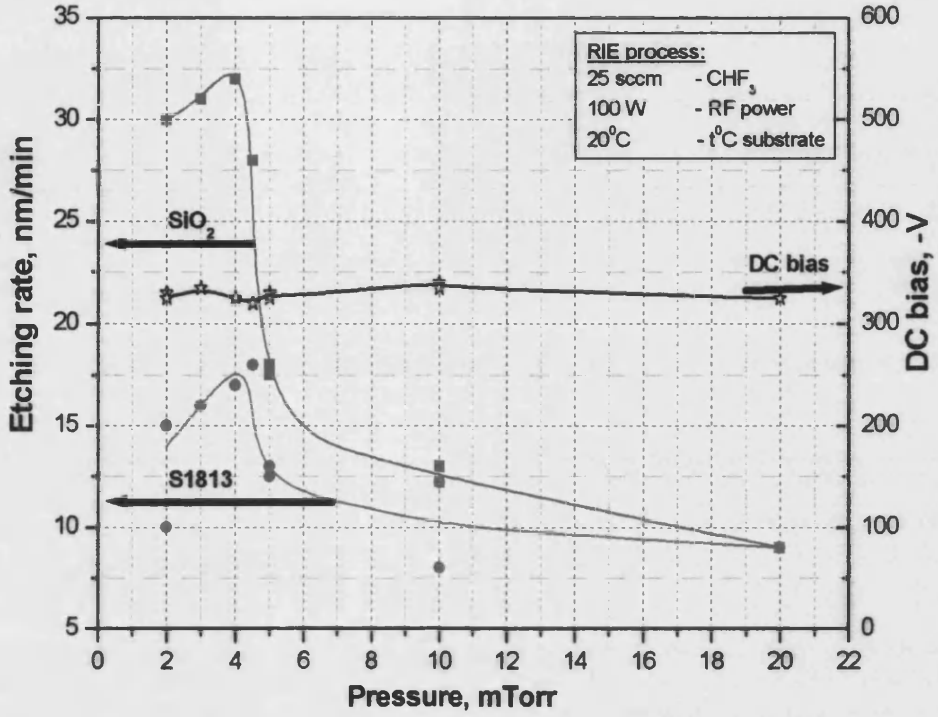

Fig. 4.32. Etch rates of SiO_2 and photoresist as a function of process pressure.

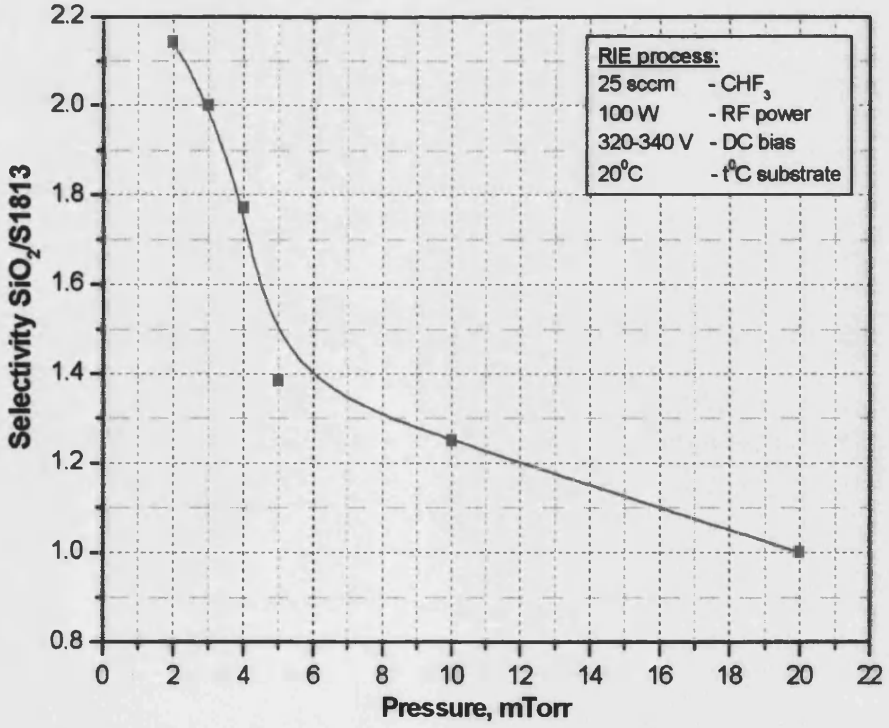

Fig. 4.33. Selectivity of SiO_2 over photoresist as a function of process pressure.

limited regime at low pressures where the active species are pumped away from the surface before they could react. The selectivity of SiO_2 over the photoresist as a function of the process pressure is presented in Fig. 4.33. As can be seen, the selectivity also decreased with increasing pressure.

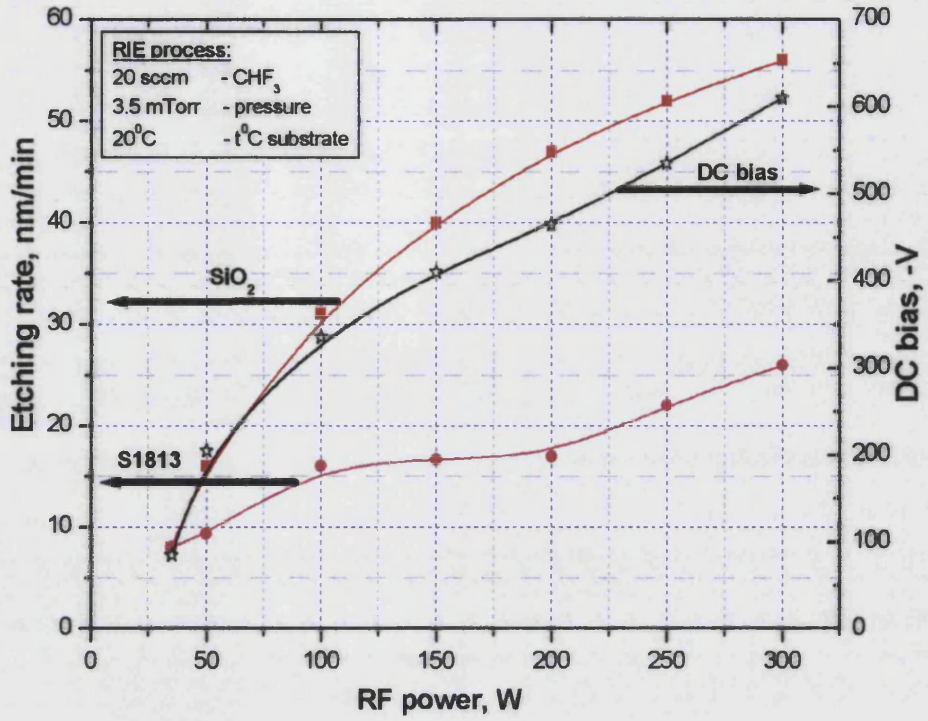

Fig. 4.34. Etch rates of SiO_2 and photoresist as a function of RF power.

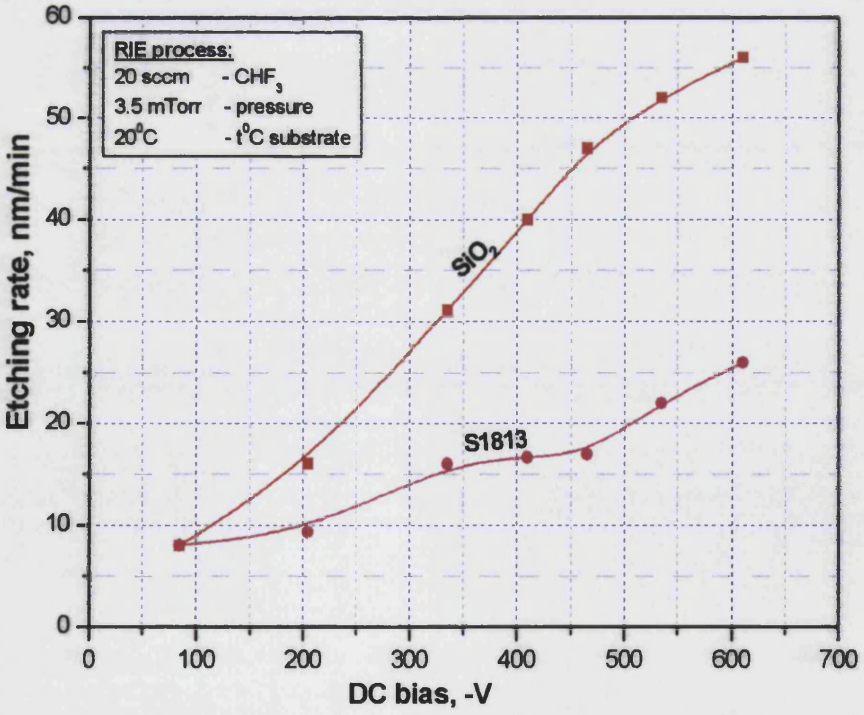

Fig. 4.35. Etch rates of SiO_2 and photoresist as a function of dc-bias.

Influence of RF power (dc-bias)

The influence of RF power on the etching rates of SiO_2 and photoresist is shown in Fig. 4.34. The process parameters used were as follows: 20 sccm CHF_3 flow, 3.5 mTorr pressure, 20 °C cathode temperature. The process pressure was chosen from the first series of the experiments and corresponded to the maximal etching rate for SiO_2. As can be seen, the etching rates increased with increasing RF power. Figure 4.35 shows that the etching rates were nearly linearly proportional to the dc-bias voltage. This probably indicates that the increase in the etching rates for both SiO_2 and the photoresist was mainly caused by an

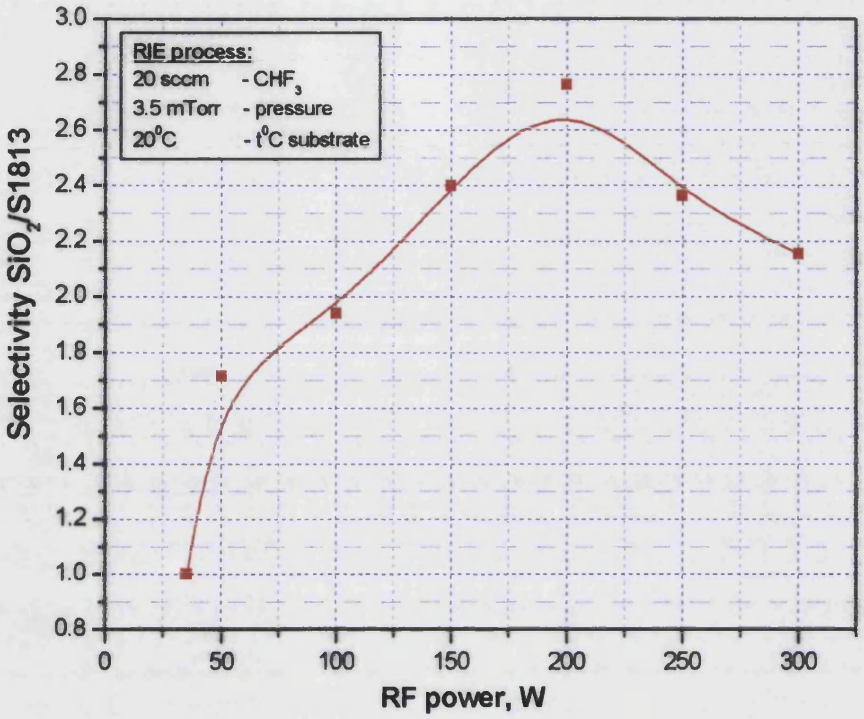

Fig. 4.36. Selectivity of SiO_2 over photoresist as a function of RF power.

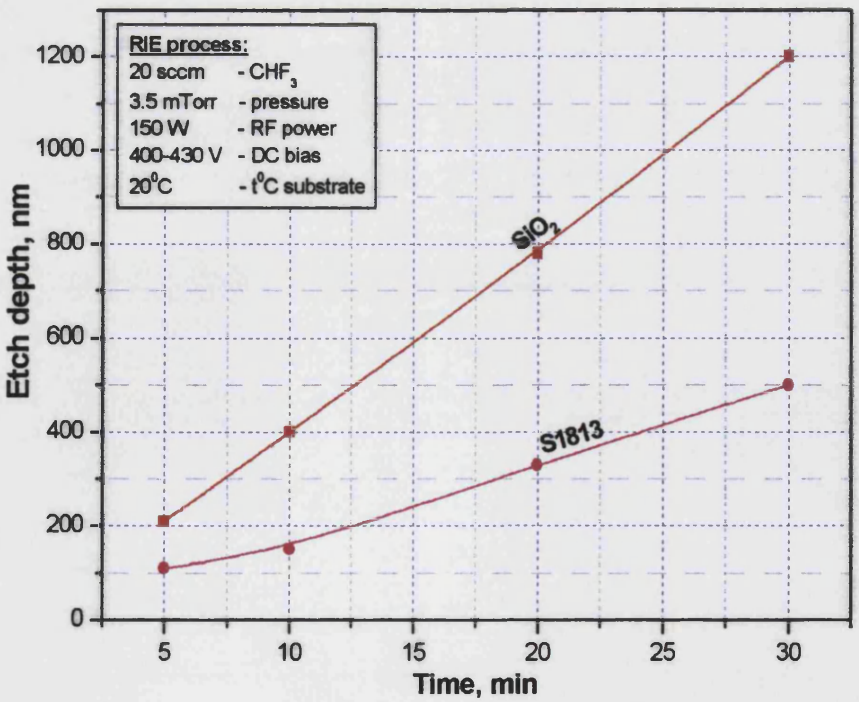

Fig. 4.37. Etch depth of SiO_2 and photoresist as a function of etching time.

increase in the energy of the ions. However, the dependence for the photoresist was not as strong as for SiO_2. This resulted in increased selectivity of SiO_2 over the resist at higher RF power as shown in Fig. 4.36. The maximal selectivity was obtained at 200 W RF power corresponding to -465 V dc-bias.

Influence of etching time

During plasma processing the temperature of the etched surface may be increased due to an exothermic reaction between SiO_2 and fluorine and poor thermal contact with the water-cooled electrode. This may lead to an increased SiO_2 etching rate with increasing etching time due to a decrease in the steady-state fluorocarbon film thickness with higher substrate temperatures. Additionally, the etching rate of the photoresist mask significantly increases with the temperature. All this can result in poor reproducibility of the etching rates and reduced selectivity of SiO_2 over the photoresist.

A series of experiments was conducted to determine the influence of processing time on etching of SiO_2 and the photoresist. The process parameters used were as follows: 20 sccm CHF_3 flow, 3.5 mTorr pressure, 150 W RF power corresponding to dc-bias of -(400–430) V, and 20 °C cathode temperature. The results are presented in Fig. 4.37. As can be seen from the linearity of the data sets, the etching rates of both SiO_2 and the photoresist were not affected by the processing time. This probably indicates that the substrate temperature was almost constant during the etching. Figure 4.38 shows a SEM image of the SiO_2 profile formed by etching at these conditions. The etch profile was slightly sloped due to the sloped profile of the photoresist mask. However, the etch sidewalls were reasonably smooth and the etch surface was clean from any contamination.

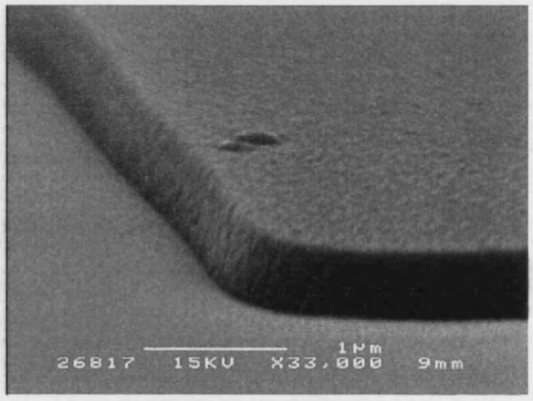

Fig. 4.38. SEM image of SiO_2 profile after the etching.

4.4.5 Conclusion

The influence of RIE parameters (process pressure, RF power, dc-bias, and etching time) on the SiO_2 etching rate and selectivity of SiO_2 over Shipley 1813S photoresist in CHF_3 plasma was investigated. It was found that the SiO_2 etching rate and the selectivity can be significantly increased by using low pressures and intermediate RF power. The optimized RIE process resulted in reproducible etching rates regardless of processing time. The etch sidewalls were reasonably smooth and vertical and the etch surface was clean from any residual contamination. Thereby, the developed process can be successfully employed for the fabrication of an etch mask suitable for III-nitride laser diode processing.

4.5 Influence of cathode material and $SiCl_4$ gas on ICP etching of Al-containing layers with Cl_2/Ar plasma

4.5.1 Introduction

Cl_2-based plasmas are commonly used for dry etching III-nitride semiconductors due to their low etch damage, high etching rates, and superior uniformity. However, rough morphology of the surface with grass and nanotips has been observed after etching by several research groups.[38, 106, 107, 108] The mechanism of GaN whiskers formed during photoelectrochemical (PEC) wet etching is well-established to be due to threading dislocations in *n*-GaN layers.[109, 110, 111, 112, 113] However, there are only a few reports on the formation of GaN nanotips by plasma etching techniques. Yoshida *et al.* reported that a GaN self-organized nanotip structure was formed during RIE etching of GaN with Cl_2 plasma. The authors found that the nanotip structure depended on the direction of ion injection, implying that nanotip formation was not caused by threading dislocations in GaN layers. The model of GaN nanotip formation during RIE etching was proposed as redeposition of SiO_2 particles on the GaN surface due to the quartz cathode coverplate. The nanotips were attributed to nanometer-scale SiO_2 particles with slower etching rates than GaN. In contrast, a smooth etched surface with no nanotips was obtained when a Si wafer or a Ge plate were located between the GaN samples and the quartz coverplate. The authors suggested that Si and Ge are so reactive with Cl_2 plasma that the masking effect disappeared. Optical emission spectroscopy (OES) revealed strong optical emission lines related to $SiCl_x^+$ and $GeCl_x^+$ ions with the Si and Ge plates, respectively. It was proposed that heavy $SiCl_x^+$ and $GeCl_x^+$ ions play an important role in obtaining a smooth GaN etched surface. However, this effect was observed at relatively high pressures (15–150 mTorr) where redeposition of etch products could take place. In our experiments on ICP etching of GaN in Cl_2/Ar plasmas with a quartz cathode coverplate nanotips were observed at these pressures as well, but at pressure between 3 and 5 mTorr the surface was smooth. Yu *et al.* reported similar results and attributed them to the crystalline quality of epitaxially grown GaN material and the ability of the ICP process with Cl_2-based plasmas to dissociate GaN bonding. The authors observed an uniform etched surface with no nanotips at 2.5 mTorr pressure. As the chamber pressure was increased to 10 mTorr, GaN nanotips appeared. The density of the nanotips significantly increased, as the chamber pressure was further increased to 20 and 30 mTorr. The increased density of the nanotips with increasing chamber pressure was attributed to degradation of the ICP dissociation ability at high process pressures. Nevertheless, it could also be caused by either poor desorption of GaN etch products at high pressures or SiO_2 micromasking effects if the authors used a quartz coverplate. Lee *et al.* also observed the formation of nanotips on the etched GaN surface after ICP etching with Cl_2/Ar plasma at 10 mTorr and explained it by a micromasking effect of a SiO_2 mask, which was sputtered by energetic ions.

Slow etching rates and a rough grassy morphology of the etched surface have been reported for $Al_xGa_{1-x}N$ layers by several research groups. Zhu *et al.*[114] observed slow unstable etching rates for AlN and AlGaN layers compared to GaN during ICP etching with Cl_2/Ar. The authors found that AlN did not etch for the first 45 s, after which a constant etching rate of 200 nm/min was established. This delay was attributed to an aluminum oxide formed on the surface. Buttari *et al.*[115] reported an etch duration dependence for the etching rate of AlGaN and also attributed it to the formation of an aluminum oxide on the surface. Basak *et al.*[44, 116] observed selectivity of 3.0 between GaN and $Al_{0.15}Ga_{0.85}N$ in RIE etching with a Cl_2/Ar plasma, while the selectivity was decreased to 1.0 by adding 10% CH_4. Wu *et al.*[117] observed a rough etched surface after ICP etching of a $Al_{0.28}Ga_{0.72}N$/GaN heterostructure with Cl_2/Ar and Cl_2/H_2. In contrast, the surface was very smooth after etching with a BCl_3/Cl_2 plasma. The different surface morphology was

explained by different oxide formation levels on AlGaN layers during plasma processing. AES analysis confirmed that the morphology of the etched surface was substantially related to the remaining oxygen on the surface. A decrease in oxygen surface fraction using the BCl_3/Cl_2 plasma was attributed to a reaction of oxygen with BCl_3 forming $B_3Cl_3O_3$ trimers, a chemically inert gas which can be easily pumped out from a system.[118] Thus, BCl_3 scavenges oxygen in a chamber and prevents it from interfering with AlGaN etching with the formation of surface aluminum oxides. At the same time, several research groups have reported that etching rates in Cl_2 plasmas for Al-containing layers were comparable to GaN etching rates.[2, 22] Discrepancy of the published results seems to be related to different process chamber constructions.

Our initial experiments showed that etching of Al-containing layers and super-lattice (SL) Ga/AlGaN structures, even with a very low Al content, always resulted in extremely slow etching rates and very rough etched surfaces and sidewalls. This seriously hindered progress in laser diode development due to the impossibility of forming any proper contacts to the etched surface and due to an excessively thick mask required for sufficient etching depth. Thereby, the initial aim of experiments was to optimize the etching conditions for laser diode fabrication. During the experiments it was revealed that the coverplate cathode material has a great influence on the etching of Al-containing layers. In this section, the impact of different coverplate materials, such as an anodized aluminum cathode with no coverplate, quartz coverplate, quartz coverplate covered with a 6-inch Si wafer, graphite coverplate, and graphite coverplate covered with a 6-inch Si wafer on etching rates, etch sidewalls/surface morphology of GaN, $Al_xGa_{1-x}N$ (x=0.01 and 0.1) and a laser structure containing SL of $Al_{0.1}Ga_{0.9}N/GaN$ in ICP etching with a Cl_2/Ar plasma is considered. The etching rates and sidewalls/surface morphology were also estimated in the etching with a $SiCl_4/Cl_2/Ar$ plasma at different gas mixtures (0–100% $SiCl_4$) in the case of the quartz coverplate only. This study has also been recently published ["Influence of cathode material and $SiCl_4$ gas on inductively coupled plasma etching of AlGaN layers with Cl_2/Ar plasma" E. Zhirnov, S. Stepanov, W. N. Wang, Y. G. Shreter, D. V. Takhin, and N. I. Bochkareva, *J. Vac. Sci. Technol. A* 22, 2336 (2004).]. In summary, it was found that the graphite coverplate and the Si wafer on top of the quartz coverplate greatly improved the etching of Al-containing layers resulting in fast etching rates, smooth vertical etch sidewalls, a smooth contamination-free surface, and high selectivity over a SiO_2 etch mask.

4.5.2 Experimental

Bulk 2 μm-thick GaN, $Al_{0.01}Ga_{0.99}N$, $Al_{0.1}Ga_{0.9}N$, and a laser structure containing SL of $Al_{0.1}Ga_{0.9}N/GaN$ were grown on Al_2O_3 substrates by metallorganic chemical vapor deposition (MOCVD). The mole fraction of Al in the AlGaN layers was determined by X-ray diffraction (XRD) measurements. 300 nm of SiO_2 was deposited on samples as a mask layer by plasma enhanced chemical vapor deposition (PECVD), and coated with carbon-based Shipley 1813S photoresist of thickness 1.3 μm. After photolithography via conventional flood exposure, photoresist descumming etching with O_2 plasma was performed in an ICP system (Oxford PlasmaLab 80) to remove thin residual layers of the photoresist and other organic films following resist development and hard bake.[119] All samples were mounted onto a graphite coverplate, which covered an anodized aluminium cathode. Energetic ion bombardment was provided by superimposing RF bias (13.56 MHz) to the samples. ICP process parameters used were as follows: 20 mTorr pressure, 40 sccm O_2 flow, 250 W ICP power, 100 W RF power, -(320–330) V dc-bias, 20 °C cathode temperature, 2 min process time. The thickness of the photoresist after the descumming was around 900 nm. A SiO_2 mask was patterned by RIE etching with CHF_3 plasma in the

same reactor using a process described in details in section 4.4 of this chapter. The RIE process parameters used were: 3.5 mTorr pressure, 20 sccm CHF_3 flow, 150 W RF power, -(390–405) V dc-bias, 20 °C cathode temperature, 14 min process time. After etching the photoresist was stripped away using Shipley Remover 1165 in a hot bath at 60 °C. H_2SO_4:H_2O_2 (1:1) solution was used to remove any organic contamination following the resist removal. HCl:H_2O (1:1) solution was used for 5 min to remove an oxide layer from the surface before GaN etching.[120]

An Oxford PlasmaLab 80 ICP reactor was used for the III-nitride etching experiments. In the first series of experiments, samples were mounted onto the 10-inch anodized aluminum cathode covered with no coverplate and with different coverplates, such as quartz, graphite, quartz or graphite with a 6-inch Si wafer located between the coverplates and the samples. All the experiments were conducted after the background pressure was reduced to less than 7×10^{-6} Torr. The ICP process parameters used were: 4.0 mTorr pressure, 15 sccm Cl_2 flow, 4 sccm Ar flow, 450 W ICP power, 150 W RF power, 20 °C cathode temperature. The dc-bias voltage measured at these conditions with no coverplate was -(300–340) V. The etching time was varied from 2 to 5 min depending on the etching rate of the SiO_2 mask. In the second series of experiments, samples were mounted onto the 10-inch cathode covered with the quartz coverplate only. $SiCl_4$ was added to the Cl_2/Ar gas mixture in order to examine its effect on the etching rates and etch surface morphology. The background pressure reached 9×10^{-6} Torr prior to the etching experiments. The ICP parameters used were: 4.0 mTorr pressure, 15 sccm (Cl_2 + $SiCl_4$) flow, 4 sccm Ar flow, 450 W ICP power, 150 W RF power, 20 °C cathode temperature, 6 min process time. The dc-bias voltage measured at these conditions with no coverplate was -(240–260) V, relatively independent of Cl_2/$SiCl_4$ ratio. The dc-bias voltage and etching rates were slightly lower than those in the first series of experiments under the same process parameters due to a difference in the chamber conditions. Shul *et al.* also observed a similar difference after the reconstruction of the process chamber.

After completion of plasma etching the SiO_2 mask was stripped away using a buffered-HF (1:4) solution. The etching rates were calculated from the depth of etched features measured with a stylus profilometer before and after the SiO_2 mask was removed. The surface morphology, anisotropy, and sidewall undercutting were evaluated using a scanning electron microscope (SEM) at an angle of 30° with the surface. The root-mean-square (RMS) surface roughness was quantified using an atomic force microscope (AFM) operating in contact mode with Si tips. The RMS roughness for unetched samples is shown in Table 4-2.

4.5.3 Results and discussion

Influence of coverplate material

The results of experiments with different coverplate materials are summarized in Table 4-2. As can be seen, the etching rate and RMS surface roughness for GaN were relatively independent of the coverplate used. In contrast, for Al-containing layers the etching rate and the RMS roughness changed with coverplate material dramatically.

Figure 4.41 demonstrates SEM images of samples etched with no coverplate for 3 min, whilst AFM surface images are presented in Fig. 4.47. As can be seen, the GaN etch surface was relatively smooth except for a small amount of nanotips, which were probably caused by redeposition of Al from the cathode. In contrast, the etched surface of Al-containing layers was very grassy. Table 4-2 shows a slight difference in etching rates for GaN and AlGaN layers which is probably related to a difference in bond energies (8.92 eV for GaN and 11.52 eV for AlN). However, the grassy surface observed for the

Table 4-2. Results of experiments with coverplate material.

Sample	Etching rate (nm/min)	RMS roughness (nm)
Unetched		
GaN	-	0.355
AlGaN (1% Al)	-	0.230
AlGaN (10% Al)	-	0.245
LD	-	0.417
Al_2O_3 cathode (no coverplate)		
GaN	283	0.326
AlGaN (1% Al)	243	28
AlGaN (10% Al)	227	18
LD	287	0.496
SiO_2 mask	30	
Quartz coverplate		
GaN	280	0.630
AlGaN (1% Al)	80	12
AlGaN (10% Al)	52	7
LD	80	16
SiO_2 mask	22	
Quartz coverplate + 6-inch Si wafer		
GaN	275	0.769
AlGaN (1% Al)	300	1.061
AlGaN (10% Al)	288	0.583
LD	263	1.230
SiO_2 mask	37	
Graphite coverplate		
GaN	230	0.398
AlGaN (1% Al)	275	1.114
AlGaN (10% Al)	275	0.514
LD	250	0.458
SiO_2 mask	65	
Graphite coverplate + 6-inch Si wafer		
GaN	335	1.113
AlGaN (1% Al)	320	1.581
AlGaN (10% Al)	320	1.725
LD	320	0.929
SiO_2 mask	65	

Al-containing layers cannot be explained by this factor due to the fact that the largest RMS roughness was observed for an AlGaN layer containing only 1% Al, which had an etching rate very close to that of GaN. In contrast, for a AlGaN layer containing 10% Al the RMS roughness was less, in spite of the fact that the etching rate was slower. This cannot be ascribed to the etch products as well, since Cl-based plasmas form $GaCl_3$ and $AlCl_3$, which are volatile at 201 °C and 183 °C respectively.[1] Presumably the grassy surface observed in our case was caused by the presence of water vapors or background oxygen in a process chamber. Atomic oxygen generated at the beginning of a plasma discharge could readily react with III-nitrides forming a thin layer of oxide on the surface. Unfortunately chlorine is a very poor etcher of III-nitride oxides. Once the oxide layer is formed on a surface, etching is limited before the surface oxide is broken. The bond strength for Al–O (21.2 eV/atom) is larger than that for Ga–O (14.7 eV/atom). Thereby the oxide on Al-containing layers is more resistant to ion bombardment. Furthermore, AlGaN was found to be more reactive with oxygen compared to GaN forming a thicker oxide layer. It is well known that

a small amount of oxygen, added to Cl-based plasmas, significantly increases the selectivity of GaN over AlGaN due to the aluminum oxide produced.[42, 115, 121] The thickness of the aluminum oxide layer is probably irregular and initially causes a rough etched morphology before the surface is completely free from the oxide and stable etching rate is achieved. Larger RMS roughness in the case of AlGaN with lower Al content can be caused by larger variations in surface oxide thickness compared to a thicker and more uniform oxide layer on AlGaN with higher Al content. This model is supported by the fact that grass was eliminated in the case of a laser structure also containing AlGaN layers in the super-lattices. A GaN contact layer on the top of the structure probably prevented the atomic oxygen, produced at the beginning of a plasma discharge, to react with Al-containing layers. The nanotips on the LD etched surface could be caused by redeposition of Al from the cathode. However, it is not quite clear why the nanotip density was higher than for the GaN layer.

Wu *et al.* also observed a very rough surface after etching a AlGaN(28% Al)/GaN heterostructure with Cl_2/Ar and Cl_2/H_2 ICP plasmas. In contrast, the etched surface of GaN was very smooth under these conditions. Thereby, roughening of the etched AlGaN/GaN heterostructure was attributed to etching of the top AlGaN layer. The oxidation of this layer was suggested to greatly influence subsequent etching of the AlGaN/GaN heterostructure resulting in a rough etched surface morphology. AES analysis revealed a high atomic fraction of oxygen at the surface after the etching, which was 32% and 24% for the samples etched in the Cl_2/H_2 and Cl_2/Ar plasma, respectively. The authors also found that the etched surface was very smooth and the fraction of oxygen was significantly reduced (13%) when BCl_3 gas was added to a Cl_2 plasma. These results were attributed to the ability of BCl_3 to scavenge oxygen in a chamber and to prevent it from interfering with AlGaN etching with the formation of aluminum oxides. The atomic oxygen reacts with BCl_3 forming $B_xCl_yO_z$ trimers, a chemically inert gas which can be easily pumped out from the system. Juang *et al.* also noticed that BCl_3 reacts with oxygen in a plasma discharge and oxidizes forming B_2O_3 on chamber sidewalls. They also mentioned that an aluminum surface oxide can be easily removed in a BCl_3 plasma. Similar observations were made by Smolinsky *et al.*[122] Buttari *et al.* used a short exposure to a low power BCl_3 plasma at the beginning of an etching process in a more effective Cl_2 plasma to remove residual oxidizing agents in a process chamber and to reduce native surface oxides. As a result, equal etching rates were obtained for GaN and $Al_{0.35}Ga_{0.65}N$ layers. It is important to note that background oxygen in a process chamber can also be significantly reduced by using a load-lock system.[2, 123]

Figure 4.42 shows SEM images of samples etched with a quartz cathode coverplate for 5 min, whilst AFM surface images are presented in Fig. 4.48. As can be seen, a significant amount of nanotips was produced on the GaN etched surface. In all probability this was caused by redeposition of nanometer-scale SiO_2 particles from the coverplate. The model of GaN nanotip formation during plasma etching was proposed by Urushido *et al.*[106, 107] and is considered above. More importantly, a very rough grassy surface was observed for the Al-containing layers and for the laser structure. Furthermore, the etching rates of these layers, even with a low aluminum content, were much slower than that for GaN (Table 4-2). The reason for this seems to be the quartz coverplate. Buttari *et al.* also observed that AlGaN etching rates were significantly reduced when a SiO_2 coated coverplate was employed. The authors attributed this phenomenon to traces of oxygen introduced in a plasma discharge as a result of etching of coverplate material. Zhu *et al.* observed that AlN did not etch for the first 45 s, after which a constant etch rate of 200 nm/min was established. The authors mounted samples onto a silicon wafer coated on the processing side with SiO_2. Thereby, the delay in etching could also be caused by this SiO_2 coating until it was etched away. The influence of the quartz coverplate on an etching

process with Cl_2 plasmas may be understood from the research of Thomas *et al.*[124, 125, 126] The authors studied the etching of silicon in Cl_2-based plasmas. Samples were positioned on a quartz coverplate to prevent backsputtering of electrode material. Quadrupole mass spectrometry (QMS) measurements revealed a significant rise in O_2^+ during the etching suggesting that oxygen was liberated from quartz predominantly as molecular O_2. The authors concluded that SiO_2 reacted with the Cl_2 plasma producing $SiCl_x$ and O_2. Thereby etching in the Cl_2 plasma with the quartz coverplate causes a constant influx of oxygen forming a stable aluminium oxide on AlGaN surface. This oxide significantly reduces the etching rates as it has been observed for Cl_2/O_2 plasmas[42, 115, 121] and causes a grassy surface morphology. This model is supported by the fact that the surface of the LD structure was also grassy after the etching and the etching rate was also significantly reduced. This implies that oxygen was present in the process chamber constantly and not just at the beginning of the discharge as in the case when no coverplate was employed.

Figure 4.43 shows SEM images of samples etched with the quartz coverplate and a 6-inch Si wafer on the top of it for 4 min, whilst AFM surface images are presented in Fig. 4.49. As can be seen, no nanotips were observed on the surface, which was probably related to the protective role of the Si wafer for the redeposition of SiO_2 nano-particles from the quartz coverplate.[106, 107] More importantly, smooth etched surfaces and relatively equal etching rates were obtained for all the structures. As considered above, the presence of the quartz coverplate should result in a constant influx of oxygen during etching with a Cl_2 plasma. Nevertheless, the presence of the Si wafer eliminated this effect.

Urushido *et al.* employed optical emission spectroscopy (OES) to monitor emissions from a RIE Cl_2 plasma in a process chamber with either a quartz coverplate or with a Si coverplate. In the case of the quartz coverplate, as shown in Fig. 4.39, several broad lines from 195 to 315 nm of Cl^+ ions and a weak continuous spectrum from 400 to 650 nm of both molecular Cl_2 species and molecular Cl_2^+ ions were observed. Over 20 intense peaks from Cl radicals were also detected in the range from 720 to 950 nm. The Cl radicals and Cl^+ ions were suggested to be the main constituents in the chemical and physical components of plasma etching, respectively. As shown in Fig. 4.40, the emission spectrum was very different in the case of the Si coverplate. A number of lines from 220 to 288 nm of atomic Si and several strong broadband emissions from 300 to 450 nm, related to both molecular $SiCl_x$ species and molecular $SiCl_x^+$ ions, were detected. In our case a change in a plasma color from blue without the Si plate to bright violet after several seconds with the Si plate was visually observed as well. This probably implies a significant amount of $SiCl_x$ species and $SiCl_x^+$ ions generated in the plasma.

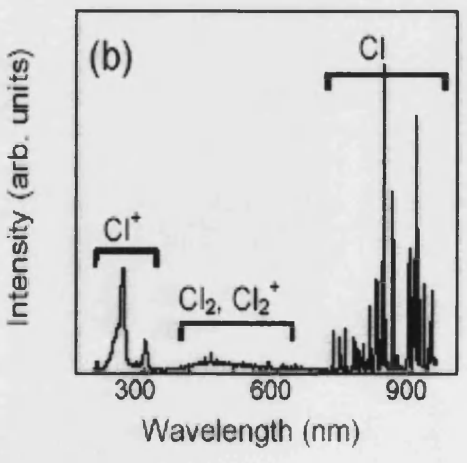

Fig. 4.39. Optical emission spectrum from the Cl_2 plasma with the quartz coverplate.

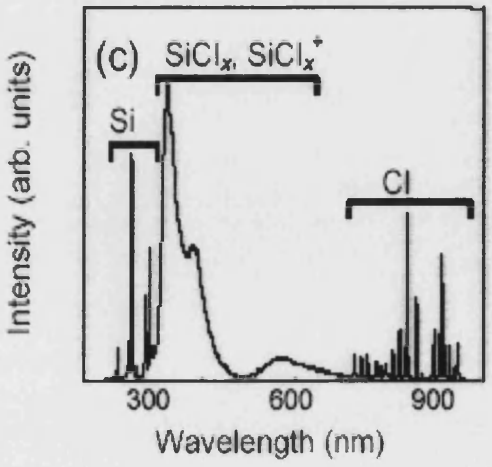

Fig. 4.40. Optical emission spectrum from the Cl_2 plasma with the Si coverplate.

Matsutani *et al.*[127, 128] observed a similar behavior in ICP plasma etching of InP with a Cl_2 plasma and with a Si wafer, located between the samples and a Al_2O_3 coverplate. Quadrupole mass spectroscopy (QMS) measurements revealed positive signals of Si^+, Cl^+, and $SiCl_x^+$ ions originated from the Si wafer, whereas Cl_2^+ signals were significantly reduced compared to those with the coverplate only. The authors found that the Cl_2 plasma with no Si wafer resulted in a grassy etch surface attributed to low volatile $InCl_x$ products. In contrast, using a Si wafer resulted in a smooth etch surface which was ascribed to the $InCl_x$ products sputtered away by heavy $SiCl_x^+$ ions. To avoid the effect of coverplates, an ECR-RIE process was conducted. A grassy surface was obtained in the case of Cl_2 plasma etching, while a $SiCl_4$ plasma gave a smooth mirror-like surface. The authors concluded that heavy $SiCl_x^+$ ions, either produced in a $SiCl_4$ plasma discharge or generated by a Si wafer in a Cl_2 plasma, are responsible for smooth etching of InP.

We believe that the $SiCl_x$ reactive radicals and $SiCl_x^+$ ions, produced in the Cl_2 plasma due to the presence of the Si wafer, play the same role as a BCl_3 plasma in scavenging oxygen in the process chamber and preventing it from interfering with the AlGaN etching. Thereby oxygen liberated from the quartz coverplate is consumed as a result of internal reactions in the plasma discharge. This model is supported by findings of Ullal *et al.*[129] on etching of Si in a Cl_2/O_2 plasma. The authors showed that $SiCl_x$ etch products, generated during the etching of Si, readily react with oxygen forming a silicon oxychloride film on the process chamber walls. In addition, the $SiCl_x^+$ ions may be very useful to remove native oxide layers due to their heavy mass, as considered above for low volatile $InCl_x$ products. As can be seen in Table 4.2, the etching rate of a SiO_2 mask was higher with the Si wafer than for the quartz coverplate alone, which could also be caused by the heavy ions. It is important to note that the presence of a thin native oxide layer on the Si wafer also causes rough grassy etching of Al-containing layers probably due to oxygen released from both this oxide and the quartz coverplate, and a low concentration of the $SiCl_x$ radicals and $SiCl_x^+$ ions until the oxide is removed. A second series of experiments with $SiCl_4$ gas added to the Cl_2 plasma with the quartz coverplate only was conducted to avoid the effect of the Si wafer, which could partially protect the quartz coverplate from reaction with the plasma.

Figure 4.44 shows SEM images of samples etched with a graphite coverplate for 4 min, whereas AFM surface images are presented in Fig. 4.50. As can be seen, ultra smooth etched surfaces and relatively equal etching rates were obtained for all the structures. The absence of quartz in the process and, hence, no oxygen influx during the etching was probably one of the reasons. Moreover, the grass observed for the AlGaN layers after etching with no coverplate was eliminated using the graphite coverplate. Hence it seems to be reasonable that graphite was effective in reducing water vapor and background oxygen in the process chamber and/or removing oxide layers on the samples. Additionally, no nanotips were detected on the surface implying that graphite does not induce redeposition micromasking as in the case of the Al_2O_3 cathode and SiO_2 coverplate. Pits observed after etching of the GaN sample were probably related to an exposed sapphire substrate due to the top GaN epilayer having been etched away.

We believe that the etch products of graphite etched in a Cl_2 plasma are CCl_x species. Similarly, Thomas *et al.*[124, 126] observed high QMS levels of CCl_3^+ and CCl_2^+ ions during erosion of carbon-based photoresist in a Cl_2 plasma. Presumably, these ions were present during etching with the graphite coverplate as well. The increased etching rate of a SiO_2 mask with the graphite coverplate is also evidence of the CCl_x species. Korman[130] reported that the etching rate of SiO_2 was much slower in a pure Cl_2 discharge compared to a Cl_2/CCl_4 discharge under the same process conditions. At the same time, the CCl_x^+ ions are well known to etch aluminum oxides and to scavenge oxygen and water vapors in a process chamber forming volatile oxycarbons.[122, 130, 131, 132] As a result, extremely smooth

surfaces and fast etching rates for the Al-containing layers were obtained. Unfortunately, a relatively low etch selectivity of III-nitrides over SiO_2 (about 4:1) with the graphite coverplate requires a thick etch mask for laser diode fabrication which may result in the degradation in anisotropy and sidewall smoothness of etched facets.

Figure 4.45 shows SEM images of samples etched with the graphite coverplate and a 6-inch Si wafer on the top of it for 2 min, whilst AFM surface images are presented in Fig. 4.51. In this case the positive effects of both the graphite coverplate and the Si wafer were expected. A smooth etched surface and equal etching rates were obtained for all the structures. The etching rates were maximal for the experiments with the coverplates, and the relatively low etch selectivity (5:1) of III-nitrides over SiO_2 is probably related to the ability of CCl_x^+ ions to etch the oxide mask.

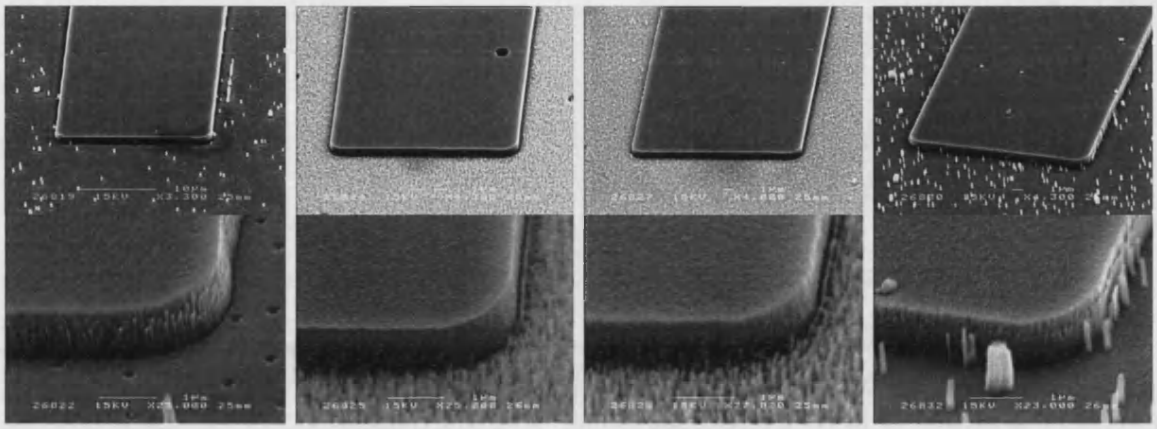

GaN AlGaN (1% Al) AlGaN (10% Al) LD

Fig. 4.41. SEM images of samples etched with no coverplate (after 3 min etch).

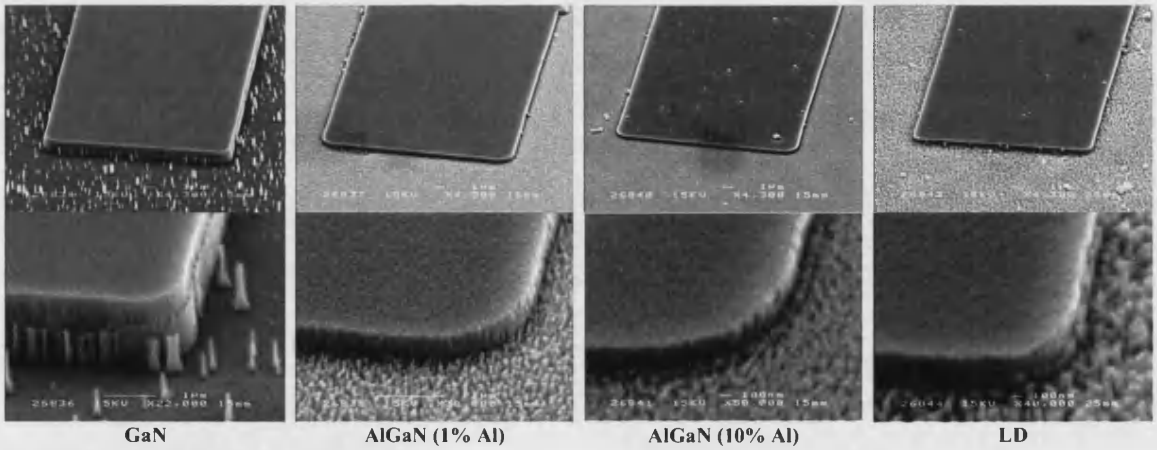

GaN AlGaN (1% Al) AlGaN (10% Al) LD

Fig. 4.42. SEM images of samples etched with a quartz coverplate (after 5 min etch).

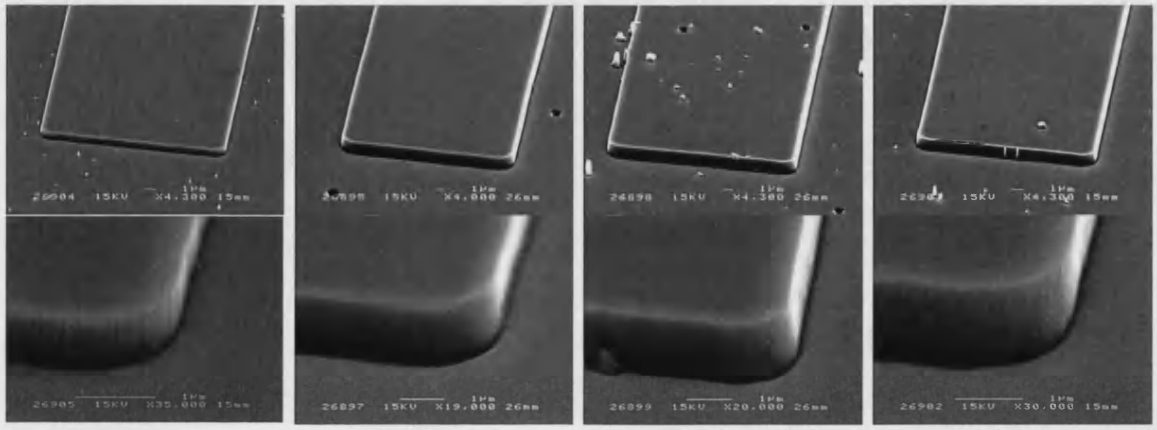

GaN AlGaN (1% Al) AlGaN (10% Al) LD

Fig. 4.43. SEM images of samples etched with a quartz coverplate and a 6-inch Si wafer (after 4 min etch).

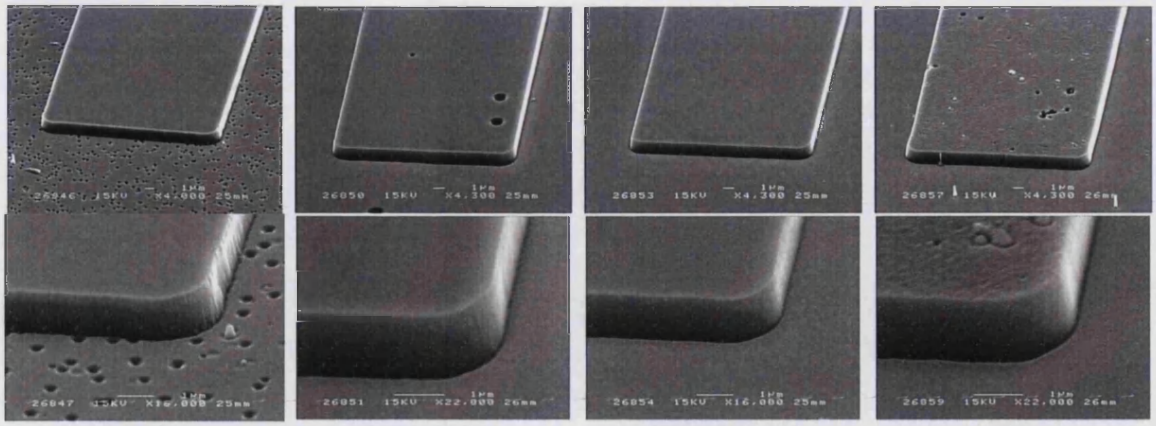

GaN AlGaN (1% Al) AlGaN (10% Al) LD

Fig. 4.44. SEM images of samples etched with a graphite coverplate (after 4 min etch).

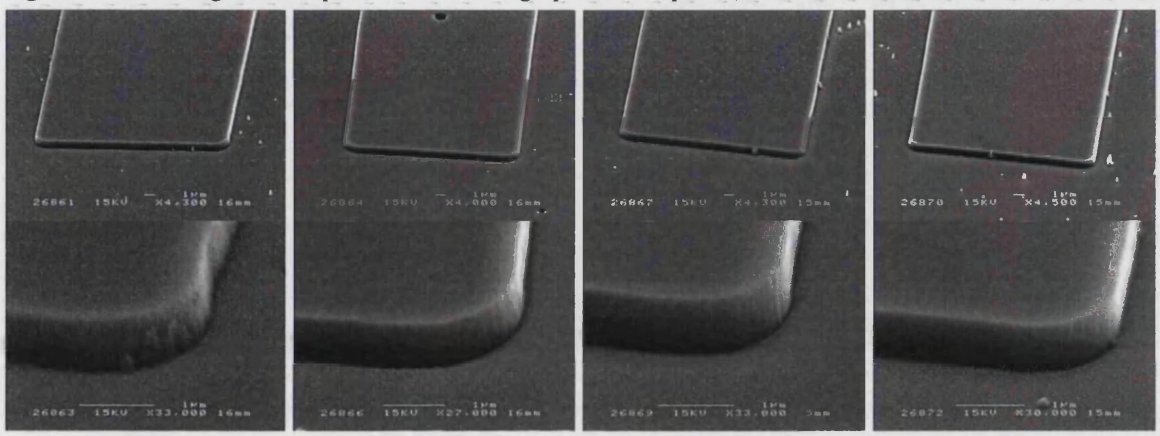

GaN AlGaN (1% Al) AlGaN (10% Al) LD

Fig. 4.45. SEM images of samples etched with a graphite coverplate and a 6-inch Si wafer (after 2 min etch).

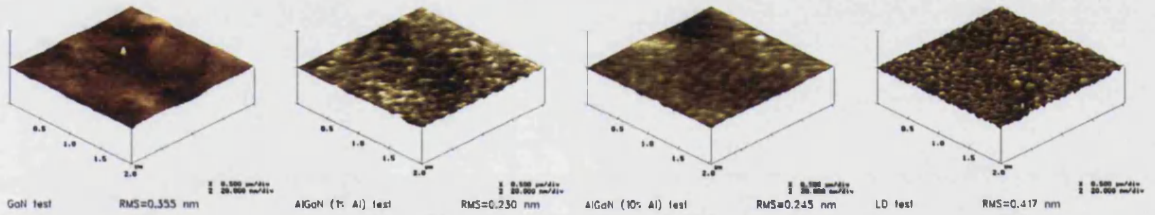

GaN AlGaN (1% Al) AlGaN (10% Al) LD

Fig. 4.46. AFM images of unetched test samples (scale=20 nm/div).

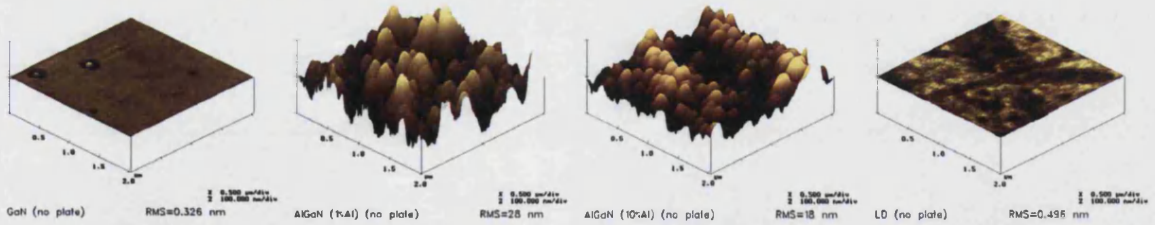

GaN AlGaN (1% Al) AlGaN (10% Al) LD

Fig. 4.47. AFM images of samples etched with no coverplate (scale=100 nm/div).

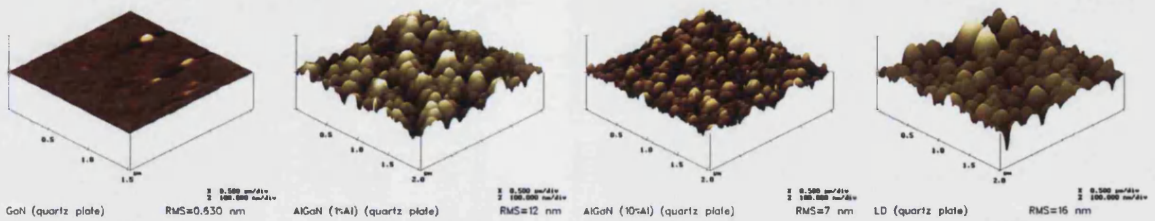

GaN AlGaN (1% Al) AlGaN (10% Al) LD

Fig. 4.48. AFM images of samples etched with a quartz coverplate (scale=100 nm/div).

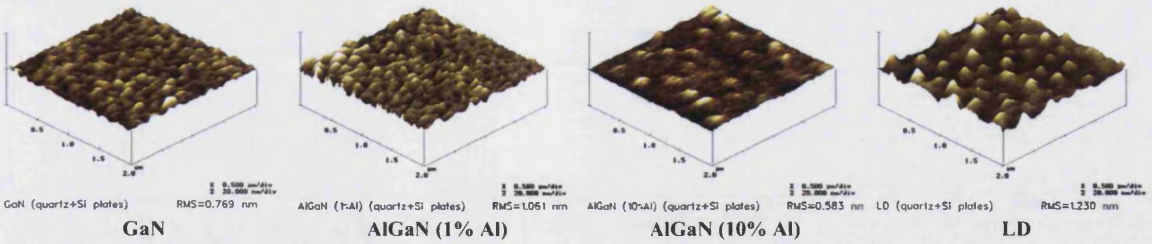

Fig. 4.49. AFM images of samples etched with a quartz coverplate and a Si wafer (scale=20 nm/div).

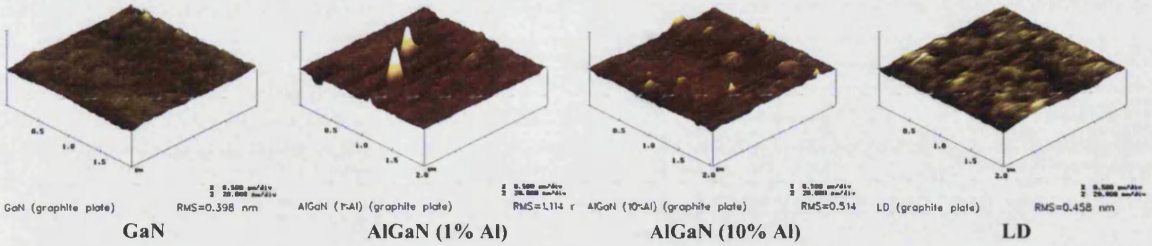

Fig. 4.50. AFM images of samples etched with a graphite coverplate (scale=20 nm/div).

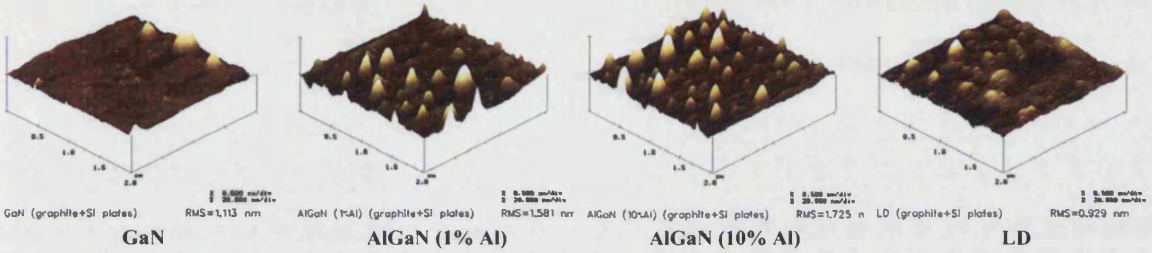

Fig. 4.51. AFM images of samples etched with a graphite coverplate and a Si wafer (scale=20 nm/div).

Influence of SiC_4 added to Cl_2/Ar plasma

$SiCl_4$-based plasmas are widely used for etching GaN material.[57, 46, 55] Adesida *et al.* were the first to report RIE etching of GaN in a $SiCl_4$ plasma. However, in our knowledge, there are no papers on the etching of Al-containing III-nitrides in a $SiCl_4$ discharge, thus implying the significance of these experiments. According to the first series of experiments, the etching rates of AlGaN layers were equal to that of GaN and the etched surface was very smooth when a Si wafer was located between the exposed samples and a quartz coverplate. However, this wafer could partially protect the quartz from reactions with a Cl_2 plasma. The results of these experiments on $SiCl_4$ gas added to a Cl_2/Ar mixture with the quartz coverplate only clearly show that the $SiCl_x$ reactive radicals and $SiCl_x^+$ ions are responsible for the fast and smooth etching of AlGaN.

SEM images of samples etched at different flows of $SiCl_4$ added to the plasma gas mixture are presented in Fig. 4.54 – Fig. 4.58, whereas AFM surface images are shown in Fig. 4.59 – Fig. 4.63. As can be seen, a smooth etch surface was obtained for over 2 sccm $SiCl_4$ for all the structures. The etching rates of the structures and the RMS surface roughness as functions of $SiCl_4$ flow are presented in Fig. 4.52 and Fig. 4.53, respectively. Presumably, the effect of $SiCl_4$ is related to its ability to scavenge oxygen in a process chamber. As in the case of a Si wafer in a Cl_2/Ar plasma, the SiC_4/Cl_2/Ar discharge generated the $SiCl_x$ reactive radicals and $SiCl_x^+$ ions along with typical Cl, Cl^+, Cl_2, and Cl_2^+ species.[127, 133] Thereby oxygen liberated from the quartz coverplate as a result of the etching was consumed in the plasma discharge, resulting in smooth and fast etching of Al-containing layers. Furthermore, nanotip formation was eliminated which could be caused by the heavy $SiCl_x^+$ ions and/or internal reactions in the plasma. As can be seen in Fig. 4.54, 1 sccm $SiCl_4$ flow was probably not enough to scavenge all the oxygen and prevent the oxidation of aluminium, but it was enough to reduce the concentration for smooth

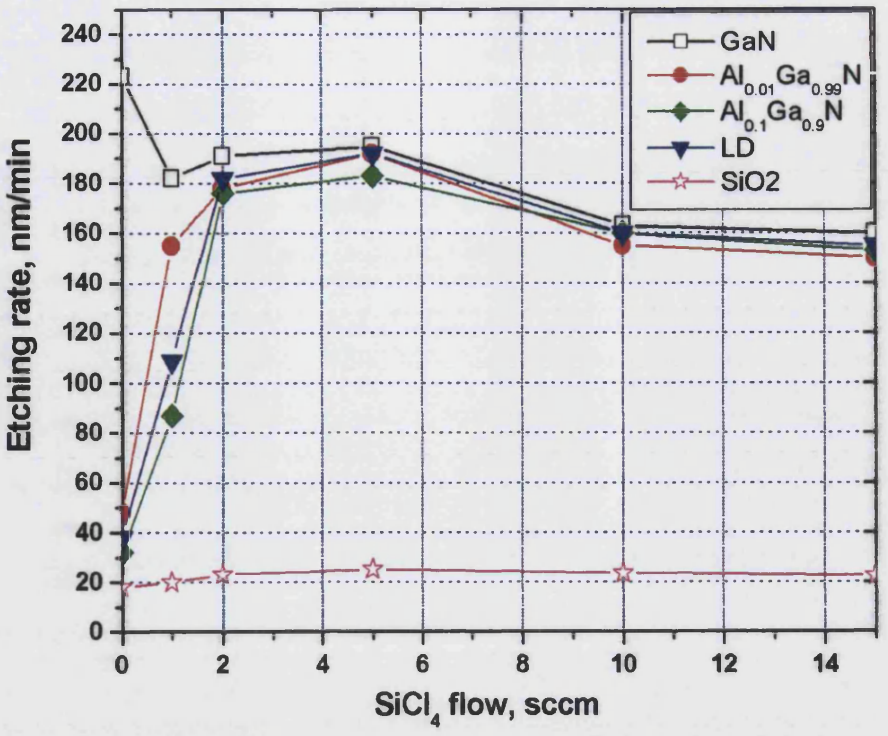

Fig. 4.52. Etching rates at different flow of $SiCl_4$ (Cl_2+$SiCl_4$ flow = 15 sccm).

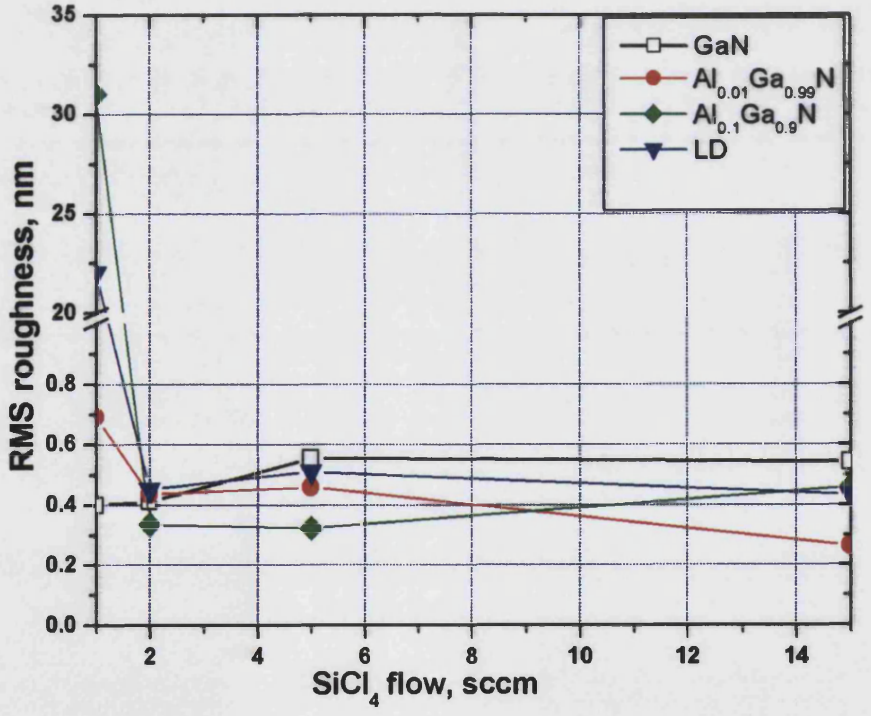

Fig. 4.53. RMS Roughness at different flow of $SiCl_4$ (Cl_2+$SiCl_4$ flow = 15 sccm).

etching of AlGaN with only 1% Al. Rough sidewalls in this case could be caused by higher surface oxidation near the SiO_2 etch mask. However, at more than 2 sccm $SiCl_4$ the surface and sidewalls became very smooth and the etching rates became equal for all the structures. A further increase in the $SiCl_4$ flow led to a decrease in the etching rates probably due to a reduction in the number of reactive Cl radicals and Cl^+ ions in the

chamber. The initial drop of the GaN etching rate at 1 sccm $SiCl_4$ is not clear and requires further investigations.

Unfortunately, the ICP ceramic tube was heavily contaminated inside after several minutes in the $SiCl_4/Cl_2/Ar$ discharge. X-ray analysis revealed mostly Si present in this deposition. Rahman *et al.* observed that at very low energies (~50 eV) Si^+ present in a $SiCl_4$ discharge prefers to deposit on a GaAs surface. In all probability, a similar situation occurred in the ICP tube, which is at a slight negative potential relative to the positively charged (+10–30 V) plasma. The Si deposited in the tube results in a heavily contaminated etched surface after long-term processing. This makes $SiCl_4$-based plasmas unsuitable for reliable and reproducible ICP etching.

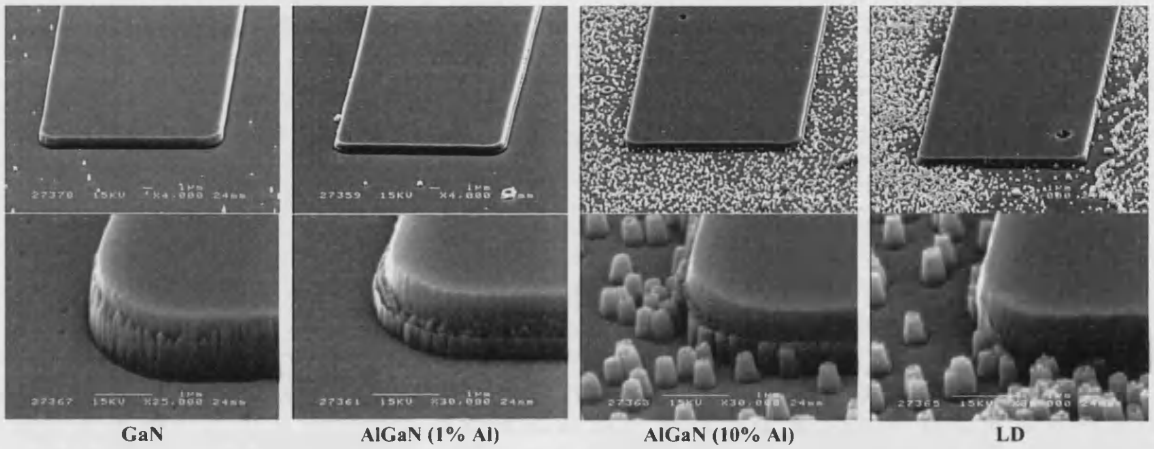

GaN AlGaN (1% Al) AlGaN (10% Al) LD

Fig. 4.54. SEM images of samples etched with 1 sccm $SiCl_4$ added.

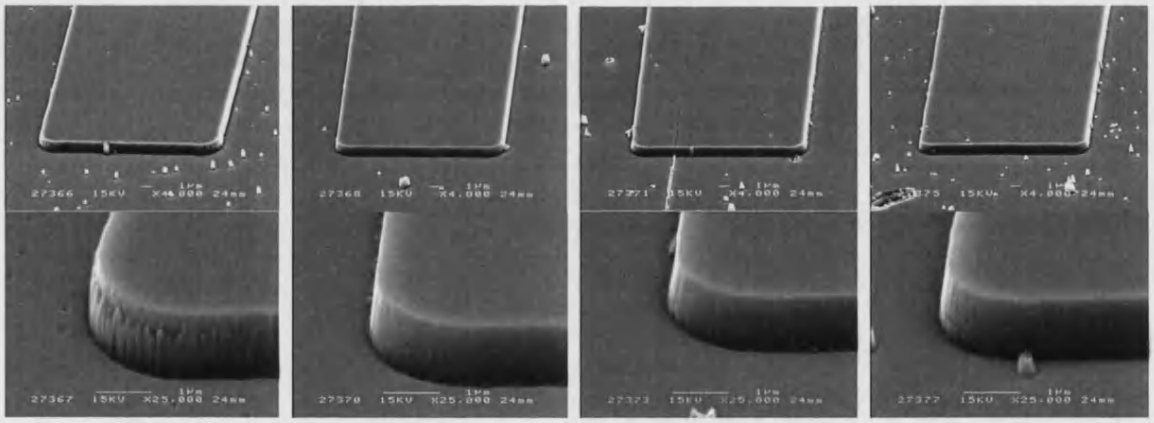

GaN AlGaN (1% Al) AlGaN (10% Al) LD

Fig. 4.55. SEM images of samples etched with 2 sccm $SiCl_4$ added.

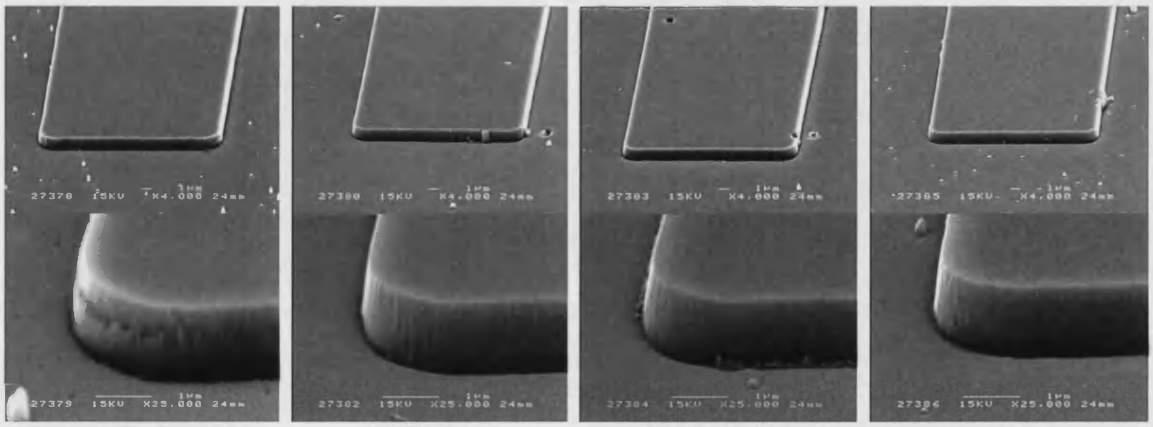

GaN AlGaN (1% Al) AlGaN (10% Al) LD

Fig. 4.56. SEM images of samples etched with 5 sccm $SiCl_4$ added.

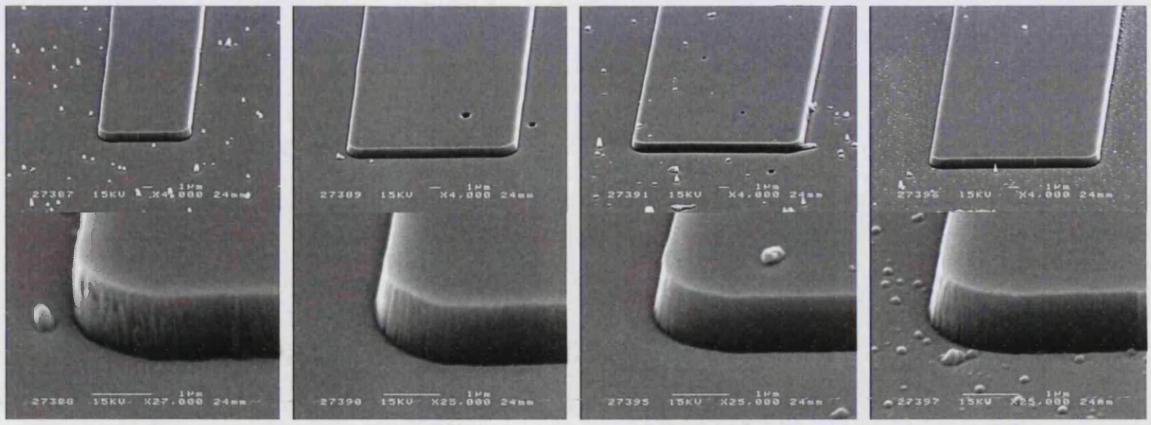

GaN AlGaN (1% Al) AlGaN (10% Al) LD

Fig. 4.57. SEM images of samples etched with 10 sccm $SiCl_4$ added.

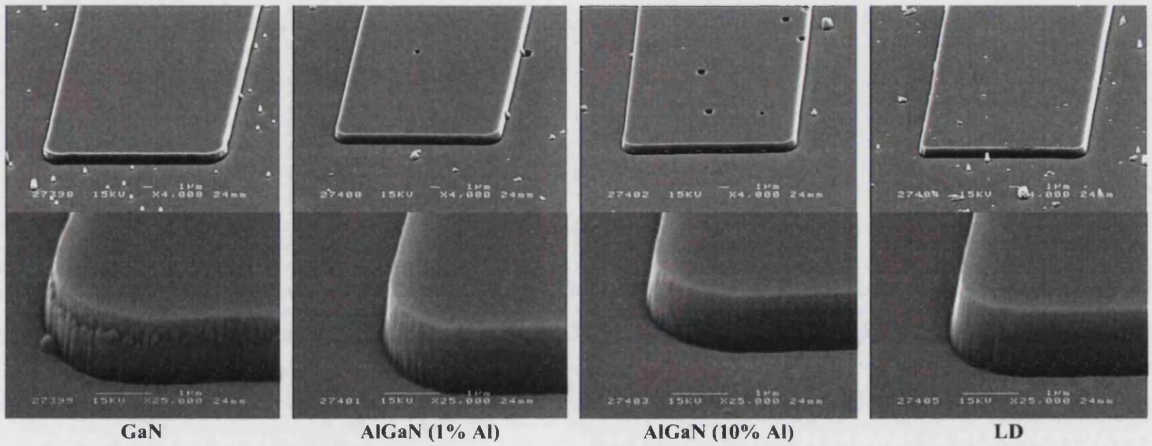

GaN AlGaN (1% Al) AlGaN (10% Al) LD

Fig. 4.58. SEM images of samples etched with 15 sccm $SiCl_4$ added.

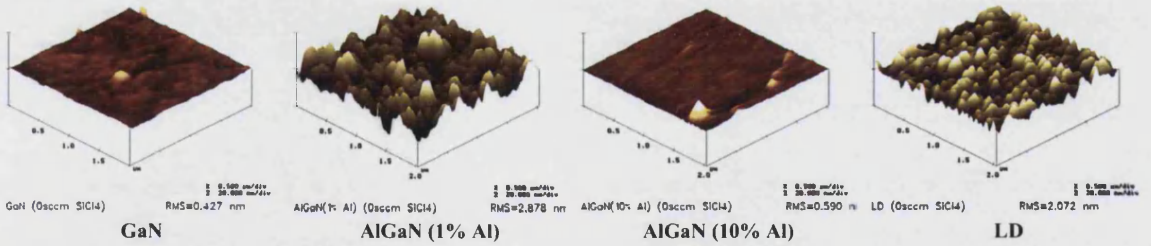

GaN AlGaN (1% Al) AlGaN (10% Al) LD

Fig. 4.59. AFM images of samples etched with 0 sccm $SiCl_4$ (scale=20 nm/div).

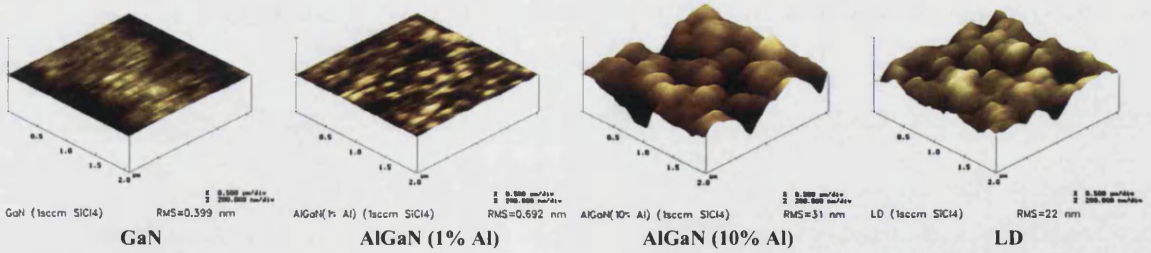

GaN AlGaN (1% Al) AlGaN (10% Al) LD

Fig. 4.60. AFM images of samples etched with 1 sccm $SiCl_4$ (scale=200 nm/div).

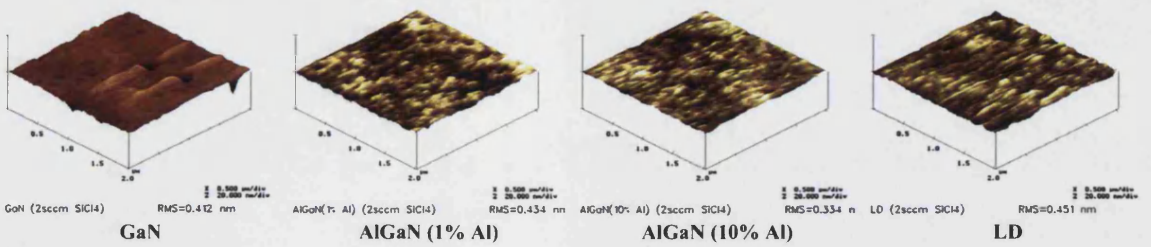

GaN AlGaN (1% Al) AlGaN (10% Al) LD

Fig. 4.61. AFM images of samples etched with 2 sccm $SiCl_4$ (scale=20 nm/div).

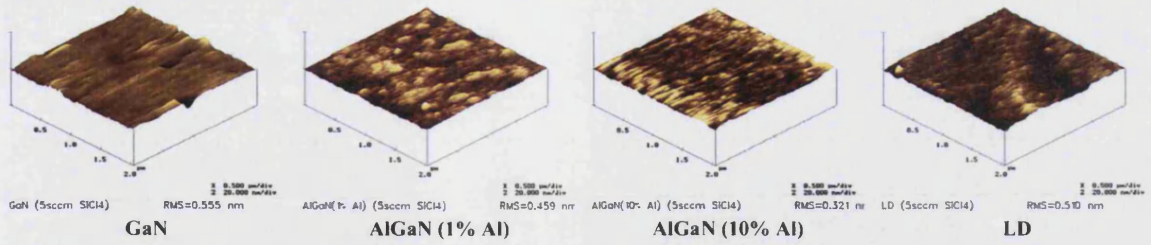

Fig. 4.62. AFM images of samples etched with 5 sccm $SiCl_4$ (scale=20 nm/div).

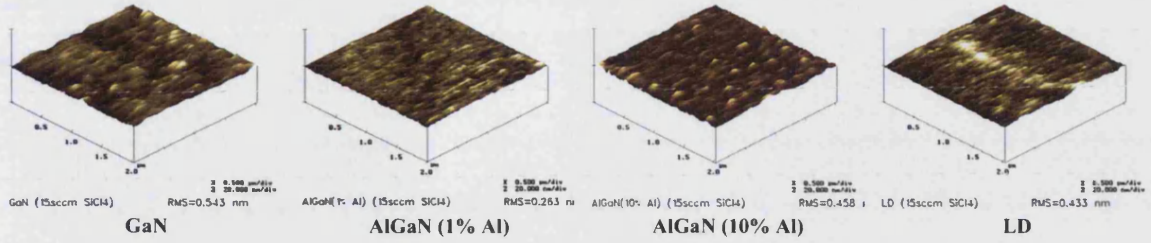

Fig. 4.63. AFM images of samples etched with 15 sccm $SiCl_4$ (scale=20 nm/div).

4.5.4 Conclusion

The influence of the cathode coverplate material on ICP etching of GaN, AlGaN containing 1 and 10% of Al, and a LD structure with a Cl_2/Ar plasma was investigated. It was revealed that the coverplate material has a great impact on the etching of Al-containing layers. We suggest that etching in a Cl_2 plasma with a quartz coverplate accompanies with a constant influx of oxygen from SiO_2, which forms a stable aluminium oxide on an AlGaN surface and, hence, results in extremely slow etching rates and a rough grassy surface. Using an anodized aluminium cathode with no coverplate also results in a grassy surface caused by the presence of water vapors and/or background oxygen in the process chamber. These residuals form a thin layer of oxide on the surface at the beginning of a plasma discharge resulting in a grassy etch surface for Al-containing layers. The results obtained with a graphite coverplate and with a Si wafer on the top of the quartz coverplate indicate that $SiCl_x$, CCl_x reactive radicals and $SiCl_x^+$, CCl_x^+ ions, as the etch products of the Cl_2 plasma with coverplate material, are responsible for fast and smooth etching of Al-containing layers. We believe that these species scavenge oxygen in the process chamber and effectively remove oxide layers on the surface. The experiments with $SiCl_4$ gas added to a Cl_2/Ar mixture with the quartz coverplate only confirmed the role of $SiCl_x$ species for fast and smooth etching of AlGaN layers. The obtained data provide the optimal chamber configurations suitable for laser diode processing.

4.6 Optimization of ICP etching of a GaN-based laser structure with Cl_2/Ar plasma assisted by Si coverplate

4.6.1 Introduction

The results presented in the section above suggest that a Si wafer, located on the top of a quartz coverplate, greatly improves etching of Al-containing layers in a Cl_2/Ar plasma and can be used for laser diode fabrication. This chamber configuration provides fast III-nitride etching rates, smooth vertical etch sidewalls, smooth contamination-free surfaces, and high selectivity over a SiO_2 etch mask. This section presents a study of ICP etching of GaN, $Al_{0.1}Ga_{0.9}N$, and a laser diode structure with a Cl_2/Ar plasma assisted by a Si wafer. The influence of process pressure, RF and ICP power on etching rates, surface/sidewalls morphology, and selectivity of the LD structure over a SiO_2 mask was investigated. The obtained data provide a wide range of parameters where smooth anisotropic etch profile, smooth etch surface, and a high selectivity over a SiO_2 etching mask are easily achieved. Furthermore, the behavior of an Oxford PlasmaLab 80 ICP reactor, used for the experiments, was found to be different from that of conventional ICP systems. This behavior was also studied and explained to give a fuller understanding of the mechanisms involved in the etching. The study has also been recently accepted for publication ["ICP etching of III-nitride based laser structure with Cl_2/Ar plasma assisted by Si coverplate material" E. Zhirnov, S. Stepanov, W. N. Wang, A. Gott, Y. G. Shreter, D. V. Takhin, and N. I. Bochkareva, *J. Vac. Sci. Technol. A* 23, XXX (2005).].

4.6.2 Experimental

Bulk 2 μm-thick GaN, $Al_{0.1}Ga_{0.9}N$, and a laser structure containing SL of $Al_{0.1}Ga_{0.9}N$/GaN were grown on Al_2O_3 substrates by metallorganic chemical vapor deposition (MOCVD). The mole fraction of Al in the AlGaN layer was determined by X-ray diffraction (XRD) measurements. 300 nm of SiO_2 was deposited on the samples as a mask layer by plasma enhanced chemical vapor deposition (PECVD). The mask pattern was defined and the surface was cleaned prior to GaN etching using the same procedure as was used for the experiments with the coverplates (section 4.5).

An Oxford PlasmaLab 80 ICP reactor was used for III-nitride etching experiments. The samples were mounted onto the 10-inch anodized aluminum cathode covered with a quartz coverplate and a 6-inch Si wafer located between the coverplate and the samples. All the experiments were conducted after the background pressure was reduced to less than 6×10^{-6} Torr. The ICP process parameters used were as follows: 15 sccm Cl_2 flow, 4 sccm Ar flow, and 20 °C cathode temperature. The dc-bias voltage was measured separately without the coverplate under all sets of etching conditions used. The etching time was varied from 3 to 23 min, depending on the etching rates, to pattern 600–1500 nm-deep III-nitride features.

After completion of plasma etching the SiO_2 mask was stripped away using a buffered-HF (1:4) solution. The etching rates were calculated from the depth of the etched features measured with a stylus profilometer. Surface morphology, anisotropy, and sidewall undercutting were evaluated using a scanning electron microscope (SEM) at an angle of 30° with the surface.

4.6.3 Results and discussion

Influence of pressure

Figure 4.64 shows the influence of process pressure on cathode dc-bias at fixed 450 W ICP and 150 W RF power. As can be seen, the dc-bias voltage was relatively independent of the pressure up to 20 mTorr and was gradually reduced above 20 mTorr. At fixed RF power this behavior implies that the ion density in the process chamber was constant at pressures below 20 mTorr whilst it increased at higher pressures:

RF power ~ (Ion flux to substrate) × (dc-bias)

Here, (ion flux to substrate) is the amount of positive ions crossing the cathode sheath per second. These results are different from those reported for conventional ICP systems by Sheu *et al.* and Shul *et al.* These authors observed that the dc-bias was significantly increased with increasing pressure from 1 to 10 mTorr at fixed RF and ICP power. It was attributed to enhanced collisional recombination with increasing pressure, which subsequently decreased the plasma density (density of ions and reactive radicals) generated by the ICP source and, hence, increased the dc-bias voltage.

The discrepancy with published results is related to the specific design of the ICP system used. The ICP PlasmaLab System 80 Plus system employs an ICP65 plasma source, which is located as a remote plasma source. Generally speaking, the ICP tube is intentionally spaced away from the cathode to allow active species to diffuse laterally. In this case, charged particles from the ICP tube do not reach the cathode and the etching process is mainly promoted by long-lived radicals generated in the source. Thus, the radical density in the process chamber is essentially defined by the ICP power, while the ion density near the cathode sheath is relatively independent of the ICP source. Accordingly, both the ion density and the dc-bias voltage are defined by the RF power as in the case of an RIE-only system. In conventional RIE systems the ion density becomes higher at higher pressures due to the reduced amount of generated ions compared to

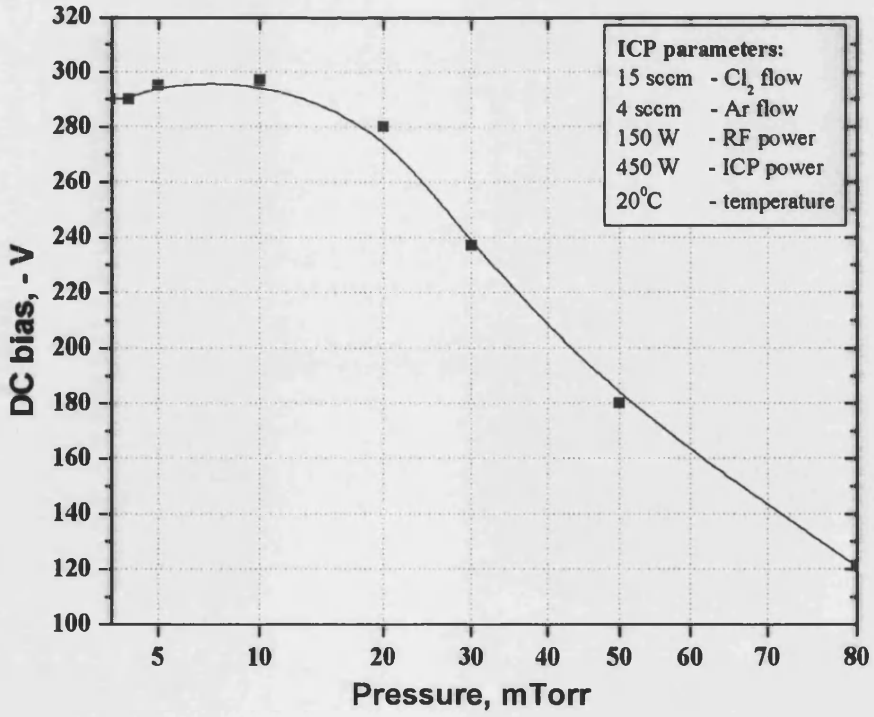

Fig. 4.64. Dc-bias voltage as a function of process pressure.

conventional ICP systems. The increased frequency of collisions leads to the increased density of ions in the RIE system. In contrast, this leads to increased collisional recombination of ions and to a decrease of the ion density in the ICP source. Thereby, in our system the increase in the pressure results in a decreased density of ions in the ICP tube and an increased density of ions in the RIE part of the chamber near the cathode. Accordingly, the dc-bias decreases with increasing pressure at fixed RF power. Lin *et al.* also reported that the dc-bias was decreased from -231 to -42 V with increasing pressure from 10 to 100 mTorr in a Plasma-Therm 700 RIE system. The fairly constant dc-bias at pressures from 3 to 20 mTorr was probably caused by improved ion transport from the ICP source at lower pressures (increased mean free path of ions), which compensates the low ion density generated in the chamber by RF power.

Figure 4.65 presents the etching rates of GaN, $Al_{0.1}Ga_{0.9}N$, a LD structure, and a SiO_2 mask as a function of the process pressure in the range from 3 to 20 mTorr. This range corresponds to approximately constant dc-bias voltage and ion density near the cathode sheath, as considered above. As can be seen, the etching rates were equal for all nitride structures, which is consistent with the results presented in the previous section. The selectivity of the III-nitrides over the SiO_2 mask was about (9:1) independent of the pressure. For all the materials, including the SiO_2 mask, the etching rates significantly decreased with increasing pressure. This cannot be related to reduced density of ions or increased dc-bias (the sputter desorption of reactive plasma species prior to reactions) as in the case of other studies published.[2, 23, 41] However, increasing the pressure results in a decrease in the quantity of both ions and reactive radicals generated in the ICP tube. Although most of the ions cannot reach the cathode, the radicals can diffuse into the chamber and promote a chemical component of the etching. Thus, the increased pressure results in a reduced density of reactive radicals in the chamber and, hence, in the decreased etching rates. Additionally, the decrease of the etching rates with increasing pressure may also be related to redeposition and/or polymer formation on the surface, reduced mean free path of ions, and the collisional scattering of ions in the sheath region.[1, 53]

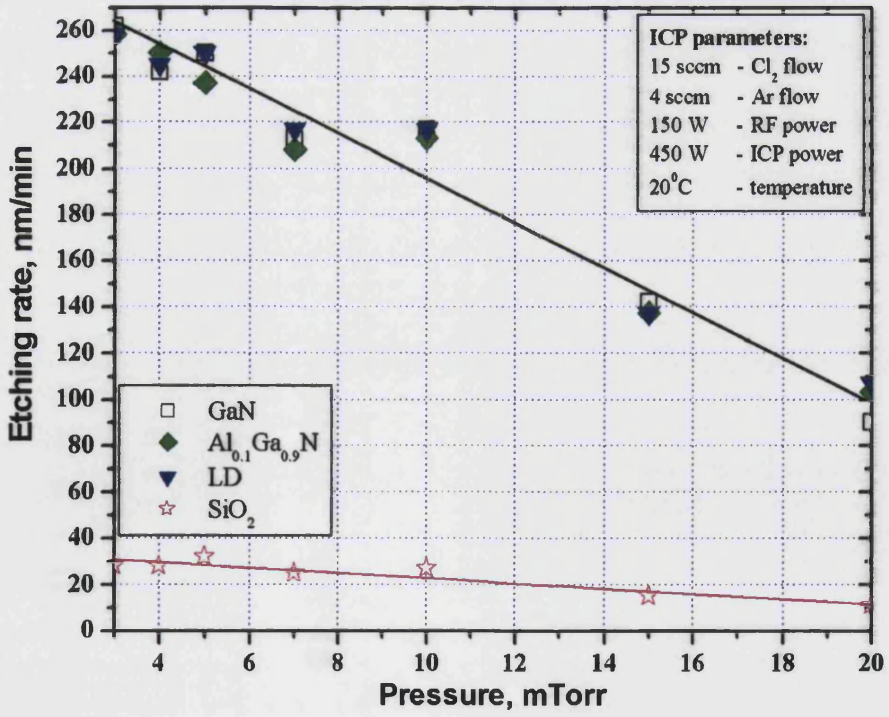

Fig. 4.65. Etching rates as a function of process pressure.

Figure 4.66 shows SEM images of the LD structure etched at different pressures. As can be seen, the etch profile was anisotropic and smooth for all conditions. Nonetheless, the etched surface tended to be more contaminated at higher pressures. This could be related to pre-etch contamination on the surface. Although not shown, the etched surface and profile were smooth for GaN and $Al_{0.1}Ga_{0.9}N$ layers as well.

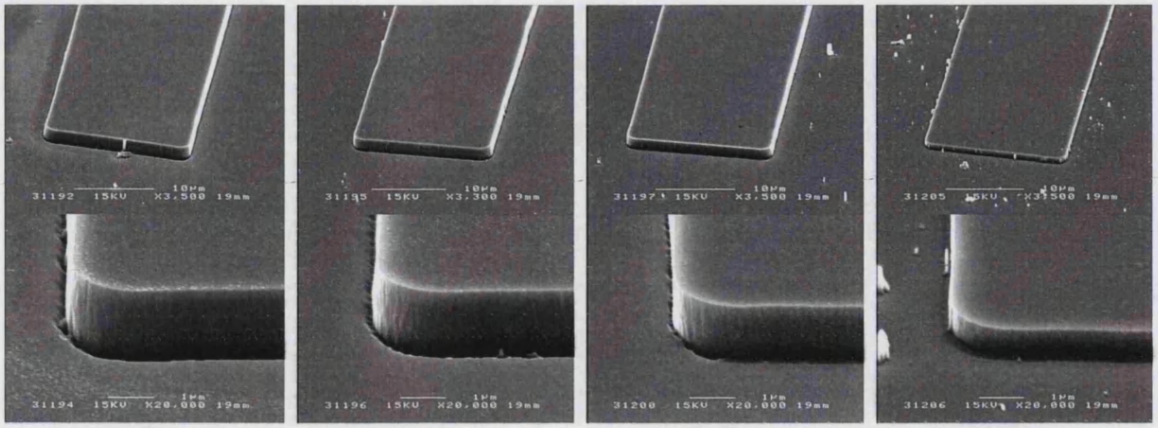

Fig. 4.66. SEM images of a laser structure etched at different process pressures.

Influence of RF power

Figure 4.67 shows the influence of RF power on cathode dc-bias at fixed 450 W ICP power and 4 mTorr pressure. As can be seen, the dc-bias was linearly dependent on the RF power, indicating that the ion density in the chamber was constant and independent of the RF power at these conditions. However, the ion density near the cathode sheath in our ICP system should depend on the RF power, as considered in the previous section. These unexpected results were possibly related to inefficient impact ionization by the RF source at low pressures. Most of the RF power was wasted in increased ion bombardment

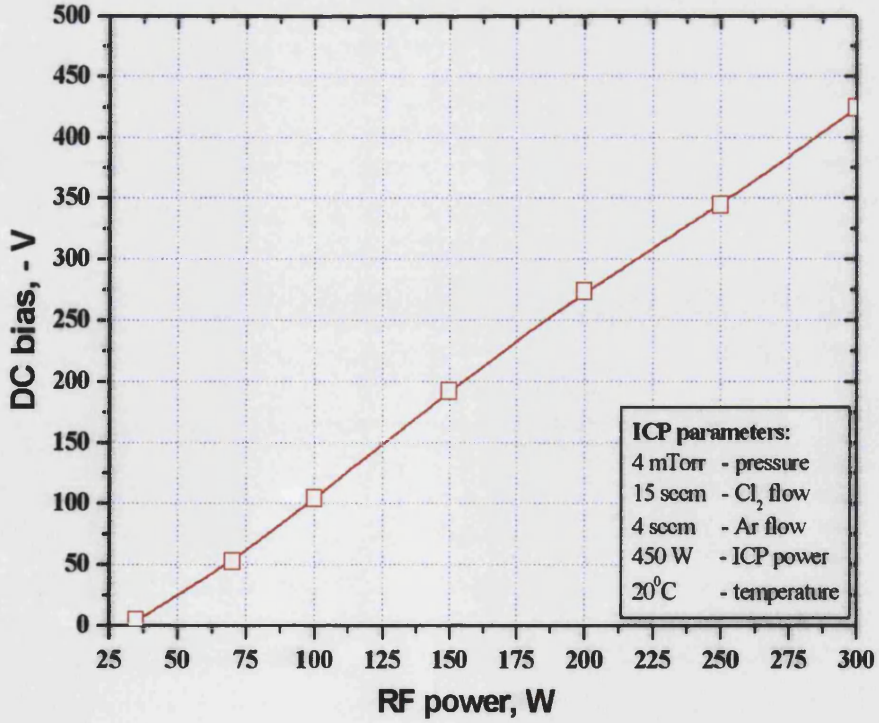

Fig. 4.67. Dc-bias voltage as a function of RF power.

and hot electron creation instead of contributing to ionization. Consequently, the ion density saturated and remained unchanged as the RF power increases.

Figure 4.68 presents etching rates of GaN, $Al_{0.1}Ga_{0.9}N$, the LD structure, and the SiO_2 mask as a function of the RF power. As can be seen, the etching rates for all nitride materials were equal at RF power higher than 70 W, which is consistent with results presented in the previous section. However, the etching rate of GaN was much larger (29 nm/min) than that of $Al_{0.1}Ga_{0.9}N$ (0 nm/min) and the LD structure (4 nm/min) at 35 W RF power (-4 V dc-bias). It is probably related to different bond energies of GaN (8.92 eV/atom) and AlN (11.52 eV/ atom) and, hence, different threshold energy of ions required to break the III-V bonds. It is also important to note that the potential of plasma with respect to grounded electrode is equal to +(10–30) V. Thereby, the ion impact energy on the cathode is equal to the dc-bias voltage minus this potential. The dependence presented in Fig. 4.68 is very similar to that reported by Smith *et al.* at fixed ICP power. The authors also observed that etching rates increased dramatically up to -250 V dc-bias at which point a plateau occurred. In all probability, this was caused by the sputter desorption of active chlorine species from the surface before they could react.

Figure 4.69 presents the selectivity of the LD structure over the SiO_2 mask as a function of RF power. As can be seen, the largest selectivity was obtained at 150 W RF power (-192 V dc-bias). The etching rate of the LD saturated above this power, as considered above. In contrast, the etching rate of SiO_2 was probably dominated by physical sputtering rather than by a chemical component and it continued increasing.

Figure 4.70 shows SEM images of the LD structure etched at different RF power. As can be seen, etch profile was anisotropic and smooth at all conditions. Nonetheless, the etch surface was slightly contaminated with pillars at the lowest RF power. The micromasking effect of a thin InGaN top contact layer might be the reasons for this due to the low volatility of $InCl_3$ etch products (boiling point of ~600 °C). Under higher plasma conditions these etch products were probably sputtered away before they could passivate the surface. Although not shown, the etched surface and profile were smooth for GaN and $Al_{0.1}Ga_{0.9}N$ at all conditions.

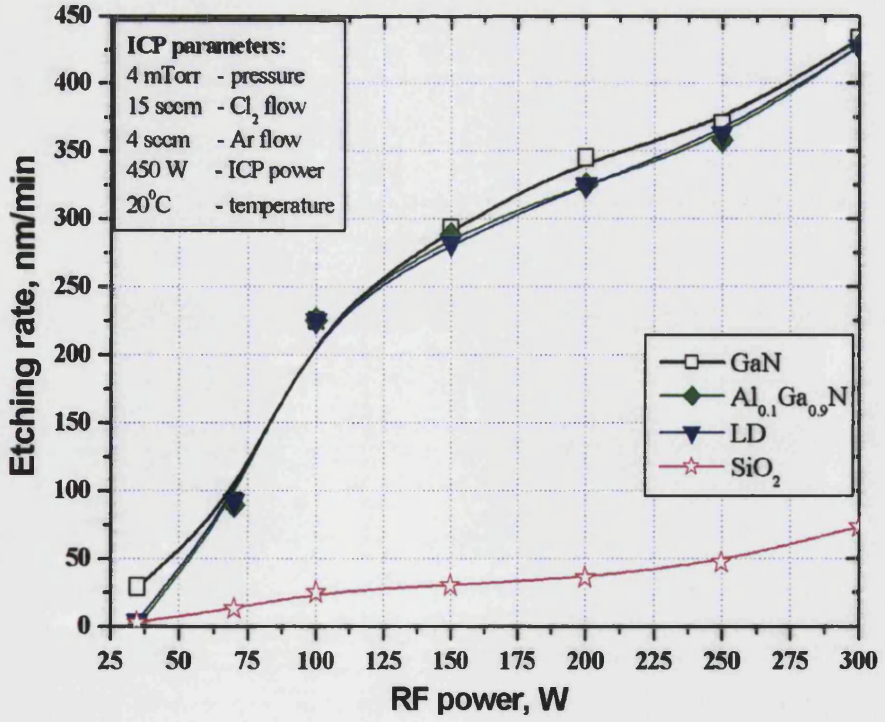

Fig. 4.68. Etching rates as a function of RF power.

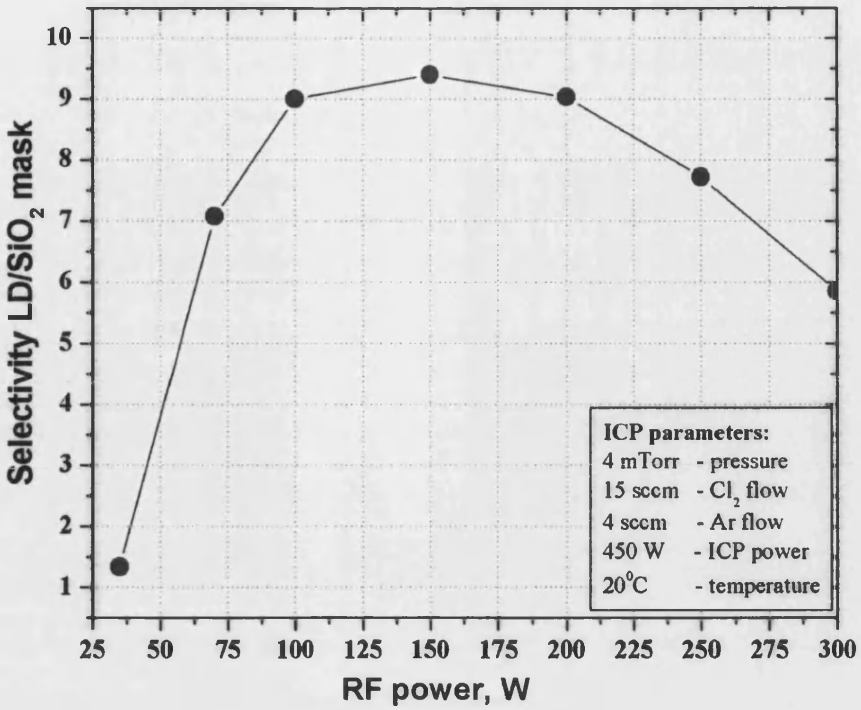

Fig. 4.69. Selectivity of a laser structure over a SiO_2 mask as a function of RF power.

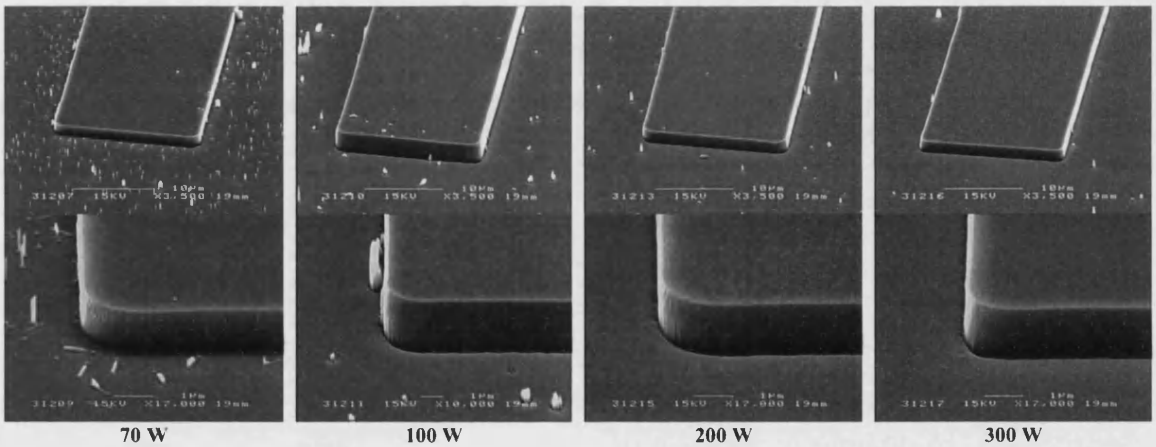

Fig. 4.70. SEM images of a laser structure etched at different RF power.

Influence of ICP power

For these experiments the process pressure and RF power were fixed at 4 mTorr and 150 W, respectively. The cathode dc-bias was found to be nearly constant (about -300 V) and independent of the ICP power. These results are different from those reported for conventional ICP systems, where an increasing ICP power at fixed RF power results in a decrease of the cathode dc-bias due to an increased ion density in the process chamber.[11, 23, 28, 30, 41, 45] However, this is consistent with the findings of Cooke *et al.* for the ICP65 source employed in the Oxford PlasmaLab 80 ICP reactor. The authors stated that charged ions from the ICP tube do not reach the cathode due to the remote location of the source. Thus, both the density of ions near the cathode sheath and the dc-bias are determined by the RF power, which was fixed during these experiments.

Figure 4.71 presents the etching rates of GaN, $Al_{0.1}Ga_{0.9}N$, the LD structure, and the SiO_2 mask as a function of the ICP power. As can be seen, the etching rates increased with increasing ICP power. However, the ion density near the cathode sheath and the dc-bias were invariable during the experiments, as it was stated above. This behavior is probably related to an increase in a number of reactive radicals generated in the ICP tube. Although ions from the ICP source cannot reach the cathode, the radicals can diffuse into the chamber and promote a chemical component of etching. The selectivity of the LD structure over the SiO_2 mask as a function of the ICP power is presented in Fig. 4.72.

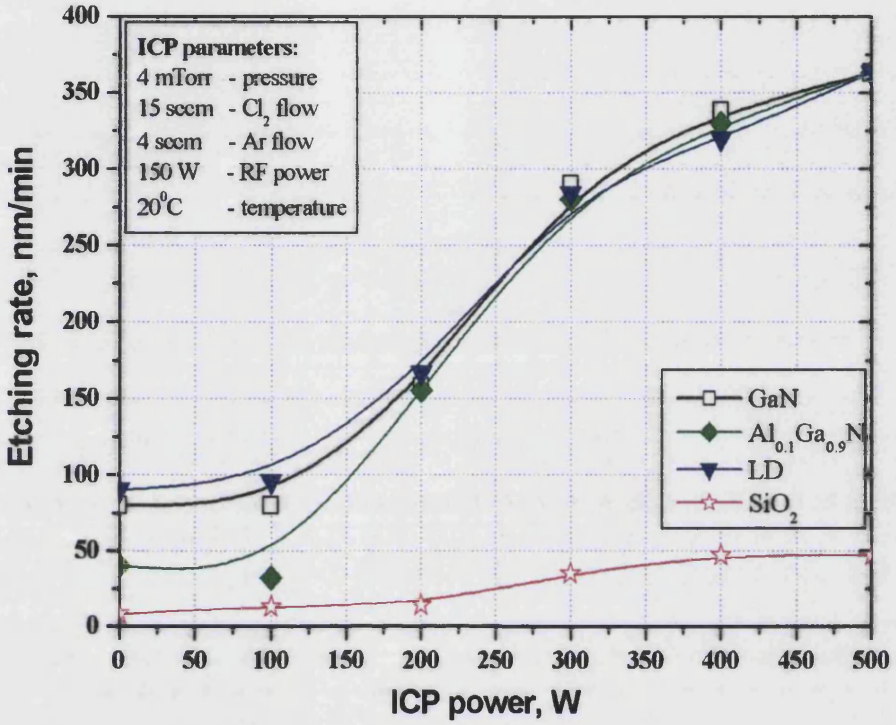

Fig. 4.71. Etching rates as a function of ICP power.

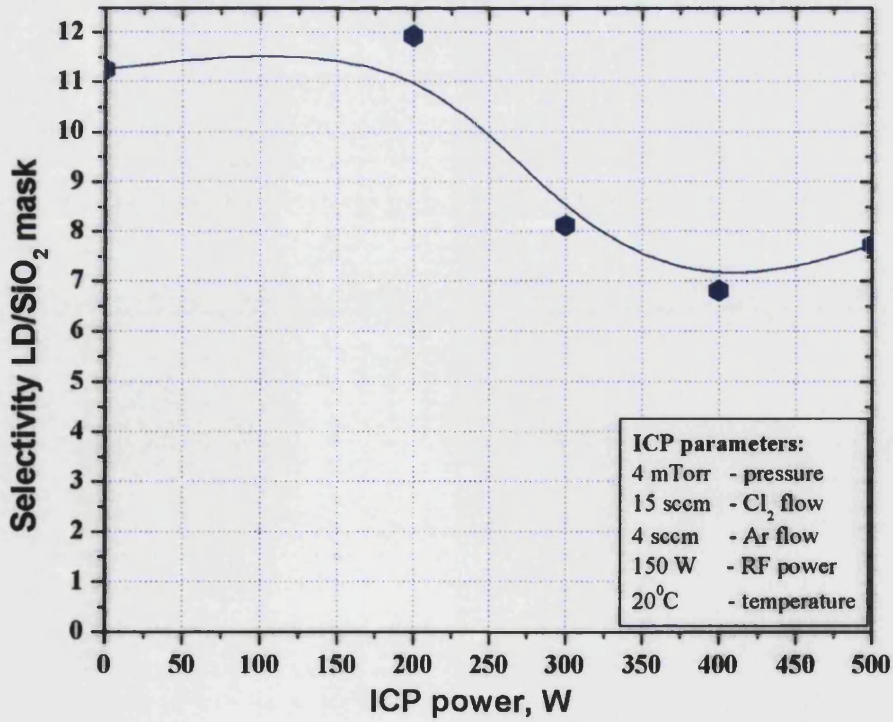

Fig. 4.72. Selectivity of a laser structure over a SiO_2 mask as a function of ICP power.

As can be seen, the etching rates were equal for all nitride materials above 200 W ICP power, which is consistent with the results presented in the previous section. However, below 200 W ICP power the etching rate of $Al_{0.1}Ga_{0.9}N$ was slower in comparison with GaN and the LD structure, and the etch surface of $Al_{0.1}Ga_{0.9}N$ was very grassy, as shown in Fig. 4.73. The slow etching rate and the grassy etch surface morphology of Al-containing layers probably resulted in pillars after etching the LD structure (Fig. 4.74) containing $Al_{0.1}Ga_{0.9}N$ layers in super-lattices. In contrast, the etched surface of GaN was fairly smooth for all conditions, as shown in Fig. 4.75. These results confirm the role of $SiCl_x$ reactive radicals and $SiCl_x^+$ ions for smooth and fast etching of AlGaN layers.

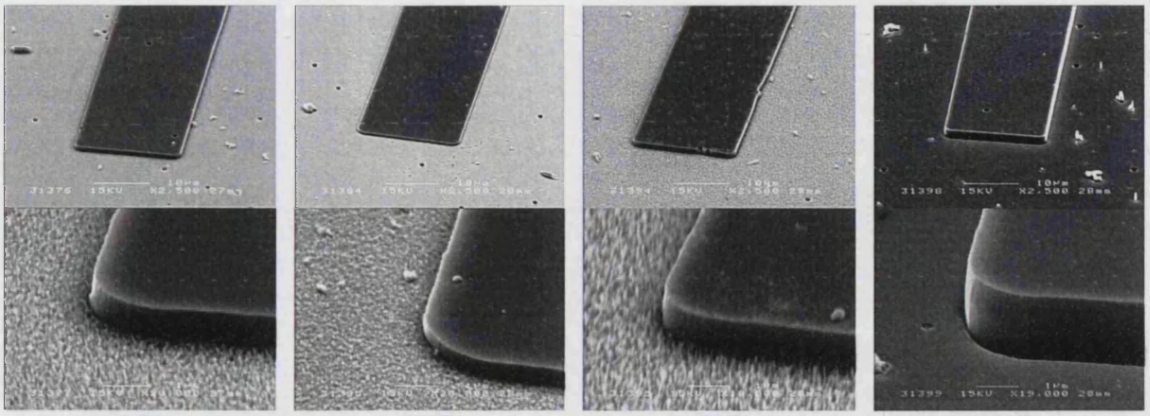

0 W 100 W 200 W 300 W

Fig. 4.73. SEM images of $Al_{0.1}Ga_{0.9}N$ etched at different ICP power.

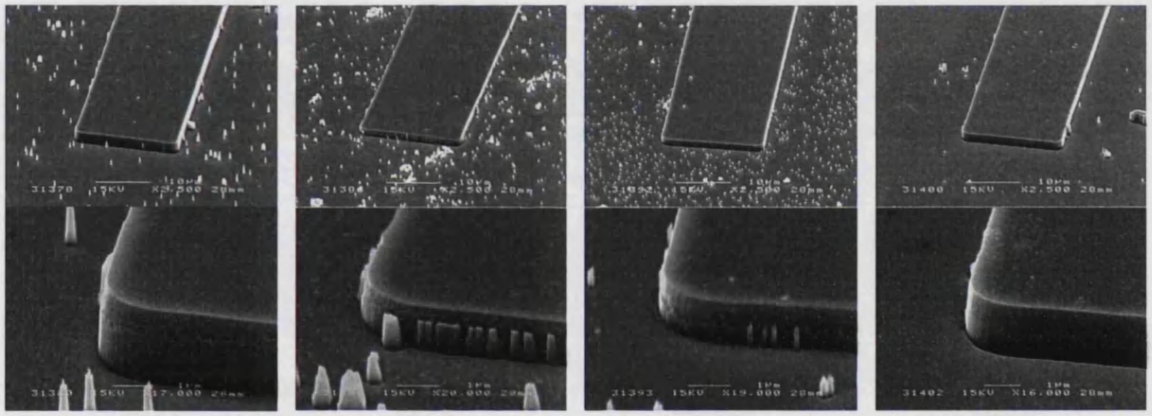

0 W 100 W 200 W 300 W

Fig. 4.74. SEM images of a laser structure etched at different ICP power.

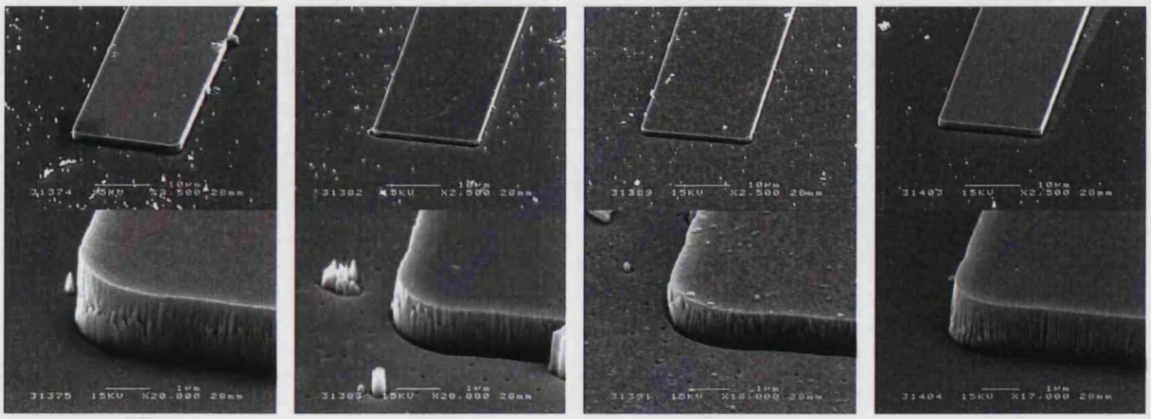

0 W 100 W 200 W 300 W

Fig. 4.75. SEM images of GaN etched at different ICP power.

Low ICP power results in a low density of reactive radicals in the process chamber and, hence, in slow etching of the Si wafer. This leads to a low density of $SiCl_x$ etch products in the chamber. Thus, oxygen liberated from the quartz coverplate cannot be scavenged completely and it interferes with $Al_{0.1}Ga_{0.9}N$ etching by forming aluminium oxides. It finally results in the slow etching rates and the grassy etch surface for $Al_{0.1}Ga_{0.9}N$ and in the pillars for the LD structure. Roughening of the Si wafer observed at less than 200 W ICP power also indicates the presence of background oxygen in the process chamber.[124, 125, 126]

It is important to note that under the same base conditions (4 mTorr pressure, 15 sccm Cl_2, 4 sccm Ar, 450 W ICP power, 150 W RF power) the dc-bias voltage and the etching rates were different during experiments with pressure (-290 V, 250 nm/min), RF power (-192 V, 285 nm/min), and ICP power (-300 V, 350 nm/min). In all probability, this was related to differences in the process chamber conditions due the cleaning of the chamber between these experiments. Shul *et al.* also observed a similar difference after the reconstruction of a process chamber.

4.6.4 Conclusion

ICP etching of GaN, $Al_{0.1}Ga_{0.9}N$, and a laser diode structure with a Cl_2/Ar plasma assisted by a Si wafer was systematically studied. The influence of process pressure, RF and ICP power on the etching rates, surface/sidewalls morphology, and selectivity of the LD structure over the SiO_2 mask was investigated. The experiments confirmed the role of $SiCl_x$ etch products, produced as a result of etching the Si wafer with the Cl_2 plasma, for smooth and fast etching of Al-containing layers, as considered previously. A smooth anisotropic etch profile, smooth etch surface, and high selectivity over SiO_2 were obtained for the laser diode structure in a wide range of process parameters. Thereby, the developed process can be successfully employed for III-nitride laser diode processing. Furthermore, it was found that the Oxford PlasmaLab 80 reactor, used for the experiments, behaves differently compared to conventional ICP systems. The ICP65 source employed in the system does not significantly effect the sheath ion density and cathode dc-bias, due to its remote location. However, the ICP source generates a large amount of reactive radicals, which facilitate fast and smooth etching of Al-containing layers. At low pressure (4 mTorr) the plasma density was found to be independent of both the ICP and RF power, which is possibly related to inefficient impact ionization by the RF source at low pressures.

4.7 References

[1] S. J. Pearton, R. J. Shul, and F. Ren, MRS Internet J. Nitride Semicond. Res. 5, 11 (2000).

[2] F. A. Khan, L. Zhou, A. T. Ping, and I. Adesida, J. Vac. Sci. Technol. B 17, 2750 (1999).

[3] W. M. Moreau, Semiconductor Lithography: Principles, Practices, and Materials, Plenum Press, New York, 1998.

[4] B. Chapman, Glow Discharge Processes, Sputtering and Plasma Etching, Wiley, New York, 1980.

[5] M. Kanon, M. Yamage, and H. Takada, Jpn. J. Appl. Phys. 40, 1457 (2001).

[6] M. Lieberman and A. Lichtenberg, Principles of Plasma Discharges and Materials Processing, Wiley, New York, 1994.

[7] M. Schaepkens, G. S. Oehrlein, and J. M. Cook, J. Vac. Sci. Technol. B, Vol. 18, No. 2, 856 (2000).

[8] M. A. Sobolewski, J. K. Olthoff, and Y. Wang, J. Appl. Phys., Vol. 85, 3966 (1999).

[9] M. J. Cooke and G. Hassall, Plasma Sources Sci. Technol., 11, 1 (2002).

[10] N. R. Rueger, M. F. Doemling, M. Schaepkens, J. J. Beulens, T. E. F. M. Standaert, and G. S. Oehrlein, J. Vac. Sci. Technol. A 17, 2492 (1999).

[11] R. J. Shul, L. Zhang, C. G. Willison, J. Han, S. J. Pearton, J. Hong, C. R. Abernathy, and L. F. Lester, MRS Internet J. Nitride Semicond. Res. 4S1, G8.1 (1999).

[12] J. W. Lee, J. Hong, and S. J. Pearton, Appl. Phys. Lett. 68, 847 (1996).

[13] C. Constantine, C. Barratt, S. J. Pearton, F. Ren, and J. R. Lothian, Electron. Lett. 28, 1749 (1992).

[14] C. Constantine, C. Barratt, S. J. Pearton, F. Ren, and J. R. Lothian, Appl. Phys. Lett. 61, 2899 (1992).

[15] R. J. Shul, S. P. Kilcoyne, M. H. Crawford, J. E. Parmeter, C. B. Vartuli, C. R. Abernathy, and S. J. Pearton, Appl. Phys. Lett. 66, 1761 (1995).

[16] S. J. Pearton, C. R. Abernathy, and F. Ren, Appl. Phys. Lett. 64, 3643 (1994).

[17] Y. Z. Juang, Y. K. Su, S. C. Shei, and B. C. Fang, J. Vac. Sci. Technol. A 12, 75 (1994).

[18] H. Cho, Y. B. Hahn, D. C. Hays, C. R. Abernathy, S. M. Donovan, J. D. MacKenzie, S. J. Pearton, J. Han, and R. J. Shul, J. Vac. Sci. Technol. A 17, 2202 (1999).

[19] R. J. Shul, C. G. Willison, M. M. Bridges, J. Han, J. W. Lee, S. J. Pearton, C. R. Abernathy, J. D. MacKenzie, S. M. Donovan, L. Zhang, and L. F. Lester, J. Vac. Sci. Technol. A 16, 1621 (1998).

[20] H.-S. Kim, G.-Y. Yeom, J.-W. Lee, and T.-I. Kim, Thin Solid Films 341, 180, (1999).

[21] R. J. Shul, G. A. Vawter, C. G. Willison, M. M. Bridges, J. W. Lee, S. J. Pearton, and C. R. Abernathy, Solid-State Electronics 42, 2259 (1998).

[22] S. A. Smith, C. A. Wolden, M. D. Bremser, A. D. Hanser, R. F. Davis, and W. V. Lampert, Appl. Phys. Lett. 71, 3631 (1997).

[23] J. K. Sheu, Y. K. Su, G. C. Chi, M. J. Jou, C. C. Liu, C. M. Chang, and W. C. Hung, J. Appl. Phys. 85, 1970 (1999).

[24] Y. B. Hahn, R. J. Choi, J. H. Hong, H. J. Park, C. S. Choi, and H. J. Lee, J. Appl. Phys. 92, 1189 (2002).

[25] H. Cho, C. B. Vartuli, S. M. Donovan, C. R. Abernathy, S. J. Pearton, R. J. Shul, and C. Constantine, J. Vac. Sci. Technol. A 16, 1631 (1998).

[26] J. K. Sheu, Y. K. Su, G. C. Chi, M. J. Jou, C. C. Liu, C. M. Chang, and W. C. Hung, J. Appl. Phys. 85, No. 3, 1970 (1999).

[27] I. Song, S. Lee, K. Lee, S. Park, and J. Han, Jpn. J. Appl. Phys. 41, L317 (2002).

[28] H. Cho, Y. B. Hahn, D. C. Hays, K. B. Jung, S. M. Donovan, C. R. Abernathy, S. J. Pearton, and R. J. Shul, MRS Internet J. Nitride Semicond. Res. 4S1, G6.56 (1999).

[29] R. J. Shul, C. G. Willison, M. M. Bridges, J. Han, J. W. Lee, S. J. Pearton, C. R. Abernathy, J. D. Mackenzie, and S. M. Donovan, Solid-State Electronics 42, 2269 (1998).

[30] B. C. Cho, Y. H. Im, Y. B. Hahn, K. S. Nahm, Y. S. Lee, and S. J. Pearton, Journal of The Electrochemical Society 147, 3914 (2000).

[31] M. V. Malyshev, V. M. Donnelly, A. Kornblit, and N. A. Ciampa, J. Appl. Phys. 84, 137 (1998).

[32] K. Remashan, S. J. Chua, A. Ramam, S. Prakash, and W. Liu, Semicond. Sci. Technol. 15, 386 (2000).

[33] T. Wu, Z. Hao, G. Tang, and Y. Luo, Jpn. J. Appl. Phys. 42, L257 (2003).

[34] S. C. McNevin, J. Vac. Sci. & Technol. B 8, 1212 (1990).

[35] R. J. Shul, L. Zhang, A. G. Baca, C. G. Willison, J. Han, S. J. Pearton, and F. Ren, J. Vac. Sci. Technol. A 18, 1139 (2000).

[36] I. Adesida, C. Youtsey, A. T. Ping, F. Khan, L. T. Romano, and G. Bulman, MRS Internet J. Nitride Semiconductor Res. 4S1, G1.4 (1999).

[37] R. J. Shul, R. D. Briggs, J. Han, S. J. Pearton, J. W. Lee, C. B. Vartuli, K. P. Killeen, and M. J. Ludowise, Mater. Res. Soc. Symp. Proc. 468, 355 (1997).

[38] J. Lee, K. Chang, I.. Lee, and S. Park, Journal of The Electrochemical Society 147, 1859 (2000).

[39] J. Vechten, J. Zook, R. Horning, and B. Goldenberg, Jpn. J. Appl. Phys. 31, 3662 (1992).

[40] S. Pearton, C. Abernathy, C. Vartuli, J. Mackenzie, R. Shul, R. Wilson, and J. Zavada, Electron. Lett. 31, 836 (1995).

[41] R. J. Shul, G. B. McClellan, S. A. Casalnuova, D. J. Rieger, S. J. Pearton, C. Constantine, C. Barrat, R. F. Karlicek Jr., C. Tran, and M. Schurman, Appl. Phys. Lett. 69, 1119 (1996).

[42] J. Lee, K. Chang, I.. Lee, and S. Park, J. Vac. Sci. Technol. B 18, 1409 (2000).

[43] C. B. Vartuli, J. W. Lee, J. D. MacKenzie, S. M. Donovan, C. R. Abernathy, S. J. Pearton, R. J. Shul, C. Constantine, C. Barratt, A. Katz, A. Y. Poyakov, M. Shin, and M. Skowronski, Materials Research Society Symposium Proceedings 468, 393 (1997).

[44] D. Basak, K. Yamashita, T. Sugahara, D. Nakagawa, Q. Fareed, K. Nishino, and S. Sakai, Jpn. J. Appl. Phys. 38, 2646 (1999).

[45] J. Lee, S. Kim, and S. Park, Journal of The Electrochemical Society 148, G254 (2001).

[46] F. Karouta, B. Jacobs, P. Vreugdewater, N. G. H. van Melick, O. Schoen, H. Protzmann, and M. Heuken, Electrochemical and Solid-State Letters 2, 240 (1999).

[47] D. Buttari, A. Chini, T. Palacios, R. Coffie, L. Shen, H. Xing, S. Heikman, L. McCarthy, A. Chakraborty, S. Keller, and U. K. Mishra, Appl. Phys. Lett. 83, 4779 (2003).

[48] H. Cho, S. M. Donovan, J. D. Mackenzie, C. R. Abernathy, S. J. Pearton, J. Han, R. J. Shul, and J. W. Lee, Solid-State Electronics 42, 1719 (1998).

[49] T. Maeda, J.W. Lee, R.J. Shul, J. Han, J. Hong, E.S. Lambers, S.J. Pearton, C.R. Abernathy, W.S. Hobson, Applied Surface Science 143, 174 (1999).

[50] F. Ren, J. R. Lothian, J. M. Kuo, W. S. Hobson, J. Lopata, J. A. Caballero, S. J. Pearton, and M. W. Cole, J. Vac. Sci. Technol. B 14, 1 (1995).

[51] F. Ren, W. S. Hobson, J. R. Lothian, J. Lopata, J. A. Caballero, S. J. Pearton, and M. W. Cole, Appl. Phys. Lett. 67, 2497 (1995).

[52] C. S. Oh, T. H. Kim, K. Y. Lim, and J. W. Yang, Semicond. Sci. Technol. 19, 172 (2004).

[53] B. Lee, S. Jung, J. Lee, Y. Park, M. Paek, and K. Cho, Semicond. Sci. Technol. 16, 471 (2001).

[54] L. Zhang, J. Ramer, J. Brown, K. Zheng, L. F. Lester, and S. D. Hersee, Appl. Phys. Lett. 68, 367 (1996).

[55] I. Adesida, A. Mahajan, E. Andideh, M. A. Khan, D. T. Olsen, and J. N. Kuznia, Appl. Phys. Lett. 63, 2777 (1993).

[56] A. Matsutani, H. Ohtsuki, S. Muta, F. Koyama, and K. Iga, Jpn. J. Appl. Phys. 40, 1528 (2001).

[57] M. E. Lin, Z. F. Fan, Z. Ma, L. H. Allen, and H. Morkoc, Appl. Phys. Lett. 64, 887 (1994).

[58] F. Karouta, B. Jacobs, I. Moerman, K. Jacobs, J. Weyher, S. Porowski, R. Crane, and P. Hageman, MRS Internet J. Nitride Semicond. Res. 5S1, W11.76 (2000).

[59] S. J. Pearton and R. J. Shul,"Dry Etching" in Gallium Nitride I, edited by J. I. Pankove and T. D. Moustakas (Academic, San Diego, 1998).

[60] J. Lee, K. Chang, S. Kim, C. Huh, I.. Lee, and S. Park, J. Appl. Phys. 87, 7667 (2000).

[61] X. A. Cao, H. Cho, S. J. Pearton, G. T. Dang, A. P. Zhang, F. Ren, R. J. Shul, L. Zhang, R. Hickman, and J. M. Van Hove, Appl. Phys. Lett. 75, 232 (1999).

[62] F. Ren, S. J. Pearton, R. J. Shul, and J. Han, J. Electron. Mater. 27, 175 (1998).

[63] X. A. Cao, A. P. Zhang, G. T. Dang, H. Cho, F. Ren, S. J. Pearton, R. J. Shul, L. Zhang, R. Hickman, and J. M. Van Hove, J. Vac. Sci. Technol. B 17, 1540 (1999).

[64] X. A. Cao, A. P. Zhang, G. T. Dang, F. Ren, S. J. Pearton, J. M. Van Hove, R. A. Hickman, R. J. Shul, and L. Zhang, Journal of Electronic Materials 29, 256 (2000).

[65] A. T. Ping, A. C. Schmitz, M. Asif Khan, Q. Chen, J. W. Yang, and I. Adesida, J. Electron. Mater. 26, 266 (1997).

[66] A.T. Ping, Q. Chen, J. W. Yang, M. Asif Khan, and I. Adesida, J. Electron. Mater. 27, 261 (1998).

[67] H. W. Choi, S. J. Chua, A. Raman, J. S. Pan, and A. T. S. Wee, Appl. Phys. Lett. 77, 1795 (2000).

[68] Z. Fang, S. N. Mohammad, W. Kim, O. Aktas, A. E. Botchkarev, and H. Morkov, Appl. Phys. Lett. 68, 1672 (1996).

[69] J. K. Kim, J.-L. Lee, J. W. Lee, H. E. Shin, Y. J. Park, T. Kim, Appl. Phys. Lett. 73, 2953 (1998).

[70] H. W. Jang, J. K. Kim, C. M. Jeon, and J.-L. Lee, MRS Internet J. Nitride Semicond. Res. 6.8, 1 (2001).

[71] Y.-J. Han, S. Xue, W.-P. Guo, C.-Z. Sun, Z.-B. Hao, and Y. Luo, Jpn. J. Appl. Phys. 42, 6409 (2003).

[72] D. C. Look, D. C. Reynolds, J. W. Hemsky, J. R. Sizelove, R. L. Jones, R. J. Molnar, Phys. Rev. Lett. 79, 2273 (1997).

[73] P. Boguslawski , E. L. Briggs, J. Bernholc , Phys. Rev. B 51, 17255 (1995).

[74] S. N. Mohammad, J. Appl. Phys. 95, 7940 (2004).

[75] S. J. Pearton, J. W. Lee, J. D. MacKenzie, C. R. Abernathy, and R. J. Shul, Appl. Phys. Lett. 67, 2329 (1995).

[76] C. R. Eddy, Jr. and B. Molnar, Mater. Res. Soc. Symp. Proc. 395, 745 (1996).

[77] B. Molnar, C. R. Eddy, Jr. and K. Doverspike, J. Appl. Phys. 78, 6132 (1995).

[78] D. Mistele, J. Aderhold, H. Klausing, T. Rotter, O. Semchinova, J. Stemmer, D. Uffmann, J. Graul, F. Eberhard, M. Mayer, M. Schauler, M. Kamp, and C. Ahrens, Semicond. Sci. Technol. 14, 637 (1999).

[79] S. J. Chua, H. W. Choi, J. Zhang, and P. Li, Physical review 64, 205302 (2001).

[80] J. Elsner, R. Jones, M. I. Heggie, P. K. Sitch, M. Haugk, T. Frauenheim, S. Oberg, and P.R. Briddon, Phys. Rev. B 58, 12 571 (1998).

[81] A. P. Zhang, G. Dang, F. Ren, X. A. Cao, H. Cho, E. S. Lambers, S. J. Pearton, R. J. Shul, L. Zhang, A. G. Baca, R. Hickman, and J. M. Van Hove, Journal of The Electrochemical Society 147, 719 (2000).

[82] H. Choi, S. Chua, and S. Tripathy, J. Appl. Phys. 92, 4381 (2002).

[83] J. C. Zolper, D. J. Rieger, A. G. Baca, S. J. Pearton, J. W. Lee, and R. A. Stall, Appl. Phys. Lett. 69, 538 (1996).

[84] J. Yan, M. J. Kappers, A. Crossley, C. McAleese, W. A. Phillips, and C. J. Humphreys, Phys. Stat. Sol. (b) 241, 2820 (2004).

[85] J. Yan, M.J. Kappers, Z.H. Barber, and C.J. Humphreys, Appl. Surface Science 234, 328 (2004).

[86] H. W. Jang and J.-L. Lee, Journal of The Electrochemical Society 150, G513 (2003).

[87] K.-M. Chang, C.-C. Cheng, and J.-Y. Chu, Journal of The Electrochemical Society, 149, G367 (2002).

[88] S. Tripathy, S. J. Chua, and A. Ramam, J. Phys.: Condens. Matter 14, 4461 (2002).

[89] M. Toth, K. Fleischer, and M. Phillips, Phys. Rev. B, 59, 1575 (1999).

[90] J. Neugebauer and C. Van de Walle, Appl. Phys. Lett. 69, 503 (1996).

[91] T. Mattila and R. Nieminen, Phys. Rev. B 55, 9571 (1997).

[92] L. W. Tu, Y. C. Lee, S. J. Chen, I. Lo, D. Stocker, and E. F. Schubert, Appl. Phys. Lett. 75, 2802 (1998).

[93] H. W. Choi, S. J. Chua, A. Raman, J. S. Pan, and A. T. S. Wee: Appl. Phys. Lett. 77, 1795 (2000).

[94] D. Basak, M. Lachab, T. Nakanishi, and S. Sakai, Appl. Phys. Lett. 75, 3710 (1999).

[95] W. M. Moreau, Semiconductor Lithography: Principles, Practices, and Materials, Plenum Press, New York, 1998.

[96] M. Schaepkens and G. S. Oehrlein, Journal of The Electrochemical Society, 148, C211 (2001).

[97] M. Schaepkens, T. E. F. M. Standaert, N. R. Rueger, P. G. M. Sebel, G. S. Oehrlein, and J. M. Cook, J. Vac. Sci. Technol. A 17, 26 (1999).

[98] M. Schaepkens, G. S. Oehrlein, C. Hedlund, L. B. Jonsson, and H.-O. Blom, J. Vac. Sci. Technol. A 16, 3281 (1998).

[99] M. Schaepkens, G. S. Oehrlein, and J. M. Cook, J. Vac. Sci. Technol. B 18, 848 (2000).

[100] M. Schaepkens, G. S. Oehrlein, and J. M. Cook, J. Vac. Sci. Technol. B 18, 856 (2000).

[101] C. Chu, T. Ahn, J. Kim, S. Jeong, and J. Moon, J. Vac. Sci. Technol. B 18, 2763 (2000).

[102] C. Chu, K.-K. Chi, and J.-T. Moon, J. Vac. Sci. Technol. A 20, 2042 (2002).

[103] X. Li, X. Hua, L. Ling, G. S. Oehrlein, M. Barela, and H. M. Anderson, J. Vac. Sci. Technol. A 20, 2052 (2002).

[104] N. R. Rueger, M. F. Doemling, M. Schaepkens, J. J. Beulens, T. E. F. M. Standaert, and G. S. Oehrlein, J. Vac. Sci. Technol. A 17, 2492 (1999).

[105] F. Gaboriau, G. Cartry, M-C. Peignon, and C. Cardinaud, J. Vac. Sci. Technol. B 20, 1514 (2002).

[106] H. Yoshida, T. Urushido, H. Miyake, and K. Hiramatsu, Jpn. J. Appl. Phys. 40, L1301 (2001).

[107] T. Urushido, H. Yoshida, H. Miyake, and K. Hiramatsu, Jpn. J. Appl. Phys. 41, L31 (2002).

[108] C. Yu, C. Chu, J. Tsai, H. Huang, T. Hsueh, C. Lin, and S. Wang, Jpn. J. Appl. Phys. 41, L910 (2002).

[109] C. Youtesy, L. T. Romano and I. Adesida, Appl. Phys. Lett. 73, 797 (1998).

[110] C.Youtesy, L. T. Romano, R. J. Molnar, and I. Adesida, Appl. Phys. Lett. 74, 3537 (1999).

[111] P. Visconti, K. M. Jones, M. A. Reshchikov, R. Cingolani, R. J. Molnar, and H. Morkoc, Appl. Phys. Lett. 77, 3532 (2000).

[112] T. Rotter, D. Uffmann, J. Ackermann, J. Aderhold, J. Stemmer, and J. Graul Mat. Res. Soc. Symp. Proc. 482 (1997).

[113] N.G. Weimann, L.F. Eastman, D. Doppalapudi, H.M. Ng, and T.D. Moustakas, J. Appl. Phys. 83, 3656 (1998).

[114] K. Zhu, V. Kuryatkov, B. Borisov, G. Kipshidze, S. A. Nikishin, H. Temkin and M. Holtz, Appl. Phys. Lett. 81, 4688 (2002).

[115] D. Buttari, A. Chini, G. Meneghesso, E. Zanoni, B. Moran, S. Heikman, N. Q. Zhang, L. Shen, R. Coffie, S. P. Denbaars, and U. K. Mishra, IEEE Electron Device Lett. 23, 76 (2002).

[116] D. Basak, K. Yamashita, T. Sugahara, D. Nakagawa, Q. Fareed, K. Nishino, and S. Sakai, Jpn. J. Appl. Phys. 38, 42 (1999).

[117] T. Wu, Z. Hao, G. Tang, and Y. Luo, Jpn. J. Appl. Phys. 42, L257 (2003).

[118] S. C. McNevin, J. Vac. Sci. & Technol. B 8, 1212 (1990).

[119] L. Shon-Roy, A. Wiesnoski, and R. Zorich, *Advanced Semiconductor Fabrication Handbook.* Integrated Circuit Engineering Corporation (ICE), (1998).

[120] S. King, J. Barnak, M. Bremser, K. Tracy, C. Ronning, R. Davis and R. Nemanich, J. Appl. Phys. 84, 5248 (1998).

[121] 42 - R.J. Shul, "ICP Etching of III-Nitrides," in GaN and Related Materials II, edited by S.J. Pearton (Gordon and Breach, New York 1998).

[122] G. Smolinsky, R. A. Gottscho and S. M. Abys, J. Appl. Phys. 54, 3518 (1983).

[123] A. T. Ping, M. A. Khan, and I. Adesida, Semicond. Sci. Technol. **12**, 133 (1997).

[124] D. J. Thomas, P. Southworth, M. C. Flowers, and R. Greef, J. Vac. Sci. Technol. B 7, 1325 (1989).

[125] D. J. Thomas, P. Southworth, M. C. Flowers, and R. Greef, J. Vac. Sci. Technol. B 8, 516 (1990).

[126] D. J. Thomas, P. Southworth, M. C. Flowers, and R. Greef, J. Vac. Sci. Technol. B 8, 1044 (1990).

[127] A. Matsutani, H. Ohtsuki, S. Muta, F. Koyama, and K. Iga, Jpn. J. Appl. Phys. 40, 1528 (2001).

[128] A. Matsutani, H. Ohtsuki, F. Koyama, and K. Iga, Jpn. J. Appl. Phys. 39, 1435 (2000).

[129] S. J. Ullal, H. Singh, V. Vahedi, and E. S. Aydil, J. Vac. Sci. Technol. A 20, 499 (2002).

[130] C. S. Korman, J. Vac. Sci. Technol. 20, 476 (1982).

[131] R. A. Gottscho, G. Smolinsky, and R. H. Burton, J. Appl. Phys. 53, 5908 (1982).

[132] D. A. Danner, M. Dalvie, and D. W. Hess, J. Electrochem. Soc. 134, 669 (1987).

[133] M. Rahman, L. G. Deng, J. van den Berg, and C. D. W. Wilkinson, J. Phys. D: Appl. Phys. 34, 2792 (2001).

5 Ridge waveguide fabrication

The ridge waveguide fabrication process has been developed to simplify the laser fabrication procedure and to meet some critical requirements for the best laser performance. The process includes the fabrication of a narrow ridge waveguide stripe (typically 2–4 μm), the passivation of the surface with SiO_2, and the opening of a window on the top of the stripe for *p*-contact deposition. It is very important to obtain a ridge stripe with smooth vertical sidewalls and a clean GaN surface with no contamination. The rough non-vertical sidewalls of the stripe can result in poor optical confinement in the waveguide and an increase of the threshold current for laser generation. The passivation with SiO_2 is used for the isolation of the etched surface and the ridge sidewalls during the *p*-contact deposition. The poor surface isolation may result in poor current confinement and leakages outside the waveguide. The open sidewalls of the stripe can initiate the loss of light by metal coating and an increase of the threshold current. The opening of the window on the top of the ridge waveguide stripe is used for *p*-contact deposition. For standard photolithography processing this step tends to be a challenge due to the extremely small dimensions (1–3 μm). It requires precise photolithography equipment for proper alignment and exposure. Additionally, the process of the opening has difficulties such as the serious damage of the *p*-layer of GaN after the dry etching of SiO_2 and the lateral etching of SiO_2 during wet etching. The developed procedure allows the avoidance of these problems due to self-alignment during the process and the protected surface of the ridge waveguide during the etching.

A metal Al (500 nm)/Ni (100 nm) mask was selected for the etching of the waveguide. Photoresist was found to be not stable during the etching in Cl_2-based ICP plasma due to low selectivity to GaN and a low melting temperature. The developed ICP process results in a fairly high temperature of GaN during the processing and can cause the photoresist to be melted and sublimated from the surface before the etching is finished. In contrast, the top Ni layer was found to be very stable in Cl_2-based ICP plasma. The bottom thick Al layer serves as an intermediate layer. Aluminum is very reactive with Cl_2 plasma that finally results in very suitable profile for the following lift-off of SiO_2.

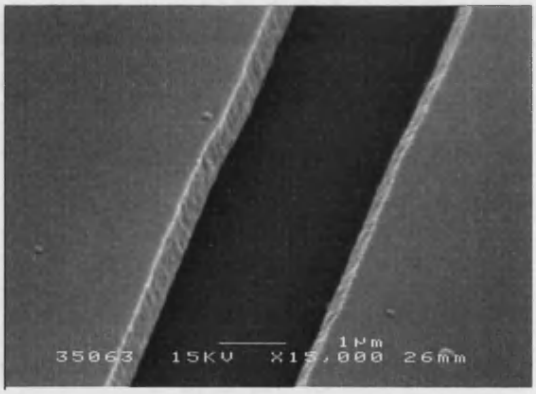

Fig. 5.1. SEM image of double-layer resist pattern before metal deposition.

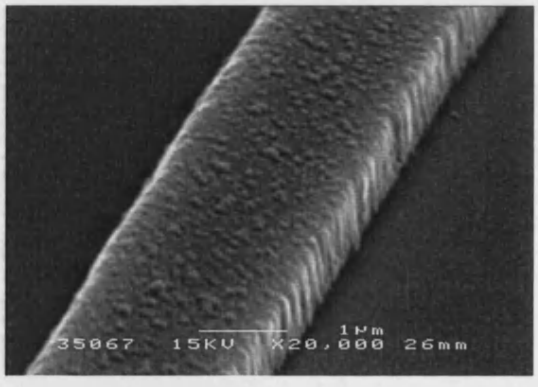

Fig. 5.2. SEM image of Al/Ni pattern for ridge waveguide fabrication.

A double-layer photolithography process with LOR-10B lift-off resist was selected to obtain the metal mask. This process results in a high quality metal pattern and allows obtaining fairly thick (<1.0 μm) and narrow (>2.0 μm) patterns without problems with the following lift-off of the deposited metal. Figure 5.1 shows an SEM image of the resist pattern after development. As can be seen, the quality of the top photoresist 1813S Shipley is quite reasonable. As a result, the Al/Ni pattern after the lift-off (Fig. 5.2) has fairly smooth vertical sidewalls suitable for the vertical etching of GaN material. The metal is deposited using an e-beam evaporator. It is

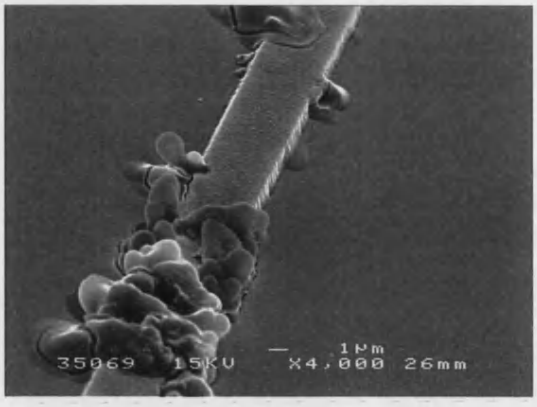

Fig. 5.3. SEM image Al/Ni mask after ridge etching.

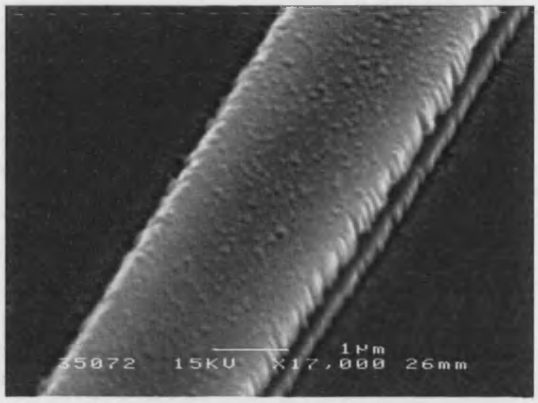

Fig. 5.4. SEM image of Al/Ni mask after cleaning in buffered HF (20:1) solution.

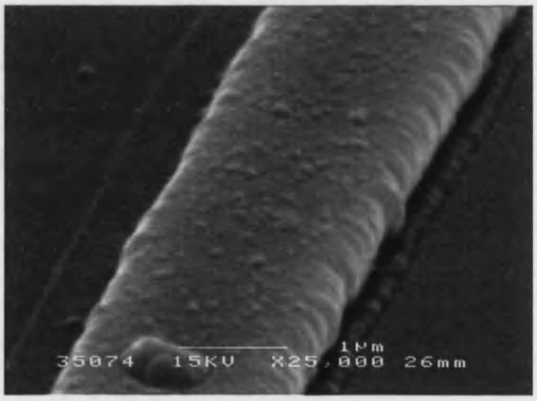

Fig. 5.5. SEM image of sputtered SiO_2 on the ridge stripe with Al/Ni mask on the top.

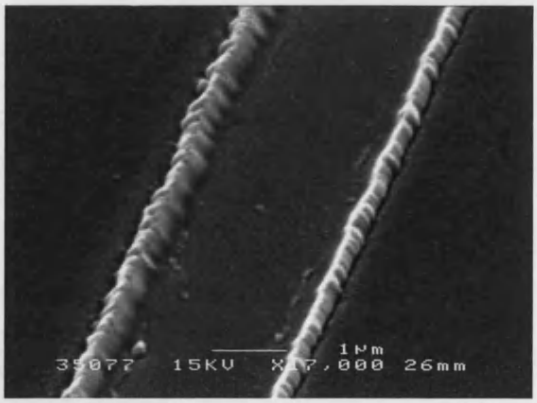

Fig. 5.6. SEM image of a contact window on top of ridge stripe after Al/Ni mask removal.

important to note that the deposition conditions can significantly affect the quality of the metal pattern. It was found that Al deposited at low rates (<2 nm/sec) tends to have very rough surface and sidewalls. Thereby the deposition rates above 5 nm/sec for Al are preferable.

The Al/Ni mask is used for the etching of the ridge waveguide in the laser structure (typical etch depth is 300–400 nm). The Ni layer serves as an actual mask to protect the Al and GaN during the etching. Aluminum is readily etched by chlorine to form $AlCl_3$, even in the absence of gas plasma.[1, 2] The passivating $AlCl_3$, which remains on the Al sidewalls after the etching is very hydroscopic and results in different forms of aluminum hydroxides when exposed to air containing water vapors.[1] In addition, HCl is liberated upon reaction of $AlCl_3$ with water. When a sample is removed from the ICP chamber the formed HCl proceeds to corrode aluminum. It results in heavily infected stripes after Cl_2 plasma etching (Fig. 5.3). Fortunately, these products were found to be easily removed in buffered HF solution (NH_4F/HF). Furthermore, the final mask shape is especially suitable for the following lift-off process due to the lateral overetch of Al under the intact Ni layer (Fig. 5.4). The cleaning in the buffered HF can also improve the undercut due to the additional etching of Al by HF acid. It is important to note that excessive exposure to the buffered HF can result in the complete removal of Al. Thereby this step should be carefully controlled and low concentrated HF solutions such as 20:1 NH_4F/HF are preferable.

The SiO_2 passivation layer is deposited by ion beam sputtering employing Ar plasma. This sputtering takes place at low process pressures (10^{-3} - 10^{-4} Torr) that results in the anisotropic deposition of SiO_2 due to the long mean free paths of species in the process chamber. The quality of deposition was found to be sufficient for proper surface isolation. In contrast, e-beam evaporated SiO_2, which also has an anisotropic profile, was found to be very porous and not suitable for proper laser processing. SiO_2 deposited by plasma enhanced chemical vapor deposition (PECVD) cannot be applied for this process due to the isotropic deposition nature, which hinders the following lift-off of SiO_2 to open the contact window on

the top of the ridge stripe. Figure 5.5 presents the sputtered SiO_2 layer (350 nm thick) on the ridge stripe with the Al/Ni pattern on the top. As can be seen, the undercut profile of the metal mask and the anisotropic deposition result in separated oxides on the GaN surface and on the top of the metal. As a result, the following removal of the metal takes also away the top oxide, opening the window for *p*-contact deposition (Fig. 5.6). It is important to note that the thickness of sputtered SiO_2 should be the same as the height of the ridge waveguide to cover the ridge sidewalls. Also the thickness of the Al mask layer should be at least the same as thickness of the oxide to prevent the joining of separated SiO_2 parts. The removal of the metal mask is performed in aqua-regia solution (3:1 HCl/HNO_3). This solution can easily etch both Al and Ni and results in a very fast reaction with a large number of gas bubbles assisting the removal of the top oxide layer. The obtained contact window allows a *p*-contact to be deposited without special concern about alignment. Figure 5.7 shows the *p*-contact deposited on the ridge waveguide. As can be seen, the contact can be significantly larger than the contact window. This makes the post-growth process much simpler and more reproducible.

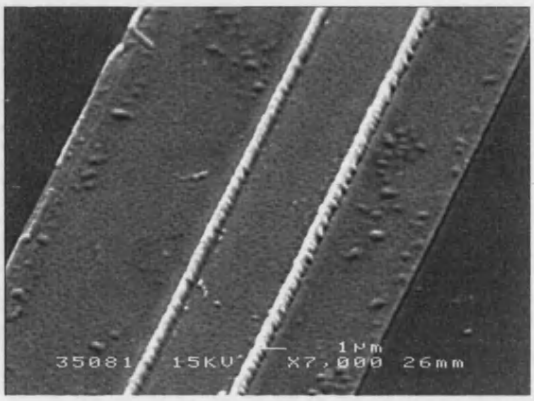

Fig. 5.7. SEM image of *p*-contact deposited in the open contact window.

[1] W. M. Moreau, Semiconductor Lithography: Principles, Practices, and Materials, Plenum Press, New York, 1998.

[2] L. Shon-Roy, A. Wiesnoski, R. Zorich (1998). Advanced Semiconductor Fabrication Handbook. Integrated Circuit Engineering Corporation (ICE).

6 Ohmic contacts to GaN

6.1 Introduction

Contacts are an integral part of the fabrication of semiconductor devices. For advanced GaN-based optical and electrical devices, it is essential to fabricate high-quality ohmic contacts, which have low resistance, excellent reliability, and thermal stability. A high contact resistance at metal/GaN interfaces results in a large voltage drop across the interface and, thereby, leads to poor device performance and reliability. To avoid excessive heating resulting in the failure of a device, a specific contact resistivity in the order of 10^{-3} $\Omega\cdot cm^2$ for light-emitting diodes (LEDs) and 10^{-4} $\Omega\cdot cm^2$ for laser diodes is required for both *n*- and *p*-contacts to GaN.

Generally, the formation of low-resistance contacts is a challenging problem for GaN-based devices, which arises from the wide band gap of GaN, with a direct band gap of 3.4 eV and an electron affinity of 4.1 eV.[1] It usually results in a large barrier height when a metal is deposited on the semiconductor material. Ohmic contacts to *n*-type GaN are usually achieved by electron tunneling through the barrier thinned by heavy doping on the semiconductor side. For contacts to *p*-type GaN, however, it entails particular problems due to the resistive nature of GaN obtained by standard *p*-type doping techniques. Nevertheless, significant progress has been made during the last few years. This chapter provides an up-to-date review of contact technologies for both *p*- and *n*-type GaN along with a theory associated with contact mechanisms. The results obtained by our group for the most promising contact systems are also presented and discussed.

6.2 Metal/GaN contact mechanisms

Contacting a metal to a semiconductor layer results in bending of the valence and the conduction bands within the semiconductor and an energy barrier for carriers at the interface. The barrier height for an ideal Schottky contact (ϕ_B) is equal to the difference between the work function of a metal (ϕ_m) and either the electron affinity of a semiconductor (χ_s) [Fig. 6.1(a)] for *n*-type or the sum of the electron affinity and bandgap of a semiconductor (E_g) [Fig. 6.1(b)] for *p*-type.

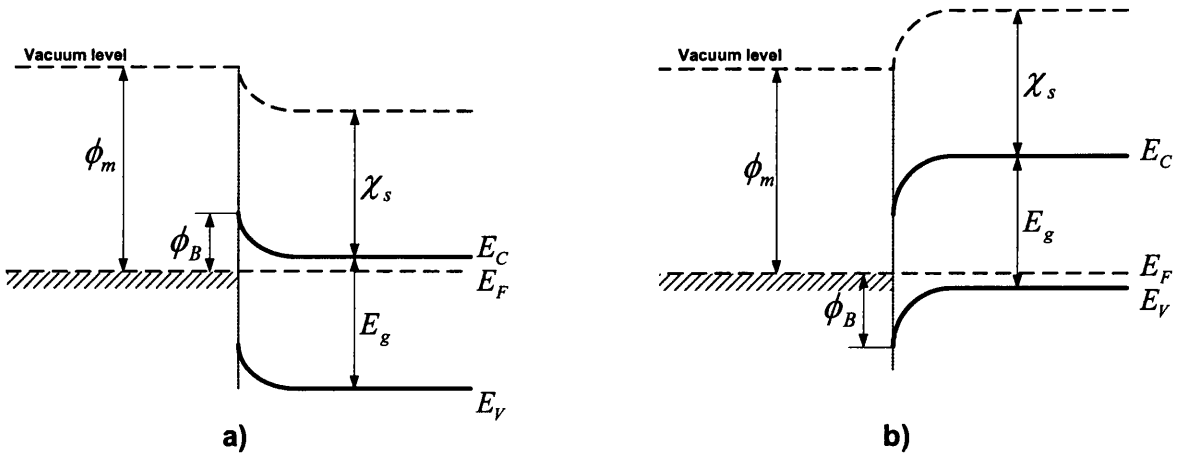

Fig. 6.1. Schematic diagram of band offsets for a metal on n-type (a) and p-type (b) semiconductor.

However, this dependence has not been observed for a large number of semiconductors, including Si, GaAs etc. It was attributed to the existence of surface states within a semiconductor bandgap, which pin the Fermi level at the interface. As a result, the barrier height would be independent of the metal work function.[2] Which contact mechanism dominates, depends on the semiconductor material and the interface conditions. According to Kurtin *et al.*[3] GaN has a large electronegativity difference between the constituent elements (1.87 eV) and, thereby, the Schottky barrier heights between metals and GaN should be totally unaffected by Fermi level pinning type effects. Figure 6.2 shows the change in the barrier height over the change in the metal work function ($S = d\phi_B / d\phi_m$) as a function of electronegativity difference between the components of a compound (ΔX). As can be seen, the Schottky barrier height on GaN should directly depend on the work function of a metal. The electron affinity and bandgap of GaN has been measured to be 4.1 eV and 3.4 eV, respectively. Therefore, any metal with a work function equal to or lower than 4.1 eV should form an ohmic contact to *n*-type GaN and any metal with a work function equal to or higher than 7.5 eV is expected to form an ohmic contact to *p*-type GaN.

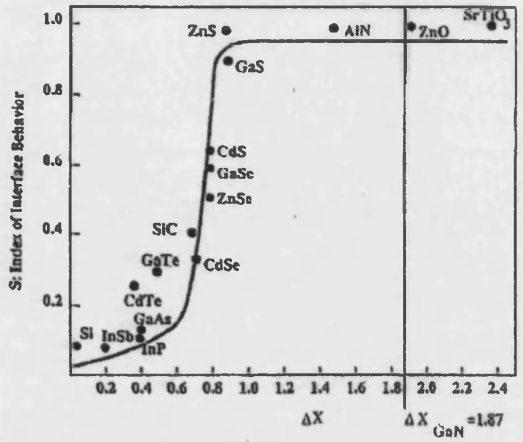

Fig. 6.2. Dependence of $S = d\phi_B / d\phi_m$ (change in barrier height over the change in metal work function) on the electronegativity difference between the components of a compound.

In practice, the agreement with the Schottky rule is not entirely conclusive. On the one hand, Schottky barrier measurements on *n*-type GaN revealed that ϕ_B does vary with ϕ_m.[1, 4, 5, 6] On the other hand, Mori *et al.*[7] reported that Schottky barrier heights on *p*-type GaN only weakly depend on the work function of a metal, even though they tend to decrease with an increase in the metal work function. They concluded that the metal work function is not the predominant factor affecting the Schottky barrier characteristics on *p*-GaN. The reported results are difficult to compare due to the differences in sample carrier concentration, surface preparation prior to deposition, method of metal deposition, and in the techniques used to characterize contacts (current-voltage, capacitance-voltage, internal photoemission etc.). Furthermore, current-voltage (*I-V*) and capacitance-voltage (*CV*) measurements could be significantly affected by defects at the semiconductor/metal interface. Recently Rickert *et al.*[8] determined Schottky barrier heights of metals to both *n*- and *p*-type GaN using synchrotron radiation-based x-ray photoemission spectroscopy. The results obtained for metals deposited on the *n*-GaN and on the *p*-GaN are presented in Fig. 6.3(a) and Fig. 6.3(b) respectively. As can be seen, the results yield roughly linear trends, although the slopes of linear fits, corresponding to the change in the barrier height over the change in the metal work function ($S = d\phi_B / d\phi_m$), are lower than predicted by Kurtin *et al.* A slope with a value of 0.7 and 0.8 was observed for *n*- and *p*-GaN, respectively. The authors investigated two different Fermi-level pinning behaviors observed over the range of metals investigated. They found that for Au, Ti, and Pt, the surface Fermi level lies about 0.5 eV higher in the gap for *n*-type than for *p*-type GaN. It was suggested that two pinning positions exist within the bandgap, depending on the carrier type, indicating the presence of two types of surface states. For three other metals, Ni, Al, and Pd, the surface Fermi level position is independent of doping, but varies from one metal to the other. It was concluded that the barrier heights for Ni, Pd, and Al exhibit a modified Schottky (not pinned) behavior. Thereby non-ideal behavior of a metal on GaN appears to result from the

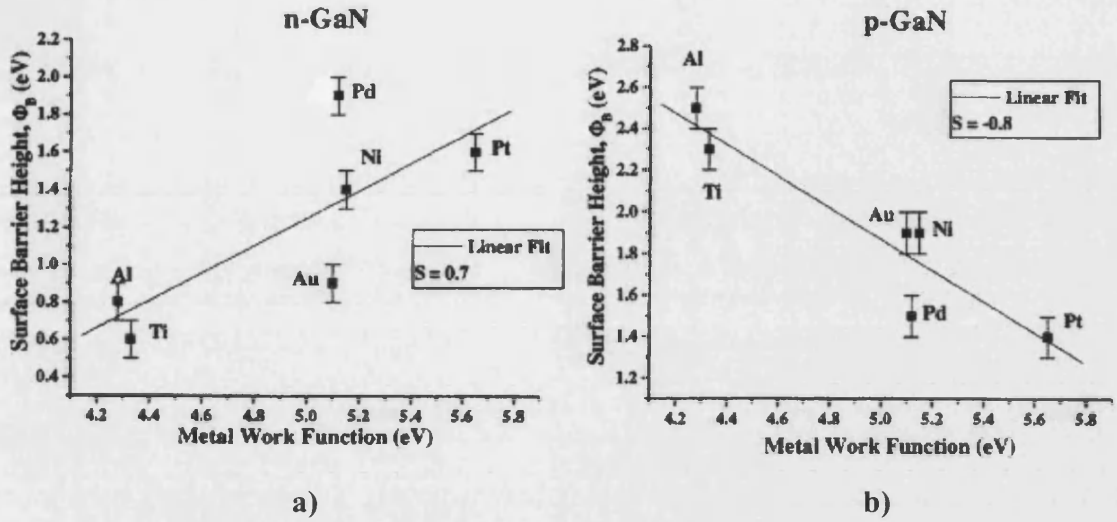

Fig. 6.3. The measured surface-barrier heights as a function of the work function of a metal for *n*-GaN (a) and for *p*-GaN (b). $S = d\phi_B / d\phi_m$ is the slope of a linear fit.

presence of several transport mechanisms, depending on many factors, such as the type of metal deposited, carrier type and concentration, stoichiometry and roughness of GaN surface, defects present in a film, surface preparation prior to deposition, etc.

There are four main mechanisms for the transport of carriers over a Schottky barrier, thermionic emission (TE), field emission (FE), thermionic field emission (TFE), and tunneling through deep levels.[9] For a contact on a low-doped semiconductor, the thermionic emission, when thermally energetic electrons (holes) pass over the barrier, dominates the current transport. In this case the specific contact resistivity (ρ_c) is given by

$$\rho_c = \frac{k}{qA^*T}\exp\left(\frac{\phi_B}{kT}\right) \qquad [6.1]$$

k – Boltzman constant
q – elementary charge
A^* – Richardson constant
ϕ_B – barrier height (eV)
T – temperature (K)

For a contact on a high-doped semiconductor, the field emission (tunneling) dominates the current transport, when electrons (holes) pass through very thin barrier. The specific contact resistivity is given by

$$\rho_c = \frac{k}{qA^*}\exp\left(\frac{\phi_B}{E_{00}}\right)\left(\frac{\pi T}{\sin(\pi c_1 kT)} - \frac{1}{c_1 k}\exp\left(-c_1 E_f\right)\right)^{-1} \qquad [6.2]$$

where

$$E_{00} = \frac{hq}{4\pi}\sqrt{\frac{N_d}{m^*\varepsilon_s}} \qquad [6.3]$$

$$c_1 = \frac{1}{2E_{00}} \ln\left(\frac{4\phi_B}{E_f}\right) \qquad [6.4]$$

ε_s – semiconductor permittivity
m^* – effective carrier mass
h – Plank's constant
N_d – effective carrier concentration
E_f – position of the Fermi level, defined as positive above the bottom of the conductive band (see Fig. 6.4)

In the case of thermionic field emission, when both the thermionic and field emission mechanisms are involved in the transport of carriers over a Schottky barrier, the specific contact resistivity is given by

$$\rho_c = \frac{k^2}{qA^*} \frac{1}{\sqrt{\pi(\phi_B + E_f)E_{00}}} \cosh\left(\frac{E_{00}}{kT}\right) \sqrt{\coth\left(\frac{E_{00}}{kT}\right)} \times \exp\left(\frac{\phi_B + E_f}{E_0} - \frac{E_f}{kT}\right) \qquad [6.5]$$

where

$$E_0 = E_{00} \coth\left(\frac{E_{00}}{kT}\right) \qquad [6.6]$$

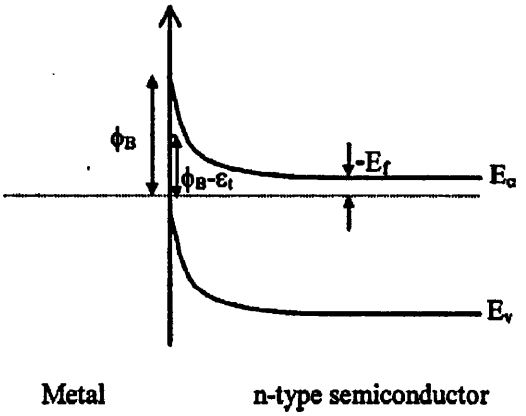

Field emission becomes dominant for $qE_{00}/kT > 1$, thermionic field emission for $qE_{00}/kT \approx 1$, and thermionic emission for $qE_{00}/kT < 1$, with $q/kT \approx 0.026$ eV at 300 K.[10]

Fig. 6.4. Schematic description of the band bending at the metal/semiconductor interface.

In addition to the mechanisms illustrated above, the current transport over the Schottky barrier can also be affected by Fermi level pinning effects, caused by interface states within the semiconductor bandgap. A large concentration of deep energy levels at an energy ε_t (see Fig. 6.4) in the depletion semiconductor layer may significantly enhance tunneling through the barrier via these levels. The contact resistivity in this case is given by

$$\rho_c = \frac{2kT}{q^2 N_t \upsilon w_t} \exp(\alpha_t w_t) \exp\left(\frac{\phi_B - \varepsilon_t}{kT}\right) \qquad [6.7]$$

where

$$\alpha_t = \frac{2}{h}\sqrt{2m^* \varepsilon_t} \qquad [6.8]$$

N_t – concentration of deep levels
υ – jump attempt frequency
w_t – average distance between states

As can be seen, the contact resistivity at the metal/semiconductor contact depends only on the Schottky barrier height in the case of thermionic emission (see Eq. 6.1), whereas for field emission it directly depends on the Schottky barrier height and inversely depends on the square root of the carrier concentration (see Eq. 6.2). Thereby, the tunneling becomes the dominant transport mechanism for heavily doped semiconductors if the Schottky barrier is high enough to pass it over at operation temperatures. The tunneling mechanism can also be enhanced for moderately doped semiconductors if the material is heavily doped in the proximity of the metal/semiconductor interface. It leads to significant band bending of the conduction and valence band, as shown in Fig. 6.5. The semiconductor region at the interface thus becomes degenerate and very thin, allowing unhindered flow of carriers via tunneling. Heavy doping of the semiconductor surface adjacent to the metal can be achieved by epitaxial growth, ion implantation and annealing of the surface, or by the deposition and subsequent annealing of a metallization, which effectively dopes the surface through interfacial reactions with the semiconductor.

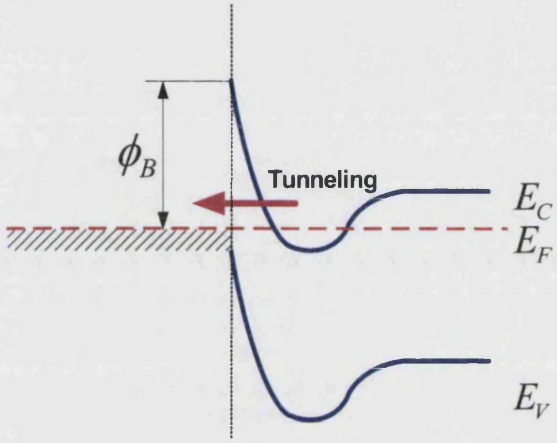

Fig. 6.5. Schematic diagram of the band bending due to heavy doping of the semiconductor surface, and tunneling through the metal/semiconductor interface.

The mechanism that is predominant in the transport of carriers over the Schottky barrier can be verified from the $\rho_c(T)$ dependence. The thermionic emission is an activated process and it responds significantly to the temperature, as can be seen from Eq. 6.1. In contrast, the field emission is not an activated process, and hence it is weakly dependent on the temperature (see Eq. 6.2). However, if the effective carrier concentration depends on the temperature (for deep-level doping materials, such as Mg-doped *p*-GaN material), the increased concentration at elevated temperatures significantly enhances the tunneling probability.

Metals with a work function lower than 4.1 eV, required for ohmic contact to *n*-GaN, are not widely available. Metals with a work function higher than 7.5 eV, required for *p*-GaN, do not exist at all. Therefore, the possibility of thermionic emission as a mechanism for carrier transport through the contact is low for both *n*-type and *p*-type GaN. Today, it is widely believed that the formation of good ohmic contacts to *n*-GaN necessitates a special transport mechanism, such as tunneling.[11, 12] A high doping concentration at the *n*-GaN surface can easily be obtained by introducing dopants from overlay metals through an annealing process, Si-implantation and subsequent activation annealing, reactive ion etching (RIE), wet chemical treatment, etc. For *p*-GaN, a large

Schottky barrier and the low doping level ($<10^{18}$ cm^{-3}) achieved by standard *p*-type doping techniques, make the tunneling probability very low. It is difficult to increase surface *p*-type doping by implantation in GaN because of the large ionization levels of acceptor species and the *n*-type character of residual lattice damage. Furthermore, while a carrier concentration of 2×10^{18} cm^{-3} is sufficient to raise the Fermi level to the conduction band in *n*-type GaN, in *p*-type GaN a much higher value of 2×10^{19} cm^{-3} is required. It has been suggested that the surface defects, generated during predeposition chemical treatment[13] and/or high temperature contact annealing, can be responsible for carrier transport in a metal/*p*-GaN system. They introduce deep energy levels inside the depletion layer, pinning the Fermi level in *p*-GaN. Which specific mechanism is responsible for the current transport through a metal/GaN contact depends on many factors, such as the type of metal deposited, conditions for contact annealing, carrier type and concentration in GaN, stoichiometry of GaN surface, surface preparation prior to deposition, etc.

6.3 Methods of contact characterization

Ohmic contacts are usually characterized by measuring the specific contact resistivity ρ_c between a metal and a semiconductor. The specific contact resistivity is independent of the contact area and represents the resistance of a 1 cm^2 contact. The commonly used characterization technique is a transmission line method. In this method, the contact is treated as a transmission line and equations are derived and solved to yield the specific contact resistivity and related parameters. There are two main modifications of this method, with a rectangular and with a circular contact geometry, called a linear transmission line model (TLM) and a circular transmission line model (CTLM), respectively. Both of them are extensively used for characterizing contacts on GaN.

TLM requires the formation of a contact pattern consisting of an array of rectangular pads of equal size separated by varying distances [Fig. 6.6(a)]. To confine the current flow only between the contact pads, the model also involves mesa etching to remove the semiconductor around the TLM pattern. The total resistance R_{pp} between a pair of contacts, obtained as V/I from the *I-V* curve, can be expressed by

$$R_{pp} = R_{sh}\frac{d + 2L_T}{Z} \qquad [6.9]$$

R_{sh} – sheet resistance of a semiconductor layer
d – spacing between contact pads
Z – length of a rectangular pad
L_T – transfer length

CTLM eliminates the need for the mesa etching required for the TLM pattern. The CTLM contact pattern is shown in Fig. 6.6(b). The total resistance R_{pp} between an inner circle and an adjacent field, evaluated from the *I-V* curve, can be expressed by

$$R_{pp} = \frac{R_{sh}}{2\pi}\left[\ln\left(\frac{r_o}{r_i}\right) + L_T\left(\frac{1}{r_o} + \frac{1}{r_i}\right)\right] \qquad [6.10]$$

r_o – outer radii of a circular pattern
r_i – inner radii of a circular pattern

The transfer length L_T is the averaged part of a contact involved in the current flow. It depends on the ratio of the specific contact resistivity ρ_c in $\Omega \cdot cm^2$ and sheet resistance R_{sh} in Ω under the contact and can be expressed by

$$L_T = \sqrt{\rho_c / R_{sh}} \qquad [6.11]$$

Both techniques use the difference in the total resistance between pairs of contacts separated by different distances. Free parameters R_{sh}, ρ_c, and L_T can be matched to fit R_{pp} values of different spacings using Eq. 6.9 and 6.10. The validity of the method depends on general conditions, such as $L_T<W$ or $L_T<r_i$, d or (r_o-r_i) much larger than the thickness of the semiconductor layer, and a negligible metal sheet resistance. The accuracy of this method mainly depends on the spacing error. The accuracy increases with decreasing sheet resistance and increasing the contact resistivity, which both lead to a higher value of L_T. In general, contact resistivities down to 10^{-7} $\Omega \cdot cm^2$ can be determined fairly accurately using the transmission line method.[14]

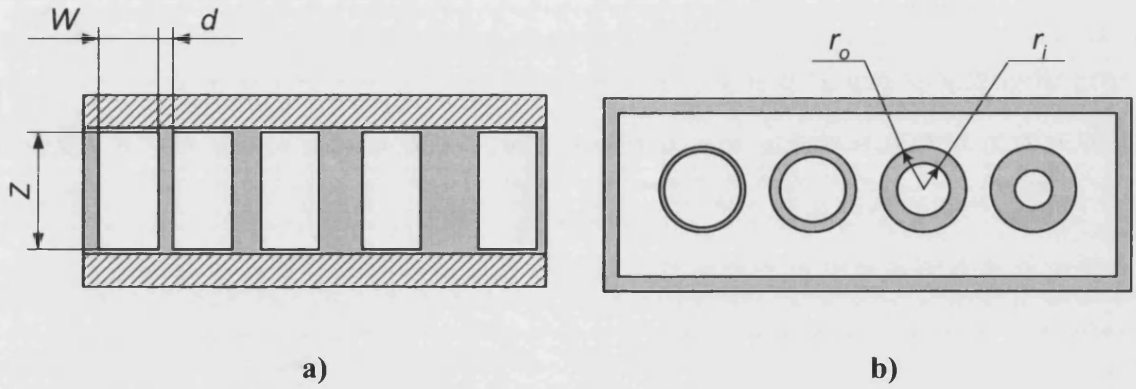

Fig. 6.6. A linear transmission line model (TLM) contact pattern (a) and a circular transmission line model (CTLM) contact pattern (b) (white – metallization, grey – semiconductor, hatched – substrate).

6.4 A review of ohmic contacts to *n*-GaN

The first published investigation of contacts to *n*-GaN was reported by Foresi and Moustakas. Contact resistivities of 10^{-4} and 10^{-3} $\Omega \cdot cm^2$ were realized using Al and Au metallizations, respectively. They suggested that the Schottky barrier heights are dependent on the metallic work function and that the surface Fermi level of GaN is unpinned. We showed above that the barrier height does vary with the metal work function, although the change in the barrier over the change in the work function ($S = d\phi_B / d\phi_m$) is lower than that predicted by the Schottky theory. As a result, metals with a work function equal to or lower than the GaN electron affinity (4.1 eV) are expected to form ohmic contacts to *n*-type GaN in the case of only thermionic emission. However, it was also shown above that different transport mechanisms (tunneling, thermionic emission, Fermi level pinning) can be involved in a metal/GaN contact depending on the materials and process factors. Tunneling is believed to be the main mechanism for metals contacting *n*-type GaN.[11, 12] Low work function metals indeed yield the most promising contacts, which is in agreement with Eq. 6.2 for field emission transport. Work functions of some representative metals are presented in Table 6-1.

Table 6-1. Work functions of some metals.

Metal	Work function (eV)	Reference
Au	5.1 - 5.2	6, 7, 8, 15
Pt	5.6 - 5.7	6, 7, 8, 15
Al	4.1 – 4.3	8, 15, 16
Ti	4.0 - 4.3	6, 7, 8, 15, 16
Pd	5.1 - 5.2	6, 8, 15, 16
Ni	5.1 - 5.2	6, 7, 8
Ag	4.3	6
Pb	4.3	6
Cr	4.5	6
Rh	5.0	17
Re	5.1	18
Ga	4.0	16
Ta	4.3	16
V	4.3	19
Mo	4.7	11
Cu	4.5	11

A wide variety of ohmic contact systems have been employed and reported for *n*-type GaN. Among them, Ti/Al system has become the conventional widely used contact, often protected with capping metal layers to reduce contact degradation. However, many other contact schemes also showed low-resistivity ohmic behavior and reliable performance. A summary of the published contacts is presented in Table 6-2.

Table 6-2. Characteristics of published results on ohmic contacts to *n*-GaN.

Mater.	Contact layers	Contact resistiv. ($\Omega \cdot cm^2$)	Carrier density (cm^{-3})	Treatment before photo-lithography	Treatment before metal deposition	Alloying condition	Ref.
GaN	Al	$\sim 10^{-4}$	3.0×10^{18}			no	4
GaN	Al 150 nm	8.0×10^{-6}	7.0×10^{17}			600°C/5 min /Ar(4% H_2)	20
GaN	Ti 20 and 250 nm	3.0×10^{-6}	1.7×10^{17}			975 °C/30 s	21
GaN	Ti 3 nm	8.7×10^{-5}	6.0×10^{17}		Aqua-regia /10 min	700 °C /40 s/N_2	22
GaN	Ti/Al 20/100 nm	8.0×10^{-6}	1.0×10^{17}			900 °C /30 s/N_2	23
GaN	Ti/Al 30/200 nm	1.3×10^{-3}	2.0×10^{17}	1120°C/15 s/N_2		no	24
		1.0×10^{-5}	2.0×10^{17}	Si implant. + 1120°C/15 s/N_2		no	
GaN	Ti/Al 35/115 nm	7.0×10^{-6}	5.0×10^{17}			400 °C /5 min/Ar	20

GaN	Ti/Al 40/100 nm	5.0×10^{-5}	6.0×10^{16}		NH_4OH 50°C/15 min	600 °C /1 min/N_2	25
GaN	Ti/Al 50/150 nm	5.0×10^{-5}	5.0×10^{17}		$(NH_4)_2S_x$ 60°C/20 min	no	26
GaN	Ti/Al 30/100 nm	9.4×10^{-6}	1.2×10^{18}	ICP in Cl_2 /3 min	HCl:H_2O (1:1)/3 min	no	27
GaN	Ti/Al 30/100 nm	6.8×10^{-6}	1.0×10^{18}	ICP in Cl_2 /1 min	HCl:H_2O (1:1)/2 min	no	28
GaN	Ti/Al 30/80 nm	4.8×10^{-4}	3.0×10^{18}	CH_3CSNH_2/NH $_4$OH/60°C/10 m		no	29
		3.1×10^{-6}	3.0×10^{18}	CH_3CSNH_2/NH $_4$OH/60°C/10 m		700 °C /1 min/N_2	
GaN	Ti/Al 25/100 nm	1.2×10^{-5}	1.1×10^{18}		H_2O:NH_4OH (10:1)/10 s	950°C/2 min /vacuum	30
GaN	Ti/Al 10/100 nm	2.0×10^{-4}	5.0×10^{18}	NH_4OH /20 min	O_2 plasma /20 s	no	31
		$\sim 10^{-7}$	5.0×10^{18}	NH_4OH /20 min	O_2 plasma /20 s	500 °C /1 min/Ar	
GaN	Ti/Al/Ni/Au 25/100/20/80 nm	1.2×10^{-5}	1.1×10^{18}		H_2O:NH_4OH (10:1)/10 s	1100°C/2 m /vacuum	30
GaN	Ti/Al/Ni/Au 15/220/40/50 nm	3.3×10^{-6}	4.0×10^{17}	RIE		no	14
		8.9×10^{-8}	4.0×10^{17}	RIE		900 °C/30 s	
GaN	Ti/Al/Pt/Au 20/200/40/200 nm	3.8×10^{-5}	9.0×10^{18}			675 °C /2 min/Ar	32
GaN	Ti/Al/Pt/Au 25/100/50/200 nm	7.0×10^{-6}	6.7×10^{17}		HCl:H_2O (1:10)/3 min	850 °C /5 min/N_2	33
AlGaN	Ti/Al/Pt/Au 15/100/40/200 nm	1.6×10^{-4}	1.3×10^{18}			850 °C /5 min/N_2	34
AlGaN	Ti/Al/Cu/Au 85/50/80/100 nm	3.9×10^{-4}	5.0×10^{17}			800 °C /30 s/N_2	35
AlGaN	Si/ Ti/Al/Cu/Au 3/85/50/80/100 nm	3.8×10^{-5}	5.0×10^{17}			800 °C /30 s/N_2	35
GaN	Ti/Al/Ti/Au 30/100/30/30 nm	5.2×10^{-6}	1.4×10^{20}	RIE		no	36
		6.0×10^{-7}	1.4×10^{20}	RIE		750 °C/30 s	
		5.1×10^{-5}	5.2×10^{17}	RIE		900 °C/30 s	
GaN	Ti/Al/Ti/Au 30/100/30/30 nm	9.8×10^{-6}	5.0×10^{17}		HF:HCl:H_2O (1:1:10)/30 s	650 °C /30 s/Ar	37
		3.0×10^{-6}	5.0×10^{17}		HF:HCl:H_2O (1:1:10)/30 s	800 °C /30 s/Ar	
GaN	Ti/Al/Ti/Au 30/100/30/30 nm	1.2×10^{-3}	6.0×10^{17}	RIE	HF:HCl:H_2O (1:1:10)/10 s	no	38
		3.6×10^{-4}	6.0×10^{17}	RIE + Aqua- regia/5min	HF:HCl:H_2O (1:1:10)/10 s	no	
		7.0×10^{-5}	6.0×10^{17}	RIE + KOH/5 min	HF:HCl:H_2O (1:1:10)/10 s	no	
GaN	Ti/Al/Mo/Au 15/60/35/50 nm	4.7×10^{-7}	1.0×10^{18}	RIE in $SiCl_4$		850 °C /30 s/N_2	39
GaN	Ti/Al/Pd/Au 25/220/60/200 nm	2.8×10^{-4}	1.0×10^{19}		Aqua-regia /10 min	no	40
		4.2×10^{-8}	1.0×10^{19}		Aqua-regia /10 min	500 °C /8 min/N_2	
GaN	Ti/Al/$TiAl_3$ 35/115/50 nm	1.1×10^{-5}	3.0×10^{18}	H_2SO_4:H_3PO_4: H_2O (1:1:2)/5 s	HCl:H_2O (1:4)/25 s	600 °C /5 min/air	41
GaN	Cr 80 nm	1.0×10^{-4}	1.1×10^{18}		H_2O:NH_4OH (10:1)/10 s	800°C/2 min /vacuum	42
GaN	Cr/Al 25/120 nm	3.8×10^{-5}	1.1×10^{18}		H_2O:NH_4OH (10:1)/10 s	700°C/2 min /vacuum	42
GaN	Cr/Al/Ni/Au 25/120/40/80 nm	2.4×10^{-5}	1.1×10^{18}		H_2O:NH_4OH (10:1)/10 s	950°C/2 min /vacuum	42
GaN	Pd/Al 25/125 nm	6.0×10^{-5}	7.0×10^{17}		HCl:H_2O (1:1)/3 min	600 °C /30 s/Ar	43
GaN	Ti/Au	9.2×10^{-5}	2.2×10^{16}	1150°C/30 s/N_2		no	44

	3/300 nm	3.6×10^{-8}	2.2×10^{16}	Si implant. + 1150°C/30 s/N_2		no	
GaN	Ti/Pd/Au 40/40/200 nm	6.4×10^{-4}	1.0×10^{19}		Aqua-regia /10 min	no	40
GaN	Ti/Au/Pd/Au 20/60/40/50 nm	1.0×10^{-4}	6.0×10^{17}		$HCl:H_2O$ (1:1)/3 min	800 °C /30 s/air	45
		8.0×10^{-7}	6.0×10^{17}		$HCl:H_2O$ (1:1)/3 min	800 °C /30+15 s/air	
		2.4×10^{-9}	1.0×10^{20}		$HCl:H_2O$ (1:1)/3 min	800 °C /30 s/air	
GaN	Ti/Ag 15/150 nm	6.5×10^{-5}	1.7×10^{19}		BOE /5 min	no	46
GaN	W 50 nm	8.0×10^{-5}	1.5×10^{19}		$H_2O:NH_4OH$ (20:1)	600 °C /1 min/N2	47
GaN	W 300 nm	2.6×10^{-6}	1.0×10^{20}	Si implant. + 1150°C		950 °C /10 s/N2	48
GaN	W and $WSi_{0.45}$ 50 nm	$\sim 10^{-4}$	1.0×10^{19}			800 °C /1 min/N_2	49
		$\sim 10^{-6}$	$\sim 10^{16}$	Si implant. + 1400°C/10 s		950 °C /1 min/N_2	
GaN	W 200 nm	3.6×10^{-4}	1.8×10^{19}		HCl /1 min	no	50
		1.0×10^{-4}	1.8×10^{19}		HCl /1 min	1000 °C /30 s/N_2	
GaN	Ti/W/Au 12/20/50 nm	8.4×10^{-6}	4.0×10^{18}	BOE /10 min	BOE /1 min	900 °C /1 min/N_2	51
GaN	NiAl (50:50) 120 nm	9.4×10^{-6}	2.5×10^{17}	$H_2SO_4:H_3PO_4:H_2O$ (1:1:2)/5 s	$HCl:H_2O$ (1:3)/20 s	850 °C /5 min/Ar	52
GaN	Ti/Si/Ti/Au 15/146/40/100	7.5×10^{-6}	1.5×10^{18}		$HCl:H_2O$ /1 min	900 °C /3 min/N_2	10
GaN	Hf 100 nm	7.5×10^{-5}	2.5×10^{18}	KOH (45%) /70°C/60 min		no	53
GaN	V 60 nm	2.3×10^{-4}	2.0×10^{18}	BOE /20 min	BOE /3 min	850 °C /2 min/N_2	19
GaN	V/Ti/Au 20/60/20 nm	4.0×10^{-6}	2.0×10^{18}	BOE /20 min	BOE /3 min	850 °C /2 min/N_2	19
GaN	Ta/Ti/Ni/Au 5/50/20/15 nm	5.0×10^{-6}	5.0×10^{17}	$HCl:H_2O_2:H_2O$ (1:1:5)/3 min	$HF:HCl:H_2O$ (1:1:10)/15 s	750 °C /45 s/Ar	16

As can be seen, there are large discrepancies in the results reported by different groups for standard contacts on GaN. They appear to result from variations in the many material and process factors, such as semiconductor doping level, material quality, surface roughness, predeposition treatment, alloying conditions, etc. However, the optimized processing conditions (annealing, predeposition treatment) for each metallization scheme should yield optimal results for *n*-GaN layers of different doping level and quality. The optimal alloying conditions (temperature, time, ambient) depend on the contact system used, whereas the predeposition treatment affects contact quality independently of the contact scheme and can be considered separately.

6.4.1 Predeposition surface treatment

Surface doping level is the primary factor affecting the contact resistance at a metal/*n*-GaN interface where tunneling is the main transport mechanism. Thereby, any predeposition treatment that enhances the surface carrier concentration should reduce the contact resistance (see Eq. 6.2). For *n*-GaN layers this is usually achieved by the accumulation of N-vacancies in a near-surface region. The nitrogen vacancies act as donors in GaN and can be sufficient to generate about a 100 Å thick layer with a doping concentration as high as 10^{19}–10^{20} cm^{-3}. Furthermore the treatment should efficiently remove native surface oxides and hydroxides. It has been shown that the residual oxide

acts as an additional barrier to current flow through the metal/*n*-GaN interface[54] hampering the formation of low-resistivity ohmic contacts. Thus, the removal of the oxide layer is also essential prior to metal deposition. The commonly used techniques employed before metallization to *n*-GaN are illustrated below.

RIE surface treatment

Reactive ion etching (RIE) and its high plasma density variations, such as inductively coupled plasma etching (ICP), electron cyclotron resonance etching (ECR-RIE), and chemically assisted ion beam etching (CAIBE), are widely employed to etch III-nitride materials. For optical devices (LED, LD), RIE is used to etch through the structure and to get access to *n*-type layers. Thereby, the *n*-GaN surface is exposed by plasma treatment before contact deposition. Fortunately, it has been found that the RIE exposure leaves the surface highly *n*-type as a result of preferential sputtering of nitrogen from the GaN surface.[11, 14, 27, 55] As a result, the Fermi level at the surface of *n*-type GaN shifts to the conduction band edge, resulting in a decrease of the Schottky barrier height for electron transport.[27, 28, 55] Both a reduction of the barrier and an increase of the surface electron concentration greatly enhances the tunneling probability through the metal/*n*-GaN interface. Besides, the RIE treatment provides a clean oxide-free surface ready for metal deposition. Plasma etching also often increases the GaN surface roughness and, hence, increases the contact area and improves metal adhesion. As a result of RIE treatment, a reduced contact resistivity for standard contacts both alloyed and non-alloyed have been reported by a large number of groups.[14, 27, 28, 31, 36, 38, 39, 55, 56, 57] The simplicity of this method, its compatibility with the device fabrication process, and the possibility to avoid contact alloying make this predeposition treatment very promising for *n*-contact formation.

High temperature premetallization annealing

High temperature annealing can also modify the GaN surface through preferential loss of nitrogen. It was reported that nitrogen desorbs from the surface at temperatures higher than 600 °C.[58] At temperatures close to the GaN decomposition temperature (1000–1100 °C), serious nitrogen desorption occurs. The N-vacancies lead to an increased electron concentration in a near-surface region and, hence, to the improved tunneling of carriers through metal/*n*-GaN interface. Lester *et al.* and Burm *et al.* have reported that the annealing of *n*-GaN at 1120–1150 °C for 15–30 s prior to metallization allowed low-resistance ohmic contacts to be formed without postdeposition alloying. Unfortunately, the annealing at such high temperatures seriously degrades *p*-GaN layers. It makes this method difficult to employ for optical devices where ohmic contact to both *n*- and *p*-GaN are required.

Dopant implantation

Another method of increasing the surface electron concentration is ion implantation and subsequent activation annealing. Si^+ implantation was found to produce *n*-type doping levels up to 5×10^{20} cm^{-3}, while other donors were less effective.[59, 60] The process also requires a high temperature (~1100 °C) annealing step to activate implanted donors in GaN. It increases the surface doping level even more due to the large number of nitrogen vacancies produced. It finally results in low-resistance ohmic contacts even without postdeposition annealing.[24, 44] However, this technique is also dangerous for *p*-GaN layers due to the high temperature annealing step involved and can not be easily applied for the fabrication of optical devices.

Chemical surface treatment

A large number of chemical solutions have been employed to remove surface oxides and to modify the surface prior to metallization. The commonly used solutions are HCl, HF, buffered oxide etch (BOE), aqua-regia, KOH, $(NH_4)_2S_x$, NH_4OH, NaOH, and different combinations of these chemicals. The impact of some of them for contacts to *n*-GaN is illustrated below.

HCl-based solutions As with other III-V compound semiconductors, HCl acid, often diluted with H_2O, is very effective in removing the native oxide on GaN surface though not completely.[11, 54] HCl treatment has also been found to result in a higher Ga/N ratio relative to an untreated surface due to the removal of N-based species from the surface.[28, 61, 62] It leads to a shift of the surface Fermi level toward the surface conduction band minimum and, hence, causes a decrease in band bending and the surface barrier height. Indeed, it was reported that the HCl treatment for 20 min prior to deposition of a standard *n*-contact (Ti/Al) on *n*-GaN produced a specific contact resistivity about 5 times lower compared with that for untreated *n*-GaN.[63] Thereby, this ordinary treatment is fairy effective for *n*-contact formation. Although it is not as successful as RIE treatment, the HCl solution was found to improve RIE results through removing Ga-oxides unintentionally formed under plasma exposure.[27, 55]

HF-based solutions Treatment in HF acid or in a buffered oxide etch solution ($HF:NH_4F$) is also fairly effective in removing the native oxide on a GaN surface although it is not as successful as treatment in HCl solutions. Additionally this common acid was reported to be very efficient for removing carbon and hydrocarbon contaminations on GaN.[11, 54]

Aqua-regia solution Aqua-regia [HNO_3:HCl (1:3)] is also a very effective solution to remove the native oxide on GaN surface.[40, 63] Treating RIE etched *n*-GaN in the boiling solution was found to reduce greatly the contact resistivity for non-alloyed Ti/Al/Ti/Au contacts which was attributed to the effective removal of surface oxides formed during the RIE exposure. This treatment also provides excellent contact adhesion and good metal morphology.

KOH solution Treatment in a hot (~70 °C) KOH solution can also be used to remove the surface oxide and carbon contamination on GaN.[53, 64] However, KOH was found to decrease the Ga/N ratio at the surface, which was attributed to the formation and dissolution of Ga-based hydroxides.[8, 61, 62] The Ga-vacancies act as acceptors in GaN and partially compensate the electron concentration at the surface. X-ray photoelectron spectroscopy (XPS) analysis showed that the surface Fermi level shifted by 0.3–0.4 eV towards the valence band as a result of the treatment.[53, 61, 62] The KOH was also found to leave a lot of hydroxyls chemisorbed on the *n*-GaN surface. It results in an isolated interlayer, which hinders ohmic contact formation. These changes cause an increase in band bending and a surface barrier height in *n*-GaN making the KOH treatment very unsuitable for *n*-contact formation.

$(NH_4)_2S_x$ solution Boiling $(NH_4)_2S_x$ (~60 °C) is a very effective solution to remove the native surface oxide on GaN surface and to protect GaN from reoxidation since a Ga-monosulfide (GaS) layer is formed on the surface.[26, 54, 65, 66] As a result, deposited Ti is in intimate contact with the cleaned GaN surface and easily forms TiN. It leads to a standard Ti/Al contact formed on *n*-GaN even without postdeposition annealing.[26, 66] However, if the treatment time is too long, it can result in a thick sulfide layer accumulated on the surface. This also impedes *n*-contact formation.

NH_4OH-based solutions NH_4OH, often diluted with H_2O, is an excellent choice for removing the native oxide on a GaN surface. This treatment was also found to

maintain the original surface stoichiometry, which can be important for some applications. Recently Song *et al.* reported that treatment in a hot $NH_4OH:CH_3CSNH_2$ solution (~60 °C) for 10 min allowed a low-resistance Ti/Al contact to be formed on *n*-GaN without postdeposition annealing. XPS analysis showed a shift of the surface Fermi level toward the conduction-band edge resulting in a reduction of the surface-barrier height to *n*-GaN. It was attributed to the efficient removal of the surface oxide and a sulfide layer formed on the GaN surface. This layer prevents reoxidation of GaN under exposure in air.

6.4.2 Contact systems

Al *n*-contact

Aluminum, with a work function of 4.2 eV, which is close to the electron affinity of GaN (4.1 eV), is an excellent candidate for forming ohmic contacts to *n*-GaN. Al is also known to reduce Ga_2O_3 on GaAs and it is expected to do the same on GaN. As a result, Al ohmic contacts can be formed even without removing the oxide layer.[4, 20] An as-deposited contact was reported to yield a specific contact resistivity in the range of $\sim 10^{-4}$ $\Omega \cdot cm^2$. Annealing can reduce the resistivity further, which is probably related to the formation of a thin interfacial AlN layer observed by X-ray measurements.[67] This process introduces a considerable amount of nitrogen vacancies that heavily dope the GaN near the interface. It causes a decrease of the depletion region width and leads to increased electron tunneling through the barrier. However, due to the low-melting point (660 °C), Al melts and tends to ball up at high temperatures, resulting in a rough surface. Furthermore, the Al surface easily oxidizes at elevated temperatures with the formation of isolating Al_2O_3. This often leads to an increased contact resistivity after high temperature annealing. To some extent this problem can be solved by annealing in forming gas.[20] However, the propensity of Al to oxidation degrades the electrical performance of the contact and makes it unreliable for high performance device applications.

Ti *n*-contact

Titanium, with a work function of 4.2 eV close to an electron affinity of GaN, is widely used in multilayer ohmic contacts to *n*-GaN. After annealing Ti penetrates the oxide and other possible contamination on the GaN surface and allows intimate contact to be made.[68] It also provides excellent adhesion to GaN and serves the purpose of a barrier layer for multilayer contacts. As deposited, Ti was reported to produce a Schottky contact to *n*-GaN.[21, 22] The published data provided different values of the barrier height from 0.07 to 0.58 eV.[22, 46, 69] However, postdeposition annealing led to interfacial reactions between the metal layer and *n*-GaN, resulting in the formation of low-resistance ohmic contacts. XPS analysis showed that TiN was formed at the annealed Ti/*n*-GaN interface. A large number of N-vacancies, generated in GaN near the interface, left the GaN surface heavily *n*-type, forming a tunneling junction. Only two monolayers of TiN formed at the interface are necessary to generate a 100 Å thick layer of GaN with a doping concentration of $\sim 10^{20}$ cm^{-3}.[37, 70] XPS analysis also revealed that TiN formation led to an increase in the barrier height by 0.3 eV. The energy band diagrams

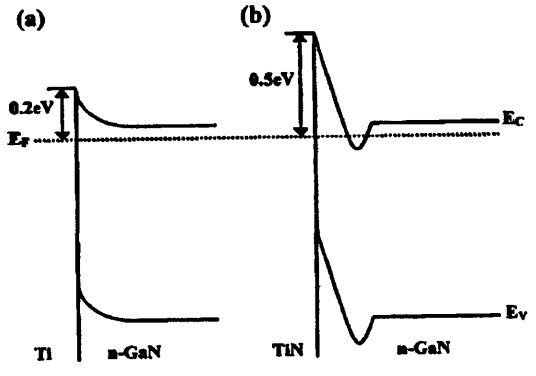

Fig. 6.7. Energy band diagrams of Ti/n-GaN; as-deposited (a) and annealed (b).

of the Ti/*n*-GaN interface before and after annealing are displayed in Fig. 6.7. Kim *et al.*[71] used synchrotron radiation photoemission spectroscopy (SRPES) and also observed TiN formation and an increase in the barrier height, though by 0.65 eV, under annealing. These results are very surprising because TiN is a semi-metal and has a work function of 3.74 eV, which is lower than that of both Ti and GaN. However, they imply that the ohmic contact behavior of the alloyed Ti contact is caused by an increase of the tunneling probability of electrons and cannot be attributed to the change in the surface barrier height. Despite the excellent properties, a single Ti layer does not produce a reliable contact due to poor electrical conductivity and a high affinity to oxygen. Titanium is well known to be easily oxidized even at room temperature, which makes the Ti-only contact unsuitable for high performance device applications.

Ti/Al-based *n*-contacts

Ti/Al is a commonly accepted contact to *n*-GaN, often capped with overlayers of different metals to protect it from oxidation and to provide a contact surface for wire bonding. Contact mechanisms and design principles for this system have recently been summarized by Mohammad.[11, 12] The first contact layer (Ti) is used to form a barrier compound layer (TiN) in immediate proximity to *n*-GaN. It prevents the diffusion of metal(s), which have larger work functions, into *n*-GaN during high temperature operation. The formation of TiN is accompanied with the creation of a Ga-terminated surface and with the formation of a large number of N-vacancies below the contact due to out-diffusion of nitrogen atoms from GaN. As a result, a heavily *n*-doped GaN surface is produced. The second contact layer (Al) plays the catalytic role as a sink for N atoms into the Ti layer enhancing the solid phase reaction between nitrogen and Ti. Under alloying or under high temperature operation for non-alloyed contacts, Al and Ti intermix and produce a robust Al-Ti intermetallic compound. This significantly reduces Al and Ti diffusion to the contact surface where they have a high propensity for oxidation. One or two cap layer metals are deposited on the top of Al to prevent contact oxidation and to ensure that the total free energy of the contact system is reduced. Among all contact metals, there should not be an excessive difference in the melting point, at least of any two metals deposited successively. This guarantees that the metal combination will provide robustness and good thermal stability even at high temperatures.

Ti/Al n-contact In this contact two low work function metals are placed together with Ti underside as a good sticking and reactive layer. The behavior of as-deposited Ti/Al contacts has been reported to range from ohmic[23, 25, 30, 40] to rectifying, which is probably related to the surface conditions and semiconductor doping level. Predeposition surface treatment in $(NH_4)_2S_x$ (60 °C) for 20 min or in CH_3CSNH_2/NH_4OH (60 °C) for 10 min was found to produce non-alloyed ohmic contacts with resistivities in the range of 10^{-4}–10^{-5} $\Omega\cdot cm^2$. The detailed mechanisms of these chemicals are considered above (see "Chemical surface treatment"). RIE (ICP) treatment was also reported to result in low-resistance (~10^{-6} $\Omega\cdot cm^2$) ohmic contacts without postdeposition annealing[27, 28] (for the mechanism, see "RIE surface treatment"). Non-alloyed low-resistance ohmic contacts were also formed on GaN treated by Si^+ implantation and subsequent activation annealing (for mechanism, see "Dopants implantation"). All these treatments have been found either to remove the native oxide on the GaN surface[26, 29] or to increase the surface carrier concentration[24, 27, 28] through the formation of nitrogen vacancies. This implies that the tunneling mechanism is probably responsible for ohmic contact formation for non-alloyed Ti/Al contacts.

Postdeposition annealing at 400–500 °C for 1 min has been reported to degrade the Ti/Al contact.[20, 30, 40] However, the contact recovered after longer annealing and reached a

contact resistivity of 7×10^{-6} Ω·cm^2 after being alloyed at 400 °C for 5 min. It is important to note that a similar tendency has also been observed for all multilayer Ti/Al-based contacts. Temperatures higher than 600 °C resulted in a low-resistance ohmic contact even after a very short annealing step (~15 s). The specific contact resistivity of Ti/Al contacts alloyed at 600 °C is usually in the range of 10^{-5}–10^{-6} Ω·cm^2.[20, 25, 30, 40] In order to explain the behavior of the alloyed Ti/Al contact, two mechanisms were proposed. The first one suggests that titanium is mainly responsible for ohmic contact formation.[72] As in the case of the Ti-only contact, it provides a heavily *n*-type GaN surface under annealing through the formation of a TiN layer and nitrogen vacancies in GaN (for mechanism, see "Ti *n*-contact"). The second mechanism attributes the ohmic behavior to a reduction of the native oxide on GaN by titanium and diffusion of Al through the Ti layer into the GaN layer. It was suggested that a low-resistance ohmic contact is only produced after Al reaches the GaN interface and forms a thin interfacial AlN layer. This layer was identified at the interface of the Ti/Al contact annealed at 600 °C using high-resolution transmission electron microscopy (HRTEM) and energy dispersive x-ray spectroscopy (EDS). As a result, the AlN layer affects the barrier in GaN allowing current to flow by tunneling. It can be caused either by nitrogen vacancies produced due to a reaction between Al and GaN, or by a reduced barrier in GaN due to a potential drop across the AlN. Luther *et al.* assumed that the specific mechanism, responsible for Ti/Al ohmic behavior, depends on the predeposition surface conditions. For example, RIE treatment was suggested to affect the kinetics of the reaction between Ti and GaN resulting in TiN to be formed before Al diffuses to the interface and reacts with GaN. The TiN layer may act as a diffusion barrier and inhibit the formation of AlN. Independent on the mechanism, Ti and Al layers intermix during annealing forming an Al-Ti alloy, as has been confirmed by X-ray diffraction (XRD) and Auger electron spectroscopy (AES) measurements.[20, 23, 36] In all probability this alloy is mainly Al_3Ti, which has a higher resistance to oxidation than both Al and Ti, and a higher melting point than Al. The optimal Al:Ti thickness ratio was reported to be approximately 3:1, which probably corresponds to both layers being completely consumed during the annealing forming the alloy. It makes the entire contact thermally more stable and reliable.

The major problem for the Ti/Al bilayer contact is that both metals have a high propensity to oxidation. Even a very low oxygen concentration during annealing (parts per million) was found to affect the contact due to an insulating Al_2O_3 layer formed on Al. Furthermore Al tends to ball up during alloying, resulting in a rough surface morphology for Ti/Al contacts. The long-term thermal stability of the Ti/Al contact can also be affected by the inevitable oxidation. This should be more relevant for non-alloyed Ti/Al contacts and for alloyed contacts with non-optimal Ti:Al ratio, forming Ti-rich or Al-rich alloys under annealing.

Ti/Al/Ni/Au n-contact In this contact a Ti/Al bilayer is capped with Ni/Au overlayers to form a non-oxidizing contact surface suitable for wire bonding. The Ni layer is used to prevent rapid diffusion of Au into the multilayer during annealing. Without this barrier Au with a high work function (5.1 eV) would easily diffuse through the Al layer to the interface and increase the resistance by increasing the barrier height. The first contact with a resistivity as low as 3.3×10^{-6} Ω·cm^2 before and 8.9×10^{-8} Ω·cm^2 after annealing (900 °C for 30 s) was reported by Fan *et al.* (the GaN surface was treated by RIE before the deposition). The annealed Ti/Al/Ni/Au contact results in a Ti-Al/Au-Ni system, where the top Au-Ni layer is a very robust and thermally stable alloy. This allows the contact to be excellent even at very high temperatures. Papanicolaou *et al.* showed that the contact remained reliably stable under high temperature operating conditions up to 400 °C. However, it was observed that Ni (work function of 5.1 eV) can also diffuse into GaN during high temperature annealing and can increase the contact resistivity. The authors

suggested making the Al layer much thicker than in common Ti/Al contacts. The thicker layer of Al provides reactions from both sides and keeps the high work function metals away from the interface.

Ti/Al/Pt/Au n-contact This contact is also widely used *n*-GaN[32, 33] and *n*-AlGaN[34, 73] contact layers. In this scheme the Pt layer acts as a barrier for the penetration of Au. A contact resistivity in the range of 10^{-5}–10^{-6} Ω·cm^2 after postdeposition annealing has been reported.[32, 33]

(Si)Ti/Al/Cu/Au n-contact The Ti/Al/Cu/Au and Si/Ti/Al/Cu/Au systems were employed for AlGaN and produced a contact resistivity of 3.9×10^{-4} and 3.8×10^{-5} Ω·cm^2, respectively, after annealing at 800 °C for 30 sec. In this contact the Cu layer is used as a barrier. The lower resistivity for the Si/Ti/Al/Cu/Au contact was explained by the diffusion of Si and, hence, by the increase of carrier concentration in AlGaN. This effect was only observed after annealing at temperatures higher than 800 °C due to the activation of Si dopants.

Ti/Al/Ti/Au n-contact Ti/Al/Ti/Au is also widely used as a contact for *n*-GaN.[36, 37, 38] In this contact the Ti layer is a barrier instead of problematic Ni and Pt with high work functions. It was suggested that the top Ti layer consumes excess Al, preventing it from balling up.[36, 37] Ti also reacts with Au forming a robust Au-Ti contact layer suitable for high-temperature applications. The contact was stressed at 400 °C for 24 h and showed no surface or contact resistivity degradation. The specific contact resistivity has been reported to be in the range of 10^{-5}–10^{-7} Ω·cm^2 for both alloyed[36, 37] and non-alloyed (to RIE-treated GaN)[36, 38] contacts.

Ti/Al/Mo/Au n-contact In this contact the Mo layer is used as a diffusion barrier. Mo has much higher melting point than Ni, Ti, Pd, and Pt. Additionally, Au has less than 1% solubility in Mo at a common contact annealing temperature of 850 °C. A specific contact resistivity as low as 4.7×10^{-7} Ω·cm^2 was achieved after annealing at 850 °C for 30 s (GaN surface was treated by RIE before the deposition). No degradation in the contact resistivity or in surface morphology was observed during long-term annealing at 500 °C for 360 h.

Ti/Al/Pd/Au n-contact The Ti/Al/Pd/Au system employs the Pd layer as a barrier. This scheme was reported to produce a resistivity of 2.8×10^{-4} and 4.2×10^{-8} Ω·cm^2 for as-deposited and for annealed (500 °C for 8 min) contacts, respectively (GaN surface was treated in aqua-regia to facilitate contact formation). The long-term thermal stability analysis revealed that the Ti/Al/Pd/Au contact is more stable than the Ti/Al contact on *n*-GaN.

Ti/Al/TiAl$_3$ n-contact $TiAl_3$ is used in this contact as a capping layer for the Ti/Al contact. According to the bulk phase diagram, $TiAl_3$ is in equilibrium with Al, thus, it should not adversely affect the reaction between the Ti and Al layers. Furthermore, $TiAl_3$ is an excellent oxidation cap due to the formation of a very thin but continuous Al_2O_3 layer at the surface, protecting the bulk of the film from further oxidation.[74, 75] The Ti/Al/$TiAl_3$ contact was reported to produce a contact resistivity of 1.1×10^{-5} Ω·cm^2 after being alloyed at 600 °C for 5 min. Performance of the contact was insensitive to the amount of oxygen in the annealing ambient. This implies that the Ti/Al/$TiAl_3$ contact is a potential candidate for the fabrication of optical devices that require both *n*- and *p*-GaN contacts, since it is not affected by oxidizing annealing ambients often used for common Ni/Au contacts to *p*-GaN. The contact also demonstrated excellent long-term thermal stability. No significant degradation in electrical performance was observed after 30 days in air at 350 °C.

Cr-based *n*-contacts

Chromium, with a work function of 4.5 eV, can also be used for contact systems to *n*-GaN. It is also known as an effective oxide reducing agent. A study of Cr-based contacts has recently been reported by Papanicolaou *et al.*

Cr n-contact The Cr-only contact was ohmic as-deposited and remained so for all annealing temperatures up to 1000 °C with a specific contact resistivity in the range of 1–5 × 10^{-4} Ω·cm^2. Formation of an intermetallic CrN phase was suggested to be responsible for ohmic contact formation.

Cr/Al n-contact The as-deposited Cr/Al contact was nearly ohmic. Upon annealing at temperatures in the range of 450–550 °C for 2 min, the contact became increasingly nonlinear. However, above 650 °C, the contact became ohmic again and did not change significantly between 650 and 850 °C. The minimum resistivity of 3.8 × 10^{-5} Ω·cm^2 was obtained after 700 °C annealing for 2 min. As can be seen, this behavior is very similar to that for the Ti/Al contact. It was attributed to CrN phase formation with subsequent reactions and penetration of Al to the GaN/Cr interface during annealing. AES analysis confirmed that, after the 650 °C anneal, where the electrical characteristics became ohmic, Al diffused through the Cr layer and reached the interface. As a result of the 850 °C anneal, a considerable increase in the thickness of the surface oxide was observed, which corresponded to an increase in the contact resistivity. The Cr/Al contact showed stable morphological stability, but displayed some degradation in electrical characteristics after long-term (100 h) aging at 400 °C.[76]

Cr/Al/Ni/Au n-contact For the Cr/Al/Ni/Au contact, the effect of annealing was the same as that for Cr/Al contacts. Annealing at 950 °C for 2 min resulted in a contact resistivity of 2.4 × 10^{-5} Ω·cm^2, slightly lower than that for the Cr/Al contact. Additionally, the Cr/Al/Ni/Au contact was found to be more stable in terms of both electrical performance and surface morphology after being stressed at 400 °C for 100 h.

Pd/Al *n*-contact

This contact was reported to yield a specific contact resistivity as low as 6 × 10^{-5} Ω·cm^2 after 30 s annealing at 600 °C. The ohmic behavior was also attributed to Al diffusion to a metal/GaN interface and AlN formation, as in the case of the Ti/Al contact.[77]

Ti/Au *n*-contact

The non-alloyed Ti/Au contact was found to yield a specific contact resistivity of 3.6 × 10^{-8} Ω·cm^2 for Si-implanted and annealed (4 × 10^{20} cm^{-3}) GaN. The extremely low resistivity is probably caused by both high carrier concentration at the surface and the low work function of Ti.

Ti/Pd/Au *n*-contact

The Ti/Pd/Au contact was reported to be ohmic as-deposited with a contact resistivity of 6.4 × 10^{-4} Ω·cm^2. After annealing at 400–600 °C, the contact was non-ohmic. However, at a higher annealing temperature of 700 °C, it became ohmic again.

Ti/Au/Pd/Au *n*-contact

This contact was also found to be very effective for *n*-GaN. It produced a contact resistivity of 8.0 × 10^{-7} Ω·cm^2 after two-step annealing for 30 and 15 s at 800 °C. AES and

XRD analysis showed that Ti, Pd, and Au generated substantial interactions upon annealing leading to the formation of face-centered tetragonal TiAu and TiPd alloys.[12, 45] It was also found that Au diffused into the bulk of GaN forming Au-Ga intermetallic phases, such as GaAu and/or $GaAu_2$. Extracted nitrogen was suggested to react with Ti forming TiN, which accompanies a heavy accumulation of N vacancies at the GaN surface. As a result, the tunneling probability for carriers greatly increases and a low resistance ohmic contact is formed.

Ti/Ag *n*-contact

Silver, Ag, with a work function of 4.3 eV close to an electron affinity of GaN, is a good candidate for forming ohmic contacts to *n*-GaN. The Ti/Ag contact scheme to n^+-GaN (1.7×10^{19} cm^{-3}) was reported to produce a specific contact resistivity of 6.5×10^{-5} $\Omega \cdot cm^2$ without thermal annealing. However, the poor thermal stability of Ag makes this system impractical for high-temperature applications.

W-based *n*-contacts

W and WSi_x are excellent candidates for high temperature electronics applications. Both of them have been found to produce reasonable contacts to *n*-GaN and extremely stable behavior up to annealing temperatures of 1000 °C, with only minimal reaction between W and GaN. For n^+-GaN ($\sim 10^{19}$–10^{20} cm^{-3}), achieved either by Si implantation and activation annealing[9, 48, 49, 59, 60] or by growth,[47, 49, 50] W and WSi_x have been reported to produce a contact resistivity in the range of 10^{-4}–10^{-6} $\Omega \cdot cm^2$ after postdeposition annealing. A mechanism of W ohmic contact formation was investigated and reported by Cole *et al.* Rutherford backscattering spectroscopy (RBS), XRS, and AES analysis showed that the low resistance accompanies the formation of β-W_2N and W-N interfacial phases at annealing temperatures between 600 and 1000 °C. In the case of WSi_x, no interfacial reactions up to 600 °C were observed, but the β-W_2N phase was formed between 700–800 °C. As a result, a large number of nitrogen vacancies accumulate near the GaN/W interface and significantly increase the tunneling probability for electrons. The W-N interfacial phase also functions as an efficient barrier to out-diffusion of Ga. AES analysis showed no apparent Ga diffusion through the W film to the surface at temperatures as high as 1000 °C. Scanning electron micrographs of W surfaces, at annealing temperatures up to 1000 °C, showed them to be smooth and void of reaction.

Ti/W/Au *n*-contact

The Ti/W/Au scheme was also employed as a contact to *n*-GaN. As deposited and annealed at temperatures below 750 °C, the contact showed non-linear electrical behavior. However, it was improved drastically at temperatures higher than 850 °C and produced a contact resistance as low as 8.4×10^{-6} $\Omega \cdot cm^2$ after being alloyed at 900 °C for 1 min. AES and XRD analysis showed that Ti-N and W-N interfacial phases were formed at annealing temperatures above 850 °C. Thereby the increase in carrier concentration, induced by generated N-vacancies, was suggested to be responsible for Ti/W/Au ohmic behavior. An atomic force microscope (AFM) showed no degradation in surface morphology after a 900 °C anneal implying that Ti/W/Au can be used for high temperature applications.

NiAl *n*-contact

The intermetallic compound, NiAl (50:50 at.%), is an excellent candidate for high temperature applications due to its melting point of 1638 °C and its oxidation resistance. A

Ni-Al-Ga-N system meets the criteria for participating in an exchange reaction. During this reaction, one element of the metal phase exchanges with another element of the semiconductor. In the case of NiAl on GaN, there should be an exchange of Al from the metal for Ga from the semiconductor. Ingerly *et al.* showed that NiAl produced a low-resistance ohmic contact to *n*-GaN with a resistivity as low as 9.4×10^{-6} $\Omega \cdot cm^2$ after annealing at 850 °C for 5 min. A mechanism of ohmic contact formation for the NiAl contact was suggested to be similar to that for the Ti/Al contact. AES and XRD analysis confirmed formation of a thin AlN layer, however, no conclusive evidence was observed. AES also showed no significant increase of oxygen in the NiAl film after annealing at 850 °C implying excellent oxidation resistance. Furthermore, the NiAl contact was proposed to be less affected than the common Ti/Al contact by increasing the Al content in *n*-AlGaN layers.

Ti/Si/Ti/Au *n*-contact

Ti silicides have good thermal stability and low work functions from 3.7 to 4.2 eV, depending on the Ti/Si ratio. In addition, Si is a common *n*-type dopant for GaN, and Ti can reduce the native oxide of GaN. This makes a Ti/Si-based scheme very promising as an ohmic contact to *n*-GaN. The Ti/Si/Ti/Au contact was found to yield a resistivity of 7.5×10^{-6} $\Omega \cdot cm^2$ after being alloyed at 900 °C for 3 min. According to AES, XRD, transmission electron microscopy (TEM), and energy dispersive x-ray spectrometry (EDS) analysis, ohmic behavior of the annealed Ti/Si/Ti/Au system was caused by the formation of Ti silicides at the interface. Temperature-dependent contact resistance measurements revealed that thermionic emission over a low Ti silicide/GaN barrier is the dominant transport mechanism for this contact.

V-based *n*-contacts

Vanadium, with a work function of 4.3 eV close to the electron affinity of GaN, was also used in contact systems to *n*-GaN. As deposited V and V/Ti/Au contacts were found to be nearly ohmic. Annealing at 850 °C for 2 min reduced the contact resistivity to 2.3×10^{-4} and to 4.0×10^{-6} $\Omega \cdot cm^2$ for V and for V/Ti/Au, respectively. XRD and AES analysis showed that nitride phases were predominantly formed in the annealed samples. This results in an increase in the surface carrier concentration in GaN due to the accumulation of nitrogen vacancies. As a result, the tunneling probability for electrons increases and the contact resistivity drops.

Ta/Ti/Ni/Au *n*-contact

Both Ta and Ti have low work functions and both are known to react with GaN forming nitrides. Recently the Ta/Ti/Ni/Au system was studied by Motayed *et al.* to investigate the combined effect of Ta and Ti. The contact was non-ohmic as deposited and showed no improvement after annealing at 550 °C. However, after 45s at 750 °C the *I-V* characteristics became linear and yielded a contact resistivity as low as 5.0×10^{-6} $\Omega \cdot cm^2$. XRD, AES, TEM, and EDS analysis showed the presence of Au(Ni,Ti) amorphous solid solutions and metal nitrides, (Ti, Ta)N, formed under annealing. This implies that the ohmic behavior was caused by an increase in the carrier concentration below the contact induced by N-vacancies. The analysis also indicates that Ni performed very poorly as a diffusion barrier against the out-diffusion of Ti and the in-diffusion of Au. This resulted in significant contact degradation under high temperature thermal stressing (400 °C for 24 h) due to the enhanced diffusivity of Ti through Ni and oxidation of Ti at the surface. The poor thermal stability makes this system impractical for high-temperature applications.

6.5 A review of ohmic contacts to *p*-GaN

The development of low-resistance and thermally stable ohmic contacts to *p*-GaN is one of the key issues for the fabrication of GaN-based laser diodes. A high contact resistance results in overheating at a metal/*p*-GaN interface as current flows across a *p-n* junction, leading to metal migration down threading dislocations and eventual shorting of the junction. In order to fabricate a continuous-wave (CW) operating laser diode with a low threshold voltage, a contact resistivity as low as 10^{-4} Ω·cm^2 is required. However, it is difficult to achieve such a low resistivity on *p*-type GaN. According to Schottky theory any metal with a work function equal to or higher than the sum of the electron affinity and bandgap of GaN (7.5 eV) is expected to form an ohmic contact to *p*-type GaN. However, metals with work functions higher than 6 eV do not exist. This results in a very high Schottky barrier at the metal/*p*-GaN interface implying that current transport through thermionic emission requires an equivalent bias. In most semiconductors, including *n*-type GaN, a high surface doping level is used to fabricate low-resistance ohmic contacts operating through a tunneling mechanism. However, this is extremely difficult in *p*-GaN, since it has a doping level much lower than that in other semiconductors. The hole concentration in GaN, achieved by standard *p*-type doping techniques, is generally less than 10^{18} cm^{-3} due to the deep ionization level of the most common *p*-type dopant, Mg (~170 meV). Other methods, such as diffusion and ion implantation, showed no significant improvement. In addition, *p*-GaN has a tendency for the preferential loss of nitrogen from the surface during processing, which may significantly reduce the surface doping level and even produce surface conversion to *n*-type conductivity. Furthermore, while a carrier concentration of 2×10^{18} cm^{-3} is sufficient to raise the Fermi level to the conduction band in *n*-type GaN, in *p*-type GaN a much higher value of 2×10^{19} cm^{-3} is required. All this makes the tunneling probability also extremely low. Nevertheless, significant progress in *p*-contacts during the last few years suggests the possible existence of other transport mechanisms through the metal/*p*-GaN barrier. Zeitouny *et al.* suggested that surface defects, generated during the high temperature contact anneal, can be responsible for carrier transport in a metal/*p*-GaN system. They introduce deep energy levels inside the depletion layer, pinning the Fermi level in *p*-GaN. Lee *et al.* proposed that Ga-vacancies, formed at the surface by some chemical treatments, can also act as interface states pinning the Fermi level and reducing the contact resistivity.

To develop low-resistance ohmic contacts to *p*-GaN, a large number of contact schemes have been investigated, most of them contain high work function metals (Ni, Au, Pt, Pd, etc). Different methods have been employed to improve the contacts including predeposition surface treatments to remove native oxides, to introduce surface defects, and to passivate semiconductor surfaces; the use of superlattice structures to increase hole concentrations by spontaneous polarization and piezoelectric effects, etc. The summary of the published contacts is presented in Table 6-3.

Table 6-3. Characteristics of published results on ohmic contact to *p*-GaN.

Mater.	Contact layers	Contact resistiv. (Ω·cm^2)	Carrier density (cm^{-3})	Treatment before photo-lithography	Treatment before metal deposition	Alloying condition	Ref.
GaN	Ni/Au 10/5 nm	1.0×10^{-4}	2.0×10^{17}			400 °C /10 min/air	78
GaN	Ni/Au 5/5 nm; 20/20 nm	4.0×10^{-6}	2.0×10^{17}		$HCl:H_2O$ (1:1)/1 min	500 °C /10 m/air(O_2)	79
GaN	Ni/Au 20/500 nm	6.1×10^{-4}	2.9×10^{17}		Aqua-regia /10 min	600 °C /30s/N_2	80

GaN	Ni/Au 20/50 nm	6.1×10^{-4}	2.9×10^{17}	Aqua-regia		600 °C /30 s/N_2	81
GaN	Ni/Au 30/150 nm	9.0×10^{-4}	-		KOH /30 s	500 °C /1 min/air	82
SL:GaN /AlGaN	Ni/Au 30/150 nm	9.0×10^{-5}	-		KOH /30 s	500 °C /1 min/air	82
GaN	Ni/Au 20/100 nm	6.1×10^{-3}	3.4×10^{17}			500 °C /10 min/air	83
		5.0×10^{-5}	3.4×10^{17}		$(NH_4)_2S$ /60°C/30min	500 °C /10 min/air	
		4.5×10^{-6}	3.4×10^{17}		750 °C /30min/air + $(NH_4)_2S$ /60°C/30min	500 °C /10 min/air	
SL:GaN /AlGaN	Ni/Au 6/14 nm	4.0×10^{-6}	1.0×10^{18}		$HCl:H_2O$ (1:1)	650 °C /5 min/N_2	84
InGaN/ GaN	Ni/Au 10/30 nm	6.0×10^{-3}	-		BOE /3 min	500 °C /3 min/O_2	85
GaN	Ni/Au 5/5 nm	3.4×10^{-3}	2.0×10^{17}	$HCl:H_2O$ (3:1)		500 °C /1 min/N_2	86
		1.2×10^{-4}	2.0×10^{17}	$HCl:H_2O$ (3:1)		500 °C /1 min/N_2	
GaN	Ni/Au-Zn 45/46	3.6×10^{-3}	4.4×10^{17}		$HCl:H_2O$ /5 min	600 °C /2 min/N2	87
GaN	Au/Ni/Au 5/8/4 nm	$\sim 10^{-5}$	5.0×10^{17}		$HCl:H_2O$ (1:1)/2 min	500 °C /10 min/air	88
GaN	Ni/Pt/Au 20/30/80 nm	2.1×10^{-2}	9.4×10^{16}		BOE	500 °C /30 s/Ar	89
GaN	Ni/Pd/Au 20/20/100 nm	1.1×10^{-2}	4.1×10^{17}			550 °C /5 min/air	90
		1.5×10^{-3}	4.1×10^{17}			550 °C /5 min/N_2	
		1.0×10^{-4}	4.1×10^{17}			550 °C /5 min/O_2	
GaN	Pd 20 nm	3.6×10^{-1}	1.9×10^{17}		$HCl:H_2O$ (1:1)/1 min	no	91
		7.0×10^{-3}	1.9×10^{17}		Aqua-regia /10 min	no	
		2.9×10^{-4}	1.9×10^{17}		Aqua-regia+ $(NH_4)_2S_x$ /10 +10 min	no	
GaN	Pd/Au 20/500 nm	2.9×10^{-2}	3.0×10^{17}			no	92
		4.3×10^{-4}	3.0×10^{17}		Aqua-regia /10 min	no	
GaN	Pd/Au 12/500 nm	2.9×10^{-2}	1.9×10^{17}		HCl /1 min	no	93
		4.3×10^{-4}	1.9×10^{17}		Aqua-regia /10 min	no	
GaN	Pd/Au 20/500 nm	2.9×10^{-1}	2.9×10^{16}		HCl /1 min	no	94
		7.1×10^{-3}	2.9×10^{16}		KOH /10 s	no	
GaN	Pd/Au 20/500 nm	1.3×10^{-1}	2.8×10^{16}	$HCl:H_2O$ (1:1)/30 s		no	95
		3.7×10^{-3}	2.8×10^{16}	Aqua-regia /10 min		no	
		3.0×10^{-2}	2.8×10^{16}	H_3PO_4 /10 s		no	
		8.6×10^{-3}	2.8×10^{16}	KOH /10 s		no	
InGaN/ GaN	Pd/Au 20/130 nm	1.1×10^{-6}	8.0×10^{18}		$HCl:H_2O$ (1:1)	no	96 97
InGaN/ GaN	Pd/Au 20/130 nm	1.1×10^{-6}	$\sim 10^{19}$		$HCl:H_2O$ (1:1)	no	98
GaN	Pd/Au 5/5 nm	6.4×10^{-4}	3.3×10^{17}	Aqua-regia		500 °C /1 min/air	99
InGaN/ GaN	Pd/Au 20/130 nm	1.4×10^{-5}	-			no	100

p^+-GaN /GaN	Pd/Au 20/130 nm	2.0×10^{-5}	-			no	100
GaN	Pd/Ni 3/7 nm	5.7×10^{-5}	3.3×10^{17}	Aqua-regia		500 °C /1 min/air	101
GaN	Pd/Ni 5/5 nm	9.6×10^{-5}	3.3×10^{17}	Aqua-regia		500 °C /1 min/air	99
GaN	Pd/Mo 15/15 nm	5.0×10^{-4}	5.0×10^{17}		HCl /3 min	no	102
		2.0×10^{-4}	5.0×10^{17}		HCl /3 min	500 °C /vacuum	
GaN	Pd/Re 20/25 nm	1.4×10^{-3}	1.1×10^{17}	Aqua-regia /10 min	BOE /30 s	no	103
		8.7×10^{-4}	1.1×10^{17}	Aqua-regia /10 min	BOE /30 s	550 °C /1 min/N_2	
GaN	Pd/Ag/Au/Ti/Au 1/50/10/30/20 nm	1.1×10^{-6}	6.0×10^{17}			800 °C /1 min/N_2	104
GaN	Pt 25 nm	2.1×10^{-2}	1.8×10^{17}		BOE /30 s	no	105
		3.7×10^{-3}	1.8×10^{17}	BOE /10 min	BOE /30 s	no	
		3.8×10^{-3}	1.8×10^{17}	$(NH_4)_2S_x$ /10 min	BOE /30 s	no	
		2.0×10^{-5}	1.8×10^{17}	BOE/10 min + $(NH_4)_2S_x$/10min	BOE /30 s	no	
GaN	Pt 10 nm	5.1×10^{-1}	1.9×10^{17}	$HCl:H_2O$ (1:1)/1 min		no	106
		4.8×10^{-4}	1.9×10^{17}	Aqua-regia /10 min		no	
		2.5×10^{-5}	1.9×10^{17}	Aqua-regia+ $(NH_4)_2S_x$ /10 +10 min		no	
GaN	Pt 25 nm	3.1×10^{-2}	1.8×10^{17}		BOE /30 s	no	107
		3.0×10^{-5}	1.8×10^{17}	BOE/20 min + $(NH_4)_2S_x$/10min	BOE /30 s	no	
GaN	Pt 20 nm	3.1×10^{-2}	3.0×10^{17}	BOE /0.5 min	BOE	no	108
		2.1×10^{-3}	3.0×10^{17}	BOE /10 min	BOE	no	
		7.1×10^{-4}	3.0×10^{17}	BOE /20 min	BOE	no	
GaN	Pt 8 nm	4.7×10^{-5}	2.0×10^{17}		$t\text{-}C_4H_9OH$ +$(NH_4)_2S$ /60°C/10min	no	109
GaN	Pt 10 nm	5.1×10^{-1}	1.9×10^{17}	$HCl:H_2O$ (1:1)/30 s		no	110
		9.3×10^{-5}	1.9×10^{17}	Aqua-regia /10 min		no	
GaN	Pt 10 nm	1.4×10^{-3}	1.9×10^{17}	Aqua-regia		no	111
		1.3×10^{-4}	1.9×10^{17}	Aqua-regia		450 °C /N_2	
GaN	Pt/Ni/Au 20/30/80 nm	3.0×10^{-3}	3.0×10^{17}		BHF	no	112
		5.1×10^{-4}	3.0×10^{17}		BHF	350 °C /1 min	
GaN	Pt/Pd/Au 7/7/15 nm	3.1×10^{-5}	2.5×10^{17}	BHF /10 min	BHF /1 min	600 °C /2 min/N_2	113
GaN	Pt/Ru 20/50 nm	7.8×10^{-4}	2.0×10^{17}	BOE /20 min	BOE /30 s	no	114
		2.2×10^{-6}	2.0×10^{17}	BOE /20 min	BOE /20 min	600 °C /2 min	
GaN	Pt/Re/Au 20/30/80 nm	2.8×10^{-3}	1.1×10^{17}	Aqua-regia /10 min	BOE /30 s	no	115
		1.4×10^{-3}	1.1×10^{17}	Aqua-regia /10 min	BOE /30 s	600 °C /1 min/N_2	
GaN	Rh 10 nm	1.7×10^{-5}	4.0×10^{17}	BOE /20 min	BOE /1 min	no	116
GaN	Rh/Au 5/5 nm	9.3×10^{-6}	4.0×10^{17}	BOE /20 min	BOE /1 min	no	116

GaN	Rh/Ni 5/5 nm	6.0×10^{-5}	4.0×10^{17}	BOE /20 min	BOE /1 min	no	116
SL:GaN /AlGaN	Ti/Pt/Au 15/50/80 nm	4.6×10^{-4}	5.0×10^{18}		O_2 plasma+ $HCl:H_2O$/1:2	no	117
		1.3×10^{-4}	5.0×10^{18}		O_2 plasma+ $HCl:H_2O$/1:2	300 °C /5 min/N_2	
GaN	Ti/Pt/Au 15/50/80 nm	4.2×10^{-5}	2.5×10^{17}		O_2 plasma+ $HCl:H_2O$/1:2	800 °C /2 min/N_2	118
GaN	Ta/Ti 60/40 nm	3.2×10^{-5}	7.0×10^{17}		HF /5 min	800 °C/20 min/vacuum	119 120
GaN	CuNi/Ag 5/200 nm	6.0×10^{-6}	5.0×10^{17}	BOE /20 min	BOE /5 min	450 °C /1 min/air	121
GaN	NiZn/Pd 5/5 nm	4.8×10^{-5}	5.0×10^{17}	BOE /20 min	BOE /5 min	530 °C /1 min/air	122

As in the case of contacts to *n*-GaN, there are large discrepancies in the results reported by different groups for standard contacts to *p*-GaN. This results from variations in many material and process factors, such as semiconductor doping level, material quality, surface roughness, predeposition treatment, alloying conditions, etc. The optimal alloying conditions (temperature, time, ambient) depend on the metallization scheme used and should be discussed for each contact system. In contrast, the predeposition treatment affects the contact quality independently of the contact scheme and can be considered separately. As can be seen from Table 6-3, *p*-contacts can also be significantly improved by a contact layer with a high hole concentration, such as a AlGaN/GaN superlattice, thin InGaN or p^+-GaN layer. The effect of these layers is also discussed below.

6.5.1 Predeposition surface treatment

The surface treatment prior to metal deposition can significantly improve a contact to *p*-GaN due to the removal of the native oxide and a shift of the surface Fermi level towards the valence-band edge. It has been shown that the surface oxide on GaN acts as an additional barrier to current transport through the metal/*p*-GaN interface hampering the formation of low-resistivity ohmic contacts. The effective Schottky barrier height, ϕ_B, can be expressed as

$$\phi_B = \phi_{B_0} + \frac{2kT}{h}(2m\chi)^{1/2}\delta \qquad [6.12]$$

ϕ_{B_0} – Schottky barrier height without a surface oxide (eV)

δ – thickness of an isolation layer

m – the mean tunneling effective masses of carriers

χ – the mean tunneling barrier for hole injection from metal to *p*-GaN

The increase in the barrier height caused by a 20 Å-thick oxide isolation layer was calculated to be 0.2–0.3 eV. Thus, the removal of the oxide layer is essential prior to metal deposition. However, for *p*-type GaN, the oxide removal alone is not sufficient for ohmic contact formation due to a very high Schottky barrier at the metal/*p*-GaN interface. It was stated above that surface defects are responsible for carrier transport in a metal/*p*-GaN system. They introduce deep energy states inside the depletion layer and shift the surface Fermi level towards their location in the bandgap. Ga-vacancies, known as triply charged acceptors, were found to produce such interface states pinning the Fermi level near the valence band in *p*-GaN. This implies that any surface treatment introducing Ga-vacancies at the interface should promote ohmic contact formation to *p*-GaN and reduce the contact resistivity. In contrast, any treatment generating N-vacancies is expected to increase the

resistivity due to related interface states near the conduction band and due to a decrease in the effective hole concentration near the interface or even surface conversion to *n*-type conductivity. For this reason RIE (ICP) treatment or high-temperature annealing prior to metal deposition result in severe degradation of *p*-contact ohmic characteristics.[28, 31, 56,] Instead, to obtain low-resistance ohmic contacts to *p*-GaN, a large number of chemicals have been employed including HCl, HF, buffered oxide etch (BOE), aqua-regia, KOH, $(NH_4)_2S_x$, NH_4OH, NaOH, and different combinations of these chemicals. The impact of some of them is illustrated below.

HCl-based solutions HCl acid, often diluted with H_2O, is fairly effective in removing the native oxide on a GaN surface.[11, 54] However HCl treatment has also been found to result in a higher Ga/N ratio relative to an untreated surface due to the preferable removal of N-based species from the surface.[61, 62] The nitrogen vacancies introduced reduce the effective hole concentration near the interface and shift the surface Fermi level towards the surface conduction band minimum leading to an increased surface barrier height on *p*-GaN. Thereby, this treatment is not very effective for *p*-contact formation.

HF-based solutions Treatment in HF acid or in a buffered oxide etch solution ($HF:NH_4F$) is fairly effective in removing the native oxide, carbon, and hydrocarbon contaminations on a GaN surface.[11, 54] Jang *et al.*[63, 105, 108] reported that prolonged BOE treatment prior to metallization resulted in the decrease of the Schottky barrier height for non-alloyed Pt contacts leading to a significant reduction in the contact resistivity. It was attributed to the combined effects of the effective removal of the surface oxide and the shift of the surface Fermi level towards the valence-band edge due to Ga-vacancies produced at the surface.

Aqua-regia solution Aqua-regia [HNO_3:HCl (1:3)] is also a very effective solution to remove the native oxide on a GaN surface.[40, 63] Lee *et al.*[93, 95, 106] and Kim *et al.*[91, 92, 110] have reported that treatment in boiling aqua-regia for 10 min effectively removed the surface oxide and reduced the contact resistivity of non-alloyed Pd, Pt, and Pd/Au contacts by two to four orders of magnitude. It has also been found that the aqua-regia treatment left the surface N-rich.[91, 106, 110] As a result of the Ga-vacancies, the surface Fermi level was pinned near the valence band, reducing the Schottky barrier height.

KOH solution Treatment in KOH can also be used to remove the surface oxide and carbon contamination on GaN.[53, 64] Additionally, this solution has been found to decrease the Ga/N ratio at the surface, which was attributed to the formation and dissolution of Ga-based hydroxides.[8, 61, 62] XPS analysis showed that the surface Fermi level shifted by 0.3–0.4 eV towards the valence band as a result of the Ga-vacancies introduced.[53, 61, 62] For the *p*-type GaN, the shift of the Fermi level in this direction should lead to a reduction in the surface barrier height and subsequent improved metal contact behavior. Indeed Lee *et al.*[94, 95] reported that the contact resistivity of a non-alloyed Pd/Au contact was significantly reduced for KOH treated *p*-GaN. Consequently, the KOH solution is very effective in removing surface oxide and plays a significant role to reduce the contact resistivity for ohmic contact to *p*-type GaN.

$(NH_4)_2S_x$ solution Boiling $(NH_4)_2S_x$ (~60 °C) is a very effective solution to remove the native surface oxide on a GaN surface and to protect GaN from reoxidation since a Ga-monosulfide (GaS) layer is formed on the surface.[26, 54, 65, 66] Lee *et al.* found that a Ni/Au contact was significantly improved by the $(NH_4)_2S_x$ treatment for 30 min prior to the metallization. The better performance was attributed to a complete removal of the native oxide and to Ga-vacancies left on the oxidation-free surface. The authors also proposed using a preoxidation process prior to the $(NH_4)_2S_x$ treatment to improve the contact even more. They found that thermal annealing in air ambient (750 °C for 30 min) promoted additional GaO_x formation on the surface. As a result more Ga-vacancies were

induced after removal of the native oxide in $(NH_4)_2S_x$ and the contact resistivity was further reduced.

BOE + $(NH_4)_2S_x$ treatment Treatment in the buffered oxide etch (BOE) solution followed by dipping in $(NH_4)_2S_x$ has been found to be very effective for ohmic contact formation to *p*-GaN.[105, 107] The contact resistivity of a non-alloyed Pt contact was reduced by about three orders of magnitude compared to untreated GaN, which was attributed to the effective removal of the native oxide on the surface and an increase in the carrier concentration near the GaN surface. The Hall-effect measurements showed that the treatment resulted in an increase (by about a factor of 10) in the free hole concentration. In all probability this was caused by Ga-vacancies produced at the surface as a result of both BOE and $(NH_4)_2S_x$ treatment. It was also shown above that both these chemicals effectively remove the native oxide, and $(NH_4)_2S_x$ protects the surface from reoxidation under air exposure.

Aqua-regia + $(NH_4)_2S_x$ treatment Treatment in aqua-regia followed by dipping in $(NH_4)_2S_x$ has also been reported to be very effective for ohmic contact formation to *p*-GaN.[91, 106] The contact resistivity of non-alloyed Pd and Pt contacts was decreased by three and four orders of magnitude, respectively, compared to untreated GaN. The authors suggested that aqua-regia removed the surface oxide, and $(NH_4)_2S_x$ suppressed oxide formation under subsequent air exposure. XPS analysis showed that the Ga/N ratio at the surface was decreased after the treatment. This is consistent with the results for only-aqua-regia and for only-$(NH_4)_2S_x$ treatment. As a result of the Ga-vacancies introduced, the surface Fermi level was pinned near the valence band, reducing the Schottky barrier height and the contact resistivity.

[t-C_4H_9OH + $(NH_4)_2S_x$] solution The alcohol-based $(NH_4)_2S_x$ solution has been reported to be more effective for Ga-oxide removal than a normal $(NH_4)_2S_x$ solution.[109, 123] As a result of the treatment [90 vol.% tert-butanol (t-C_4H_9OH) and 10 vol.% $(NH_4)_2S$] at 60 °C for 10 min, the contact resistivity of a non-alloyed Pt contact was decreased by three orders of magnitude compared to untreated GaN. XPS analysis showed that this solution efficiently removed the surface oxide and shifted the surface Fermi level toward the valence-band edge by 0.25 eV. The authors suggested that the oxide layer was removed through the formation of gallium hydroxide, which was produced via OH^- groups present in the solution. The selective removal of Ga resulted in the formation of Ga vacancies near the interface and in the surface Fermi level being pinned near the valence band. A very thin sulfide layer left on the surface after the treatment was suggested to prevent surface reoxidation under exposure to air.

6.5.2 Sub-contact layers

Standard contacts employ the metallization of a *p*-type GaN layer. However, certain sub-contact layers grown epitaxially on the top of *p*-GaN can significantly improve contact performance. The impact of the most commonly used layers is illustrated below.

p^+-GaN layer

A heavily doped GaN:Mg sub-contact layer has been found to improve contacts due to an increased surface carrier concentration. A contact resistivity of 2×10^{-5} $\Omega \cdot cm^2$ was achieved for a non-alloyed Pd/Au contact without any special predeposition treatment. However, growth of this layer requires careful control over the doping level. Although the Mg concentration in GaN can be easily increased by increasing the Mg/Ga flux ratio during the growth, it does not guarantee an increased free hole concentration. It is known

that a drop in the effective hole concentration at high Mg concentration (magnesium segregation) is accompanied by the formation of pyramidal defects on the surface. Thereby, control over the surface defects can be employed during the growth to keep the magnesium flux below a critical level.

InGaN layer

P-type InGaN is also a very promising material to reduce the contact resistivity because of the narrower band gap than GaN and a high free hole concentration above 10^{18} cm^{-3}.[124, 125] Furthermore, *p*-type InGaN/GaN superlattices show hole concentrations above 10^{19} cm^{-3} due to a large piezoelectric polarization and a large valence band discontinuity between GaN and InGaN.[126] Kumaruka *et al.*[96, 97, 98] reported a non-alloyed Pd/Au ohmic contact to *p*-type GaN using *p*-InGaN as a contact layer. The lowest contact resistivity of 1.1×10^{-6} $\Omega \cdot cm^2$ was achieved using a strained $In_{0.19}Ga_{0.81}N$ layer with a hole concentration of 8×10^{18} and a thickness of 2 nm. Figure 6.8 shows the contact resistivity as a function of the *p*-type InGaN contact layer thickness. The authors suggested that the contact characteristics are very sensitive to an electric field induced in the thin InGaN contact layer. This electric field consists of a piezoelectric polarization field and an electric field due to ionized acceptors in the surface depletion layer. As a result, the tunneling barrier width is decreased, enhancing tunneling transport. Furthermore, the high free hole concentration in InGaN also plays an important role in the reduction of the surface depletion layer. Therefore, the tunneling barrier becomes thinner as shown in Fig. 6.9 (a), resulting in the drastic reduction of the contact resistivity. However, if the InGaN contact layer exceeds the critical layer thickness, the strain-induced piezoelectric field disappears due to lattice relaxation, resulting in the increase of the tunneling barrier width [Fig. 6.9 (b)]. Therefore, the contact resistance gradually increases with the contact layer thickness. The critical thickness of InGaN was estimated to be from 3 to 5 nm with the largest piezoelectric polarization effect at 2 nm. Significant improvement using a strained *p*-InGaN sub-contact layer was also reported for Pd/Au and for Ni/Au contacts by Dennemarck *et al.* and Gessmann *et al.*, respectively, and was also attributed to the increased free hole concentration and to the band bending induced by polarization fields.

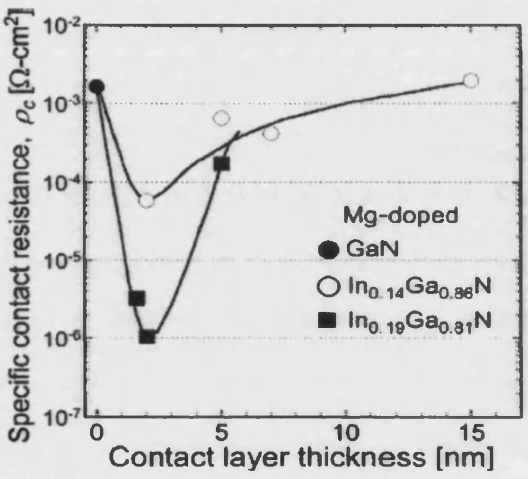

Fig. 6.8. Specific contact resistivity of a non-alloyed Pd/Au contact as a function of p-InGaN contact layer thickness.

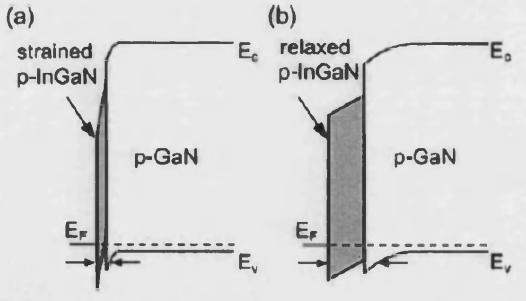

Fig. 6.9. Band diagrams of a InGaN/GaN interface near the surface: (a) with a strained InGaN contact layer; (b) with a relaxed InGaN contact layer.

AlGaN/GaN superlattice

Using *p*-type AlGaN/GaN superlattices (SL) is an effective method to enhance the hole concentration under a contact. It is well known that a hole concentration above 10^{18} cm^{-3} can easily be achieved in the superlattice due to the effects of piezoelectric and

spontaneous polarization.[127, 128, 129, 130, 131, 132] The periodic oscillation of the valence band edge is superimposed with the oscillation generated by the piezoelectric field, significantly reducing the Mg acceptor ionization energy and, hence, increasing the carrier concentration. Furthermore, for contacts to *p*-type AlGaN/GaN SL polarization charges near the surface can also enhance tunneling transport through the interface. Indeed, Zhang *et al.* and Zhou *et al.* have reported that the contact resistivity was reduced by an order of magnitude using a *p*-SL AlGaN/GaN sub-contact layer compared to a single *p*-GaN layer. The improvement was attributed to an enhancement in the free hole concentration.

6.5.3 Contact systems

Ni/Au-based *p*-contacts

Ni/Au p-contact The Ni/Au system is intensively used as an ohmic contact to *p*-type GaN. A contact resistivity in the range of 10^{-3}–10^{-4} $\Omega \cdot cm^2$ is typically obtained after annealing at 500–600 °C in N_2.[80, 81, 86] The mechanism of ohmic contact formation in N_2 ambient has been studied by Kim *et al.*[80, 81] The authors suggested that a decrease of the Ni/Au contact resistivity during annealing at 500–600 °C originates from outdiffusion of Ga atoms from *p*-type GaN into a Au-Ni solid solution. Ga-vacancies generated below the contact act as acceptors reducing the Schottky barrier height for hole transport. The shift of the surface Fermi level towards the valence band minimum was estimated to be 0.2 eV. When the contact is annealed at higher temperatures, free Ni atoms start reacting with N forming nickel nitrides. The N-vacancies produced reduce the effective hole concentration near the interface, leading to an increase in the Schottky barrier height and contact resistivity. These findings were confirmed by an only-Ni contact annealed in N_2 ambient. This contact showed no changes up to 500 °C annealing and gradual degradation at higher annealing temperatures. X-ray diffraction (XRD) analysis verified that only Ni_3N compound was produced in the Ni contact, whereas AuNi, Au_7Ga, Ga_3Ni_5, $Au_{0.79}Ga_{0.21}$, Ga_3Ni_2 Ni_3N, and Ni_4N compounds were detected in the Ni/Au contact after annealing.

Annealing in oxidizing ambients, such as air or O_2, has been found to reduce the contact resistivity of Ni/Au contacts by one-two orders of magnitude compared to a pure N_2 ambient.[78, 79, 82, 83] Many studies on the interfacial reactions between the metal and GaN have been carried out to determine the mechanisms responsible for ohmic contact formation. However, the results are still conflicting and the nature of the interfacial reactions and microstructures in the metal/*p*-GaN system remains unclear. The proposed mechanisms are illustrated and discussed below.

Koide *et al.*[133] found that annealing in oxygen-containing ambients reduced both the contact resistivity of Ni/Au contacts and the sheet resistance of *p*-GaN epilayers. The reason was suggested to be due to formation of an intermediate semiconductor layer (ISL) with a high hole concentration, caused by the removal of hydrogen atoms from epilayers in the presence of oxygen. However, this hypothesis appears to be very questionable. It is well established that hydrogen becomes mobile in *p*-GaN at temperatures higher than 350 °C.[134, 135] The much higher temperatures required for *p*-contact annealing should result in an uniform distribution of H atoms in epilayers after the alloying. Maeda *et al.*[136] continued this study to clarify the role of NiO produced during the oxidation of a Ni/Au contact. The authors deposited a variety of NiAu-based contacts on *p*-GaN with either NiO or Li doped *p*-type NiO(Li) layers, such as NiO/Au, NiO(Li)/Au, Ni/NiO(Li)/Au, $Ni/Li_2O/NiO/Au$, and $Ni/Li_2O/Ni/NiO/Au$. However, none of these contacts provided specific contact resistances lower than that of the conventional Ni/Au contacts prepared by annealing in N_2 ambient. From these results, the authors concluded that the *p*-NiO layer is

not responsible for the Ni/Au ohmic behavior. However, Chen *et al.*[137] suggested that crystalline NiO produced by Ni/Au contact annealing is very different from polycrystalline sputter-deposited NiO. Furthermore, sputter deposition used by Maeda *et al.* could introduce structural defects at the NiO/*p*-GaN interface. These factors may result in a significant variation of contact characteristics and leave the interpretations of this group open to discussion.

Another research group suggested that crystalline NiO produced as a result of annealing in oxygen-containing ambients is responsible for the low-resistance Ni/Au contact to *p*-GaN.[78, 79, 137, 138, 139] Using XRD analysis and cross-sectional TEM examination the authors proposed the following picture of structural transformation of Ni/Au metallization under annealing in air (O_2) [Fig. 6.10]. The Ni/Au bi-layer annealed at 350 °C transforms to a microstructure with discrete crystalline islands of Au, a non-uniform crystalline thin film of NiO covering the islands, and an amorphous Ga-Ni-O layer between some of these features and *p*-type GaN [Fig. 6.10 (b)]. Annealing at 500 °C results in the NiO film and the Au islands epitaxially constructed on *p*-type GaN with an amorphous Ga-Ni-O phase and small voids among Au islands [Fig. 6.10 (c)]. At a temperature of 600 °C disassociated nitrogen enlarges the voids separating the crystalline NiO from *p*-type GaN and reducing the contacting area [Fig. 6.10 (d)]. The authors suggested that the crystalline NiO film contacting *p*-GaN is crucial to obtain a low-resistance Ni/Au contact. Thereby the optimal annealing temperature was suggested to be around 500 °C to prevent a decrease in a contact area between NiO and *p*-GaN. This is in good agreement with electrical contact characteristics. The Au islands were suggested to act as a conductive matrix for NiO reducing the sheet resistance of a final contact layer. The NiO produced by oxidation of Ni was reported to act as a *p*-type semiconductor due to nickel vacancies and/or interstitial O.[140] In view of that the authors proposed a model based on a Au/*p*-NiO/*p*-GaN heterostructure to explain the low-resistance ohmic behavior. The barrier heights at Au/*p*-NiO and *p*-NiO/*p*-GaN junctions were calculated to be 0.3 and 0.185 eV, respectively. However, very recently Yu *et al.*[141] corrected the calculations and estimated the barrier height at the *p*-NiO/*p*-GaN interface to be 2.28 eV, disputing this model.

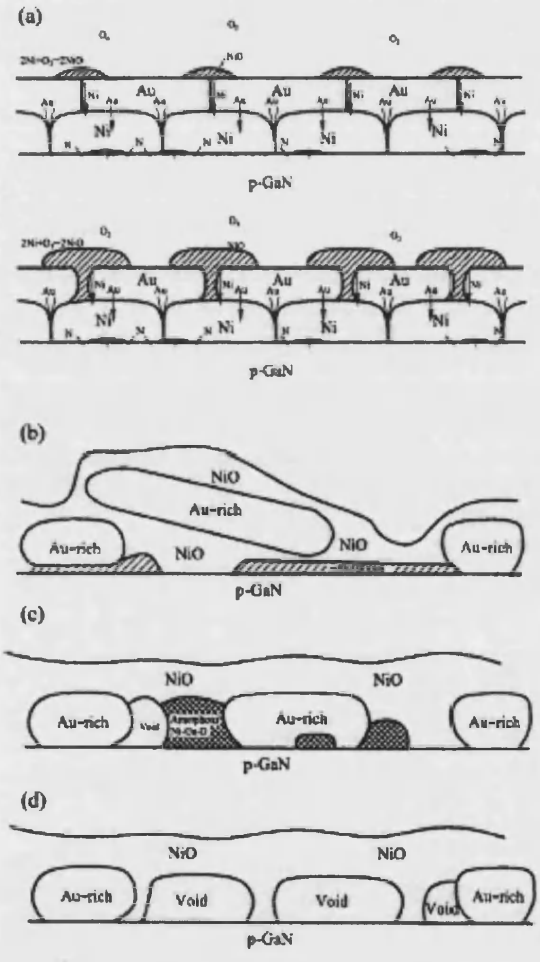

Fig. 6.10. Schematic illustration of reaction mechanism and diffusion behavior during the oxidation of p-GaN/Ni/Au: (a) initial diffusion and oxidized reaction, (b) treated at 350 °C, (c) treated at 500 °C, (d) treated at 600 °C.

Qiao *et al.*[142] suggested that Au islands contacting *p*-GaN after the oxidation are mainly responsible for Ni/Au ohmic behavior. In this model oxygen assists layer-reversal reactions forming a NiO/Au/*p*-GaN structure and causes an increase in *p*-GaN conductivity due to effective removal of H from GaN. Ni was proposed to remove or to reduce surface

contamination on the surface before or during layer reversal. Qiao *et al.* also attempted to simulate a Au/*p*-NiO/*p*-GaN contact by depositing a single layer of Ni, followed by annealing at 500 °C in air and depositing a top layer of Au. No ohmic behavior was observed and the authors called the Au/*p*-NiO/*p*-GaN model into doubt. However, Kim *et al.*[143] reported that Ni oxidation rate was greatly increased by the addition of Au overlayer, while for an only-Ni film nonoxidized Ni still existed even after annealing in air at 600 °C for 30 min. Furthermore, NiO formed after oxidation of the only-Ni film on GaN was found to be textured polycrystalline and its contact characteristics can be very different from those of crystalline NiO produced by Ni/Au contact annealing.

Very recently a contact formation mechanism for oxidized Ni/Au to *p*-GaN was proposed using three-dimensional secondary ion mass spectroscopy (3D-SIMS) mapping and synchrotron photoemission spectroscopy (SRPES). The authors suggested that oxygen accelerates Ni out-diffusion to the surface causing the complete transformation of Ni into NiO. It finally results in a NiO/Au/*p*-GaN structure as was also suggested by Qiao *et al.* However, the present work gives a different mechanism responsible for contact formation. Both Au islands contacting the GaN surface and oxygen atoms incorporated during annealing were suggested to promote significant out-diffusion of Ga atoms forming a Au-Ga solid solution due to the high solubility of Ga atoms in Au (13% at 409 °C). The surface NiO layer was suggested to suppress out-diffusion of N atoms released from the decomposed GaN. This generates a number of Ga-vacancies at the interface, which act as acceptors and reduce the Schottky barrier height for hole transport. The shift of the surface Fermi level towards the valence band minimum was estimated to be 0.4 eV compared to only 0.2 eV for N_2 ambient. As a result of both an increased surface hole concentration and the reduced barrier height, the contact resistivity of the oxidized Ni/Au contact is drastically decreased.

A number of reports have been published on the thermal stability of Ni/Au contacts.[59, 60, 144, 145] This metallization showed severe degradation of the electrical and morphological properties under high temperature annealing. However, the contact alloyed in air was found to be significantly more stable compared to that alloyed in N_2 ambient.[144, 145] The specific contact resistivity increased with increasing annealing time at 550 °C in N_2 while it was stable in air. This behavior was attributed to Ni_4N phase formation in nitrogen ambient, which is greatly accelerated in the Ni/Au system due to the catalytic action of Au. In this contact, Ni_4N begins forming at 500 °C and consumes nitrogen from GaN leaving N-vacancies near the interface. In contrast, the Ni_4N phase was not detected in air-annealed contacts where almost all Ni atoms were in a NiO form. The authors concluded that the more energy favorable NiO bonds suppress the formation of Ni_4N greatly improving contact thermal stability.

The environmental stability of Ni/Au contacts alloyed in air was studied by Wang *et al.*[146] It was found that exposure to water vapor caused the degradation of electrical characteristics even at room temperature. No change in the sheet resistance of a *p*-type GaN epilayer beneath the contact was observed. The authors speculated that hydrogen was incorporated into the contact reducing the hole concentration in *p*-NiO. These suggestions are consistent with the Au/*p*-NiO/*p*-GaN model illustrated above. The environmental stability of Ni/Au contacts at elevated temperatures (200 °C) was found to be very poor in both dry N_2 and N_2 plus water vapor. The only environment that preserved a low-resistance contact was dry O_2. This limits the use of oxidized Ni/Au contacts for open to air applications. A thick capping layer, such as Ni/Au or Ti/Au, deposited after contact oxidation can probably protect the contacts from environment-induced degradation.

Au/Ni/Au p-contact This modification of a standard Ni/Au *p*-contact was recently investigated by Narayan *et al.* A contact resistivity in the range of 10^{-5} $\Omega \cdot cm^2$ was

obtained after annealing in air at 500 °C for 10 min. TEM analysis showed that an epitaxial NiO-Au composite was formed after the annealing, where both Au and NiO were in contact with *p*-GaN. The NiO was found to grow epitaxially on the Au template, whilst making contact with the *p*-GaN substrate at the same time. The final structure of the oxidized contact is probably very similar to that of an oxidized Ni/Au contact.

Ni/Pt/Au p-contact This contact system yielded a contact resistivity of 2×10^{-2} $\Omega \cdot cm^2$ after annealing in Ar ambient at 500 °C. The fairly high resistivity compared to a standard Ni/Au contact annealed in nonoxidized ambients was probably caused by a Pt layer preventing Au and Ni intermixing. AES analysis showed that Ni diffused into the Pt layer at 500 °C, being intermixed with Pt. It is known that Au promotes out-diffusion of Ga atoms from GaN forming a Au-Ga solid solution due to the high solubility of Ga atoms in Au (13% at 409 °C). Thereby, the lack of Au near the GaN surface could result in the reduced number of Ga-vacancies near the interface compared to the annealed Ni/Au system. The ohmic behavior observed could be related to Pt diffused to the GaN surface as a result of the alloying. This metal has a higher work function (5.6 eV) compared to that of Ni (5.1 eV) and, hence, could promote ohmic contact formation.

Ni/Pd/Au p-contact The Ni/Pd/Au contact was demonstrated by Chu *et al.* A specific contact resistivity as low as 1.0×10^{-4} $\Omega \cdot cm^2$ was achieved after annealing in oxygen ambient at 550 °C for 5 min. Contacts with a resistivity in the range of 10^{-2}–10^{-3} $\Omega \cdot cm^2$ were also obtained at this temperature in air and N_2 ambient.

Pd-based *p*-contacts

Pd is widely used in ohmic contacts to *p*-GaN due to a relatively high work function (5.1 eV) and its ability to react with GaN during an annealing process to form gallides.[147] Various Pd-based metallization schemes have been reported, most of them provide low-resistance ohmic contacts even without postdeposition annealing. It makes these systems suitable for the fabrication of complicated layered structures.

Pd p-contact The non-alloyed Pd contact was reported to yield a contact resistivity of 7.0×10^{-3} and 2.9×10^{-4} $\Omega \cdot cm^2$ for *p*-GaN treated in aqua-regia and in aqua-regia followed by $(NH_4)_2S_x$, respectively. The impact of these treatments is considered above (see "Predeposition surface treatment"). Briefly, a number of Ga-vacancies was introduced near the surface as a result of these chemicals, reducing the Schottky barrier height and contact resistivity.

Pd/Au p-contact The Pd/Au contact is the most employed Pd-containing system to *p*-GaN. The non-alloyed contact has been reported to provide a contact resistivity in the range of 10^{-2}–10^{-6} $\Omega \cdot cm^2$ depending on the predeposition treatment and the contact layer used.[92, 93, 94, 95, 96, 97, 98, 99, 100] Jang *et al.* studied Pd/Au contacts alloyed in air. The lowest contact resistivity of 6.4×10^{-4} $\Omega \cdot cm^2$ was obtained after 500 °C annealing for 1 min. Cross-sectional transmission electron microscopy (XTEM) analysis showed that a Au-Pd solid solution was produced due to intermixing of Au and Pd layers during the annealing. The reduced contact resistivity was attributed to the dissolution of Ga atoms into the Au-Pd solid solution at 500 °C introducing a number of Ga-vacancies near the interface. Under annealing at 550 °C the Pd/Au contact showed rapid degradation, which was ascribed to out-diffusion of N atoms through the Au-Pd compound.

Pd/Ni p-contact The Pd/Ni scheme was stated to be more efficient and stable compared to the Pd/Au contact.[99, 101] The contact resistivity obtained after annealing in air at 500 °C was determined to be 9.6×10^{-5} $\Omega \cdot cm^2$, nearly one order of magnitude lower than that of Pd/Au at the same conditions. XTEM, XRD, and SIMS analysis showed

that a NiO layer was formed as a result of Ni oxidation during annealing in air. Below the NiO layer, Pd gallides such as Ga_2Pd_5 and Ga_5Pd were observed. Meanwhile, no Pd-related and/or Ga-related compounds were found at the surface. This indicates that the NiO layer effectively prevented Ga and Pd atoms from out-diffusing to the surface, promoting the Pd layer to react with GaN. Thereby, a large number of Ga-vacancies was produced below the contact reducing the Schottky barrier height and contact resistivity. The thermal stability of the Pd/Ni system was also found to be superior to that of the Pd/Au contact. The authors suggested that the NiO layer acted as an effective barrier for the out-diffusion of N atoms from decomposed GaN preventing high temperature contact degradation.

Pd/Mo p-contact The Pd/Mo contact was reported to yield a resistivity of 5×10^{-4} and 2×10^{-4} $\Omega \cdot cm^2$ as-deposited and annealed at 500 °C in vacuum, respectively. The hole concentration in *p*-GaN was found to follow the contact resistivity, namely 2×10^{17} cm^{-3} before the annealing and 6×10^{17} cm^{-3} after the 500 °C annealing. SIMS and Raman spectra analysis showed no substantial change of the hydrogen content in the epilayers. Thereby, this behavior cannot be attributed to the increase in activated Mg due to removal of hydrogen. The authors suggested that Ga-vacancies induced near the GaN surface were responsible for the increased hole concentration and for improved contact characteristics. In all probability, Pd gallides were produced as a result of the annealing. AES analysis showed that Mo remained on the contact surface after the alloying, promoting interface reactions between the Pd electrode and the *p*-GaN layer.

Pd/Re p-contact Re, with a relatively high work function (5.1 eV) and perfect thermal stability, is an attractive candidate for low-resistance and thermally stable ohmic contacts on *p*-GaN. The Pd/Re metallization was reported to produce a contact resistivity of 1.4×10^{-3} and 8.7×10^{-4} $\Omega \cdot cm^2$ as-deposited and annealed at 550 °C for 1 min in N_2, respectively. GaN was previously treated in aqua-regia for 10 min, which is known to promote *p*-contact formation (see "Predeposition surface treatment"). AES and XRD analysis showed that Pd reacted with GaN under the annealing producing Pd gallides, such as Ga_2Pd_5 and Ga_5Rd. The Ga-vacancies produced were suggested to improve the contact characteristics. The Re layer remained very stable after the alloying. The prolonged annealing at 550 °C did not significantly change the surface morphology and electrical characteristics indicating good thermal stability of the Pd/Re contact. However, annealing at 650 °C resulted in severe degradation of both surface morphology and contact resistivity.

Pd/Ag/Au/Ti/Au p-contact Using the Pd/Ag/Au/Ti/Au metallization, a contact resistivity as low as 1.1×10^{-6} $\Omega \cdot cm^2$ was achieved after annealing at 800 °C for 1 min in N_2. The selection of these metals was based on the realization of a Ag-Au alloy at a temperature of about 773 °C. The thin bottom Pd layer (1 nm thick) was included to improve adhesion of the Ag layer to the surface of GaN. XPS analysis showed that a $(Ag+Au)_2GaN$ compound was produced under the 800 °C annealing forming a highly doped p^+-region near the interface. As a result, a very low contact resistivity was obtained. The top Ti/Au layer provided excellent thermal stability for this contact scheme.

Pt-based *p*-contacts

Platinum has a work function of 5.6 eV, the highest value among common metals, and excellent thermal stability. Various Pt-based metallization schemes have been reported for *p*-GaN, most of them provide low-resistance ohmic contacts even without postdeposition annealing. This makes the Pt-containing contacts suitable for fabrication of complicated layered structures.

Pt p-contact The Pt-only system is widely used as an ohmic contact to *p*-GaN. The non-alloyed contact has been reported to provide a contact resistivity in the range of of 10^{-2}–10^{-5} Ω·cm^2 depending on the predeposition treatment used.[105, 106, 107, 108, 109, 110, 111] The impact of different chemicals on *p*-contact formation is considered above (see "Predeposition surface treatment").

Pt/Ni/Au p-contact The Pt/Ni/Au scheme was reported to yield a contact resistivity of 3×10^{-3} and 5.1×10^{-4} Ω·cm^2 as-deposited and annealed at 350 °C for 1 min, respectively. The low resistivity was attributed to the high work function of Pt and an increase in the contact area after the alloying. AES analysis showed that Ni diffused through the Au layer under the annealing and formed an oxide on the contact surface. The Pt layer was suggested to prevent formation of nitrogen vacancies in GaN degrading the *p*-contact performance.

Pt/Pd/Au p-contact The Pt/Pd/Au contact was reported to provide a resistivity of 3.1×10^{-5} Ω·cm^2 after being annealed at 600 °C for 2 min in nitrogen ambient. GaN was previously treated in BHF solution for 10 min, which is known to promote *p*-contact formation (see "Predeposition surface treatment"). AES and GXRD analysis showed that the annealing resulted in the formation of Pt- and Pd-gallides layers, such as $GaPt_2$, Ga_2Pt, Ga_2Pd_5, Ga_2Pd_5 , and Ga_2Pd_5, at the metal/GaN interface. Consequently the surface Fermi level shifted toward the valence-band due to the formation of a N-rich surface region in GaN. The ohmic behavior was ascribed to the combined effects of Pt- and Pd-gallide formation and an increase in a contact area.

Pt/Ru p-contact The Pt/Ru scheme was reported to yield a contact resistivity of 7.8×10^{-4} and 2.2×10^{-6} Ω·cm^2 as-deposited and annealed at 600 °C for 2 min, respectively. GaN was previously treated in BOE solution for 20 min, which is known to promote *p*-contact formation (see "Predeposition surface treatment"). An improvement in the contact resistivity after alloying was attributed to Pt-gallide formation and an increase in the contact area.

Pt/Re/Au p-contact The Pt/Re/Au scheme was investigated by Reddy *et al.* The contact provided a resistivity in the range of 10^{-3} Ω·cm^2 to *p*-GaN previously treated in aqua-regia for 10 min. AES and GXRD analysis showed that after 600 °C annealing Pt, Re, and Au diffused to GaN and participated in the formation of Ga-related interfacial products, such as $GaPt_2$, Ga_3Pt_5, Ga_3Re, and $GaAu_2$. The authors attributed the ohmic behavior to the generation of Ga-vacancies near the *p*-GaN surface reducing the Schottky barrier height for hole transport. The contact was found to be very stable during prolonged 600 °C annealing but degraded at 800 °C due to heavy intermixing between the metals and GaN, and/or dissociation of GaN.

Rh-based *p*-contacts

Rhodium, with a relatively high work function of 5.0 eV, is known to react with GaN forming gallide phases at low temperatures. For this reason Rh was employed as the first contact layer in contact systems, such as Rh-only, Rh/Au and Rh/Ni, to *p*-GaN. The contacts were found to yield a resistivity in the range of 10^{-5}–10^{-6} Ω·cm^2 without postdeposition annealing, the lowest for non-alloyed systems to *p*-GaN. GaN was previously treated in BOE solution for 20 min, which is known to promote *p*-contact formation (see "Predeposition surface treatment"). AES analysis showed that some amount of Ga outdiffused into the Rh layer implying that Rh interacted with Ga and formed interfacial phases such as gallides. The ohmic behavior was attributed to the effective removal of the native oxide and to Ga-vacancies formed near the GaN surface region as a result of both the predeposition treatment and the interaction of Rh and GaN.

Ti/Pt/Au *p*-contact

In the Ti/Pt/Au system, a thin Ti layer is employed due to its excellent adhesion and ability to reduce surface contamination and oxides on GaN. The second Pt layer is expected to promote ohmic contact formation due to its high work function (5.6 eV). A contact resistivity of 1.3×10^{-4} and 4.2×10^{-5} $\Omega \cdot cm^2$ was demonstrated for the alloyed contacts to AlGaN/GaN SL and to GaN, respectively.[117, 118]

Ta/Ti *p*-contact

Suzuki *et al.*[119, 120] employed Ti and Ta due to their ability to attract hydrogen atoms from GaN at high temperatures and, hence, to increase the hole concentration in *p*-GaN. Post-deposition contact annealing at 800 °C for 20 min provided a contact resistivity as low as 3×10^{-5} $\Omega \cdot cm^2$. The hole concentration in *p*-GaN was found to increase by 2 – 3 times after the annealing. Thereby, the reduction of the contact resistivity was attributed to the reactivation of Mg dopants by disrupting the bonding in residual Mg–H complexes. Unfortunately, this contact is very unstable in air. Electrical characteristics showed extremely fast deterioration under current injection and rapidly degraded even during room temperature storage.[148]

CuNi/Ag *p*-contact

The CuNi/Ag system was reported to yield a contact resistivity as low as 6×10^{-6} $\Omega \cdot cm^2$ after annealing in air at 450 °C for 1 min. The CuNi solid solution was employed as a sticking layer for Ag, which has very poor adhesion to GaN. Before contact deposition GaN was treated in BOE solution for 20 min, which is known to promote *p*-contact formation (see "Predeposition surface treatment"). The authors found that an oxygen ambient played an important role in lowering the contact resistivity. No ohmic behavior was observed for this contact after annealing in N_2. AES and GXRD analysis showed that during the 450 °C annealing in air Ag diffused to the GaN surface forming interfacial gallide phases, while CuNi outdiffused to the contact surface forming CuNi-oxides. As a result of the Ga-vacancies produced, the surface Fermi level shifted toward the valence band edge reducing the Schottky barrier height for hole transport. The surface CuNi-oxides were suggested to effectively prevent agglomeration of the Ag layer upon annealing, preventing an increase of its contact resistivity.

NiZn/Pd *p*-contact

Song *et al.* employed a NiZn alloy (10at.% Zn.) in this contact system as a possible solution to increase the hole concentration in *p*-GaN through indiffusion of Zn under annealing. A contact resistivity as low as 4.8×10^{-5} $\Omega \cdot cm^2$ was achieved after alloying in air at 530 °C for 1 min. GaN was previously treated in BOE solution for 20 min to promote *p*-contact formation (see "Predeposition surface treatment"). AES analysis showed that under the annealing, Pd indiffused to the GaN surface through the Ni-Zn alloy layer and interacted with GaN forming interfacial gallides. As a result of the Ga-vacancies produced near the interface, the surface Fermi level shifted towards the valence-band edge reducing the Schottky barrier height by 0.4 eV. The authors speculated that indiffusion of Zn into GaN might also contribute to the increase in surface carrier concentration.

6.6 Optimization of contacts for a laser diode application

Devices operating under high current conditions, such as laser diodes, have the potential to generate a lot of heat. To avoid excessive overheating resulting in the failure of a device, a contact resistivity in the order of 10^{-4} Ω·cm^2 for both *n*- and *p*-contacts to GaN is required. Furthermore, contact stability at higher temperatures in an air environment is also critically important for practical device operation. Poor thermal stability can result in gradual contact degradation and even metal migration along threading dislocations resulting in the eventual shorting of a device. Thereby the development of reliable low-resistance contacts is one of the key issues for good laser diode performance.

For optical devices, such as LEDs and laser diodes where ohmic contacts to both *n*- and *p*-GaN are required, special attention should be paid to the compatibility between the *p*- and *n*-contact fabrication processes. The annealing conditions (temperature, ambient) and/or predeposition treatment required for one contact may result in serious degradation of the other. Fortunately, it has been found that RIE exposure promotes the formation of non-alloyed *n*-contacts (see above). For optical devices RIE is widely used to etch through the structure and to get access to *n*-type layers. Thereby, the *n*-GaN surface is already exposed by plasma treatment before contact deposition. As a result, no special predeposition treatment and postdeposition annealing are required for the *n*-contact. If the *n*-contact fabrication follows *p*-contact formation, any necessary processing steps can be applied for *p*-contact fabrication. Nevertheless, non-alloyed or low-temperature-annealed contacts to *p*-GaN are preferable. It has been shown that contact annealing at temperatures higher than 700 °C, even for a short time, seriously degraded LED's optical and electrical characteristics due to electrical short circuits that are created in a structure.[149]

Some representative results of our group are summarized in Table 6-4. All experiments have been conducted by Dr. Margaret Hopkins. A circular transmission line model (CTLM) was used for contact resistivity measurements. An e-beam evaporator was employed for metal deposition; some contacts were subsequently annealed in a conventional oven in different gas ambients. As can be seen, the non-alloyed Ti/Al and Ti/Al/Ti/Au contacts to *n*-GaN provided reasonable resistivities appropriate for laser diode fabrication. This is consistent with the published data reported on the impact of RIE on *n*-contact formation.[14, 27, 28, 31, 36, 38, 39, 55, 56, 57] For a *p*-contact, a thin *p*-InGaN sub-contact layer (~10 nm) was employed by our group. Very low-resistance, less than 10^{-5} Ω·cm^2, ohmic contacts were produced using alloyed Ni/Au and Pt/Au, and non-alloyed Pd/Au systems. This is consistent with the published data on InGaN contacts.[85, 96, 97, 98, 100] In all probability, our results can be improved even more using the optimized thickness of the sub-layer (see "Sub-contact layers"). One can see that the Ni/Au contact was very sensitive to the annealing temperature and degraded after alloying at 550 °C in oxygen. The low-resistance non-alloyed Pd/Au also degraded after annealing at 500 °C. Thereby careful control over the annealing parameters is required.

Table 6-4. Characteristics of ohmic contacts to *p*- and *n*-GaN (Dr. Margaret Hopkins).

Material	Contact layers	Contact resistivity (Ω·cm^2)	Carrier density (cm^{-3})	Treatment before photo-lithography	Treatment before metal deposition	Alloying condition
n-GaN	Ti/Al 20/100	2.7×10^{-4}	3.0×10^{18}	ICP in Cl_2/Ar	HCl	no
		8.0×10^{-5}	3.0×10^{18}	ICP in Cl_2/Ar	HCl	400 °C /5 min/N_2
n-GaN	Ti/Al/Ti/Au 20/100/40/500 nm	3.7×10^{-4}	3.0×10^{18}	ICP in Cl_2/Ar	HCl	no

p-InGaN(10 nm) /GaN	Pt/Au 20/20 nm	$< 10^{-5}$			BOE (4:1) /2 min	600 °C/5min /O_2+N_2
p-InGaN(10 nm) /GaN	Ni/Au 20/20 nm	$< 10^{-5}$			BOE (4:1) /2 min	500 °C /5 min/O_2
p-InGaN(10 nm) /GaN	Ni/Au 20/20 nm	7.4×10^{-3}			BOE (4:1) /2 min	550 °C /5 min/O_2
p-InGaN(10 nm) /GaN	Pd/Au 20/130 nm	$< 10^{-5}$			BOE (4:1) /2 min	no
p-InGaN(10 nm) /GaN	Pd/Au 20/130 nm	5.6×10^{-4}			BOE (4:1) /2 min	500 °C /5 min/N_2

In conclusion, ohmic contacts to both *p*- and *n*-GaN were optimized. N-contacts to RIE treated *n*-GaN produce a reasonable resistivity without postdeposition annealing. In contrast, *p*-contacts, except for the Pd/Au system, require an annealing step in oxidizing ambients and should be used before *n*-contact formation to prevent subsequent oxidation of Ti and Al in *n*-contact systems.

6.7 References

[1] S. J. Pearton, J. C. Zolper, R. J. Shul, F. Ren, J. Appl. Phys. 86, 1 (1999).

[2] A. Weimar, A. Lell, G. Bruderl, S. Bader, and V. Harle, Phys. Stat. Sol. (a) 183, 169 (2001).

[3] S. Kurtin, T. C McGill, and C. A. Mead, Phys. Rev. Lett. 22, 1433 (1969).

[4] J. S. Foresi and T. D. Moustakas, Appl. Phys. Lett. 62, 2859 (1993).

[5] J. W. Orton and C. T. Foxon, Rep. Prog. Phys. 61, 1 (1998).

[6] Q. Z. Liu and S. S. Lau, Solid-State Electronics 42, 677 (1998).

[7] T. Mori, T. Kozawa, T. Ohwaki, Y. Taga, S. Nagai, S. Yamasaki, S. Asami, N. Shibata, and M. Koike, Appl. Phys. Lett. 69, 3537 (1996).

[8] K. A. Rickert, A. B. Ellis, J. K. Kim, J.-L. Lee, F. J. Himpsel, F. Dwikusuma, and T. F. Kuech, J. Appl. Phys. 92, 6671 (2002).

[9] A. Zeitouny, M. Eizenberg, S. J. Pearton, F. Ren, J. Appl. Phys. 88, 2048 (2000).

[10] D.-W. Kim and H. K. Baik, Appl. Phys. Lett. 77, 1011 (2000).

[11] S. N. Mohammad, J. Appl. Phys. 95, 4856 (2004).

[12] S. N. Mohammad, J. Appl. Phys. 95, 7940 (2004).

[13] J.-L. Lee, J. K. Kim, M. H. Weber, and K. G. Lynn, Appl. Phys. Lett. 78, 4142 (2001).

[14] Z. Fan, S. N. Mohammad, W. Kim, O. Aktas, A. E. Botchkarev, and H. Morkoc, Appl. Phys. Lett. 68, 1672 (1996).

[15] C. Lu, H. Chen, X. Lv, and X. Xie, S. N. Mohammad, J. Appl. Phys. 91, 9218 (2002).

[16] A. Motayed, K. A. Jones, M. A. Derenge, M. C. Wood, D. N. Zakharov, Z. Liliental-Weber, D. J. Smith, A. V. Davydov, W. T. Anderson, A. A. Iliadis, and S. N. Mohammad, J. Appl. Phys. 95, 1516 (2004).

[17] J. O. Song, D.-S. Leem, J. S. Kwak, O. H. Nam, Y. Park, T.-Y. Seong, Appl. Phys. Lett. 83, 2372 (2003).

[18] V. R. Reddy, S.-H. Kim, J. O. Song, and T.-Y. Seong, Semicond. Sci. Technol. 18, 541 (2003).

[19] J. O. Song, S.-H. Kim, J. S. Kwak, T.-Y. Seong, Appl. Phys. Lett. 83, 1154 (2003).

[20] B. P. Luther, S. E. Mohney, T. N. Jackson, M. Asif Khan, Q. Chen, and J. W. Yang, Appl. Phys. Lett. 70, 57 (1997).

[21] Y.-F. Wu, W.-N. Jiang, B. P. Keller, S. Keller, D. Kapolnek, S. P. Denbaars, U. K. Mishra, and B. Wilson, Solid-State Electronics 41, 165 (1997).

[22] Y.-J. Lin, Y.-M. Chen, T.-J. Cheng, and Q. Ker, J. Appl. Phys. 95, 571 (2004).

[23] M. E. Lin, Z. Ma, F. Y. Huang, Z. F. Fan, L. H. Allen, and H. Morkoc, Appt. Phys. Lett. 64 , 1003 (1994).

[24] L. F. Lester, J. M. Brown, J. C. Ramer, L. Zhang, S. D. Hersee, and J. C. Zolper, Appl. Phys. Lett. 69, 2737 (1996).

[25] Y. Koyama, T. Hashizume, H. Hasegawa, Solid-State Electronics 43, 1483 (1999).

[26] Y.-J. Lin and C.-T. Lee, Appl. Phys. Lett. 77, 3986 (2000).

[27] H. W. Jang, C. M. Jeon, J. K. Kim, and J.-L. Lee, Appl. Phys. Lett. 78, 2015 (2001).

[28] H. W. Jang and J.-L. Lee, Journal of The Electrochemical Society 150, G513 (2003).

[29] J. O. Song, S.-J. Park, and T.-Y. Seong, Appl. Phys. Lett. 80, 3129 (2002).

[30] N. A. Papanicolaou, M. V. Rao, J. Mittereder, and W. T. Anderson, J. Vac. Sci. Technol. B 19, 261 (2001).

[31] J. Yan, M. J. Kappers, A. Crossley, C. McAleese, W. A. Phillips, and C. J. Humphreys, Phys. Stat. Sol. (b) 241, 2820 (2004).

[32] Z. Kachwalla, J. W. Wiggins, S. J. Chua, and W. Wang, Phys. Stat. Sol. (a) 176, 779 (1999).

[33] C.-T. Lee and H.-W. Kao, Appl. Phys. Lett. 76, 2364 (2000).

[34] B. Shen, H.M. Zhou, J. Liu, Y.G. Zhou, R. Zhang, Y. Shi, Y.D. Zheng, T. Someya, Y. Arakawa, Optical Materials 23, 197 (2003).

[35] C.-J. Youn and K.-Y. Kang, Jpn. J. Appl. Phys. 39, 3955 (2000).

[36] D.-F. Wang, F. Shiwei, C. Lu, A. Motayed, M. Jah, S. N. Mohammad, K. A. Jones, L. Salamanca-Riba, J. Appl. Phys. 89, 6214 (2001).

[37] A. Motayed, R. Bathe, M. C. Wood, O. S. Diouf, R. D. Vispute, S. N. Mohammad, J. Appl. Phys. 93, 1087 (2003).

[38] A. Motayed, M. Jah, A. Sharma, W. T. Anderson, C. W. Litton, and S. N. Mohammad, J. Vac. Sci. Technol. B 22, 663 (2004).

[39] V. Kumar, L. Zhou, D. Selvanathan, I. Adesida, J. Appl. Phys. 92, 1712 (2002).

[40] E. F. Chor, D. Zhang, H. Gong, G. L. Chen, and T. Y. F. Liew, J. Appl. Phys. 90, 1242 (2001).

[41] C. M. Pelto, Y. A. Chang, Y. Chen, and R. S. Williams, J. Appl. Phys. 92, 4283 (2002).

[42] N. A. Papanicolaou, A. Edwards, M. V. Rao, J. Mittereder, and W. T. Anderson, J. Appl. Phys. 87, 380 (2000).

[43] B. P. Luther, J. M. DeLucca, S. E. Mohney, R. F. Karlicek, Jr., Appl. Phys. Lett. 71, 3859 (1997).

[44] J. Burm, K. Chu, W. A. Davis, W. J. Schaff, L. F. Eastman, and T. J. Eustis, Appl. Phys. Lett. 70, 464 (1997).

[45] C. Lu, H. Chen, X. Lv, and X. Xie, S. N. Mohammad, J. Appl. Phys. 91, 9218 (2002).

[46] J. D. Guo, C. I. Lin, M. S. Feng, F. M. Pan, G. C. Chi, and C. T. Lee, Appl. Phys. Lett. 68, 235 (1996).

[47] M. W. Cole, D. W. Eckart, W. Y. Han, R. L. Pfeffer, T. Monahan, F. Ren, C. Yuan, R. A. Stall, S. J. Pearton, Y. Li, and Y. Lu, J. Appl. Phys. 80, 278 (1996).

[48] A. Zeitouny, M. Eizenberg, S.J. Pearton, and F. Ren, Materials Science and Engineering B59, 358 (1999).

[49] X.A. Cao, S.J. Pearton, S.M. Donovan, C.R. Abernathy, F. Ren, J.C. Zolper, M.W. Cole, A. Zeitouny, M. Eizenberg, R.J. Shul, A.G. Baca, Materials Science and Engineering B59, 362 (1999).

[50] C.F. Lin, H.C. Cheng, G.C. Chi, Solid-State Electronics 44, 757 (2000).

[51] V. R. Reddy and T.-Y. Seong, Semicond. Sci. Technol. 19, 975 (2004).

[52] D. B. Ingerly, Y. Chen, R. S. William, T. Takeuchi, and Y. A. Chang, Appl. Phys. Lett. 77, 382 (2000).

[53] M.-S. Chung, W.-T. Lin, and J. R. Gong, J. Vac. Sci. Technol. B 19, 1976 (2001).

[54] S.J. Pearton, F. Ren, A.P. Zhang, K.P. Lee, Materials Science and Engineering R30, 55 (2000).

[55] H. W. Jang, J. K. Kim, C. M. Jeon, and J.-L. Lee, MRS Internet J. Nitride Semicond. Res. 6, 8 (2001).

[56] J. Yan, M.J. Kappers, Z.H. Barber, and C.J. Humphreys, Appl. Surface Science 234, 328 (2004).

[57] A. T. Ping, Q. Chen, J. W. Yang, M. A. Khan, and I. Adesida, J. Electron. Mater. 27, 261 (1998).

[58] M. R. Lorenz and B. B. Binkowski, J. Electrochem. Soc. 109, 24 (1962).

[59] X. A. Cao, F. Ren, J. R. Lothian, S. J. Pearton, C. R. Abernathy, J. C. Zolper, M. W. Cole, A. Zeitouny, M. Eizenberg, and R. J. Shul, MRS Internet J. Nitride Semicond. Res. 4S1, G6.39(1999).

[60] X. A. Cao, F. Ren, S. J. Pearton, A. Zeitouny, M. Eizenberg, J. C. Zolper, C. R. Abernathy, J. Han, R. J. Shul, and J. R. Lothian, J. Vac. Sci. Technol. A 17, 1221 (1999).

[61] J. Sun, K. A. Rickert, J. M. Redwing, A. B. Ellis, F. J. Himpsel, and T. F. Kuech, Appl. Phys. Lett. 76, 415 (2000).

[62] K. A. Rickert, A. B. Ellis, F. J. Himpsel, J. Sun, and T. F. Kuech, Appl. Phys. Lett. 80, 204 (2002).

[63] J.-S. Jang, S.-J. Park, and T.-Y. Seong, Phys. Stat. Sol. (a) 194, 576 (2002).

[64] J. L. Lee, J. K. Kim, J. W. Lee, Y. J. Park, and T. Kim, Solid-State Electron. 43, 435 (1999).

[65] Y. J. Lin, C. D. Tsai, Y. T. Lyu, and C. T. Lee, Appl. Phys. Lett. 77, 687 (2000).

[66] C.-T. Lee, Y.-J. Lin, and C.-H. Lin, J. Appl. Phys. 92, 3825 (2002).

[67] C. I. Wu, A. Kahn, A. E. Wickenden, D. Koleske, and R. L. Henry, J. Appl. Phys. 89, 425 (2001).

[68] C. M. Pelto, Y. A. Chang, Y. Chen, R. S. Williams, Solid-State Electronics 45, 1597 (2001).

[69] S. C. Binari, H. B. Dietrich, G. Kelner, L. B. Rowland, K. Doverspike, and D. K. Gaskill, Electron. Lett. 30, 909 (1994).

[70] S. N. Mohammad and H. Morkoc, Prog. Quant. Electr. 20, 361 (1996).

[71] J. K. Kim, H. W. Jang, and J.-L. Lee, J. Appl. Phys. 91, 9214 (2002).

[72] S. Ruvimov, Z. Liliental-Weber, J. Washburn, K. J. Duxstad, E. E. Haller, Z.-F. Fan, S. S. N. Mohammad, W. Kim, A. E. Botcharev, and H. Morkoc, Appl. Phys. Lett. 69, 1556 (1996).

[73] S. J. Cai, R. Li, Y. L. Chen, L. Wong, W. G. Wu, S. G. Thomas, and K. L. Wang, Electron. Lett. 34, 2354 (1998).

[74] J. L. Smialek and D. L. Humphrey, Scr. Metall. Mater. 26, 1763 (1992).

[75] R. Ga. Reddy, X. Wen, and I. C. I. Okafor, Metall. Mater. Trans. A 31A, 3023 (2000).

[76] N.A. Papanicolaou, K. Zekentes, Solid-State Electronics 46, 1975 (2002).

[77] A. T. Ping, M. Asif Khan, and I. Adesida, J. Electron. Mater. 25, 819 (1996).

[78] J.-K. Ho, C.-S. Jong, C. C. Chiu, C.-N. Huang, C.-Y. Chen, and K.-K. Shih, Appl. Phys. Lett. 74, 1275 (1999).

[79] J.-K. Ho, C.-S. Jong, C. C. Chiu, C.-N. Huang, K.-K. Shih, L.-C. Chen, F.-R. Chen, and J.-J. Kai, J. Appl. Phys. 86, 4491 (1999).

[80] J. K. Kim, J.-L. Lee, J. W. Lee, Y. J. Park, and T. Kim, J. Vac. Sci. Technol. B 17, 2675 (1999).

[81] J. K. Kim, J. H. Je, J.-L. Lee, Y. J. Park, and B.-T. Lee, Journal of The Electrochemical Society, 147, 4645 (2000).

[82] A. P. Zhang, B. Luo, J. W. Johnson, F. Ren, J. Han, and S. J. Pearton, Appl. Phys. Lett. 79, 3636 (2001).

[83] C.-S. Lee, Y.-J. Lin, and C.-T. Lee, Appl. Phys. Lett. 79, 3815 (2001).

[84] C. H. Kuo, J. K. Sheu, G. C. Chi, Y. L. Huang, T. W. Yen, Solid-state Electronics 45, 717 (2001).

[85] T. Gessmann, Y.-L. Li, E. L. Waldron, J. W. Graff, E. F. Schubert, and J. K. Sheu, Appl. Phys. Lett. 80, 986 (2002).

[86] H. W. Jang, S. Y. Kim, and J.-L. Lee, J. Appl. Phys. 94, 1748 (2003).

[87] D.-H. Youn, M. Hao, H. Sato, T. Sugahara, Y. Naoi, and S. Sakai, Jpn. J. Appl. Phys. 37, 1768 (1998).

[88] J. Narayan, H. Wang, T.-H. Oh, H. K. Choi, and J. C. C. Fan, Appl. Phys. Lett. 81, 3978 (2002).

[89] J.-S. Jang, K.-H. Park, H.-K. Jang, H.-G. Kim, and S.-J. Park, J. Vac. Sci. Technol. B 16, 3105 (1998).

[90] C.-F. Chu, C. C. Yu, Y. K. Wang, J. Y. Tsai, F. I. Lai, and S. C. Wang, Appl. Phys. Lett. 77, 3423 (2000).

[91] J. K. Kim, J.-L. Lee, J. W. Lee, Y. J. Park, and T. Kim, J. Vac. Sci. Technol. B 17, 497 (1999).

[92] J. K. Kim, J.-L. Lee, J. W. Lee, H. E. Shin, Y. J. Park, and T. Kim, Appl. Phys. Lett. 73, 2953 (1998).

[93] J.-L. Lee, M. Weber, J. K. Kim, J. W. Lee, Y. J. Park, T. Kim, and K. Lynn, Appl. Phys. Lett. 74, 2289 (1999).

[94] J.-L. Lee, J. K. Kim, J. W. Lee, Y. J. Park, T..Kim, Solid-State Electronics 43, 435 (1999).

[95] J.-L. Lee and J. K. Kim, Journal of The Electrochemical Society, 147, 2297 (2000).

[96] K. Kumakura, T. Makimoto, and N. Kobayashi, Appl. Phys. Lett. 79, 2588 (2001).

[97] K. Kumakura, T. Makimoto, and N. Kobayashi, Phys. Stat. Sol.(a) 188, 363 (2001).

[98] K. Kumakura, T. Makimoto, and N. Kobayashi, Jpn. J. Appl. Phys. 42, 2254 (2003).

[99] H. W. Jang, H. K. Cho, J. Y. Lee, and J.-L. Lee, Journal of The Electrochemical Society, 150, G212 (2003).

[100] J. Dennemarck, T. Böttcher, S. Figge, S. Einfeldt, R. Kröger, D. Hommel, E. Kaminska, W. Wiatroszak, and A. Piotrowska, Phys. Stat. Sol. (c) 1, 2537 (2004).

[101] H. W Jang, K. H. Kim, J. K. Kim, S.-W. Hwang, J. J. Yang, K. J. Lee, S.-J. Son, and J.-L. Lee, Appl. Phys. Lett. 79, 1822 (2001).

[102] E. Kurimoto, M. Hangyo, H. Harima, K. Takatani, M. Ishida, M. Taneya, and K. Kisoda, Jpn. J. Appl. Phys. 43, 6988 (2004).

[103] V. R. Reddy, S.-H. Kim, J. O. Song, and T.-Y. Seong, Semicond. Sci. Technol. 18, 541 (2003).

[104] V. Adivarahan, A. Lunev, M. Asif Khan, J. Yang, G. Simin, M. S. Shur, and R. Gaska, Appl. Phys. Lett. 78, 2781 (2001).

[105] J.-S. Jang, S.-J. Park, and T.-Y. Seong, J. Vac. Sci. Technol. B 17, 2667 (1999).

[106] J.-L. Lee, J. K. Kim, J. W. Lee, Y. J. Park, and T. Kim, Phys. Stat. Sol. (a) 176, 763 (1999).

[107] J.-S. Jang and T.-Y. Seong, Appl. Phys. Lett. 76, 2743 (2000).

[108] J.-S. Jang and T.-Y. Seong, J. Appl. Phys. 88, 3064 (2000).

[109] C. Huh, S.-W. Kim, H.-M. Kim, D.-J. Kim, and S.-J. Park, Appl. Phys. Lett. 78, 1942 (2001).

[110] J. K. Kim, H. W. Jang, C. Jeon, J.-L. Lee, Current Applied Physics 1, 385 (2001).

[111] J. K. Kim, H. W. Jang, C. C. Kim, J. H. Je, K. A. Rickert, T. F. Kuech, J.-L. Lee, J. Vac. Sci. Technol. B 21, 87 (2003).

[112] J.-S. Jang, I.-S. Chang, H.-K. Kim, T.-Y. Seong, S. Lee, and S.-J. Park, Appl. Phys. Lett. 74, 70 (1999).

[113] H.-K. Kim, I. Adesida, T.-Y. Seong, J. Vac. Sci. Technol. A 22, 1101 (2004).

[114] J.-S. Jang, S.-J. Park, and T.-Y. Seong, Phys. Stat. Sol. (a) 180, 103 (2000).

[115] V. R. Reddy, S.-H. Kim, J.-O. Song, T.-Y. Seong, Solid-State Electronics 48, 1563 (2004).

[116] J. O. Song, D.-S. Leem, J. S. Kwak, O. H. Nam, Y. Park, T.-Y. Seong, Appl. Phys. Lett. 83, 2372 (2003).

[117] L. Zhou, F. Khan, A.T. Ping, A. Osinski, and I. Adesida, MRS Internet J. Nitride Semicond. Res. 5S1, W10.3 (2000).

[118] L. Zhou, W. Lanford, A. T. Ping, I. Adesida, J. W. Yang, and A. Khan, Appl. Phys. Lett. 76, 3451 (2000).

[119] M. Suzuki, T. Kawakami, T. Arai, S. Kobayashi, Y. Koide, T. Uemura, N. Shibata, and M. Murakami, Appl. Phys. Lett. 74, 275 (1999).

[120] M. Suzuki, T. Arai, T. Kawakami, S. Kobayashi, S. Fujita, Y. Koide, Y. Taga, and M. Murakami, J. Appl. Phys. 86, 5079 (1999).

[121] D.-S. Leem, J.-O. Song, J. S. Kwak, J. Cho, H. Kim, O. H. Nam, Y. Park, and T.-Y. Seong, Phys. Stat. Sol. (a) 201, 2823 (2004).

[122] J.-O. Song, D.-S. Leem, and T.-Y. Seong, Semicond. Sci. Technol. 19, 669 (2004).

[123] C. Huh, S.-W. Kim, H.-S. Kim, I.-H. Lee, and S.-J. Park, J. Appl. Phys. 87, 4591 (2000).

[124] K. Kumakura, T. Makimoto, and N. Kobayashi, Jpn. J. Appl. Phys., Part 2 39, L337 (2000).

[125] K. Kumakura, T. Makimoto, and N. Kobayashi, J. Cryst. Growth 221, 267 (2000).

[126] K. Kumakura, T. Makimoto, and N. Kobayashi, Jpn. J. Appl. Phys., Part 2 39, L195 (2000).

[127] P. Kozodoy, Y. P. Smorchkova, M. Hansen, H. Xing, S. P. DenBaars, U. K. Mishra, A. W. Saxler, R. Perrin, and W. C. Mitchel, Appl. Phys. Lett. 75, 2444 (1999).

[128] M. S. Shur, A. D. Bykhovski, R. Gaska, J. W. Yang, G. Simin, and M. A. Khan, Appl. Phys. Lett. 76, 3061 (2000).

[129] I. D. Goepfert, E. F. Schubert, A. Osinsky, P. E. Norris, and N. N. Faleev, J. Appl. Phys. 88, 2030 (2000).

[130] E. F. Schubert, W. Grieshaber, and I. D. Goepfert, Appl. Phys. Lett. 69, 3737 (1996).

[131] I. D. Geopfert, E. F. Schubert, A. Osinsky, and P. E. Norris, Electron. Lett. 35, 1109 (1999).

[132] P. Kozodoy, M. Hansen, S. P. DenBaars, and U. K. Mishra, Appl. Phys. Lett. 74, 3681 (1999).

[133] Y. Koide, T. Maeda, T. Kawakami, S. Fujita, T. Uemura, N. Shibata, and M. Murakami, J. Electron. Mater. 28, 341 (1999).

[134] A. Y. Polyakov, N. B. Smirnov, S. J. Pearton, F. Ren, B. Theys, F. Jomard, Z. Teukam, V. A. Dmitriev, A. E. Nikolaev, A. S. Usikov, and I. P. Nikitina, Appl. Phys. Lett. 79, 1834 (2001).

[135] C. H. Seager,S. M. Myers, A. F. Wright, D. D. Koleske, and A. A. Allerman, J. Appl. Phys. 92, 7246 (2002).

[136] T. Maeda, Y. Koide, and M. Murakami, Appl. Phys. Lett. 75, 4145 (1999).

[137] L.-C. Chen, J.-K. Ho, C.-S. Jong, C. C. Chiu, K.-K. Shih, F.-R. Chen, J.-J. Kai, L. Chang, Appl. Phys. Lett. 76, 3703 (2000).

[138] L.-C. Chen, F.-R. Chen, J.-J. Kai, L. Chang, J.-K. Ho, C.-S. Jong, C. C. Chiu, C.-N. Huang, C.-Y. Chen, and K.-K. Shih, J. Appl. Phys. 86, 3826 (1999).

[139] L.-C. Chen, J.-K. Ho, F.-R. Chen, J.-J. Kai,.L. Chang, C.-S. Jong, C. C. Chiu,.C.-N. Huang, and K.-K. Shih, Phys. Stat. Sol. (a) 176, 773 (1999).

[140] H. Sato, T. Minami, S. Takata, and T. Yamada, Thin Solid Films 236, 27 (1993).

[141] L. Yu, D. Qiao, J. Appl. Phys. 96, 4666 (2004).

[142] D. Qiao, L. S. Yu, S. S. Lau, J. Y. Lin, H. X. Jiang, and T. E. Haynes, J. Appl. Phys. 88, 4196 (2000).

[143] C. C. Kim, J. K. Kim, J.-L. Lee, J. H. Je, M. S. Yi, D. Y. Noh, Y. Hwu, P. Ruterana, Appl. Phys. Lett. 78, 3773 (2001).

[144] C. C. Kim, S. K. Seol, J. K. Kim, J.-L. Lee, Y. Hwu, P. Ruterana, G. Magaritondo, and J. H. Je, Phys. Stat. Sol. (b) 241, 2771 (2004).

[145] C. C. Kim, J. K. Kim, J.-L. Lee, J. H. Je, M. S. Yi, D. Y. Noh, Y. Hwu, and P. Ruterana, Phys. Stat. Sol. (a) 188, 379 (2001).

[146] S. H. Wang, S. E. Mohney, R. Birkhahn, J. Appl. Phys. 91, 3711 (2002).

[147] C. C. Kim, W. H. Kim, J. H. Je, D.-W. Kim, H. K. Baik, and S.-M. Lee, Electrochem. Solid-State Lett. 3, 335 (2000).

[148] T. Arai, H. Sueyoshi, Y. Koide, M. Moriyama, and M. Murakami, J. Appl. Phys. 89, 2826 (2001).

[149] C.-Y. Hsu, W.-H. Lan, Y. S. Wu, Appl. Phys. Lett. 83, 2447 (2003).

7 GaN laser facet fabrication

7.1 Introduction

A GaN-based current injection laser diode can be fabricated using two different approaches. It can be made either as a vertical cavity surface emission laser (VCSEL), or as an edge-emitting laser. The fabrication of a VCSEL requires the deposition of quarter wave mirror stacks which demands complicated growth technique employing precise control over growth quality and uniformity. It makes this approach fairly difficult to implement. At the present time an edge-emitting structure is mainly employed for GaN-based laser diode fabrication. The critical issue of this process is the laser facet formation. In the conventional GaAs and InP material systems, laser facets are usually formed by cleaving the substrate and epilayers along a common cleavage plane. The formation of facets in GaN, however, has proven to be more difficult, as illustrated in the following sections. A variety of methods, including dry etching, wet etching, polishing, and cleaving, on a variety of substrates have been used for the laser diode fabrication. This chapter considers that cleaving is the most promising method. However, a brief outline of the other methods and the problems associated with their implementation is presented as well.

7.2 Requirements for GaN laser facets

GaN-based structures are semiconductors with a relatively low index of refraction (n~2.5) due to their large band gaps. This results in a very low reflectivity at the nitride/air interface. Theoretically, the highest value of mirror reflectivity attains only 18% at a wavelength of 400 nm even for a perfectly smooth GaN-based facet:[1]

$$R_{ideal} = (n_1 - n_2)^2 / (n_1 + n_2)^2 \qquad [7.1]$$

n_1 – refraction index of nitride
n_2 – refraction index of air

Furthermore, scattering losses significantly reduce the facet reflectivity. The surface smoothness requirements are more stringent for GaN lasers than those for near IR lasers due to the shorter emission wavelength. The ratio of the actual power reflectivity to the power reflectivity for a perfectly smooth facet is given by

$$\frac{R(\Delta d)}{R_{ideal}} = e^{-16\pi^2 (n\Delta d/\lambda_0)^2} \qquad [7.2]$$

λ_0 – emission wavelength in vacuum
Δd – RMS roughness of a facet

The calculated normalized reflectivity of a GaN surface for an InGaN/GaN laser structure with an emission wavelength of 395 nm is shown in Fig. 7.1 as a function of surface RMS roughness. A similar dependence for a GaN-based laser diode was calculated by Kneissl *et al.*[2] Published roughness measurements on GaN-based laser structures are presented in Fig. 7.1 as well. As can be seen, in order to achieve reflectivity greater than 90% from the ideal reflectivity, facets with RMS roughness less than 4 nm are required. Stoker *et al.* suggested that the low reflectivity can be compensated by lengthening the cavity to increase the round-trip gain in the laser or by coating the facets. Nevertheless, the laser performance is strongly degraded by facet roughness.

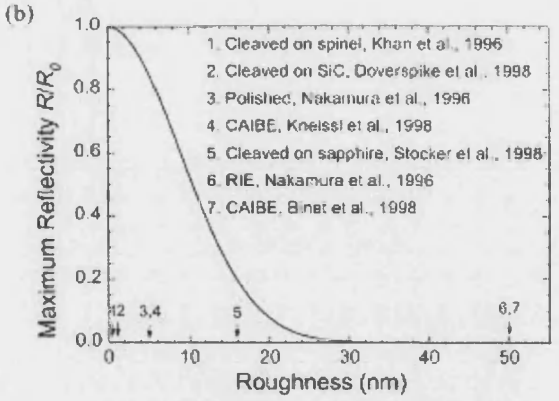

Fig. 7.1. Calculated normalized reflectivity of GaN facets as a function of surface RMS roughness.

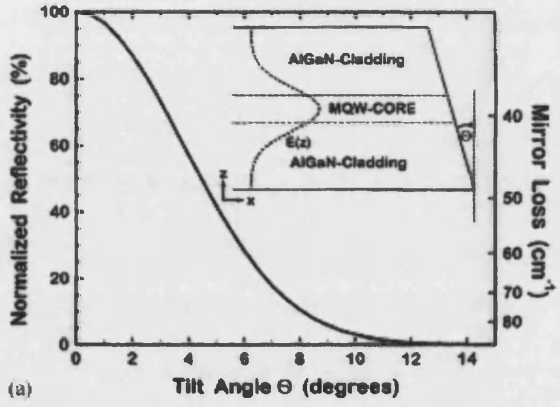

Fig. 7.2. Calculated normalized reflectivity of GaN facets as a function of inclination angle of a tilted facet.

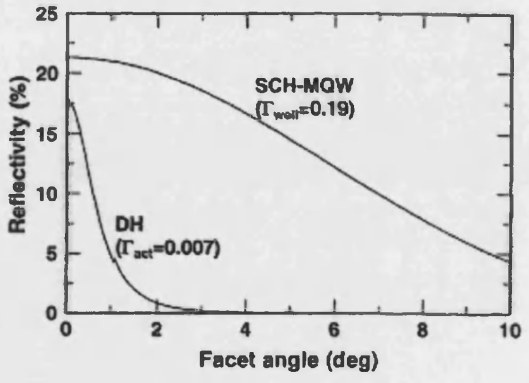

Fig. 7.3. Calculated reflectivity of GaN facets as a function of inclination angle of a tilted facet for SCH-MQW structure and DH structure.

The calculated normalized mirror reflectivity for GaN-based laser diode as a function of the inclination angle of the tilted facet is presented in Fig. 7.2. The values for the mirror losses on the right axis were calculated assuming a 500 μm cavity. As can be seen, the mirror reflectivity strongly deteriorates with increasing tilt angle. These results are fairly different from those reported by Itaya *et al.*[3] They calculated the effect of a tilt angle on facet reflectivity for both separate-confinement-heterostructure (SCH) with GaN/InGaN MQWs and a simple InGaN/AlGaN double-heterostructure (DH). As can be seen in Fig. 7.3, the reflectivity is not very sensitive to the tilt angle in the case of the SCH-MQW structure due to the fact that the optical mode is strongly confined vertically within the SCH structure. In contrast, the reflectivity of the DH with a small optical confinement has a strong dependence on the facet angle.

The experimental confirmation that facet reflectivity is relatively insensitive to the tilt angle comes from the research of Ambe *et al.*[4] They applied focused ion beam (FIB) polishing to change the tilt angle for one of laser diode facets from 0° to 5°. I-L characteristics revealed almost no changes in threshold current and differential quantum efficiency, as shown in Fig. 7.4. On the other hand, a strong variation of the threshold current on the in-plane rotation angle was observed, as shown in Fig. 7.5. Only one mirror was rotated around the (0001)-axis while the other remained fixed at 0°. These results were ascribed to the absence of optical waveguiding of the lasing mode within the plane of the layered structure.

Thereby it is very important to obtain smooth and well-aligned laser facets. However, even for ideal facets, the highest value of reflectivity can only attain 18%. It therefore usually requires an additional coating of dielectric multiple films on the facets to increase the reflectivity and to reduce threshold current.

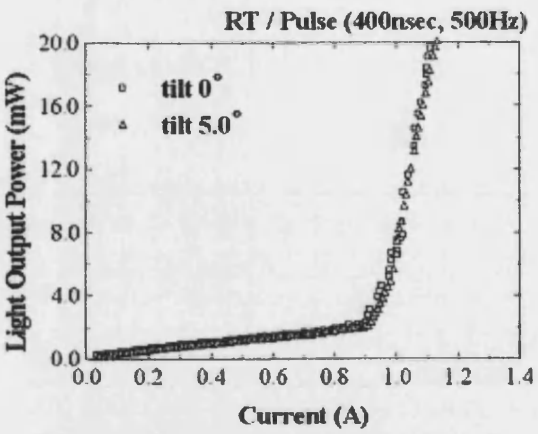

Fig. 7.4. Tilt angle dependence of the I-L characteristics.

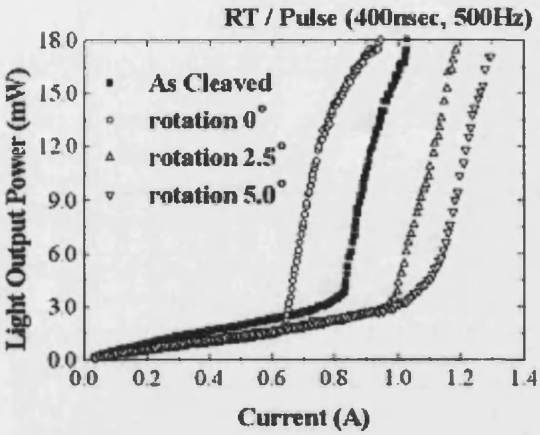

Fig. 7.5. In-plane rotation angle dependence of the I-L characteristics.

7.3 Methods of laser facet formation

7.3.1 Cleaving

Cleaving is the preferred method for the facet formation in most semiconductor systems. It is a robust and reproducible technique for forming smooth and vertical facets. The fabrication of cleaved facets is not affected by variations of process parameters as in the case of dry and wet etching. Cleaved facets are superior to the etched or polished facets because they can be fabricated with RMS roughness below 1 nm. It is at least an order of magnitude better than the values obtained for the etching and polishing methods. Cleaved-facet lasers have been fabricated for GaN grown on different substrates including SiC, a-plane sapphire, c-plane sapphire, and spinel. A detailed description of the cleaving of GaN grown on these substrates is presented below in this report.

7.3.2 Plasma etching

Many groups have used plasma-etched facets for laser diodes fabrication due to the difficulties with forming cleaved facets in III-nitride materials. Thus the first current injection GaN-based laser diode was fabricated using RIE (reactive ion etching) etching.[5] Various processing techniques of plasma etching have been employed to etch nitride materials including RIE, ECR-RIE (electron cyclotron resonance etching), CAIBE (chemically assisted ion beam etching), and ICP (inductively coupled plasma etching).[6] Etched mirrors allow for wafer scale fabrication of complete laser structures. Mirrors with different geometries can be made by dry etching. Besides, lasers can be potentially tested prior to the separation into single chips. However, it is fairly difficult to develop robust etch recipes for producing high quality reproducible facets. The etching process is greatly affected by process chamber conditions and variations of processing parameters such as temperature, gas composition, plasma density, acceleration voltage, pressure, etc.

Dry etching also leaves the facets fairly rough and slightly angled. In contrast to the cleaving technique, typical etched laser facets display nm scale roughness resulting in the reduction of reflectivity. The RIE technique with Cl_2 plasma employed for the first laser diode gave the RMS roughness of facets of about 50 nm. Other techniques, such as ICP, ECR-RIE, and CAIBE, yield much better results due to the higher level of control over etching conditions. The best results for GaN etched facets were achieved using temperature-controlled CAIBE etching employing the tilting of a substrate.[7] The estimated

RMS roughness of 5 nm and inclination angle within 2° probably resulted from the mask roughness and profile. However, this process is excessively expensive and complicated to be employed in the production of laser diodes.

Dry-etched facets are also problematic for optical disc applications. The etched facet cannot be made to extend to the free edge of the sample. This means that light reflects from the substrate surface remaining in front of the etched facet and the reflected light interferes with the direct light. As a result, a large portion of light is lost and the output laser beam and far field pattern required for optical disk applications are distorted. This problem can possibly be avoided by using precise sawing, cleaving, or laser cutting. However, it also makes the laser diode fabrication process excessively complicated and expensive.

7.3.3 Polishing

Other methods for producing laser facets are mechanical polishing and focused ion beam (FIB) polishing. Polished facets can be made fairly smooth and close to vertical. However, both methods are labor intensive and cannot easily be employed in the production of laser diodes. The mechanical polishing was first applied for GaN laser diode fabrication by Nakamura *et al.*[8] The RMS roughness of facets was estimated to be ~5 nm. This technique has not been widely adopted for laser fabrication due to process complexities. In contrast, FIB polishing has been often used to improve etched and cleaved laser facets.[4, 9] This is a useful and flexible method with the advantage of it being a maskless direct patterning technique. By using FIB polishing, the RMS roughness of facets was significantly reduced to a value from 30 Å to 6 Å. As a result of the improved mirror quality, the threshold current was reduced from 1.75 to 1.08 A, and from 1.25 to 0.75 A.

The focused ion beam (FIB) facet formation method is also expected to be a useful tool for characterizing laser diodes. Typically, gain and loss in diode lasers are determined by measuring the differential efficiency (η_d) and threshold current density (J_{th}) as a function of the cavity length (L) at the fixed facet reflectivity (R). With reproducible FIB-prepared facets it is possible to measure J_{th} and η_d against length, on a single laser bar, by sequential FIB polishing to shorten the laser. This would eliminate any scatter resulting from material non-uniformity and would also allow observing the evolution of lasing spectra with length, on a single laser bar.

7.3.4 Wet etching

A variety of methods and wet etchants have been tried for III-nitride materials. However, only a few of them have been found to etch the nitrides and with different levels of success.[10, 11] Several groups have studied photoenhanced electrochemical (PEC) etching of GaN in KOH solutions.[12, 13, 14, 15, 16, 17, 18] PEC etching has the advantage of relatively low equipment cost, room temperature etching conditions, and low surface damage. However, the sidewalls produced by PEC etching are far too rough due to light scattering and hole diffusion in GaN itself and cannot be used as laser facets. Furthermore, *p*-GaN does not etch under these conditions. Fortunately, GaN has also been found to be etched in some wet etchants without UV light assistance. The etch rates and etching crystal planes for GaN observed in various wet chemicals are summarized in Table 7-1. The c-plane (0001) of GaN is resistant to all of these chemicals, with a negligibly small etch rate.

Table 7-1. Etch rates and observed etching planes for various chemicals.

Chemical	Temperature (°C)	Etch rate (μm/min)	Etching planes observed
Acetic acid (CH_3COOH)	30	< 0.001	None
Hydrochloric acid (HCl)	50	< 0.001	None
Nitric acid (HNO_3)	81	< 0.001	None
Phosphoric acid (H_3PO_4)	108–195	0.013–3.2	{10$\bar{1}$2},{10$\bar{1}$3}
Sulphuric acid (H_2SO_4)	93	< 0.001	None
Potassium hydroxide (KOH), molten	150–247	0.003–2.3	{10$\bar{1}$0},{10$\bar{1}\bar{1}$}
50% KOH in H_2O	83	< 0.001	None
10%–50% KOH in ethylene glycol	90–182	0.0015–1.3	{10$\bar{1}$0}
50% NaOH in H_2O	100	< 0.001	None
20% NaOH in ethylene glycol	178	0.67–1.0	None

For a long time it had been generally accepted that under normal conditions, only molten salts such as KOH or NaOH at temperatures above 250 °C could etch GaN at practical rates. Only AlN and Al-rich alloys were etched in KOH-based solutions at temperatures of 50 – 100 °C.[19] The etch rates strongly depended on the material quality and Al content, with slower rates for higher quality materials and for alloys with lower Al content. Recently Stocker *et.al.*[11, 20] found that other solutions such as phosphoric acid (H_3PO_4), KOH or NaOH salts dissolved in ethylene glycol can also effectively etch GaN. The ethylene glycol was used as a solvent for KOH and NaOH. It allowed the authors to employ temperatures between 90 and 180 °C. They noticed that the etch rate of GaN in KOH dissolved in ethylene glycol was even higher than the etch rate in molten KOH at the same temperature. It was ascribed to the high solubility of the etch products in the ethylene glycol. The maximal etch rate corresponded to a value of 40% KOH by weight in the ethylene glycol.

Boiling KOH dissolved in ethylene glycol has been recently employed for the fabrication of wet-etched laser facets[20, 21, 22] due to the crystallographic nature of this etching. As can be seen in Table 7-1, the etching planes of GaN in this solution are {10$\bar{1}$0}, which correspond to vertical sidewalls after the etching. The RMS roughness of the produced sidewalls was estimated to be smaller than 5 nm. The c-plane of GaN is resistant to the chemical implying that no etch mask is required. However, if long etching times are used, the etch mask may be required to prevent the development of etch pits at defect sites. The change in doping was found not to affect the etch plane or the etch rate. All these factors imply that this wet etching method can be used for laser facet fabrication. The first fabrication step to establish the etching depth can be performed by common processing methods, such as dry etching, PEC etching in KOH solution, or cleaving. This step should produce rough vertical facets, which are aligned with the {10$\bar{1}$0} planes of GaN.

Bottcher *et al.* have recently realized a GaN-based laser diode by using crystallographic wet etching to smoothen rough facets after RIE etching. This method was mentioned to have excellent reproducibility of the facet perfection. The wet etching was performed using 50% KOH dissolved by weight in ethylene glycol at a temperature of 140 °C. The etch rates were found to be identical for alloys containing In or Al and for Mg- or Si-doped films. Laser facets were previously formed and aligned perpendicular to <10$\bar{1}$0> direction using RIE etching. As can be seen in Fig. 7.6, smooth vertical sidewalls were obtained after the wet etching step compared to rough inclined sidewalls after RIE

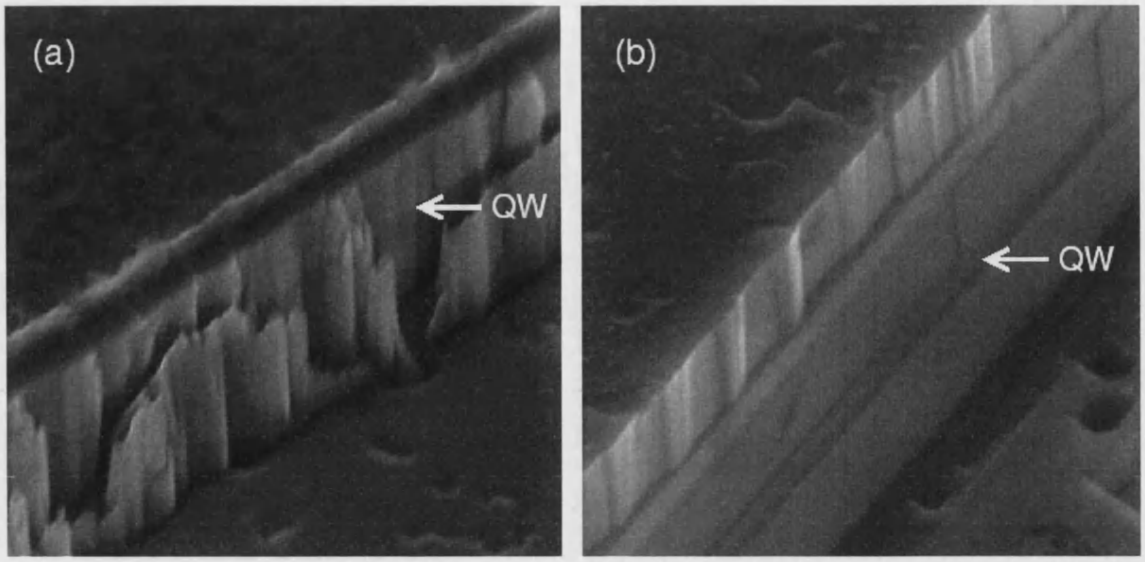

Fig. 7.6. SEM images of the mirror facets of a GaN based laser diode a) after RIE etching and b) after crystallographic wet etching.

patterning. The roughness of the facets was estimated to be comparable to that of cleaved material. As a result, a pulse operated laser diode was demonstrated with an emission wavelength of 401 nm and a threshold current density of 16.2 kA/cm^2.

7.4 Cleaved laser facets

For forming cleaved laser facets, which are both smooth and vertical across epitaxial layers, the crystal structure of the epilayers and a substrate should have vertical cleave planes. Furthermore, the vertical cleave planes of the epitaxial layers should be parallel to those of the substrate. Thereby, the important issue for GaN lasers becomes the choice of a suitable substrate. In addition to an appropriate crystal structure, a substrate must also have a lattice constant and a thermal expansion coefficient comparable to those for GaN material. At the present time, laser operation has been successfully demonstrated from devices grown on various substrates including a- or c-plane sapphire, SiC, spinel ($MgAl_2O_4$), and free-standing GaN. The crystal structures, GaN-compatible cleave planes, benefits and drawbacks for all these substrates are discussed below.

7.4.1 GaN grown on sapphire

Sapphire (α-Al_2O_3) is a substrate most widely used for GaN growth and fabrication of laser diodes. It has been employed for laser fabrication by a majority of the companies including Nichia, Sony, Toyoda Gosei, Sharp, Xerox, Samsung. Most of the advanced devices exhibiting room temperature (RT) continuous wave (CW) operation are currently grown on sapphire substrates. Sapphire is the choice substrate for nitride growth because it is transparent, relatively cheap, and stable at the high growth temperatures required for MOCVD of GaN. The technology of growth of the nitrides on sapphire is fairly mature. However, sapphire is not the perfect substrate. It has a large 13% lattice mismatch with GaN, which requires an AlN or GaN buffer layer prior to the growth. This buffer layer is deposited as an amorphous film at low temperatures (550 °C) and transformed into single crystal at a temperature over 1000 °C. Nevertheless, the residual density of threading dislocations in GaN epilayers remains as high as 10^9 - 10^{10} cm^{-2}, which significantly degrades the performance of GaN-based laser diodes, especially their lifetime. This

problem can partly be resolved using epitaxial lateral overgrowth (ELOG) technology. This method allows the reduction of the threading dislocation density to a level of ~10^6 - 10^7 cm^{-2}. Sapphire has also some drawbacks as a substrate for laser diodes. It is electrically insulating, whereby no electrode can be formed on the lower surface of the substrate. The small thermal conductivity of sapphire (0.46 W/cm·K) requires special methods to organize the proper thermal management for CW operating devices. These problems complicate the fabrication process and degrade the laser characteristics.

Sapphire has a corundum crystal structure and GaN has a wurtzite crystal structure. Both of them have 6-fold rotational symmetry around the c-axis.[23] Fig. 7.7 and Fig. 7.8 present the crystal structures of sapphire and GaN respectively, pictured in the [0001] orientation.[24] For GaN growth two crystalline orientations of sapphire (c-plane (0001) and a-planes {11$\bar{2}$0}) can be employed as a substrate with almost the same crystal quality. Both orientations can also be used, with different levels of success, for the fabrication of cleaved-facet laser diodes.

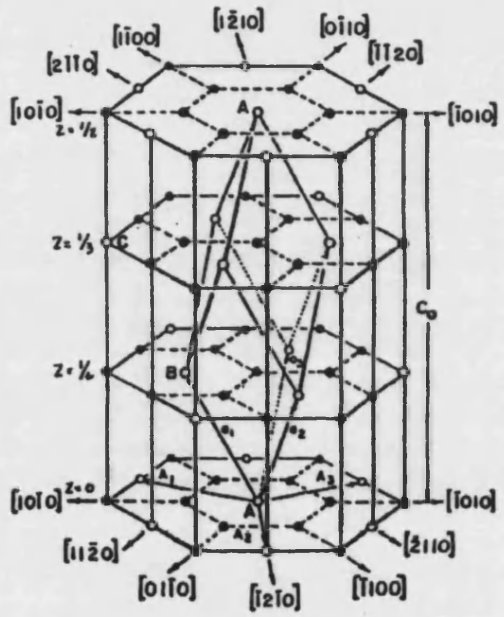

Fig. 7.7. Sapphire corundum crystal structure.

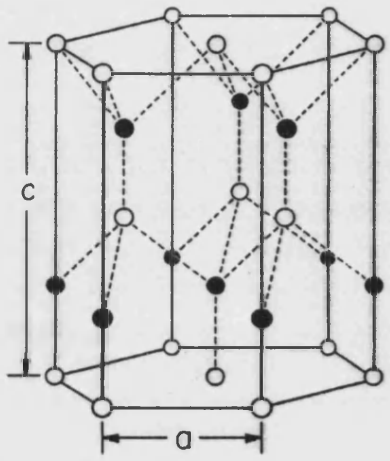

Fig. 7.8. GaN wurtzite crystal structure.

The first GaN laser diode with cleaved facets was fabricated using the a-plane sapphire substrate.[25] In this orientation sapphire can be easily cleaved along several r-planes {1$\bar{1}$02}, vertical with respect to the a-plane. The r-planes are the most natural cleave planes for sapphire and have the weakest bond strength. Previous thinning of sapphire to 70-100 μm is usually sufficient for reliable cleaving along these planes. However, cleave planes of GaN grown on the a-plane sapphire do not exactly correspond to the r-planes of sapphire. During growth, the c-axis [0001] of GaN lines up with the a-direction [11$\bar{2}$0] of sapphire and the a-direction of GaN, in its turn, lines up with the c-axis of sapphire. Figure 7.9 shows the growth direction of GaN on a-plane sapphire. In this orientation the c-plane (0001) of sapphire is vertical and parallel to the a-plane (11$\bar{2}$0) of GaN. However, this sapphire plane is polar and cannot be used for cleaving. The vertical sapphire r-planes {1$\bar{1}$02} suitable for cleaving are located 57.6° to the c-plane in sapphire, whereas the closest to them a-planes of GaN are 60° from the sapphire c-plane. This 2.4° misorientation between the cleave crystal planes in GaN and sapphire makes it nearly impossible to obtain ideal smooth mirrors by cleaving GaN-based structure on the a-plane sapphire. Cleaving along the sapphire r-plane causes the a-plane facet of GaN epitaxial

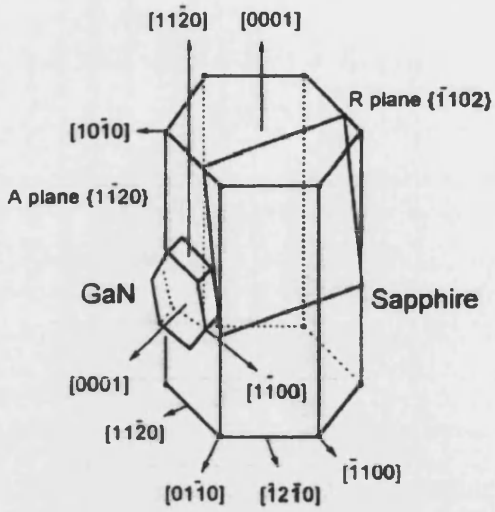

Fig. 7.9. Growth direction of GaN on a-plane sapphire.

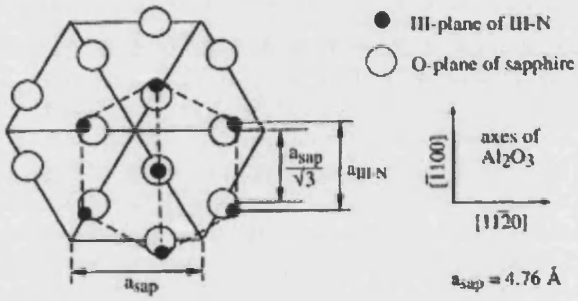

Fig. 7.10. In-plane atomic arrangement of III-nitrides on c-plane (0001) sapphire.

layers to be fractured while the sapphire facet remains smooth. Laser diodes can still be fabricated if these striations do not significantly intersect the area of the optical mode. However, this problem drastically reduces the yield of laser diodes and degrades the performance of working devices.

C-plane sapphire has also been used for cleaved-facet laser fabrication.[3, 24] This orientation of sapphire, also known as basal plane sapphire, is a common substrate for GaN growth. Crystal orientations of sapphire c-plane and GaN c-plane are parallel, but the GaN unit cell is rotated by 30° about the c-axis with respect to the sapphire unit cell. The lattice mismatch between GaN and the c-plane sapphire hexagonal unit cell is over 30%. This mismatch is significantly less (13%) between the GaN unit cell and a smaller hexagonal sapphire cell oriented 30° away from the larger sapphire unit cell.[26] The in-plane atomic arrangement of III-nitrides on the basal plane (0001) sapphire is schematically shown in Fig. 7.10.[27]

As above-mentioned the cleave planes with the lowest bond strength in sapphire are r-planes {$\bar{1}$102}. However, these planes are not vertical for c-plane sapphire and cannot be used for laser facet fabrication. Fortunately the basal plane sapphire was found to cleave vertically along a-{11$\bar{2}$0} and m-{1$\bar{1}$00} planes. A sapphire wafer needs to be thinned and polished first. Then it is mounted with wax to a thin metal plate, scribed along the a- or m-planes, and cleaved by bending the metal. Nevertheless, the cleaving of the c-plane sapphire is very difficult because the a- and m- planes of sapphire have approximately equal cleave strength. These planes are within a small angular distance (30°). Additionally only 30° separate the inclined r-planes and m-planes and the r-planes cleave preferentially. This implies that a cleave crack can easily be redirected from one cleave plane to another by a slight misalignment of the applied force which results in a jagged edge. The previous thinning to less than 100 μm can greatly improve the cleaving results. At the same time sapphire is very rigid and can easily crack when it is thinner than approximately 80 μm.[24] Thus the precise control over lapping, scribing, and breaking is required for the reliable and reproducible cleaving of basal plane sapphire.

GaN can also cleave along its vertical a {11$\bar{2}$0} and m {1$\bar{1}$00} planes. Furthermore, the a- and m- planes of GaN should be parallel to the m- and a- planes of the c-plane sapphire respectively due to the 30° shift of a GaN unit cell about the c-axis with respect to a sapphire unit cell. Thus either the a-plane or m-plane of the basal sapphire can be used to cleave GaN. The sapphire a-plane has slightly lower bond strength than the m-plane and therefore is expected to be preferable for cleaving. However, Stoker *et al.*

observed periodical vertical striations in GaN material cleaved along the a-plane of a sapphire substrate, whereas the sapphire region was smooth. These steps were ascribed to a 2.4° rotation of the GaN m-plane with respect to the sapphire a-plane observed previously by crystallographic wet etching of GaN.[11, 20] Slight misalignment was also observed for the GaN a-plane cleaved along the sapphire m-plane.[1, 3] This resulted in periodical undulations in the GaN and an estimated RMS facet roughness of 50 and 160 Å from Ref. 3 and 1 respectively. Nevertheless, this roughness is still fairly reasonable for laser facet fabrication. Laser facets can also be made using the a-plane of sapphire if the appearing striations in GaN do not significantly intersect the area of the optical mode. Recently the cleaved facets were found to be greatly improved for GaN structures employing epitaxial lateral overgrowth (ELOG) technology.[28] For these structures, GaN in the "wing" region is physically isolated from the sapphire substrate by SiO_2 stripes. This results in significantly reduced roughness in this region (Ra < 1 nm) compared to that in the "seed" region (Ra ~ 10 nm). As the active region of a laser diode is located in the "wing" area, the performance of the device can also be significantly improved.

7.4.2 GaN grown on SiC

Silicon carbide (6H SiC) is another substrate that is widely used for the growth of high quality GaN. A number of companies such as Cree, Osram Opto, and Fujitsu have decided to focus on the SiC substrate for laser diode fabrication. It allows many advantages both from the epitaxial and the device processing point of view. First, SiC has a smaller lattice mismatch with the nitrides compared to that of sapphire. It is only 3.5% between SiC and GaN and even smaller for AlN. This results in a smaller stress and a reduced threading dislocation density in the epilayers. However, a low temperature GaN or AlN buffer layer is still required before depositing the nitrides on the SiC substrate. Secondly, silicon carbide is electrically conductive, which allows a standard laser diode design with vertical current flow. This makes the processing and packaging of devices easier and minimizes the chip size because of a top *n*-contact is avoided. This design has become possible using conductive buffer technology initially developed by Cree for high-brightness GaN-based LEDs. Thirdly, the excellent thermal conductivity of SiC (4.9 W/cm·K) provides much better thermal management, enabling high power operation of laser diodes. An external heat sink made of diamond or SiC is usually used in conventional semiconductor laser diodes to remove the heat from the device to the outside. The SiC substrate can make the use of such an external heat sink unnecessary. Finally, the silicon carbide substrate has special importance for the processing of high quality facets for laser diodes. It has vertical cleave planes, which has very different bond strength than other competing planes and which can easily cleave. These planes are parallel to the GaN vertical cleave planes implying that cleaved-facet laser can easily be fabricated. Nevertheless, sapphire still remains the most popular substrate for laser diodes, despite its apparent disadvantages. The reason for that is the low availability of high quality SiC substrates and their high cost.

The 6H SiC substrate is of a hexagonal system and the crystal growth of GaN takes place in the same plane directions as those of the silicon carbide substrate.[29, 30] Consequently, the (0001) SiC substrate, together with GaN epitaxial layers, can easily be cleaved vertically along a-planes $\{11\bar{2}0\}$ which are the most natural cleave planes for SiC and have the weakest bond strength. Atomically smooth cleave planes can therefore be formed, although high tensile strain layers in laser structures grown on SiC can cause long-scale fluctuations on the facet surface. Nevertheless, a RMS roughness of less than 1 nm was reported by Osram Opto for the cleaved facets of laser diodes grown on 6H SiC substrates.

7.4.3 GaN grown on spinel

Spinel ($MgAl_2O_4$) with the (111) orientation has also been employed as a substrate for GaN growth[31, 32] and laser diode fabrication. The crystal quality of GaN laser structures grown on the spinel substrates was found to be the same as that on sapphire. The growth also requires the previous deposition of a low temperature (550 °C) buffer layer due to the 9.5% lattice mismatch with GaN. The main advantage of spinel over sapphire is that it has vertical cleave planes parallel to the vertical cleave planes of the epitaxial GaN.

Spinel has a cubic crystal structure and GaN growth on a (111) $MgAl_2O_4$ substrate occurs in a wurtzite phase with the [0001] direction of GaN parallel to the [111] direction of $MgAl_2O_4$. During the growth, the gallium and nitrogen atoms on the (0001) plane of GaN arrange to fit in with the two-dimensional hexagonal lattice on the (111) plane of the $MgAl_2O_4$ substrate. As a result, the [110] cleavage direction of spinel is parallel to the $[11\bar{2}0]$ cleavage direction of GaN.[31, 32, 33] Thus the cleavage directions of GaN coincide with those of $MgAl_2O_4$. Flat vertical $(1\bar{1}00)$ cleaved GaN facets were obtained by cleaving along these directions.[32, 33] The previous lapping of the spinel substrate to less than 100 μm was found to be effective in assisting the cleaving. Atomic force microscopy revealed extremely smooth GaN facets with RMS roughness of less than 0.3 nm. These are the best results reported to date for cleaved nitride laser facets.

7.4.4 GaN grown on freestanding GaN

Cleaved-facet GaN-based laser diodes have also been fabricated on freestanding GaN substrates.[34] The bulk GaN substrates offer high quality homoepitaxy, reasonable heat dissipation (thermal conductivity of 1.3 W/cm·K), excellent backside contact, and easily cleaved laser facets. Thick freestanding GaN films can be fabricated by HVPE growth on a host substrate, which is subsequently removed by polishing, liftoff, or laser ablation. The growth of thick high-quality GaN layers is difficult, however, a few research groups and companies have succeeded in this direction. Nevertheless, commercially available crystals are very expensive so far and have fairly poor quality to be used for commercial laser diode production.

7.5 Scribe-and-break method for cleaving

The scribe-and-break technique is as old as glass making. It has been widely employed for semiconductor processing because it is a simple and robust method to separate arrays of devices into individual chips. It is especially important for laser facet formation as other conventional separation methods, such as sawing and laser cutting, cannot produce smooth mirror-like sidewalls. The technique is commonly used for the cleaving of facets for conventional GaAs- and InP-based lasers. For GaN-based laser diodes grown on sapphire or SiC substrates this method is more difficult to implement due to the extreme hardness of the substrates and the problems outlined in the previous sections. Nevertheless, with an adequate approach, this technique produces smooth and vertical GaN facets. The process yield, therefore, is directly related to the employed equipment and the skills of an operator.

7.5.1 Conventional diamond scribing

The conventional scribe-and-break method includes three main steps. First, a wafer is thinned to a thickness below 100 μm and polished to achieve reproducible scribing and

cleaving. The process is easy to apply for soft materials such as silicon, GaAs, or InP, while it is more difficult and time consuming for sapphire or SiC due to their high bond strength. Furthermore, sapphire is very rigid and cracks easily when it is lapped thinner than approximately 80 μm. Thereby, precise control over lapping and polishing is required to achieve the best results.

The next step is to scribe the backside of the wafer with a diamond tool along the corresponding cleave planes to guide the break. Special attention at this stage should be paid to the precise alignment of the scribing along the crystal planes of the substrate. The scribing step is also very sensitive to wafer flatness, and warped, crowned, or bowed wafers cannot be processed. If the optimal scribe line is created, the deformation produced results in a crack extended vertically in the material. The proper deformation has about 1 μm depth and 3 μm width with the vertical crack extending down from the center of the deformation to a depth of about 25 μm. This conventional mechanical scribing exhibits a number of problems for extremely hard SiC and sapphire substrates. Typically, the expensive diamond scribe tips are consumed at a rate of one per wafer.

Finally, cleavage is performed along the scribe lines by means of a fracturing machine or manually. Breaking is achieved by applying tensile strain lateral to the scribe line. Two standard methods can be highlighted. The first method is to bend the wafer over a curved surface, as shown in Fig. 7.11(a). The second method, shown in Fig. 7.11(b), uses three points to break the wafer. For both of them it is highly recommended to use holding film expanded during the breaking. As a scribe line is broken, the taught holding film pulls the newly formed piece away from the wafer and a gap forms. This keeps the newly formed pieces from abrading each other.

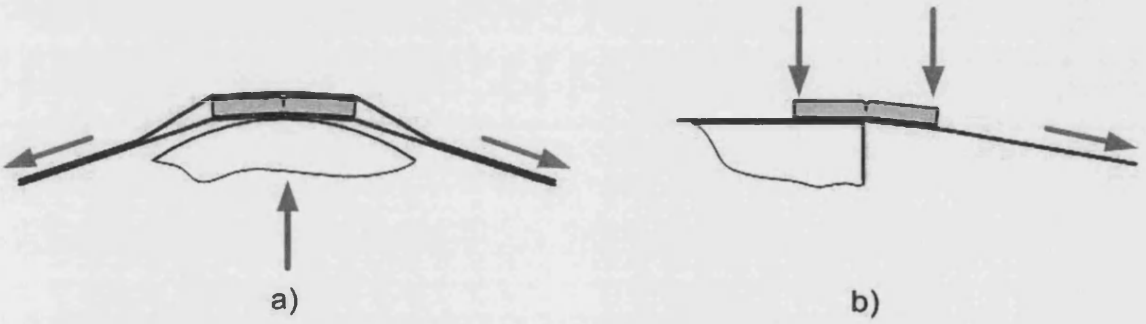

Fig. 7.11. Standard breaking methods; a) bending over a curved surface and b) three points method.

The scribe-and-break technique has been employed for GaN-based laser diodes grown on different substrates. As was considered in the previous sections, the cleaving of GaN structures grown on basal plane sapphire is very difficult due to the high bond strength of the sapphire planes suitable for cleaving. Either the a-{11$\bar{2}$0} or m-{1$\bar{1}$00} planes of sapphire can be used as the cleave plane. They correspond to m-{1$\bar{1}$00} and a-{11$\bar{2}$0} cleave planes of GaN respectively. Forcing the cleaving along these directions can be done, but it requires a very high applied force to perform the scribing and breaking. As a result, the top GaN layers can be seriously damaged during the last breaking step. Our typical results for laser diodes cleaved along the a-plane of sapphire are presented in Fig. 7.12 (unsuccessful cleaving) and Fig. 7.13 (successful cleaving). As can be seen in Fig. 7.12, the top GaN layers were broken in the ridge waveguide region resulting in the failure of the device. However, when the cleaving was done successfully, smooth and vertical laser facets were obtained, as shown in Fig. 7.13. For the reproducible and efficient cleaving of the basal plane sapphire special attention should be paid to the lapping and scribing. Thinner sapphire substrates and deeper scribe lines allow to decrease the applied pressure and to reduce the risk of device damage.

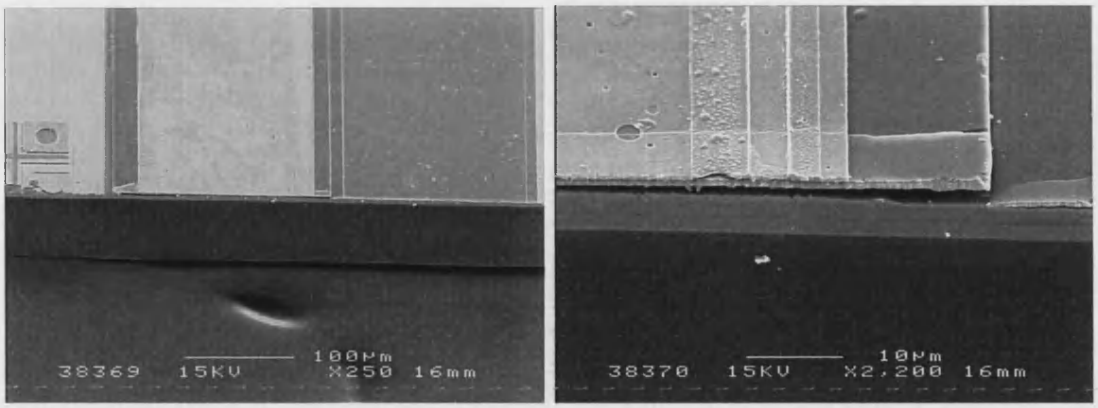

Fig. 7.12. Unsuccessful cleaving of an InGaN MQW laser diode along a-plane {11$\bar{2}$0} of sapphire.

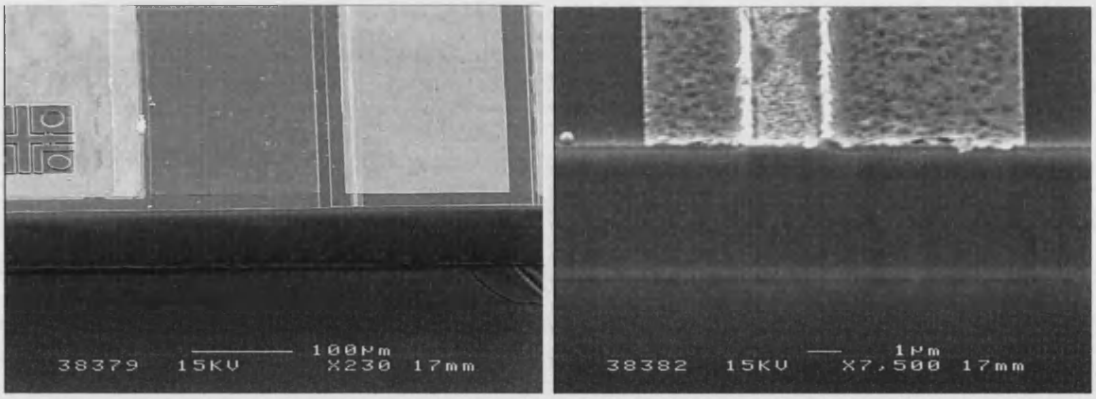

Fig. 7.13. Successful cleaving of an InGaN MQW laser diode along a-plane {11$\bar{2}$0} of sapphire.

The cleaving of GaN structures grown on other substrates, such as 6H SiC and spinel, is significantly easier and produces smoother facets in comparison with GaN/sapphire facets. Both SiC and spinel have only a few cleave planes, which break easily. These planes are vertical and parallel to the cleave planes of GaN layers. Thereby the cleaving of SiC and spinel is similar to the cleaving of conventional cubic semiconductors such as GaAs and InP. As a result, reliable cleaving can be performed and atomically smooth laser facets can be fabricated.

7.5.2 UV laser scribing

Recently, a technique called laser scribing has been developed to replace the out-of-date mechanical scribing. This method dramatically increases chip yields and process throughput, while at the same time significantly reducing the equipment operation and maintenance costs. Narrow deep scribe lines, insensitivity to wafer flatness, and precise alignment allow to improve significantly the reliability of facet formation for GaN-based lasers grown on hard sapphire and SiC substrates. With laser scribing, the scribe-and-break method is also expected to be performed without time-consuming lapping and polishing steps because the cut depth can be easily adjusted while maintaining the same width. Finally, the laser scribing process is highly automated; a single operator can simultaneously run several laser systems.

The process of laser scribing involves the moving of a wafer under a rapidly pulsed, focused laser beam. It produces an extremely narrow V-shaped cut, the depth of which is controlled by the scan speed and by the number of repeat passes. Normally, these cuts terminate 30 – 50% into the thickness of the wafer. A typical 30-µm deep cut profile

in sapphire produced by a 266 nm diode-pumped solid-state (DPSS) laser is presented in Fig. 7.14. After laser scribing, the wafer can be fractured using standard cleaving equipment. The V-shaped laser cut acts as stress concentrator and is ideal for cleaving. Nevertheless, the top GaN layers can still be seriously damaged during the breaking step.

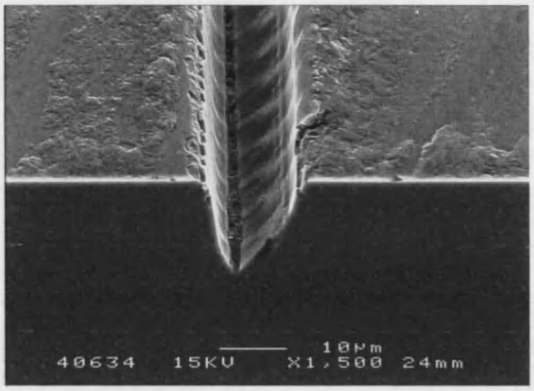

Fig. 7.14. Typical 30 µm deep cut profile in sapphire produced by 266 nm DPSS laser.

Our typical results for the laser diodes cleaved along the a-plane of sapphire are presented in Fig. 7.15 (unsuccessful cleaving) and Fig. 7.16 (successful cleaving). The scribing was performed using a 355 nm diode-pumped solid-state (DPSS) laser. The wafer was previously lapped to 80 nm and polished to assist the cleaving. As can be seen in Fig. 7.15, when the breaking step was not successful, the top GaN layers were damaged. In contrast, extremely smooth vertical laser facets were obtained when the cleaving was successfully performed, as shown in Fig. 7.16.

To achieve the best results it is important to optimize the laser parameters relevant to the material's optical, thermal, and mechanical properties. These parameters include laser wavelength, average output power, pulse repetition frequency, pulse energy, pulse duration, and intensity beam profile. In general, the scribing benefits from a shorter pulse duration and shorter laser wavelength, for both optical and thermal reasons. The shorter pulse duration allows to increase the irradiation on the target and to reduce the heat input to the substrate due to more rapid absorption and ablation. The shorter laser wavelength results in improved optical absorption, reduced absorption depth, lower irradiance required

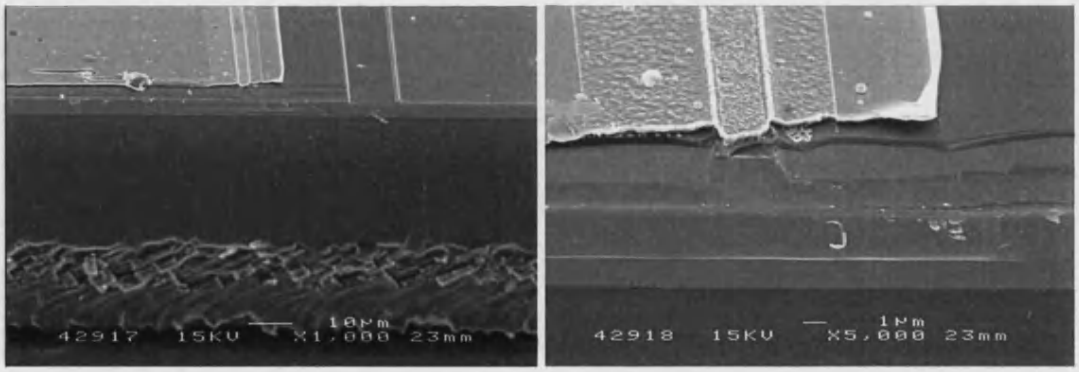

Fig. 7.15. Unsuccessful cleaving of an InGaN MQW laser diode along a-plane {11$\bar{2}$0} of sapphire. Scribing is performed using 355 nm DPSS laser.

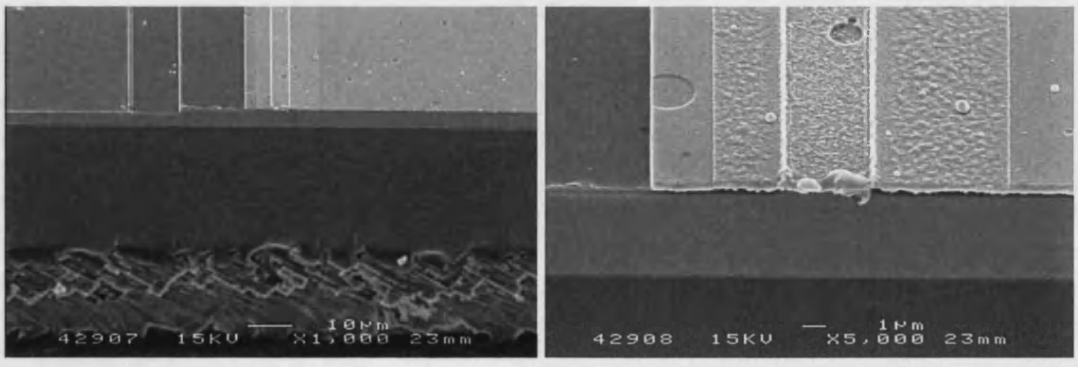

Fig. 7.16. Successful cleaving of an InGaN MQW laser diode along a-plane {11$\bar{2}$0} of sapphire. Scribing is performed using 355 nm DPSS laser.

for ablation, and reduced cut width. For SiC, laser wavelengths below 370 nm result in direct photon absorption because photon energies exceed the bandgap of the material. In contrast, efficient optical absorption in sapphire can only be achieved through multi-photon absorption because the sapphire bandgap is higher than the photon energy of any commercially available UV laser. The multi-photon absorption efficiency in sapphire is strongly wavelength dependent. Shorter wavelengths are absorbed more effectively resulting in less heat transfer to the bulk material.

Laser scribing of sapphire and SiC is usually performed using lasers with a wavelength between 177 and 365 nm. Most industrial scribing systems employ KrF excimer lasers or frequency-doubled Cu lasers operating at 248 and 255 nm, respectively. Recently, Nd:YAG diode-pumped solid-state (DPSS) lasers operating in frequency-quadrupled (266 nm) and frequency-tripled modes (355 nm) have also been employed. The DPSS lasers can achieve smaller cut widths compared to the excimer lasers (5 μm vs. 15 μm). However, sapphire scribing with a 355 nm DPSS laser can induce some performance degradation for the top GaN LEDs and LDs due to the large penetration depth of a laser beam into the sapphire. This problem is reduced by using the 266 nm DPSS laser or standard 248 and 255 nm gas lasers.

7.6 References

[1] D. A. Stocker, E. F. Schubert, W. Grieshaber, K. S. Boutros, and J. M. Redwing, Appl. Phys. Lett. 73, 1925 (1998).

[2] M. Kneissl, D. Hofstetter, D. P. Bour, R. Donaldson, J. Walker and N. M. Johnson, Journal of Crystal Growth 189/190, 846 (1998).

[3] K. Itaya, M. Onomura, J. Nishio, L. Sugiura, S. Saito, M. Suzuki, J. Rennie, S. Nunoue, M. Yamamoto, H. Fujimoto, Y. Kokubun, Y. Ohba, G. Hatakoshi, and M. Ishikawa, Jpn. J. Appl. Phys. 35, L1315 (1996).

[4] C. Ambe, T. Takeuchi, H. Katoh, K. Isomura, T. Satoh, R. Mizumoto, S.Yamaguchi, C. Wetzel, H. Amano, I. Akasaki, Y. Kaneko, and N. Yamadal, Mater. Sci. Eng. B 59, 382 (1999).

[5] S. Nakamura, M. Senoh, S. Nagahama, N. Iwasa, T. Yamada, T. Matsushita, H. Kiyoku, and Y. Sugimoto, Jpn. J. Appl. Phys. 35, L74 (1996).

[6] S.J. Pearton, R. J. Shul and Fan Ren, MRS Internet J. Nitride Semicond. Res. 5, 11 (2000).

[7] M. Kneissl, D. Hofstetter, D. P. Bour, R. Donaldson, J. Walker and N. M. Johnson, Journal of Crystal Growth 189/190, 846 (1998).

[8] S. Nakamura, M. Senoh, S. Nagahama, N. Iwasa, I. Yamada, T. Matsushita, H. Kiyoku, and Y. Sugimoto, Appl. Phys. Lett. 68, 3269 (1996).

[9] M. P. Mack, G. D. Via, A. C. Abare, M. Hansen, P. Kozodoy, S. Keller, J. S. Speck, U. K. Mishra, L. A. Coldren and S. P. DenBaars, Electon. Lett. 34, 1315 (1998).

[10] S. J. Pearton, J. C. Zolper, R. J. Shul, and F. Ren, J. Appl. Phys. 86, 1 (1999).

[11] D. A. Stocker, E. F. Schubert, and J. M. Redwing, Appl. Phys. Lett. 73, 2654 (1998).

[12] M. S. Minsky, M. White, and E. L. Hu, Appl. Phys. Lett. 68, 1531 (1996).

[13] H. Lu, Z. Wu, and I. Bhat, J. Electrochem. Soc. 144, L8 (1997).

[14] L.-H. Peng, C.-W. Chuang, J.-K. Ho, C.-N. Huang, and C.-Y. Chen, Appl. Phys. Lett. 72, 939 (1998).

[15] C. Youtsey, I. Adesida, L. T. Romano, and G. Bulman, Appl. Phys. Lett. 72, 560 (1998).

[16] C. Youtsey, I. Adesida, and G. Bulman, Electron. Lett. 33, 245 (1997).

[17] C. Youtsey, I. Adesida, and G. Bulman, Appl. Phys. Lett. 71, 2151 (1997).

[18] C. Youtsey, I. Adesida, and G. Bulman, J. Electron. Mater. 27, 282 (1998).

[19] C. B. Vartuli, S. J. Pearton, J. W. Lee, C. R. Abernathy, J. D. MacKenzie, J. C. Zolper, R. J. Shul, and F. Ren, J. Electrochem. Soc. 143, 3681 (1996).

[20] D. A. Stocker, E. F. Schubert, K. S. Boutros, and J. M. Redwing, MRS Internet J. Nitride Semicond. Res. 4S1, G7.5 (1999).

[21] T. Bottcher, Ch. Zellweger, S. Figge, R. Kroger, Ch. Petter, H.-J. Buhlmann, M. Ilegems, P. L. Ryder, and D. Hommel, Phys. Stat. Sol. (a) 191, R3 (2002).

[22] T. Bottcher, S. Figge, S. Einfeldt, R. Chierchia, R. Kroger, Ch. Petter, Ch. Zellweger, H.-J. Buhlmann, M. Dießelberg, D. Rudloff, J. Christen, H. Heinke, P. L. Ryder, M. Ilegems, and D. Hommel, Phys. Stat. Sol. (c) 0, 1846 (2003).

[23] R. W. G. Wyckoff, Crystal Structures, vol. 1, 2nd ed. New York, NY: John Wiley & Sons, 1963.

[24] R. Kehl Sink, Ph.D. Dissertation, University of California, Santa Barbara (2000).

[25] S. Nakamura, M. Senoh, S. Nagahama, N. Iwasa, T. Yamada, T. Matsushita, H. Kiyoku, and Y. Sugimoto, Jpn. J. Appl. Phys. 35, L217 (1996).

[26] T. Lei, K. F. Ludwig, and T. D. Moustakas, J. Appl. Phys. 74, 4430 (1993).

[27] S. C. Jain, M. Willander, J. Narayan, and R. Van Overstraeten, J. Appl. Phys. 87, 965 (2000).

[28] T. Miyajima, T. Tojyo, T. Asano, K. Yanashima, S. Kijima, T. Hino, M. Takeya, S. Uchida, S. Tomiya, K. Funato, T. Asatsuma, T. Kobayashi, and M. Ikeda, J. Phys.: Condens. Matter 13, 7099 (2001).

[29] K. Koga, United States Patent 5,727,008 (1996).

[30] A. Kuramata, K. Horino, and K. Domen, FUJITSU Sci. Tech. J. 34,191 (1998).

[31] C. J. Sun, J. W Yang, Q. Chen, M. Asif Khan, T. George, P. Chang-Chein, and S. Mahajan, Appl. Phys. Lett. 68, 1129 (1996).

[32] A. Kuramata, K. Horino, K. Domen, K. Shinohara, and T. Tanahashi, Appl. Phys. Lett. 67, 2521 (1995).

[33] M. Asif Khan, C. J. Sun, J. W. Yang, Q. Chen, B. W. Lim, M. Zubair Anwar, A. Osinsky and H. Temkin, Appl. Phys. Lett. 69, 2418 (1996).

[34] S. Nakamura, M. Senoh, S. Nagahama, N. Iwasa, T. Yamada, T. Matsushita, H. Kiyoku, Y. Sugimoto, T. Kozaki, H. Umemoto, M. Sano, and K. Chocho, Appl. Phys. Lett. 73, 832 (1998).

8 High reflectivity coating of GaN laser facets

Adding high reflectivity (HR) coatings to facets is a very important processing step in laser diode fabrication. It is especially important for GaN-based structures, which have much lower refractive index (approximately 2.5 at 410 nm wavelength) compared to conventional semiconductors. The low refractive index results in a very low reflectivity at the nitride/air interface. Theoretically, the highest value of the reflectivity attains only 18% for ideal GaN-based facets. Any facet roughness reduces this value even more. It therefore requires an additional coating on the facets to decrease reflection loss. Usually from 2 to 4 pairs of $\lambda/4$ SiO_2/TiO_2 layers are employed for a rear mirror or for both front and rear mirrors in nitride-based laser diodes. This gives facet reflectivities in the range from 50 to 98% and thereby reduces the threshold current of laser diodes.

The choice of dielectric materials for HR facet coating is originated in their ability to reflect light at internal interfaces without significant photon absorption and without electrical short-circuits in the structure. If two dielectric materials, with different refractive indexes, are placed together to form a junction, light is partially reflected at the discontinuity. One such junction reflects only a small amount of light. However, the periodical composition of contrasting dielectric layers, each layer with an optical thickness $\lambda/4n$, greatly increases the total reflectivity. The reflections from each of the junctions are added in phase to produce a large reflection coefficient. The final reflectivity is determined by the number of the layers and by the difference in the refractive index of the contrasting materials at a particular wavelength. The facet reflectivity for an ideally smooth facet is given by

$$R = \left[\frac{1 - \frac{n_s}{n_0}\left(\frac{n_1}{n_2}\right)^{2m}}{1 + \frac{n_s}{n_0}\left(\frac{n_1}{n_2}\right)^{2m}} \right]^2 \qquad [8.1]$$

R – facet reflectivity
n_s – refractive index of substrate
n_0 – refractive index of surrounding material (usually air)
n_1, n_2 – refractive indices of contrasting dielectric layers
m – number of periods in dielectric coating

Highly reflective mirrors can be fabricated from various combinations of dielectric materials, such as SiO_2/TiO_2, ZnSe/MgF, etc. These materials are usually deposited using low-temperature techniques, such as sputtering, evaporation, or plasma deposition. For GaN-based laser diodes, a SiO_2/TiO_2 high reflectivity coating, with different numbers of pairs, is mainly employed because of the transparency of these dielectrics at the emitted wavelengths and their high refractive index contrast. The refractive indices at a wavelength of 405 nm are 2.53 and 1.47 for TiO_2 and for SiO_2 respectively. Figure 8.1 shows the calculated reflectivity at 405 nm for an ideally smooth GaN facet as a function of the number of $\lambda/4$ SiO_2/TiO_2 pairs. As a result of an improved facet reflectivity, the threshold current of laser diodes with HR coatings can be effectively reduced by 25 – 50%.[1, 2, 3]

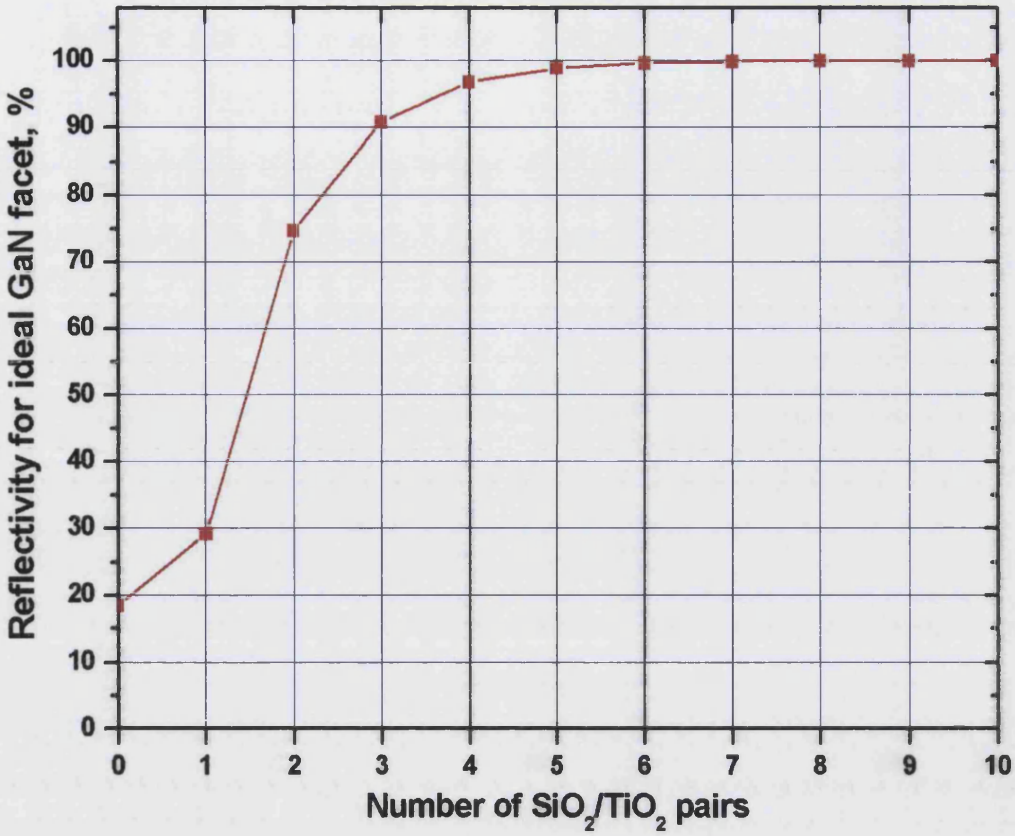

Fig. 8.1. Calculated reflectivity at 405 nm wavelength for an ideally smooth GaN facet as a function of number of λ/4 SiO_2/TiO_2 pairs.

As can be seen in Fig. 8.1, the facet reflectivity can be easily controlled by the number of deposited dielectric layers. This makes it possible to change a symmetric laser emission from both front and rear laser facets into a directed emission with the main emission power from the front facet. The relationship between the intensity of laser light emitted from the front mirror and from the rear mirror is given by

$$\frac{I_1}{I_2} = \frac{1-R_1}{1-R_2}\left(\frac{R_2}{R_1}\right)^{1/2} \qquad [8.2]$$

I_1 – light intensity from the front facet
I_2 – light intensity from the rear facet
R_1 – front facet reflectivity
R_2 – rear facet reflectivity

Another practical function of HR coating is to passivate laser diode facets and thereby to prevent laser diode degradation with operation time. Figure 8.2 shows the threshold current I_{th} (top) and slope efficiency (bottom) versus effective operation time (time × duty cycle) for GaN-based laser diodes. As can be seen, lasers with both uncoated (as-cleaved) facets, presented as thin and bold dash-dot lines (16%/16% facet reflectivity), showed very fast degradation in the threshold current and slope efficiency. A laser with only one HR-coated facet (99% reflectivity), presented as a thin dash line, also degraded during operation. On the contrary, lasers with both coated facets [either both facets with HR coatings of 99% and 50% reflectivity (a solid line) or one facet with a 99% reflective

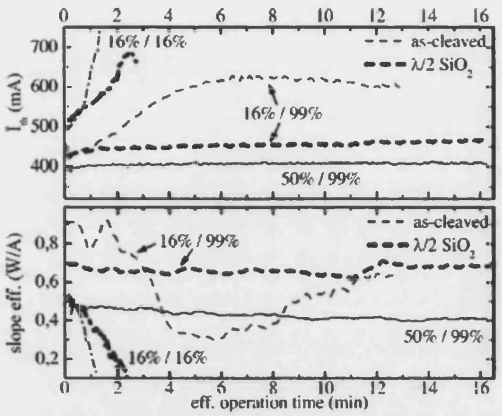

Fig. 8.2. Threshold current I_{th} and slope efficiency over effective operation time (time × duty cycle).

coating and the other with a $\lambda/2$ SiO_2 passivation coating (a bold dash line)] showed very little degradation. It was suggested that the origin of the degradation is optically enhanced oxidation of the uncoated facets. This leads to increased optical absorption in a small volume behind the facets and finally results in a rise of the threshold current and the decline of the slope efficiency. The authors also noticed that this degradation was only observed for laser diodes with cleaved facets. It was proposed that dry chemical etching could simultaneously passivate the facet surface and thereby prevent the oxidation.

Thus high reflectivity coating greatly improves the performance of GaN-based laser diodes. It significantly increases the reflectivity of laser facets and thereby reduces the threshold current. Furthermore, performing HR coatings with different reflectivities to laser facets allows changing a symmetric laser emission into a directed emission from a front mirror. And last but not least, high reflectivity coating acts as a passivation coating and prevents the degradation of cleaved GaN mirrors.

---

[1] A. Kuramata, K. Horino, K. Domen, FUJITSU Sci. Tech. J.34, 191 (1998).

[2] V. Kummler, A. Lell, V. Harle, U. T. Schwarz, T. Schoedl, and W. Wegscheider, Appl. Phys. Lett. 84, 2989 (2004).

[3] M. Koike, S. Yamasaki, Y. Tezen, S. Nagai, S. Iwayama, and A. Kojima, MRS Internet J. Nitride Semicond. Res. 5S1, W1.2 (2000).

9 Laser fabrication and characterization

9.1 Laser diode fabrication process

This section presents a complete laser fabrication process including all single processes described in detail in the previous chapters (Chapters 3 – 8). The grown laser structure and the ridge waveguide laser geometry were discussed in Chapter 2. The process-flow employed for fabrication of our laser diodes is shown in Fig. 9.1.

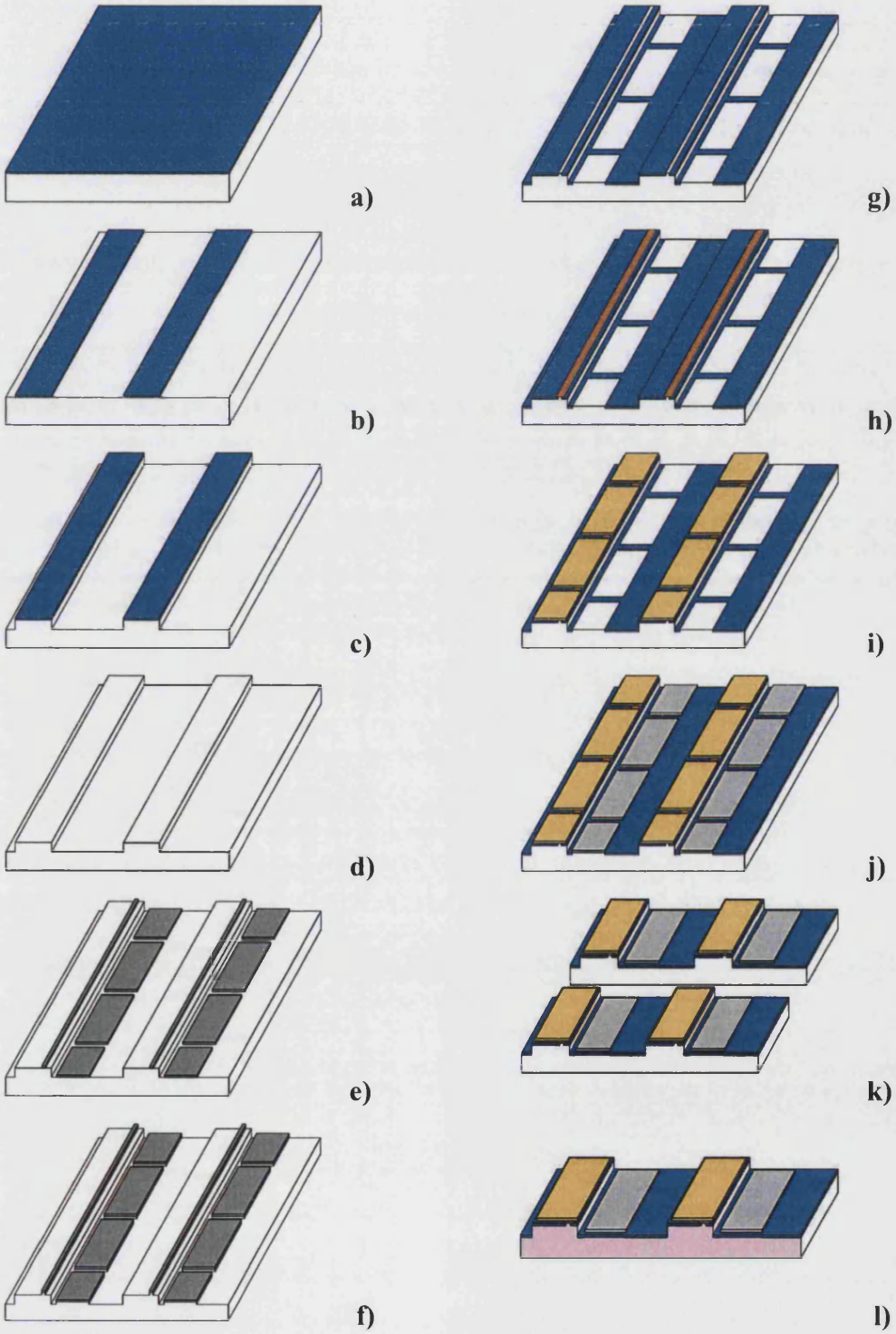

Fig. 9.1. Process-flow employed for laser diode fabrication.

The following sequence of technological processes has been used for laser fabrication.

1. Thermal activation of *p*-type layers

The activation was conducted in a rapid thermal annealing (RTA) system in air at 600 °C for 2 min. A developed process and the activation mechanisms are described in section 3.5.

2. Deposition of a SiO_2 mask layer (Fig. 9.1(a))

A 640 nm-thick SiO_2 layer was deposited using a two-step plasma enhanced chemical vapor deposition (PECVD) process. Between the steps, the wafer was cleaned in acetone under ultrasonic agitation to prevent the accidental formation of through pinholes in the layer induced by process chamber contamination. The pinholes in the mask layer would cause deep etched holes in laser mesas after GaN etching and, hence, short-circuit current in devices after *p*-contact deposition.

3. Fabrication of a SiO_2 etch mask (Fig. 9.1(b))

200 μm-wide SiO_2 mask stripes were defined along the a-plane $(11\bar{2}0)$ of III-nitrides using conventional photolithography, photoresist descumming with O_2 plasma, reactive ion etching (RIE) with CHF_3 plasma, and short etching in a buffered-HF (1:20) solution.

The photolithography was performed using 1.3 μm-thick Shipley 1813S photoresist. The resist descumming was used to remove thin residual layers of the photoresist and other organic films following resist development and hard bake.[1] These residuals would affect SiO_2 etching. The process was performed in an Oxford PlasmaLab 80 ICP system. The ICP process parameters used were as follows: 20 mTorr pressure, 40 sccm O_2 flow, 250 W ICP power, 100 W RF power, -320 V dc-bias, and 20 °C cathode temperature. The descumming process consisted of three etching steps, for 1 min each, separated by 5 min intervals without plasma discharge. These gaps allow the photoresist temperature to reduce, which would be excessively high after 3 min of continuous etching. Without the intervals the photoresist was found to melt and erode very rapidly under the strong ICP conditions used. The thickness of the photoresist after descumming was around 900 nm, which was still sufficient for SiO_2 etching.

The SiO_2 mask was patterned by RIE etching with a CHF_3 plasma in the same reactor using a process described in detail in section 4.4. The RIE process parameters used were as follows: 3.5 mTorr pressure, 20 sccm CHF_3 flow, 150 W RF power, -400 V dc-bias, and 20 °C cathode temperature. The SiO_2 etching rate at these conditions was about 34 nm/min. The etching time was set to be 3 min longer than that calculated to guarantee the complete removal of the uncovered SiO_2. Subsequently, the pattern was immersed into a buffered-HF (1:20) solution to remove about 100 nm of SiO_2 from the etched sidewalls. The etching rate of SiO_2 in this solution is about 1.0–2.0 nm/s without agitation and twice more under moderate agitation. This etching is useful to improve the quality of the sidewalls and also to remove residual SiO_2 from the etched surface. Finally, the photoresist was stripped away using Shipley Remover 1165 in a hot bath at 60 °C.

4. Etching of laser mesas (Fig. 9.1(c))

1.3–1.7 μm-high laser mesas, depending on the position across the 2-inch laser wafer, were formed using inductively coupled plasma (ICP) etching with a Cl_2/Ar plasma in an Oxford PlasmaLab 80 ICP reactor. This system employs a small-diameter remote ICP source resulting in poor etch uniformity at high ICP powers with the maximal etching rates in the centre of the cathode. A developed etching process is described in detail in section 4.6. The ICP process parameters used were: 4.0 mTorr pressure, 15 sccm Cl_2 flow, 4 sccm Ar flow, 450 W ICP power, 150 W RF power, and 20 °C cathode temperature. The etching rate of the laser structure at these conditions was from 330 nm/min (centre of the wafer) to 260 nm/min (edges of the wafer). Before the etching the wafer was cleaned in a HCl/H_2O (1:1) solution for 5 min to remove surface oxides.[2]

5. Removal of the SiO_2 etch mask (Fig. 9.1(d))

The SiO_2 etch mask was stripped away using a buffered-HF (1:5) solution. The etching rate of SiO_2 in this solution is about 200 nm/min under moderate agitation.

6. Ridge waveguide fabrication (Fig. 9.1(e)-(g))

A developed ridge fabrication process is described in detail in Chapter 5. First, 2–4 μm-wide mask stripes and 170×(500–1500) μm^2-size mask pads were formed along the a-plane $(11\bar{2}0)$ of III-nitrides (Fig. 9.1(e)) using a lift-off photolithography process and the deposition of Al/Ni (500 nm/100 nm) in an electron-beam evaporator. Photolithography was performed using a double-layer coating including lower LOR-10B lift-off resist and upper Shipley 1813S photoresist. This allows the fabrication of very narrow (up to 1 μm-wide) and fairly thick (up to 1 μm-thick) metal features with very smooth vertical sidewalls. Secondly, 300 nm-high ridge stripes and *n*-contact "lands" were formed (Fig. 9.1(f)) using ICP etching with a Cl_2/Ar plasma in an Oxford PlasmaLab 80 ICP reactor. The process conditions were the same as those for mesa etching. After the etching, an undercut metal profile was formed using a buffered-HF (1:20) solution. A 350 nm-thick SiO_2 passivation layer was subsequently deposited using an ion beam sputtering system. Finally, the metal mask was removed in a boiling aqua-regia [HCl/HNO_3 (3:1)] solution forming windows for deposition of both *p*- and *n*-contacts (Fig. 9.1(g)).

7. Fabrication of thin ohmic *p*-contacts [Fig. 9.1(h))

13 μm-wide contact stripes were formed on the top of the ridges using a lift-off photolithography process with double-layer resist and the deposition of Ni/Au (30 nm/30 nm) in an electron-beam evaporator. The contacts were subsequently annealed in an oven under O_2 at 500 °C for 5 min. This contact system is considered in section 6.5.3.

8. Fabrication of contact pads to the *p*-contacts (Fig. 9.1(i))

170×(500–1500) μm^2-size contact pads were formed on the top of the mesas using a lift-off photolithography process with double-layer resist and the deposition of Ti/Au (20 nm/300 nm) in an electron-beam evaporator. The Ti layer was used to provide adhesion of the contact pads to both the *p*-contacts and the SiO_2 passivation layer.

9. Fabrication of *n*-contacts (Fig. 9.1(j))

170×(500–1500) μm^2-size contacts were formed on the *n*-contact "lands" using a lift-off photolithography process with double-layer resist and the deposition of Ti/Al (20 nm/300 nm) in an electron-beam evaporator. This contact system is considered in section 6.4.2.

10. Fabrication of laser facets (Fig. 9.1(k))

A laser facet fabrication process is described in detail in Chapter 7. First, a sapphire substrate was thinned down to a thickness of ~100 μm and polished. Subsequently, the wafer was scribed from the sapphire side along the m-plane $(1\bar{1}00)$ of sapphire and roughly cleaved forming long narrow strips with ~10 laser diodes in line. Narrow strips are preferable for the following facet cleaving. Either a diamond scribing system or a laser scribing system was used for the scribing. The strips were then scribed from the sapphire side between the contact pads along the vertical a-plane $(11\bar{2}0)$ of sapphire, corresponding to the vertical m-plane $(1\bar{1}00)$ of GaN. Subsequently, the strips were cleaved forming a single line of laser diodes.

11. Performing high reflectivity (HR) coatings to laser facets (Fig. 9.1(l))

Finally, high reflectivity coatings were applied for some fabricated devices. HR coatings for GaN-based laser facets are considered in Chapter 8. The rear facets were coated with a 97 % reflective coating (4 pairs of $\lambda/4$ SiO_2/TiO_2); the front facets were coated with a 30 % reflective coating (1 pair of $\lambda/4$ SiO_2/TiO_2). The SiO_2 and TiO_2 layers were deposited using an ion beam sputtering system.

9.2 Laser diode characterization

As a result of the successful processing, a number of laser diodes have been fabricated with a ridge width of 2, 3, and 4 μm and a cavity length of 500, 750, 1000, and 1500 μm. Unfortunately, facet cleaving is very difficult for GaN-based lasers grown on sapphire substrates, as considered in Chapter 7. As a consequence, some of the devices had damaged or very rough facets resulting in excessively high threshold currents for lasing. However, most of the laser diodes had reasonably good facets and operated at reasonably low currents.

9.2.1 *I-V* and *L-I* characteristics

The fabricated lasers were characterized under pulsed current injection (100 ns pulse width, 1 kHz frequency) at room temperature. Time-average optical output power was measured from the front facets using an optical powermeter. Pulsed output power was calculated using the ratio of pulse width to pulse period. Typical pulsed electrical [current-voltage (*I-V*)] and optical [light output power-current (*L-I*)] characteristics measured from a 1000×4 μm^2 LD are presented in Fig. 9.2. From the *I-V* curve, the series resistance (R_s) of the LD was estimated to be 0.7 Ω. This value is very low for III-nitride based lasers where low-conductive *p*-layers and difficulties to attain low-resistance *p*-contacts often result in excessively high device resistivities. This would finally lead to a high operation voltage and a large amount of heat generated. The low resistance obtained implies that the laser fabrication process is very promising for implementation and further optimization.

The optical characteristics presented in Fig. 9.2 were measured from one of the facets of the as-cleaved device, from the front facet of the same device after a 97 % reflective coating was applied to the rear facet, and from the front facet of this device after a 30 % reflective coating was additionally applied to the front facet. All *L-I* curves show the typical transition from spontaneous to stimulated emission. The laser emission was found to be strongly transverse electric (TE)-polarized as expected for laser diodes. The threshold current (I_{th}) was estimated to be 2.25 and 1.9 A for the laser with as-cleaved and HR-coated facets. This corresponds to a threshold current density (J_{th}) of 56.5 and 47.5 $kA \cdot cm^{-2}$, respectively. The operating voltage at the threshold current (U_{th}) was ~15 V. Output optical powers as high as 52, 71, and 46 mW were achieved at a current of 3.4 A from the laser with uncoated facets, with the HR-coated rear facet, and with both HR-coated facets, respectively.

As can be seen, the threshold current was reduced by 18 % due to the increased reflectivity of the HR-coated rear facet. In contrast, the HR coating applied for the front facet did not change the threshold current significantly probably due to its fairly low (30 %) reflectivity. Furthermore, this considerably decreased the efficiency of the laser diode. The slope efficiency (η_{slope}) was estimated to be 0.047, 0.046, and 0.029 W/A for the laser with uncoated facets, with the HR-coated rear facet, and with both HR-coated facets, respectively. The external differential quantum efficiency (η_d) of a laser diode is given by

$$\eta_d = \frac{q}{h\nu} \cdot \frac{\partial P_{out}}{\partial I} \qquad [9.1]$$

q – elementary charge
$h\nu$ – photon energy
P_{out} – output optical power
I – applied current

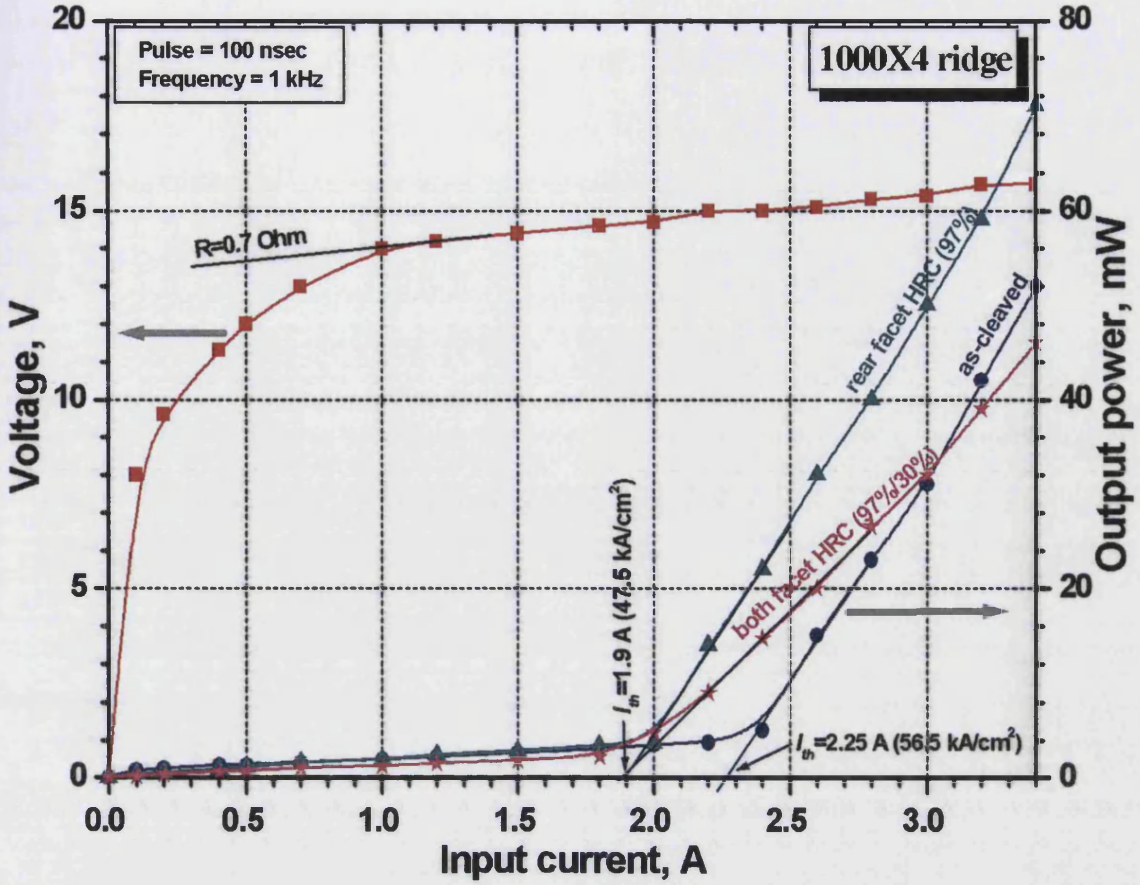

Fig. 9.2. *I-V* and *L-I* characteristics of a laser diode (1000 μm-cavity length, 4 μm-ridge width) under pulsed current injection (100 ns pulse width, 1 kHz frequency).

Thus, the external differential quantum efficiency was calculated to be 1.6, 1.5, and 0.97 % for the laser with uncoated facets, with the HR-coated rear facet, and with both HR-coated facets, respectively.

Typical characteristics of fabricated laser diodes of different ridge widths and cavity lengths are presented in Table 9.1. No HR coatings were applied to the laser facets. A common method to characterize the internal optical loss (α_i) and internal quantum efficiency (η_i) in laser structures employs the dependence of external differential quantum efficiency on the cavity length. The external differential quantum efficiency increases with increasing internal quantum efficiency or decreasing internal optical loss, as given by[3]

$$\eta_d = \eta_i \frac{\alpha_m}{\alpha_i + \alpha_m} \qquad [9.2]$$

α_m – mirror loss, defined as

$$\alpha_m = \frac{1}{L} \ln\left(\frac{1}{R}\right) \qquad [9.3]$$

R – facet reflectivity
L – cavity length

Table 9-1. Typical characteristics of fabricated laser diodes measured under pulsed current injection.

Laser diode (μm^2)	I_{th} (A)	J_{th} (kA/cm^2)	U_{th} (V)	R_s (Ω)	P_{out}/facet (mW)	η_{slope}/facet (W/A)	η_d/facet (%)
500×2	0.93	93.0	15.5	3.3	42	0.082	2.7
500×3	1.1	73.3	15.2	2.5	40	0.047	1.6
500×4	1.17	58.5	14.3	2.0	68	0.086	2.7
750×2	1.7	113.0	16.4	2.1	19	0.026	0.9
750×3	1.7	75.6	16.3	1.9	36	0.065	2.2
750×4	2.25	75.0	16.6	1.3	23	0.035	1.2
1000×2	1.7	85.0	15.4	1.4	69	0.053	1.8
1000×3	2.1	70.0	15.0	1.0	26	0.017	0.6
1000×4	2.25	56.5	15.0	0.7	52	0.047	1.6
1500×2	2.0	66.7	16.2	1.3	10	0.008	0.3
1500×3	2.7	60.0	15.0	1.0	75	0.083	2.8
1500×4	2.9	48.3	14.4	0.6	69	0.038	1.3

Substituting Eq. 9.3 into Eq. 9.2 and rearranging gives

$$\frac{1}{\eta_d} = \frac{1}{\eta_i} + \frac{\alpha_i}{\eta_i \ln\left(\frac{1}{R}\right)} L \qquad [9.4]$$

Thereby, the dependence of the reciprocal of the external differential quantum efficiency on the cavity length should result in a linear plot with an $1/\eta_d$-axis intercept (L=0) equal to $1/\eta_i$ and with a slope defined by R and α_i. Thus, for a constant facet reflectivity, both the internal optical loss and internal quantum efficiency can be extracted from the plot. However, for our devices no linear dependence was found implying a significant difference in the reflectivity of the laser facets. Furthermore, the internal efficiency and internal loss could also vary for different devices. A very promising method for characterizing laser diodes is focused ion beam (FIB) facet polishing.[4] With reproducible FIB-prepared facets it is possible to measure η_d against a cavity length on a single laser bar by sequential FIB polishing to shorten the laser. It would eliminate any scatter resulting from material and facet non-uniformity. However, a FIB polishing system is not available at the University of Bath.

Unfortunately, the threshold current was excessively high and the external differential quantum efficiency was too low compared to those for the best devices fabricated around the world (Table 1.1). The threshold current density was nearly ten times higher than that required for a laser operating in continuous wave (CW) mode. One reason could be large internal loss and/or low internal quantum efficiency in the structure induced by nonradiative recombination and/or by scattering of laser light on threading dislocations. It has been reported that epitaxial lateral overgrowth (ELOG) or pendeo-epitaxy growth techniques decreased the threshold current by 2–3 times and improved the differential efficiency due to a significantly reduced density of dislocations in the waveguide region.[5, 6, 7, 8] Another reason could be the number of quantum wells (10) in the active region of our structure. Nakamura *et al.*[9] reported that the lowest threshold current density for LDs with an emission wavelength of 390–420 nm was obtained when the number of InGaN well layers was only two. Thus, overgrowth techniques and optimization of the laser structure are expected to significantly improve the characteristics of our laser diodes.

9.2.2 Optical spectra

The same 1000×4 μm^2 LD with both HR-coated facets was characterized under pulsed current injection (100 ns pulse width, 1 kHz frequency) at room temperature using optical spectral measurements. Optical spectra measured from the front facet at an injection current of 1.9 A (I_{th}), 2.0 A (1.05·I_{th}), and 2.5 A (1.3·I_{th}) are presented in Fig. 9.3. As can be seen, strong stimulated emission with a 419 nm peak wavelength appeared when the current was slightly above the threshold. The Full Width at Half Maximum (FWHM) of the laser line was estimated to be ~1 nm, which is the resolution limit of our spectrograph. For different devices the laser emission wavelengths ranged from 416 to 420 nm depending on their position on the 2-inch wafer.

At injection currents above 2.5 A, several additional peaks appeared in the spectrum within a 416–421 nm region, as shown in Fig. 9.3. The observed peak separation is much larger than the expected longitudinal mode separation ($\Delta\lambda$) given by[10]

$$\Delta\lambda = \frac{\lambda_0^2/2L}{[n-(dn/d\lambda)\lambda_0]} \qquad [9.5]$$

λ_0 – emission wavelength
L – cavity length
n – refractive index
$(dn/d\lambda)$ – refractive dispersion

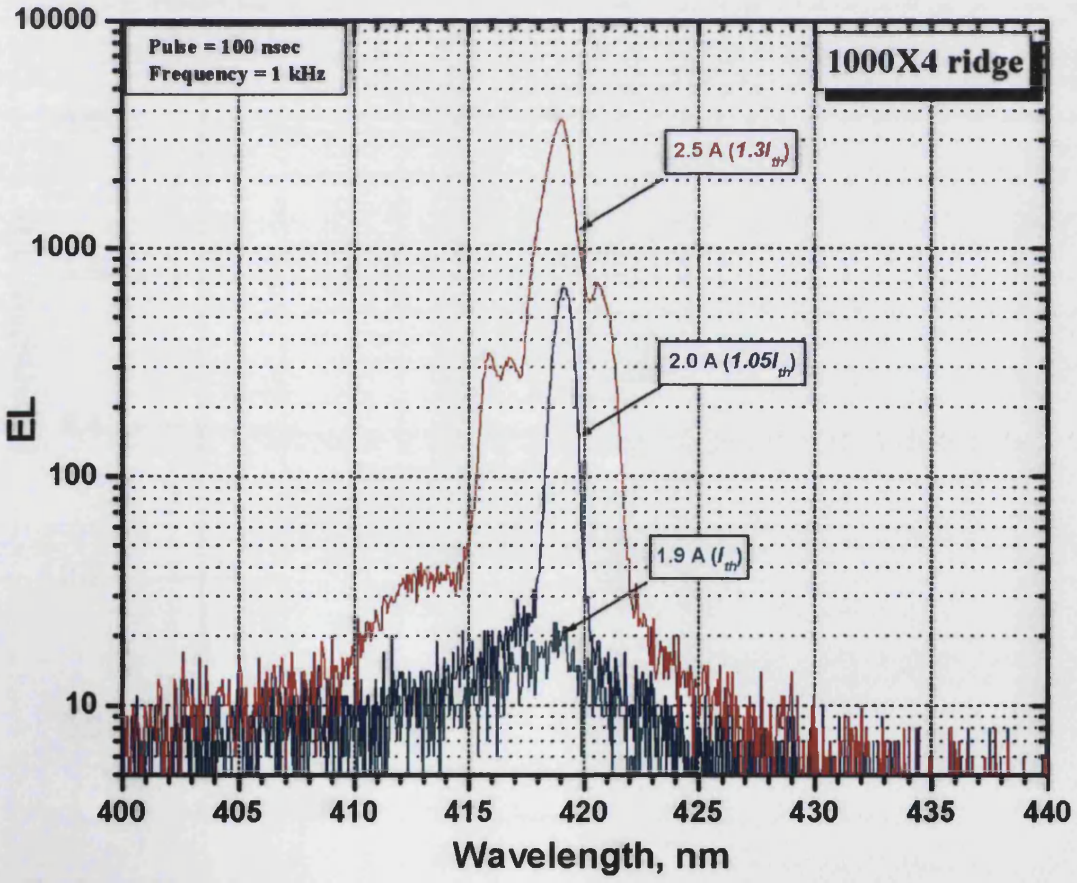

Fig. 9.3. Spectra measured from a laser diode (1000 μm-cavity length, 4 μm-ridge width) under pulsed current injection (100 ns pulse width, 1 kHz frequency).

For λ_0=419 nm, L=1000 μm, and $[n-(dn/d\lambda)\lambda_0]$=4.4 (Ref. 11) this equation gives a $\Delta\lambda$ value as low as 0.02 nm, which is impossible to resolve using our spectrograph. The observed spectral behavior is typical for InGaN-based laser diodes.[10, 12, 13, 14, 15, 16, 17, 18, 19] However, the origin of these subband emissions is not clear at present. Zubrilov *et al.*[20] suggested that they are caused by cracks within the laser cavity acting as short cavity mirrors. However, this phenomenon has also been observed for high quality structures with no cracks.[10, 18] Nakamura *et al.* performed measurements under different pulse widths and found no significant difference in the spectra. The authors concluded that the spectral changes were not caused by a change in temperature. High-resolution cross-sectional transmission electron microscopy (TEM) showed periodic indium composition fluctuations in the InGaN well layers, which were related to InGaN phase separation during growth. Thus, laser emission was suggested to originate from InGaN quantum dot-like states. The subband emissions were ascribed to the transitions between the subband energy levels of the different size InGaN quantum dots formed from In-rich regions in the InGaN well layers.

9.2.3 Near-field and far-field patterns

The transition from spontaneous to stimulated emission was also noticed from the change in near-field and far-field patterns. Typical near-field intensity profiles measured by Dr. Federica Causa (Dept. of Electronic and Electrical Engineering, Bath University) in the lateral direction from the same 1000×4 μm^2 LD are presented in Fig. 9.4. The profiles

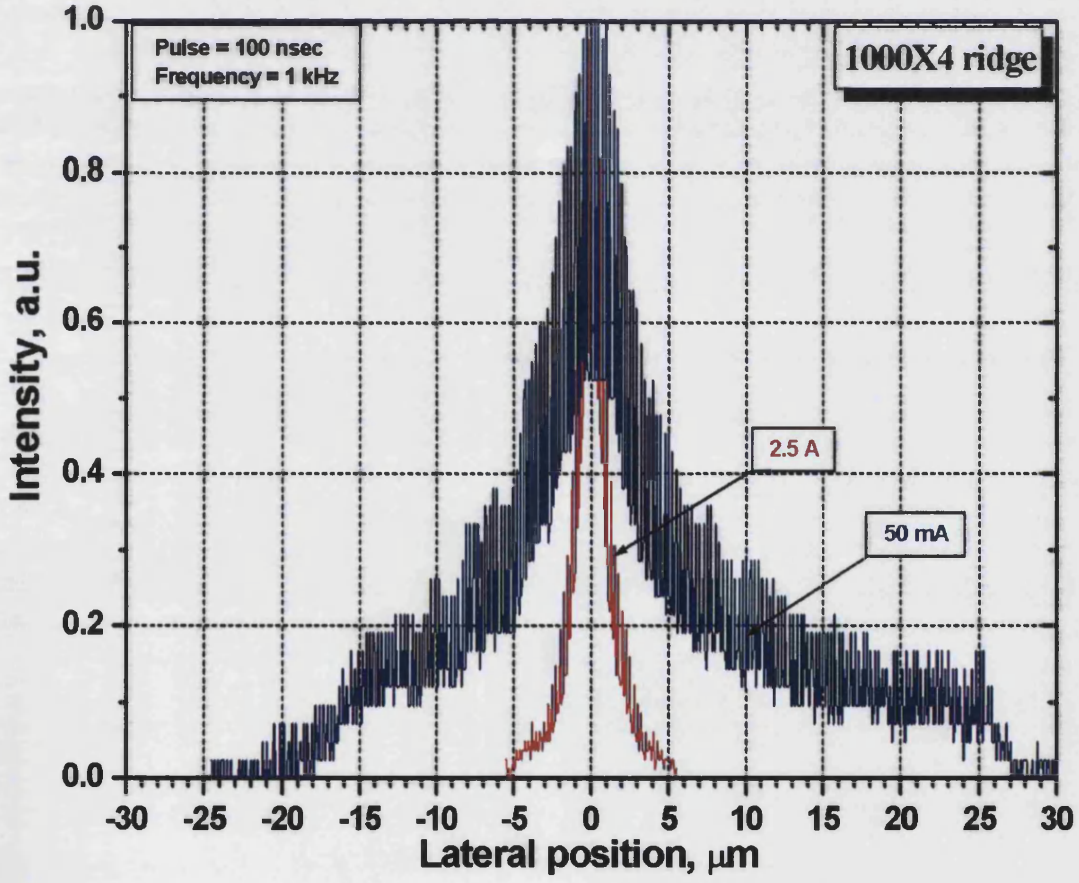

Fig. 9.4. Normalized near-field intensity profiles measured from a laser diode (1000 μm-cavity length, 4 μm-ridge width) under pulsed current injection (100 ns pulse width, 1 kHz frequency) below (50 mA) and above (2.5 A) the threshold.

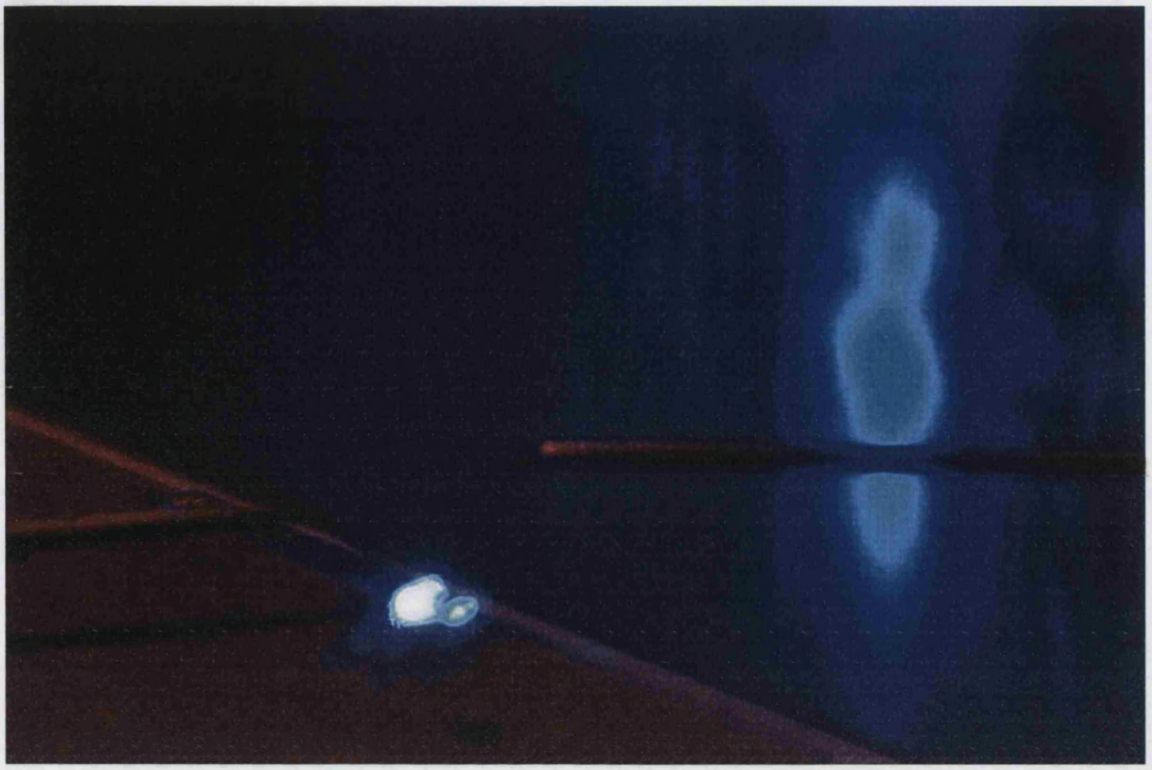

Fig. 9.5. Far-field pattern detected from a laser diode (1000 μm-cavity length, 4 μm-ridge width) under pulsed current injection (100 ns pulse width, 1 kHz frequency) at a current of 2.5 A.

were measured under pulsed current injection (100 ns pulse width, 1 kHz frequency) below (50 mA) and above (2.5 A) the threshold and normalized for comparison. As can be seen, above the threshold current the emission was well confined within a narrow region defined by the ridge stripe, whereas below threshold light propagated fairly far from the stripe. The FWHM of the intensity at an injection current of 50 mA and 2.5 A was estimated to be 8 and 2 μm, respectively. This indicates good current and optical confinement in the lateral direction.

A typical far-field pattern obtained from the same LD under a pulsed current of 2.5 A is shown in Fig. 9.5. The divergence of the laser beam in the vertical and lateral directions was estimated to be 30° and 8°, respectively. It was difficult to determine FWHM levels and the beam aspect ratio due to the absence of appropriate equipment. As can be seen, several light spots were present in the pattern. This probably indicates some contribution from higher order modes in the vertical direction. Thereby, some optimization of the laser structure is required to improve the vertical optical confinement for single-mode operation.

9.3 References

[1] L. Shon-Roy, A. Wiesnoski, and R. Zorich, *Advanced Semiconductor Fabrication Handbook.* Integrated Circuit Engineering Corporation (ICE), (1998).

[2] S. King, J. Barnak, M. Bremser, K. Tracy, C. Ronning, R. Davis and R. Nemanich, J. Appl. Phys. 84, 5248 (1998).

[3] L. A. Coldren and S. W. Corzine, *Diode Lasers and Photonic Integrated Circuits* (Wiley, New York, 1995).

[4] M. P. Mack, G. D. Via, A. C. Abare, M. Hansen, P. Kozodoy, S. Keller, J. S. Speck, U. K. Mishra, L. A. Coldren and S. P. DenBaars, Electon. Lett. 34, 1315 (1998).

[5] S. Nakamura, M. Senoh, S. Nagahama, N. Iwasa, T. Yamada, T. Matsushita, H. Kiyoku, Y. Sugimoto, T. Kozaki, H. Umemoto, M. Sano, and K. Chocho, Jpn. J. Appl. Phys. 37, L627 (1998).

[6] M. Hansen, P. Fini, L. Zhao, A. C. Abare, L. A. Coldren, J. S. Speck, S. P. DenBaars, Appl. Phys. Lett. 76, 529 (2000).

[7] S. Nakamura, Journal of Crystal Growth 201/202, 290 (1999).

[8] S. Nakamura, Semicond. Sci. Technol. 14, R27 (1999).

[9] S. Nakamura, M. Senoh, S. Nagahama, N. Iwasa, T. Yamada, T. Matsushita, H. Kiyoku, Y. Sugimoto, T. Kozaki, H. Umemoto, M. Sano, and K. Chocho, Jpn. J. Appl. Phys. 37, L1020 (1998).

[10] S. Nakamura, M. Senoh, S. Nagahama, N. Iwasa, T. Yamada, T. Matsushita, Y. Sugimoto, and H. Kiyoku, Appl. Phys. Lett. 69, 1568 (1996).

[11] R. L. Aggarwal, P. A. Maki, R. J. Molnar, Z. L. Liau, and I. Melngailis, J. Appl. Phys. 79, 2148 (1996).

[12] S. Nakamura, M. Senoh, S. Nagahama, N. Iwasa, T. Yamada, T. Matsushita, Y. Sugimoto, and H. Kiyoku, Appl. Phys. Lett. 69, 1477 (1996).

[13] S. Nakamura, M. Senoh, S. Nagahama, N. Iwasa, T. Yamada, T. Matsushita, H. Kiyoku, and Y. Sugimoto, Jpn. J. Appl. Phys. 35, L174 (1996).

[14] S. Nakamura, M. Senoh, S. Nagahama, N. Iwasa, T. Yamada, T. Matsushita, H. Kiyoku, and Y. Sugimoto, Jpn. J. Appl. Phys. 35, L217 (1996).

[15] S. Nakamura, M. Senoh, S. Nagahama, N. Iwasa, T. Yamada, T. Matsushita, H. Kiyoku, and Y. Sugimoto, Appl. Phys. Lett. 68, 2105 (1996).

[16] S. Nakamura, Adv. Mater. 8, 689 (1996).

[17] S. Nakamura, M. Senoh, S. Nagahama, N. Iwasa, T. Yamada, T. Matsushita, Y. Sugimoto, and H. Kiyoku, Appl. Phys. Lett. 70, 616 (1997).

[18] S. Nakamura, M. Senoh, S. Nagahama, N. Iwasa, T. Yamada, T. Matsushita, Y. Sugimoto, and H. Kiyoku, Appl. Phys. Lett. 70, 2753 (1997).

[19] S. Nakamura, IEEE journal of selected topics in quantum electronics 3, 435 (1997).

[20] A. S. Zubrilov, V. I. Nikolaev, D. V. Tsvetkov, V. A. Dmitriev, K. G. Irvine, J. A. Edmond, and C. H. Carter, Appl. Phys. Lett. 67, 533 (1995).

10 Conclusion

III-nitride blue-violet laser diodes are very attractive for a variety of applications, such as optical data-storage, laser printing, optical scanners, high-resolution photolithography, biomedical technology, sensing, telecommunication devices, laser projection displays, etc. A number of groups around the world have concentrated their efforts on the development of GaN-based laser diodes. Some of them have succeeded in this research and demonstrated laser emission either under pulsed or continuous wave (CW) current operation. However, leading players in this field are well-known companies producing electronics. To our knowledge only six universities, including the University of Bath, have reported on successful realization of III-nitride pulsed laser diodes. We are the first university in the UK to successfully fabricate a pulsed GaN-based laser diode, and still the only university in the UK to conduct all post-growth laser fabrication processes in-house. Within our group, I was responsible for the development of the post-growth technology. The successful realization of laser diodes demonstrates that the developed technology, presented in this dissertation, is very promising for implementation and further optimization.

The fabricated lasers with uncoated facets demonstrated laser emission wavelengths ranging from 416 to 420 nm for different devices, threshold current densities from 48 to 113 kA/cm^2, external differential quantum efficiency in the range of 0.3–2.8%, and output optical powers from 10 to 75 mW per facet. It was shown that high reflectivity (HR) facet coatings can noticeably reduce the threshold current. The laser diodes had very low series resistances from 0.6 to 3.3 Ω depending on laser cavity width and length. This implies excellent electrical characteristics of the devices and no or very low damage in the structure produced by the post-growth processing. Unfortunately, the threshold currents were excessively high for these devices to operate under DC current. Furthermore, the external differential quantum efficiency was too low compared to that for the best devices fabricated around the world. We suggest that overgrowth techniques (epitaxial lateral overgrowth (ELOG) or pendeo-epitaxy) should significantly improve laser characteristics by reducing the density of threading dislocations in the waveguide region. The dislocations induce nonradiative recombination and scattering of laser light and, hence, cause low internal quantum efficiency and large internal loss in the structure. The optimization of the laser structure (lower number of quantum wells in the active region) is expected to reduce the threshold current density further. Some optimization of the structure is also required for transverse single-mode operation, required for a DVD application, because the far-field pattern detected from our lasers showed some contribution from higher order modes in the vertical direction. The developed post-growth technology applied for the following optimized structures is expected to demonstrate laser diodes with improved optical characteristics.

A number of technological processes was developed and/or optimized within my research for the post-growth laser fabrication technology. Some of them can also be practical for other III-nitride applications. A key process of the technology is an innovative ridge waveguide fabrication process, described in Chapter 5. This considerably simplifies the laser fabrication due to a self-alignment technique employed. Thus no precise photolithography equipment is required and no surface damage is produced before *p*-contact deposition. This results in the excellent electrical characteristics of laser diodes. The process can be employed for the fabrication of any small-scale electronic devices, which also require the etching through a structure, passivation of etched sidewalls, and top-contact deposition. The fabrication of standard optoelectronic devices, such as light emitting diodes (LEDs), can also be simplified by using this technique.